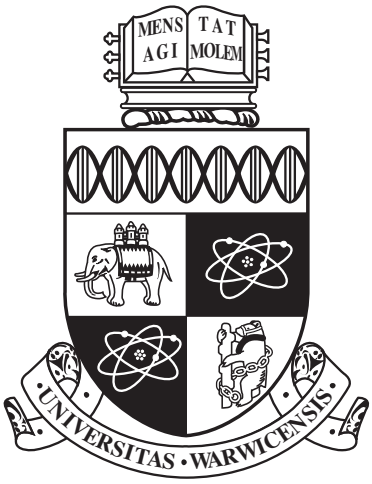

Nonlinear and multi-modal oscillatory processes in active regions of the solar atmosphere

by

Dmitrii Kolotkov

Thesis

Submitted to the University of Warwick

for the degree of

Doctor of Philosophy

Department of Physics

March 2017

THE UNIVERSITY OF
WARWICK

Contents

To my lovely wife and beautiful mother
Моей любимой жене и милой маме

Acknowledgments

I would like to thank my supervisor Prof. Valery Nakariakov for his support throughout my PhD course. I am also grateful to my co-authors and colleagues: Sergey Anfinogentov, Andrey Afanasyev, Anne-Marie Broomhal, Daniel O'Connell, Bogdan Hnat, Elena Kupriyanova, Giuseppe Nisticò, David Pascoe, Ivan Vasko, George Rowlands, Ivan Zimovets, for stimulating discussions and constructive comments. Special thanks go to Warwick Postgraduate Coordinator, Susan Tatlock, for her timely assistance and priceless advice.

Declarations

I declare that this thesis is my own work except where indicated. It has not been submitted for a degree at another university. The results presented in this thesis are based on the following peer-reviewed journal articles (8 published and 1 submitted):

- D. Y. Kolotkov, V. V. Smirnova, P. V. Strekalova, A. Riehokainen, and V. M. Nakariakov, Long-period quasi-periodic oscillations of a small-scale magnetic structure on the Sun, *Astronomy and Astrophysics*, 598:L2, 2017.
- D. Y. Kolotkov, S. A. Anfinogentov, and V. M. Nakariakov, Empirical mode decomposition analysis of random processes in the solar atmosphere, *Astronomy and Astrophysics*, 592:A153, 2016.
- D. Y. Kolotkov, V. M. Nakariakov, and G. Rowlands, Nonlinear oscillations of coalescing magnetic flux ropes, *Physical Review E*, 93(5):053205, 2016.
- D. Y. Kolotkov, G. Nisticò, and V. M. Nakariakov, Transverse oscillations and stability of prominences in a magnetic field dip, *Astronomy and Astrophysics*, 590:A120, 2016.
- V. M. Nakariakov, V. Pilipenko, B. Heilig, P. Jelínek, M. Karlický, D. Y. Klimushkin, D. Y. Kolotkov, et al., Magnetohydrodynamic oscillations in the solar corona and Earth's magnetosphere: towards consolidated understanding, *Space Science Reviews*, 200:75–203, 2016.
- D. Y. Kolotkov, I. Y. Vasko, and V. M. Nakariakov, Kinetic model of force-free current sheets with non-uniform temperature, *Physics of Plasmas*, 22(11):112902, 2015.

- D. Y. Kolotkov, A.-M. Broomhall, and V. M. Nakariakov, Hilbert–Huang transform analysis of periodicities in the last two solar activity cycles, *Monthly Notices of the Royal Astronomical Society*, 451:4360–4367, 2015.

- D. Y. Kolotkov, V. M. Nakariakov, E. G. Kupriyanova, H. Ratcliffe, and K. Shibasaki, Multi-mode quasi-periodic pulsations in a solar flare, *Astronomy and Astrophysics*, 574:A53, 2015.

- D. Y. Kolotkov, G. Rowlands, G. Nisticò, and V. M. Nakariakov, Finite amplitude transverse oscillations of prominences in a magnetic field dip (*submitted*).

and have been partly reported at the following scientific conferences and workshops:

- 1st ISSI Workshop "Quasi-periodic Pulsations in Stellar Flares: a Tool for Studying the Solar-Stellar Connection ", February–March 2017, Bern, Switzerland.
  Oral talk: *Nonlinear oscillations of coalescing magnetic ropes*
  Oral talk: *Hilbert–Huang Transform analysis of solar quasi-periodicities*

- 5th RadioSun Workshop, May 2016, Ceske Budejovice, Czech Republic.
  Oral talk: *Nonlinear oscillations of coalescing magnetic islands*

- Solar and Solar-Terrestrial Physics, October 2015, Pulkovo Observatory, Saint Petersburg, Russia.
  Oral talk: *Self-oscillations of a current sheet generated by the coalescence instability*

- 3rd SOLARNET Meeting "The Sun, the stars, and solar-stellar relations", September 2015, Freiburg, Germany.
  Poster session: *Empirical mode decomposition studies of quasi-biennial variations in helioseismic frequencies*

- 4th RadioSun Workshop, June 2015, Irkutsk, Russia.
  Oral talk: *Hilbert–Huang transform analysis of QPP in a solar flare in the radio band*

- Plasma Physics in Solar System, February 2015, Space Research Institute (IKI), Moscow, Russia.
  Poster session: *Hilbert–Huang analysis of periodicities in the last two solar activity cycles*

- 3rd ISSI Workshop "MHD Oscillations in the Solar Corona and Earth's Magnetosphere: Towards Consolidated Understanding", December 2014, Bern, Switzerland.
  Invited talk: *Analysis of nonlinear QPPs in solar flares*

- Nobeyama Solar Radiophysics symposium, September 2014, Nobeyama, Japan.
  Invited talk: *Nonlinear quasi-periodic pulsations in solar flares*

- 3rd RadioSun Workshop "Solar Flares and Energetic Particles", August 2014, Pulkovo Observatory, Saint Petersburg, Russia.
  Oral talk: *Nonlinear properties of QPPs in solar flares*

Abstract

For longer than a century, analysis of a quasi-periodic variability of the Sun on various time scales has been attracting great interest among the research community. These signals are continuously detected throughout the whole electromagnetic spectrum, and often have non-stationary oscillation periods and irregular profile shapes. The physical mechanisms responsible for such variations are usually hidden, and their revealing always require an advanced combination of powerful spectral techniques and strong theoretical foundations. This thesis considers oscillatory phenomena occurring in the solar atmosphere from these two perspectives.

For the spectral analysis of solar periodicities the self-adaptive Hilbert–Huang transform (HHT) method is employed. With the statistics of coloured noises incorporated, it allowed for the detection of a long-period oscillation of a small-scale photospheric magnetic structure, whose period grows from 80 to 230 min and positively correlates with the amplitude. A multi-modal nature of the solar flare quasi-periodic pulsations was also revealed with HHT. The detected intrinsic modes have mean periods of 15, 45, and 100 s, and can be interpreted as the kink and sausage magnetohydrodynamic oscillations of a flaring loop. Analysis of much longer solar periodicities associated with the magnetic activity cycles 22, 23, and 24 was also successfully performed with HHT, revealing a broad range of intrinsic modes with periods from about a month to several years (including the 11 yr cycle).

From the theoretical point of view, the one-dimensional equilibrium and dynamical models of current sheets in the corona have been developed. The equilibrium model provides an inhomogeneous distribution of macroscopic plasma parameters

across the current sheet, as found for realistic physical conditions. The dynamical model describes nonlinear oscillations of the current sheet formed by the coalescence of two magnetic flux ropes. The oscillation period is found to be about the ion plasma period or longer, and is prescribed by the current sheet thickness, the plasma parameter β, and the oscillation amplitude.

Analytical modelling of finite amplitude transverse oscillations in quiescent prominences situated in a magnetic field dip, is also performed in the thesis. The model is based on the line-current concept and accounts for the interaction of the prominence current with the electrically conductive photosphere. In the linear regime, the horizontal and vertical motions are considered independently, and the mechanical stability of the system is analysed. The oscillation periods are determined by the prominence current, its mass and height above the photosphere, and the properties of the magnetic dip. In the case of finite amplitudes, the horizontal and vertical modes were found to be nonlinearly coupled with each other, and a metastable equilibrium state of the prominence was revealed. The periods of nonlinear oscillations are shown to depend upon the oscillation amplitude.

Chapter 1

Introduction

Is our nearest star, the Sun, a rather quiet and boring astronomical object, or does it still provide us with research challenges full of rich interesting physics? Traditionally, the term "quiet" is indeed often applied to the Sun, characterising it as a steadily evolving massive plasma ball. However at the same time numerous observational results, continuously being obtained during the last several centuries and of continuously improved instrumental resolution and sensitivity, evidently show the presence of a variety of dynamical and transient phenomena of vast complexity, superimposed on a quiet solar atmosphere. These phenomena have very different manifestations, including rapid coronal mass ejections (CMEs), relatively cold sunspots and mysteriously levitating prominences, recently discovered solar "tsunamis", coronal holes, and solar flares. This chapter partly based on the work by Nakariakov et al. [2016b], gives state-of-the-art insights into the physics of some of them.

1.1 The atmosphere of the Sun: photosphere, chromosphere, and corona

The solar atmosphere is generally defined as the outer part of the Sun where the photons produced in the solar interior are able to escape into outer space. It is usually considered to consist of three quasi-spherical plasma shells, which can be distinguished by their unique physical properties (see Fig. 1.1). The inner, relatively thin (of a few hundred kilometres) and dense ($\sim 10^{-5} - 10^{-3}$ kg m^{-3}) layer with the lowest temperature of several thousand K is the *photosphere*. It is responsible for a major part of the solar radiation and is optically thick throughout the whole electromagnetic spectrum except for the optical band and its vicinity. This makes the photosphere to be the only solar surface visible to the naked human eye. Being

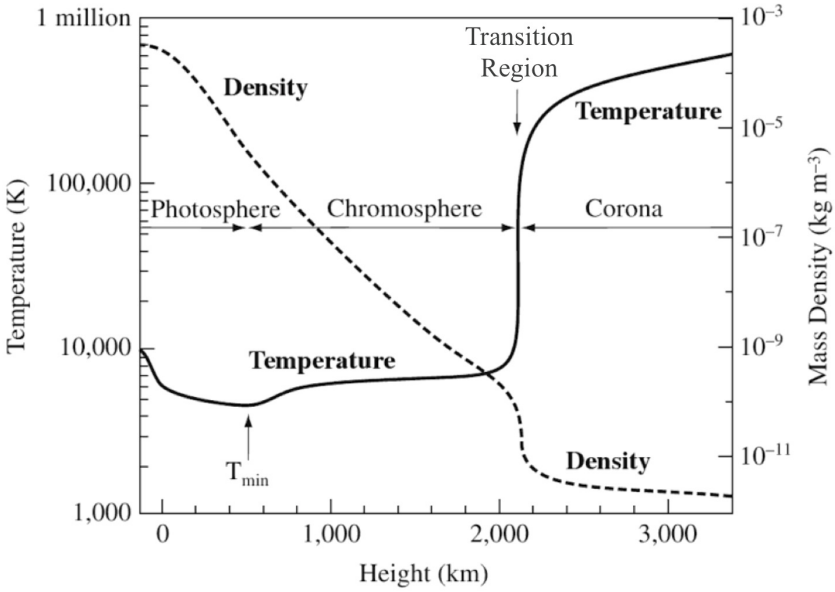

Figure 1.1: Schematic structure of the quiet solar atmosphere, i.e. the variation of the mean temperature (thick solid line) and density (dashed line) with height [adapted from Priest, 2014].

a highly dynamical medium (see e.g. Sec. 2.2, where the presence of randomly distributed processes in the solar atmosphere is shown), the photosphere represents a continuously "boiling" plasma with several types of convective motions, for example granulation and supergranulation. These bright and hot granules with a typical size of about 1 Mm are seen to cover the whole surface of the photosphere, being separated by intergranular lanes of a few hundred kilometres wide. A typical granule lifetime ranges from about 1 to 20 min. In contrast, larger-scale convective structures, supergranules, have typical sizes from about 20 to 70 Mm, and last up to a few days. Various smaller-scale structures widely manifested in the higher layers of the solar atmosphere also often have their origin at the photosphere. For instance, photospheric faculae are the magnetic elements with a diameter of a hundred kilometres or less, situated in the intergranular lanes and typically varying on the time scale of a few minutes [see e.g. Kostik and Khomenko, 2016]. Longer-period variations of these facular structures are rather exotic events, and one of them is presented in Sec. 2.3, where such a small-scale photospheric magnetic element is observed to oscillate with a period of a few hours. Another important ingredient of the photosphere is a sunspot. It is a cool and dark (relative to the surrounding plasma) photospheric region of a large concentration of nearly vertical unipolar magnetic

field lines with a typical strength of a few kilogauss, appearing during the magnetic flux emergence. Sunspots are usually about 4 to 60 Mm in diameter, while their lifetime changes proportionally to their area, typically from a few days to a few months. Sunspots are also known to be efficient waveguides and resonators supporting various oscillatory phenomena. In particular, an example of a 3-min sunspot oscillation accompanied by small-scale quasi-periodic random processes in a sunspot umbra, is considered in Sec. 2.2. Large-scale conglomerates of sunspot groups of different polarities are known as active regions. On average, in the Northern and Southern hemispheres of the Sun there is always a domination of a certain magnetic polarity, i.e. for about 11 yr one of the hemispheres is more magnetically "positive" and the other is more "negative". Then the polarity swaps, thus forming a continuous long-term chain of minimum and maximum solar activity, known as the 11 yr solar cycle [Hathaway, 2010]. Shorter-term periodicities of the global magnetic activity of the Sun, for example quasi-biennial (1–4 yr) and Reiger-type (shorter than 1 yr) oscillations, appearing over the cycles 22, 23, and 24 are addressed in Sec. 2.4.

The layer of the solar atmosphere, lying just above the photosphere, is the *chromosphere*. It is a partly-ionised, rarefied and more transparent plasma observed in the optical, ultraviolet (UV), and X-ray spectral bands. Its temperature increases gradually from about 4,500 K (the temperature minimum, see Fig. 1.1) to 10,000 K, then changes dramatically to coronal values of about 1 million K through a narrow *transition region*. Similarly to the photosphere, the chromosphere is a highly inhomogeneous and dynamic medium. It is full of various fine-scale objects and phenomena, including spicules (chromospheric plasma jets) typically observed at the limb, disk-situated fibrils, flare-induced particle beams and wave motions, and what is probably the most important – a network of the chromospheric magnetic field. It is anchored at the boundaries of photospheric supergranulation cells, and continuously spreads out with height as the background density rapidly decreases. The decrease in density leads to the decrease of the thermal pressure (according to the equation of state). Taking into account the equilibrium condition, which is the balance of the total pressure inside and outside the structure, and conservation of the magnetic flux, this process eventually forms wineglass-shaped magnetic funnels and magnetic arcs higher in the solar atmosphere. These magnetic non-uniformities play a key role in guiding of the magnetoacoustic and Alfvén magnetohydrodynamic (MHD) modes, which are believed to significantly contribute to the heating of the chromosphere [Pascoe et al., 2013; Brady and Arber, 2016].

The *corona* is the upper-most region of the solar atmosphere. It consists of a highly-ionised low-density plasma (by several orders of magnitude lower than

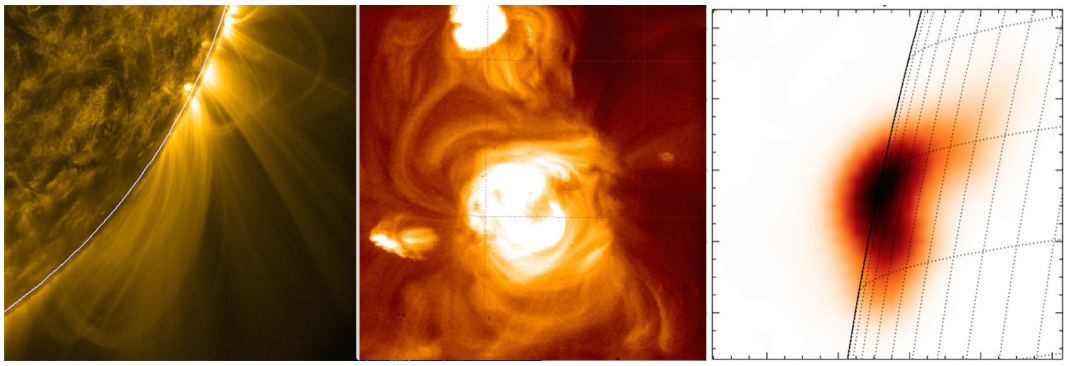

Figure 1.2: Typical examples of plasma loops in the solar corona, observed in the EUV band with the Atmospheric Imaging Assembly instrument of the Solar Dynamics Observatory (SDO/AIA) in the 171 Å channel (left-hand panel), soft X-rays with the Hinode X-Ray Telescope (XRT) (middle panel), and in microwaves with the Nobeyama Radioheliograph (NoRH) at 17 GHz (right-hand panel).

the chromospheric plasma density, see Fig. 1.1) with very high temperatures of about a million K, and reaching several tens of million K in extreme impulsive energy releases, including solar flares. Observational manifestations and aspects of a standard model of solar flares are addressed in detail in Sec. 1.2.1. The coronal plasma emits in the majority of observational bands in the optically thin regime and is mainly observed in the extreme ultraviolet (EUV) and soft X-ray wavelengths. The corona extends outwards from the Sun up to several tens of solar radii, $R_\odot$ ($R_\odot \approx 696\,\mathrm{Mm}$). At about several $R_\odot$ from the solar surface it is usually referred to as the solar wind, a continuous flow of plasma outwards from the Sun, that reaches supersonic or super-Alfvénic outward speeds of several hundreds of $\mathrm{km\,s^{-1}}$. The corona is penetrated by the magnetic field emerged from lower altitudes of the solar atmosphere, providing a very complex and essentially non-dipolar magnetic configuration. In particular, there are closed coronal magnetic configurations in which the field lines begin and end at the surface of the Sun, and open magnetic configurations with the field lines extending to outer space. The coronal value of the plasma parameter β defined as the ratio of gas and magnetic pressures, varies from a few percent in the quiet corona to about 0.5 in flaring regions [e.g. Shibasaki, 2001]. Additionally, some magnetic flux tubes are filled in with the plasma, which is typically by a factor of 3–5 denser than the surrounding coronal plasma. This density contrast can reach 100 in flaring sites. In a closed magnetic configuration such plasma structures have a loop-like geometry, and are usually referred to as coronal loops. Observational examples of typical coronal loops visible in the EUV,

soft X-ray, and microwave bands are shown in Fig. 1.2. Natural and externally-driven MHD oscillations of coronal loops are thought to produce various quasi-periodic pulsations (QPP) of the electromagnetic emission measured in solar flares. More details on this phenomenon, including other alternative physical mechanisms which can be responsible for solar flare quasi-periodicities, are given in Sec. 1.2.2. An example of such QPPs observed in a solar flare light curve in microwaves and interpreted in terms of two natural magnetoacoustic modes of a flaring loop, is shown in Sec. 2.5.

The described model of the solar atmosphere successfully fits a number of observational results and is extremely useful. However, one should admit that it is a simple one-dimensional average representation reflecting only the mean physical properties. In practice, the solar atmosphere is a highly inhomogeneous, dynamic and time-varying plasma with continuously changing temperature and density at each certain location. Hence, more realistic three-dimensional numerical models, which account for more sophisticated dynamical effects, are needed [see e.g. Gudiksen et al., 2011]. Despite intensive studies and numerous interesting and constructive results, many challenging questions in the physics of the solar atmosphere still remain unresolved. For instance, the increase in the temperature of the corona with respect to the cooler photosphere and chromosphere, and the observed high, up to 1000 $\mathrm{km\,s^{-1}}$, speeds of the solar wind constitute the "coronal heating" and "solar wind acceleration" problems, respectively. They both are commonly thought to be related to the conversion of the magnetic energy, while the specific mechanisms are still intensively debated [see e.g. Cranmer, 2012; Reale, 2014; Klimchuk, 2015]. Confident predictions of a long-term variability of the global solar magnetic activity, including the 11 yr solar cycle, are also still among the most long-standing topics of the solar physics. In particular, Pesnell [2008] summarised more than 50 different independent predictions of the amplitude of solar cycle 24, and revealed huge, up to 65%, relative uncertainties. The latter issue is directly connected to the dynamo process, which is believed to be responsible for the creation of the magnetic field below the solar surface. However, its particular models are also very much debated [see e.g. Charbonneau, 2010], and hence do not yet possess a predictive capability. Forecasting of the impulsive energy releases in the solar corona, such as solar flares and CMEs, and understanding of the physical mechanisms involved in their triggering are also of great importance [see e.g. Nakariakov et al., 2016b]. The interest is stimulated by the possibility that these coronal phenomena may directly affect the Earth and near-Earth space, playing the role of effective drivers of extreme geo-effective events of space weather.

1.2 Solar flares

1.2.1 Solar flares: observations and model

Observationally, a flare phenomenon could be defined as "a brightening of any emission across the electromagnetic spectrum occurring at a time scale of minutes" [Benz, 2008]. Sometimes this "scale of minutes" is extended for up to several hours, releasing up to 10^{26} J of energy in a form of electromagnetic radiation (from radio to gamma-rays), and producing an effective plasma heating and induced bulk flows. The question of physical mechanisms for such impulsive energy releases still remains unanswered in detail, and is therefore very attractive for researchers. In particular, it is already confidently proved that solar flares occur due to the conversion of magnetic energy into the kinetic energy of accelerated charged particles and induced plasma jets, and the internal energy of the plasma, with the temperature reaching several tens of million K. Reconnection of magnetic field lines is commonly accepted as the basic mechanism for this in a standard scenario of a solar flare.

Solar flares are usually visible in all observational bands. A typical example of the light curves of the integrated (over the solar disk) solar emission during a solar flare is presented in Fig. 1.3. The observations were made simultaneously with the Nobeyama Radioheliograph [NoRH, Nakajima et al., 1994], the Ramaty High Energy Solar Spectroscopic Imager [RHESSI, Lin et al., 2002], and the Russian SOlar Neutrons and Gamma-rays experiment (SONG) onboard CORONAS-F satellite [e.g. Myagkova et al., 2007]. Specific physical mechanisms responsible for the recorded emissions vary from bremsstrahlung radiation of colliding electrons accelerated by a flare trigger (for hard X-rays), to the gyrosynchrotron radiation of mildly relativistic electrons trapped inside a flaring magnetic structure (for microwaves), and the thermal free-free emission of the plasma evaporated from the denser chromospheric material (for the white light, UV, EUV, microwaves and soft X-rays). The physical nature of the gamma-ray band emission is likely associated with nuclear processes, for example de-excitation, neutron capture, and positron annihilation, caused by the interaction of flare accelerated ions with dense plasma targets (e.g. the photosphere).

During the flare development, different physical mechanisms dominate in the emission. According to the timing of the emission recorded in different bands, one can distinguish between several phases of a typical solar flare [see e.g. Benz, 2008]. In the so-called "pre-flare phase" one observes increasing EUV and soft X-ray radiations emitted by a gradually heated plasma of the active region. Later on, a large number of electrically charged particles get accelerated, constituting

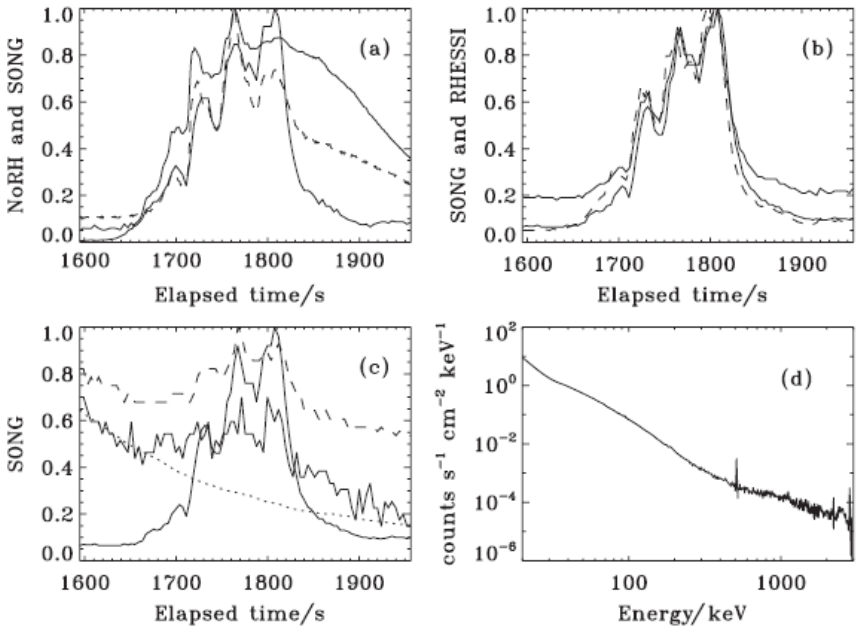

Figure 1.3: A typical solar flare occurred on 1 January 2005, with QPP of the microwave, hard X-ray and gamma-ray emission. Panel (a): intensity of the 17 GHz (solid) and 34 GHz (dashed) emissions recorded with the Nobeyama Radioheliograph, and the hard X-ray emission recorded with CORONAS-F/SONG at 42–80 keV (thick). Panel (b): 80–225 keV emission (thin) recorded with CORONAS-F/SONG; and 50–100 keV (dashed) and 100–300 keV (thick) emissions recorded with RHESSI. Panel (c): 80–225 keV (thick), 225–750 keV (dashed), and 2–6 MeV (thin solid) emissions recorded with CORONAS-F/SONG; the dashed curve shows the averaged 2–6 MeV light curve from previous orbits. The elapsed time starts at 00:00 UT on 1 January 2005. Panel (d): photon energy spectrum integrated between 00:28 UT and 00:32 UT, obtained with RHESSI. All light curves are normalised to their maximum values [taken from Nakariakov et al., 2010a].

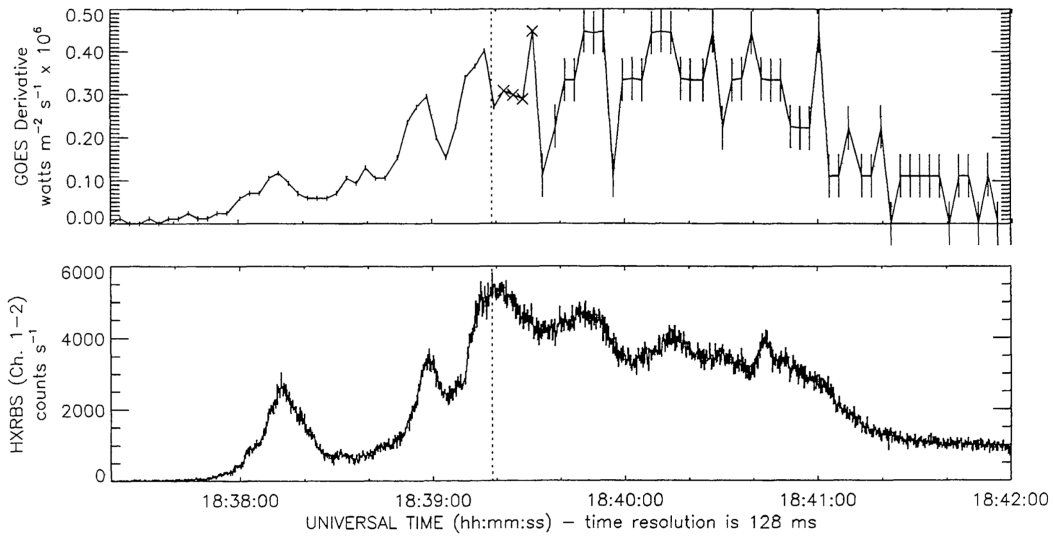

Figure 1.4: Top: Time derivative of the GOES soft X-ray (SXR) flux observed with a cadence of 3 s in a solar flare occurred on 27 March 1980. Vertical error bars represent 1-σ uncertainties generated by the digitization of the GOES data. Time interval corresponding to the GOES gain-change is replaced by the interpolated values and shown by $\times$-symbols. Bottom: Hard X-ray flux measured in the same flare with the Hard X-Ray Burst Spectrometer (HXRBS), with a time resolution of 128 ms. The vertical dotted lines in both panels indicate the position of the highest hard X-ray flux in the flare [adapted from Dennis and Zarro, 1993].

the "impulsive phase" which typically lasts up to several minutes only. In this phase hard X-ray and gamma-ray emissions rise rapidly, being often accompanied by numerous short but intense spikes, each lasting from a few seconds to tens of seconds (see e.g. Fig. 1.3). Some portion of the accelerated particles is trapped and gyrates around the magnetic field lines, producing the emission in the radio band. The following "flash phase" is characterised by the maximum of the soft X-ray and optical (in particular, Hα) emissions. After that the coronal plasma gradually returns to its initial state in the "decay phase". However, the consequent development of the flare still can be recognised in the solar corona as the follow-up magnetic reconfiguration, plasma ejections, decaying oscillations of various coronal plasma structures and radio bursts, and at the solar surface as sunquakes.

Typically, during the impulsive phase the time derivative of the soft X-ray emission is similar to the total fluxes of the hard X-ray and microwave emissions. This empirically established relationship is known as the Neupert effect [Neupert, 1968]. A very illustrative example of this effect is shown in Fig. 1.4: in the solar flare occurred on 27 March 1980, the time derivative of the soft X-ray (SXR) flux

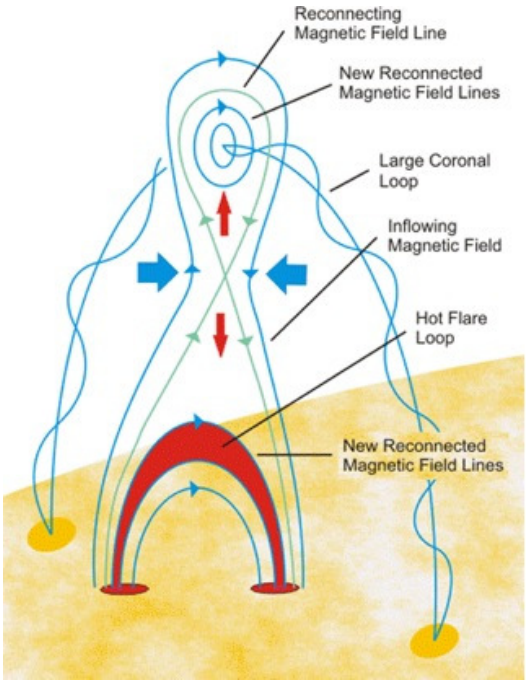

Figure 1.5: Schematic sketch of the standard model of a solar flare (courtesy Gordon Holman, NASA).

observed with the GOES satellite has a good correlation with the hard X-ray flux observed with the Hard X-Ray Burst Spectrometer (HXRBS), i.e. both light curves have nearly simultaneous peaks within the lowest time resolution provided (3 s for the SXR data). In fact, the importance of the Neupert effect is that it shows a direct relationship between the accelerated electrons and the thermal plasma in a flare. In other words, a thermal soft X-ray emission is produced in a plasma heated by energetic non-thermal electrons.

A schematic illustration of the standard model of a solar flare, based on the observational properties described above, is presented in Fig. 1.5. According to this model, the magnetic energy is initially accumulated in active regions of the corona in the form of non-potential fields. One of such magnetic configurations may become suddenly destabilised, and fast magnetic reconnection (occurring on the time scale of $10^2 - 10^4$ s) with the associated energy release begins. After a primary accelerating process at higher altitudes of the corona, associated with the release of the free magnetic energy by the phenomenon of magnetic reconnection, energetic superthermal electrons, usually having peak energies in the vicinity of 20 keV and extending sometimes to several tens of MeV, precipitate to the dense plasma in the

lower chromosphere. In the chromosphere which behaves as a thick target for these nearly relativistic particles, they lose all their kinetic energy by Coulomb collisions and produce hard X-ray bremsstrahlung emission until they finally become thermal. The chromospheric material is thus heated up to tens of million K and evaporates upwards into the corona. This evaporated thermal plasma fills in coronal magnetic flux tubes (coronal loops), emitting soft X-rays (see Fig. 1.2, where typical examples of solar coronal loop-like plasma structures are shown).

The mechanisms responsible for triggering solar flares are intensively debated in the literature and still remain unrevealed [see e.g. Shibata and Magara, 2011, for a recent comprehensive review]. However, the vast majority of views on the problem agrees that the magnetic reconnection works as a central engine of the flare production. Consider this process in more detail. Typically the onset of a flare starts with the emergence of the magnetic field into the surface of the Sun, carrying the magnetic energy from the solar interior where it is generated by dynamo, upwards to the atmosphere. This magnetic energy build-up can be characterised by the morphology of magnetic flux emergence, its dynamic and fragmented nature, and by the specific properties of magnetic structures eventually formed in the solar atmosphere [Shibata and Magara, 2011]. If the conductivity of the medium is high, as it is in the solar coronal plasma, the field-aligned electric current is not easy to dissipate, and it is stored as free energy, thus providing the energy source for flares and flare-associated phenomena and CMEs. However even a small value of resistivity can cause an effective Ohmic dissipation in the presence of large magnetic field gradients, i.e. high electric current densities, for example in current sheets. This dissipation may lead to a topological change of the magnetic field geometry – magnetic reconnection. This process releases the magnetic energy if the energy of the magnetic field in the new configuration is lower than in the initial one. Through this process the magnetic energy is converted to kinetic and thermal energies of the plasma. In addition, it is accompanied by the generation of a strong electric field, which can accelerate charged particles up to superthermal energies [see e.g. Priest and Forbes, 2000, for a detailed discussion of the concept]. Current sheets are believed to be a key element in the triggering of these magnetic energy releases and are certainly among the fundamental building blocks of various astrophysical plasma systems [e.g. Lui, 1996; Shibata and Magara, 2011]. The modelling of the processes occurring during the formation and evolution of current sheets is therefore of crucial importance (see e.g. Sec. 1.2.2). In particular, the equilibrium model of a force-free current sheet, allowing for a non-uniform transverse distribution of the plasma parameters in the current sheet, is developed in Sec. 3.1. Large am-

plitude oscillations of current sheets created by coalescing magnetic flux ropes are investigated in Sec. 3.2.

Here the basic models of magnetic reconnection are briefly overviewed, which are characterised by the speed of reconnection (or the reconnection rate) defined as the magnetic flux reconnecting per unit time, and the reconnection time defined by the reconnection rate and the spatial scale of the current sheet [Shibata and Magara, 2011]. In the incompressible Sweet–Parker model of magnetic reconnection [Sweet, 1958; Parker, 1957], based on a steady diffusion of the magnetic field in the current sheet, the estimated reconnection rate gives unrealistically long reconnection times, approximately of $10^8 - 10^9$ s for typical coronal conditions. This result is unacceptably long in comparison with the typical time scale of a flare, $10^2 - 10^4$ s. As this model cannot explain the rapid behaviour of a solar flare, the long-standing problem of fast reconnection is constituted. One of the possibilities to speed up the reconnection is offered by the Petschek model [Petschek, 1964], which accounts for the plasma compressibility and the appearance of magnetoacoustic shocks leading to a much faster energy release than in the Sweet–Parker case. The reconnection rate in the Petschek model can theoretically give a value of the reconnection time comparable to the real durations of flares. Forbes and Priest [1987] extended the Petschek model for a two-dimensional case, and demonstrated that the speed of the magnetic reconnection is also controlled by the spatial structure of the inflow region of the plasma around the current sheet. However, despite significant progress, the study of fast regimes of magnetic reconnection remains one of the central problems of plasma astrophysics.

In addition, one can phenomenologically distinguish two types of magnetic reconnection: driven reconnection [e.g. Sato and Hayashi, 1979] and spontaneous reconnection [e.g. Ugai and Tsuda, 1977], which both are important in the coronal plasma context. In the latter type, various small-scale processes, for example such as microinstabilities and microturbulences, operating inside the current sheet, are the primary factor inducing the fast reconnection by a local enhancement of the resistivity up to anomalous values. On the other hand, there is an issue connected with the origin of the external source causing the driven reconnection. Its identification is important as it determines, in particular, the time variation of the energy release rate.

1.2.2 Quasi-periodic pulsations (QPP) in solar flares

An interesting feature of flaring energy releases are quasi-periodic pulsations (QPP) often seen in the light curves of solar flares as a well-pronounced modulation of the

emission intensity. These quasi-periodic variations of the electromagnetic emission are observed throughout the whole electromagnetic spectrum, in the radio, white light, soft and hard X-ray, and gamma-ray bands. Typical periods of solar flare QPPs range from a fraction of a second to several minutes [see e.g. Sych et al., 2009; Jakimiec and Tomczak, 2010; Nakariakov et al., 2010a; Kupriyanova et al., 2010; Van Doorsselaere et al., 2011; Ning, 2014; Van Doorsselaere et al., 2016, for recent findings]. An example of QPPs is shown in Fig. 1.3 where the oscillation period is about 40 s, and QPPs are almost synchronous in all observation bands. Moreover, it often appears that QPPs exhibit non-stationary [see e.g. Nakariakov et al., 2010b] or multiple [see e.g. Kupriyanova et al., 2013, and Sec. 2.5] periods during the same event. Likewise, QPPs can have a well-pronounced amplitude modulation. Usually, the most pronounced QPPs are seen in the emission associated with non-thermal electrons, for example the gyrosynchrotron emission in the microwave band and bremsstrahlung in hard X-rays. However, QPPs are also detected in the soft X-ray radiation produced by the thermal free-free emission [Simões et al., 2015]. QPPs can be found in all stages of the flare development, from pre-flare to decay phases.

It is commonly accepted that QPPs can be produced by several non-exclusive mechanisms, such as modulation of the plasma parameters by MHD waves [e.g. Nakariakov and Melnikov, 2006], modulation of a non-thermal electron kinematics by MHD waves [e.g. Zaitsev and Stepanov, 1982], periodic triggering of energy releases by external MHD waves [e.g. Nakariakov et al., 2006], MHD flow over-stability [e.g. Ofman and Sui, 2006], and self-oscillatory regimes of magnetic reconnection [e.g. Kliem et al., 2000; Murray et al., 2009]. Short period QPPs, in the sub-second period range, could be also associated with wave-particle interactions [Aschwanden, 1987].

The importance of understanding solar QPPs is justified by several reasons. First of all, numerous studies showed that QPPs are a common and inherent feature of solar flares [see e.g. Van Doorsselaere et al., 2016, for the most recent review], carrying the information about mechanisms responsible for the energy releases, processes operating in them, and their triggering. However, the phenomenon of QPPs is not *a priori* predicted by any commonly accepted theoretical model of a flare. Hence the standard model of a flare described in Sec. 1.2.1 needs to be modified accordingly to account for observed QPPs. Besides this, another motivation is connected with a possible geophysical effect of QPPs. It is well known that strong solar electromagnetic radiation (especially produced in powerful flares) emitted towards the Earth can cause significant perturbations of physical parameters of the Earth's magnetosphere, ionosphere and upper atmosphere. It can also negatively affect spaceborne

and ground-based technological systems, for example causing distortions of the GPS navigation; disruptions of the long-distance radio communication; crucial electrical blackouts, such as the collapse of the Hydro-Quebec power network on 13 March 1989; affect on humans at and near the ground level (e.g. crews and passengers of transpolar plane routes). However such effects can hypothetically be caused even by relatively weak flares having QPPs in their light curves if the QPPs are in resonance with some geophysical oscillatory processes. Thus, understanding of QPP is certainly important for forecasting of geoeffectiveness of flares. In addition, QPPs have been recently detected in stellar flares, including superflares and megaflares too [see e.g. Anfinogentov et al., 2013; Pugh et al., 2016]. In the context of space weather it is important to understand whether similar devastating superflares and megaflares are possible on the Sun, and if they are, what their probability is. Stellar QPPs were found to be similar to those observed in solar flares [Cho et al., 2016], thus pointing out on the possible similarity of the physical processes operating in these phenomena.

MHD modes of a plasma cylinder

Wave and oscillatory phenomena in a plasma with spatial and temporal scales much longer than the ion gyroradii (typically $< 1,000$ m for almost all combinations of coronal parameters) and gyroperiods ($< 10^{-3}$ s), respectively, can be adequately described using magnetohydrodynamics. The set of ideal MHD equations considers a plasma as a single-fluid medium (assuming electrons to be inertialess and hence always providing the full electrical neutrality of the plasma), and links together the macroscopic parameters of the plasma: mass and electric current densities, temperature, gas pressure, bulk flow velocity, and the magnetic field. In the simplest case, the set of MHD equations includes the mass continuity equation, the Euler equation, the induction equation, and some form of the energy equation. On the other hand, collisionless plasma of the solar wind is observed to have anisotropic temperature distributions, i.e. the temperatures across and along the guiding field are different. This can be caused by numerous non-exclusive effects, for example such as ion-cyclotron resonance, local Ohmic heating, heating by Alfvén waves, and may lead to the development of various instabilities. In this case, the plasma pressure is a tensor with two independent components, each governed by a specific equation of state.

Linearisation of the set of ideal MHD equations over a uniform equilibrium reveals four basic types of solutions or modes. These four MHD wave modes are an essentially incompressive Alfvén wave, fast and slow magnetoacoustic waves,

which are both essentially compressive, and the entropy mode. In the ideal MHD approximation the real part of the frequency of the entropy mode is zero. According to their dispersion relation all MHD waves propagate in a uniform medium without dispersion, i.e. their phase and group speeds are independent of the frequency. The typical speeds of MHD waves are characterised by the sound speed $C_{\rm s} = (\gamma p_0/\rho_0)^{1/2}$ with the adiabatic index γ, normally taken to be from 1 to 5/3 in the corona, and the Alfvén speed, $C_{\rm A} = B_0/(\mu_0\rho_0)^{1/2}$, where μ_0 is the permeability of vacuum, B_0, p_0, and ρ_0 are the unperturbed values of the magnetic field, pressure, and mass density of the plasma, respectively. It is also useful to introduce the cusp or tube speed, $C_{\rm T} = C_{\rm s}C_{\rm A}/({C_{\rm A}}^2 + {C_{\rm s}}^2)^{1/2}$ that corresponds to the group speed of an oblique slow mode. Typical values of these speeds in coronal active regions vary from a hundred to a few thousand km $\rm s^{-1}$.

MHD waves are essentially anisotropic, their speeds strongly depend upon the angle α between the wave vector and the magnetic field. These dependencies are usually visualised by the polar plots for phase and group speeds. For example, in the case of a highly magnetised plasma (with the plasma $\beta < 1$) the phase speed of the Alfvén wave propagating strictly along the field (i.e. when $\alpha = 0$) is maximum and equals to $C_{\rm A}$, but it decreases in the case of oblique propagation, reaching zero in the perpendicular ($\alpha = \pi/2$) case. The phase speed of the slow magnetoacoustic wave is always lower than that of the Alfvén wave, but shows a similar behaviour: gradually decreases from the maximum value $C_{\rm s}$ to zero with α changing from 0 to $\pi/2$, respectively. The fast magnetoacoustic wave can propagate perpendicularly to the field with the fast phase speed $C_{\rm f} = ({C_{\rm A}}^2 + {C_{\rm s}}^2)^{1/2}$, which is certainly supersonic and super-Alfvénic. In the case of oblique propagation the phase speed of the fast mode decreases with α and tends to the Alfvén speed $C_{\rm A}$ in the limit of parallel propagation. In the strictly parallel direction the fast waves become incompressive. This classical picture of MHD wave propagation changes significantly in the presence of various plasma non-uniformities.

A standard theoretical model for linear MHD modes of coronal non-uniformities is based upon the interaction of MHD waves with a plasma cylinder stretched along the magnetic field. This simplified consideration addresses the main properties of various non-uniformities of the solar corona, for example such as coronal loops, jets, filaments, and other approximately axially-symmetric plasma structures that are characterised by the field-aligned filamentation.

Consider a straight cylindrical magnetic flux tube of a radius a, filled in with a uniform plasma of density ρ_0 and pressure p_0. The magnetic field B_0 is directed along the axis of the cylinder (see Fig. 1.6). The tube is embedded in an external

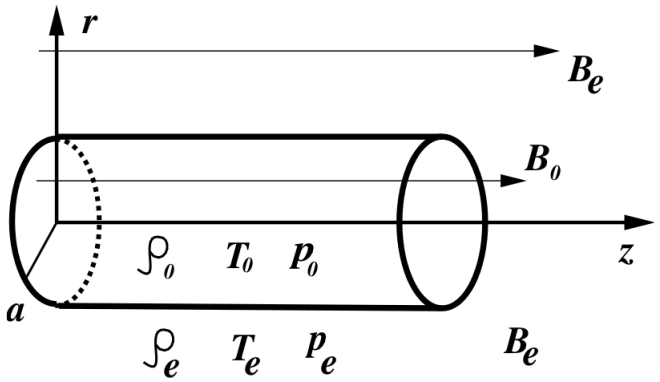

Figure 1.6: Typical model of a solar coronal plasma non-uniformity: a straight field-aligned plasma cylinder of the radius a, filled in with a uniform plasma, and embedded in an external magnetised plasma [the sketch was taken from Nakariakov and Verwichte, 2005].

plasma of density $\rho_{\rm e}$ and pressure $p_{\rm e}$ with magnetic field $B_{\rm e}$ that is also parallel to the axis of the cylinder. The equilibrium state of such a plasma configuration is determined by the balance of the total pressure, which is the sum of the plasma and magnetic pressures, at the boundary ($r = a$) of the cylinder. In the internal and external media, the sound speeds are $C_{\rm s0}$ and $C_{\rm se}$, the Alfvén speeds are $C_{\rm A0}$ and $C_{\rm Ae}$, and the tube speeds are $C_{\rm T0}$ and $C_{\rm Te}$, respectively. MHD modes supported by this model were originally determined by Zaitsev and Stepanov [1975]. Later on, their dispersion relation was independently derived by Edwin and Roberts [1983]. Besides this, the potential role of MHD waves in coronal heating was realised by Wentzel [1981]. Detailed aspects and the subsequent progress in the theoretical study of MHD modes of plasma non-uniformities are summarised by, for example, Nakariakov and Verwichte [2005], Nakariakov [2007], and Nakariakov and Melnikov [2009].

Linearising MHD equations with respect to the cylindrical equilibrium, and substituting linear perturbations in the Fourier-transformed form $\delta P(r)\exp[i(k_z z + m\phi - \omega t)]$, where the integer m is the azimuthal wave number and k_z is the parallel (or longitudinal) wave number, one obtains the following uncoupled equations

$$\omega^2 - C_{{\rm A}\alpha}^2 k_z^2 = 0, \tag{1.1}$$

$$\left[\frac{d^2}{dr^2} + \frac{1}{r}\frac{d}{dr} - \left(\kappa_\alpha^2 + \frac{m^2}{r^2}\right)\right]\delta P(r) = 0, \tag{1.2}$$

where the index $\alpha = 0, e$ labels the physical quantities inside and outside the cylin-

der, respectively, and κ_α is the transverse wave number defined as

$$\kappa_\alpha^2(\omega) = \frac{(k_z^2 C_{\mathrm{s}\alpha}^2 - \omega^2)(k_z^2 C_{\mathrm{A}\alpha}^2 - \omega^2)}{(C_{\mathrm{s}\alpha}^2 + C_{\mathrm{A}\alpha}^2)(k_z^2 C_{\mathrm{T}\alpha}^2 - \omega^2)}. \tag{1.3}$$

It is impossible to make the Fourier transform with respect to the r coordinate, because the medium is not uniform in this direction. Equations (1.1)–(1.2) represent both types of basic MHD solutions: torsional Alfvén waves whose dispersion relation has the form $\omega = \pm C_{\mathrm{A}\alpha} k_z$ (see Eq. (1.1)); and magnetoacoustic waves determined by Eq. (1.2) that is the Bessel equation describing the transverse structure of the perturbation. To match external and internal solutions the jump conditions are used: the continuity of the total pressure and the normal displacement at the cylinder's boundary $r = a$ [see e.g. Roberts, 1981a,b]. Solving the Bessel equations inside and outside the cylinder and matching the external and internal solutions with the use of the described boundary conditions, one can obtain the dispersion relation of the magnetoacoustic waves guided by the cylinder,

$$\rho_{\mathrm{e}}(\omega^2 - k_z^2 C_{\mathrm{Ae}}^2)\kappa_0 \frac{I_m'(\kappa_0 a)}{I_m(\kappa_0 a)} + \rho_0(k_z^2 C_{\mathrm{A}0}^2 - \omega^2)\kappa_{\mathrm{e}} \frac{K_m'(\kappa_{\mathrm{e}} a)}{K_m(\kappa_{\mathrm{e}} a)} = 0, \tag{1.4}$$

where $I_m(x)$ and $K_m(x)$ are the modified Bessel functions of the order m, with $I_m'(x)$ and $K_m'(x)$ being their first derivatives with respect to the argument x. In Eq. (1.4), κ_{e} plays the role of an effective refractive index of the external medium, and in dependence on its value two regimes of wave propagation are possible. More specifically, the case with $\kappa_{\mathrm{e}}^2 > 0$ corresponds to trapped modes, which are confined to the cylinder, and exponentially evanescent outside. In the opposite case of $\kappa_{\mathrm{e}}^2 < 0$ one obtains leaky modes, which have an oscillatory structure in the external medium and hence correspond to the radiation of oblique and perpendicular magnetoacoustic waves from the cylinder. In the following discussion, the condition $\kappa_{\mathrm{e},0} > 0$ is assumed to be fulfilled, i.e. the attention is concentrated only on trapped modes. More detailed theoretical aspects of the leaky regime can be found, for example, in Zaitsev and Stepanov [1975]; Cally [1986]; Vasheghani Farahani et al. [2014], while the recent numerical studies of these modes in the cylindrical and plane geometries are developed, in particular, by Nakariakov et al. [2012]; Hornsey et al. [2014].

In Fig. 1.7 a typical dispersion diagram for MHD modes of a coronal loop, combining the set of all possible trapped solutions of Eq. (1.4), is shown. The azimuthal symmetry of the modes is determined by the azimuthal wave number m: the waves with $m = 0$ are called sausage modes, waves with $m = \pm 1$ are kink modes, waves with higher $|m|$ are referred to as ballooning modes (only two types

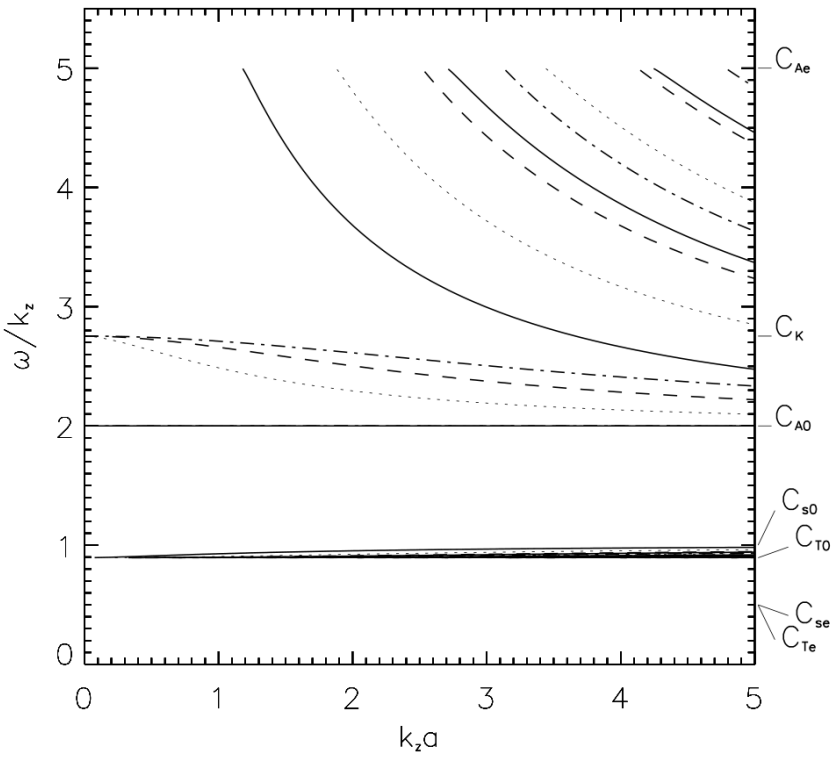

Figure 1.7: Dispersion diagram showing the real phase speed solutions of dispersion relation (1.4) for MHD waves in a magnetic cylinder as a function of the longitudinal wave number $k_z a$, normalised to the radius of the cylinder. The typical speeds in the internal and external media are normalised to the internal sound speed: $C_{\rm A0} = 2C_{\rm s0}$, $C_{\rm Ae} = 5C_{\rm s0}$, and $C_{\rm se} = 0.5C_{\rm s0}$, and are shown by the horizontal straight lines. The solid, dotted, dashed and dash-dotted curves correspond to solutions with the azimuthal wave number m equal to 0, 1, 2 and 3, respectively. For fast modes ($C_{\rm A0} < \omega/k_z < C_{\rm Ae}$), the lowest phase speed curves of each line style correspond to the radial $l = 0$ mode. The curves corresponding to higher l harmonics are located above in the top right corner. The torsional Alfvén solution is shown by the horizontal solid line at $\omega/k_z = C_{\rm A0}$ [Nakariakov and Verwichte, 2005].

of ballooning solutions with $|m| = 2$ and 3, are shown in Fig. 1.7, while other modes appear for higher k_z). Phase speeds of the trapped MHD modes guided by the cylinder occupy two distinct regions in the dispersion plot: they lie either between $C_{\rm A0}$ and $C_{\rm Ae}$ (in a typical coronal loop $C_{\rm A0} < C_{\rm Ae}$, so that $B_0 < B_{\rm e}$), or between $C_{\rm T0}$ and $C_{\rm s0}$. The wave modes in these two bands are the modified fast and slow magnetoacoustic waves, respectively. Despite this apparent classification, MHD waves can have mixed properties due to the presence of plasma non-uniformity. For instance, the fundamental radial modes of a kink symmetry (non-axisymmetric) with phase speeds between $C_{\rm A0}$ and $C_{\rm Ae}$ possess very similar properties to surface Alfén waves, while higher radial overtones behave as fast magnetoacoustic modes in a uniform medium [Goossens et al., 2009, 2012]. The fast modes in a magnetic cylinder are seen to be highly dispersive, as their phase and group speeds depend strongly on the wave number. Also, in a low-β plasma, the fast modes are almost transverse: the radial flows induced by these modes have much higher speeds than the longitudinal flows. In turn, the slow magnetoacoustic waves are almost dispersionless, and are mainly characterised by the longitudinal flows. In the research literature the slow modes are often referred to as longitudinal. In the limit of infinitely small plasma β the phase speed $C_{\rm T0}$ of the slow magnetoacoustic waves tends to the internal sound speed $C_{\rm s0}$, and slow waves degenerate to acoustic waves.

For a fixed value of the azimuthal number m and sufficiently large value of the parallel wavenumber k_z, Eq. (1.4) has several solutions, which could be parametrised by the integer number l. This additional quantisation is caused by the quasi-periodic behaviour of the radial component of the Bessel functions $I_m(x)$ and $K_m(x)$, and finite radius of the plasma cylinder. The integer l thus represents a number of nulls in the radial velocity perturbation, which appear inside the cylinder (i.e. for $r < a$), excluding the axis of the cylinder. For the considered combination of the physical parameters of the plasma inside and outside the cylinder, the phase speed of the fast modes increases with the increase in l. In Fig. 1.7 the lowest phase speed curves of each mode correspond to $l = 0$.

In the long wavelength limit $k_z \to 0$, phase speeds of all but sausage fast modes of the first radial harmonic ($l = 0$) tend to the so-called kink speed

$$C_{\rm k} = \left(\frac{B_0^2/\mu_0 + B_{\rm e}^2/\mu_0}{\rho_0 + \rho_{\rm e}}\right)^{1/2} \approx \left(\frac{2}{1 + \rho_{\rm e}/\rho_0}\right)^{1/2} C_{\rm A0}. \tag{1.5}$$

In a low-β plasma, the kink speed is rather close to the internal Alfvén speed $C_{\rm A0}$. The sausage mode approaches a cut-off at the external Alfvén speed $C_{\rm Ae}$ and becomes leaky in the long wavelength limit.

For standing modes, the boundary conditions in the longitudinal direction lead to an additional quantisation of the parallel wave number k_z, introducing a parallel wavenumber n that is an integer corresponding to the number of extrema (antinodes) of the transverse velocity perturbations along the loop. Thus, dispersion relation (1.4) allows one to determine the frequency of a trapped magnetoacoustic mode if the integer mode numbers, the longitudinal number n, the radial number l and the azimuthal number m are given or observationally measured.

In closed magnetic configurations, for example in coronal loops, the longest period standing modes of each kind, with the wavelengths equal to the doubled loop length, are called global (or fundamental, principal). In particular, in the trapped regime the period $P_{\rm saus}$ of the global sausage mode of a coronal loop of the length L, determined by $m = 0$, $n = 1$, $l = 0$, is

$$P_{\rm saus} = 2L/C_{\rm p}, \tag{1.6}$$

where $C_{\rm p}$ is the phase speed of the sausage mode corresponding to the wave number $k_z = \pi/L$, $C_{\rm A0} < C_{\rm p} < C_{\rm Ae}$ [see e.g. Vasheghani Farahani et al., 2014, for absolute values]. Typically, the period of the global sausage mode of coronal loops varies from several seconds to several tens of seconds.

The period of the global kink mode with $m = 1$, $n = 1$, $l = 0$, is

$$P_{\rm kink} = 2L/C_{\rm k}, \tag{1.7}$$

where $C_{\rm k}$ is the kink speed determined by Eq. (1.5). In typical coronal conditions, the kink speed is slightly, by about a factor of 1.4, higher than the Alfvén speed inside the loop. The period $P_{\rm kink}$ is typically about a few hundreds of seconds.

In the low-β plasma of the corona, the period of the global longitudinal mode is defined mainly by the parallel wave number $n = 1$. The period is almost independent of the azimuthal m and radial l wave numbers, because the dispersion curves corresponding to the slow magnetoacoustic modes with different m and l, are located indistinguishably close to each other in the dispersion diagram (see Fig. 1.7). The period of the global longitudinal mode is given by

$$P_{\rm long} = 2L/C_{\rm T0}. \tag{1.8}$$

As in the low-β coronal plasma, the internal tube speed $C_{\rm T0}$ is very close to the internal sound speed $C_{\rm s0}$, the period $P_{\rm long}$ is practically determined by the temperature in the loop and should evolve in anti-correlation with it. The typical values

of the global longitudinal mode period range from a few minutes to several tens of minutes.

In addition, the cylindrical geometry implies the existence of a torsional Alfvén wave in the model, which can be considered as a wave of plasma rotation and magnetic field twisting. In the discussed small amplitude linear regime, this wave is essentially incompressive and dispersionless, propagating at the local Alfvén speed. It moves the plasma in the direction locally parallel to the boundary of the cylinder, and hence does not perturb the boundary. Strictly speaking, in the absence of viscous effects torsional Alfvén waves are not the oscillations of the cylinder as a whole, as they can have an arbitrary radial profile determined only by the initial excitation, and the variations of the neighbouring concentric magnetic surfaces do not "feel" each other. It is in contrast to the kink, sausage, longitudinal and ballooning modes, which all are essentially collective oscillations of the cylinder. In a coronal loop, the resonant period of the global torsional mode is

$$P_{\rm tors} = 2L/C_{\rm A0}, \tag{1.9}$$

and is of the same order of magnitude as the periods of the kink modes.

Typical periods of MHD oscillations of solar coronal plasma structures, determined by Eqs. (1.6)–(1.9), range from several seconds to several tens of minutes. All these modes, except the Alfvén wave, have been confidently identified in the solar corona with the use of high-precision imaging observational data obtained in the EUV, soft X-ray and microwave bands. In particular, multiple periods of about 15 s and 100 s detected in the same solar flare QPP in Sec. 2.5, are interpreted in terms of the sausage and kink oscillations of a flaring loop, respectively.

MHD-driven mechanisms of QPP: modulation by natural MHD modes and periodic triggering by external MHD oscillations

Quasi-periodic pulsations in the microwave band have been extensively investigated for more than fifty years. Recent achievements obtained with modern observational instruments provide the microwave data with excellent time and spatial resolutions. In some cases spectral resolution is also available. Based on these facts, QPPs in the microwave emission of solar flares are the most suitable natural tool for studying MHD oscillations in the corona and diagnostic of the macroscopic parameters of the plasma.

Periods of QPPs in solar flares are observed to range from a fraction of a second up to several tens of minutes. These observed periodicities are in a good

agreement with the global periods of the standing MHD modes in coronal plasma structures, described in the previous section in terms of the straight cylinder model. Such an apparent correspondence of QPP in flares and the observed and theoretically predicted parameters of MHD oscillations of coronal plasma structures leads to the idea of generating QPPs by intrinsic MHD modes of a plasma non-uniformity, for example a loop (see e.g. Fig. 1.2) in the flaring active region. There are several possible mechanisms for MHD oscillations to induce QPP in flares [Nakariakov and Melnikov, 2009]: either by direct periodic variations of the plasma conditions which define the intensity of the emitted electromagnetic radiation; or by affecting the primary energy release process, for example periodically triggering a flare and thus modulating the density of accelerated non-thermal electrons; or by affecting the kinematics of the non-thermal electrons and hence modulating their precipitation rate.

To demonstrate the first possibility, consider the mechanisms for modulation of the gyrosynchrotron emission produced by mildly relativistic electrons accelerated in solar flares, by MHD waves. These electrons have peaking energies at about 20 keV, and usually have the lower threshold value of 10 keV [Benz, 2008]. The radiation caused by these non-thermal electrons is emitted due to their interaction with the plasma of the flaring coronal loop, penetrated by the background magnetic field. A typical image of such a microwave emission is shown in the right-hand panel of Fig. 1.2. Generally the intensity I_f of the gyrosynchrotron emission at a certain frequency f has a peak value at some peak frequency $f_{\rm peak}$ (typically $f_{\rm peak} > 10$ GHz) and is determined by macroscopic parameters of the plasma, such as the absolute value of the background magnetic field B_0, the electron concentration n_0 in the loop, the angle θ between the line-of-sight (LOS) and the magnetic field; and by the characteristics of the injected non-thermal particles: their total number N in the emitting volume, the energy power law index δ and the pitch-angle anisotropy of the non-thermal electron distributions [see e.g. Ramaty, 1969; Fleishman and Melnikov, 2003].

The gyrosynchrotron radiation in flares can occur in both optically thin and optically thick regimes. Usually the optically thin regime is observed at frequencies higher than the peak frequency $f_{\rm peak}$, while the optically thick emission radiates at lower frequencies, $f < f_{\rm peak}$. The intensity I_f depends upon the parameters described above differently in different regimes [Dulk, 1985],

$$I_f \propto \begin{cases} N B_0^{0.9\delta - 0.22} & \text{in optically thin regime,} \\ B_0^{-0.5 - 0.09\delta} & \text{in optically thick regime.} \end{cases} \tag{1.10}$$

For $\delta > 0.25$ (plausible values of δ are usually greater than 3) the increase in the magnetic field leads to the increase in the emission intensity in the optically thin regime, and to the decrease in the intensity in the optically thick regime. In the optically thin case the gyrosynchrotron radiation is especially sensitive to variations of the magnetic field amplitude B_0, due to the strong power-law dependence. In particular, for $\delta = 4$ this proportionality becomes $I_f \propto B_0^{3.4}$. Hence even relatively low perturbations of the magnetic field, typical for MHD waves observed in the corona, can cause a significant modulation of the observed gyrosynchrotron signal. In particular, sausage oscillations generating variations of the magnetic field strength are able to produce significant modulation of the microwave gyrosynchrotron emission in the optically thin part of the spectrum [e.g. Reznikova et al., 2014].

Similarly, consider the dependence of the intensity of the gyrosynchrotron emission upon the angle θ between the LOS and the magnetic field lines,

$$I_f \propto \begin{cases} (\sin\theta)^{-0.43+0.65\delta} & \text{in optically thin regime,} \\ (\sin\theta)^{-0.36-0.06\delta} & \text{in optically thick regime.} \end{cases} \tag{1.11}$$

In the optically thin regime small amplitude variations of the angle θ, generated, for example, by the kink or torsional standing modes, are amplified in the emission intensity for $\delta > 0.67$, according to Eq. (1.11). Hence, for the observed realistic values of $\delta > 3$ this effect should be certainly pronounced. Similarly to Eq. (1.10), signals from the optically thick part of the gyrosynchrotron spectrum show an anti-phase behaviour [Mossessian and Fleishman, 2012].

Consequently, fast magnetoacoustic waves are readily able to produce a significant quasi-periodic modulation of the gyrosynchrotron emission intensity at high frequencies. Moreover, slow magnetoacoustic waves can also cause quasi-periodicities, which are manly pronounced at lower frequencies, $f < 10$ GHz [lower than $f_{\rm peak}$, Nakariakov and Melnikov, 2006]. Usually this part of the gyrosynchrotron spectrum is optically thick for radiation, but it becomes optically thin in the case of a relatively high plasma density, according to the effect of Razin suppression often observed in the flaring loops [see e.g. Melnikov et al., 2008]. A threshold characteristic frequency distinguishing between optically thick and optically thin regimes, is referred to as the Razin frequency $f_{\rm R}$, and is determined as $f_{\rm R} \approx 20\ n_0/B_0$, where n_0 is measured in cm^{-3} and B_0 is in G. For typical coronal conditions, its value is in the vicinity of 10 GHz, reaching 20 GHz in some special cases [e.g. Melnikov et al., 2005]. In the case of periodic variations of the plasma concentration n_0, for example, by a compressible longitudinal wave in which the magnetic field remains almost constant, the Razin frequency also experiences oscil-

lations. It results in a continuous swapping of the emission regimes, pronounced as a quasi-periodic modulation of the observed microwave radiation. The modulation amplitude can become up to a factor of ten higher than the amplitude of the modulating signal.

All magnetoacoustic modes (sausage, kink, ballooning, and longitudinal) and torsional waves can produce quasi-periodic modulation of the microwave emission of solar flares by direct perturbation of the macroscopic parameters of the emitting plasma. Moreover, the observed amplitude of the emission intensity variation (the modulation depth) can be several times higher than the amplitude of the modulating oscillation. However, in some cases the observed modulation depth reaches 50% or even 100%, which is difficult to explain by this mechanism. In addition, this mechanism does not explain simultaneous and coherent QPP observed in different bands. For example, panel (a) of Fig. 1.3 shows that QPPs in the radio emission correlate well with the modulation of the hard X-ray and gamma-ray curves. In a standard model of a solar flare the hard X-ray and gamma-ray emissions are associated with the footpoints sources, generated by the bremsstrahlung radiation of highly energetic electrons in the dense chromospheric plasma. QPP of the hard X-ray and gamma-ray emissions can be explained by the modulation of non-thermal charged particle trajectories by an MHD oscillation.

A substantial portion of the accelerated particles, with pitch angles greater than the critical value $\alpha_{\rm c}$ determined as $\sin^2\alpha_{\rm c} = B_{\rm top}/B_{\rm fp}$, where $B_{\rm top}$ and $B_{\rm fp}$ are the values of the magnetic field at the loop top and at the loop footpoints, respectively (with $B_{\rm top} \leq B_{\rm fp}$), is confined inside the magnetic trap configured by the magnetic flux tube of a non-uniform cross-section. The legs of the magnetic flux tube, where its cross-sectional area decreases, act as the magnetic mirrors for the population of non-thermal electrons. In case of periodic variations of the "mirror ratio" $B_{\rm top}/B_{\rm fp}$, the critical value of the pitch angle $\alpha_{\rm c}$ changes periodically too, allowing for the periodic passage of accelerated electrons through the magnetic mirrors and consequent precipitation at the dense plasma layers. This process known as the Zaitsev–Stepanov mechanism [Zaitsev and Stepanov, 1982], can lead to QPP of the hard X-ray emission radiated by the footpoint sources. Simultaneously, this scenario produces QPP of the gyrosynchrotron emission generated by the non-thermal electrons periodically filling in the loop legs. In the context of MHD oscillations of coronal loops, this effect can be produced, for example, by a sausage mode, which efficiently perturbs the magnetic field in the loop (see Fig. 1.8). It should be noted that the Zaitsev–Stepanov mechanism requires further detailed investigations and modelling.

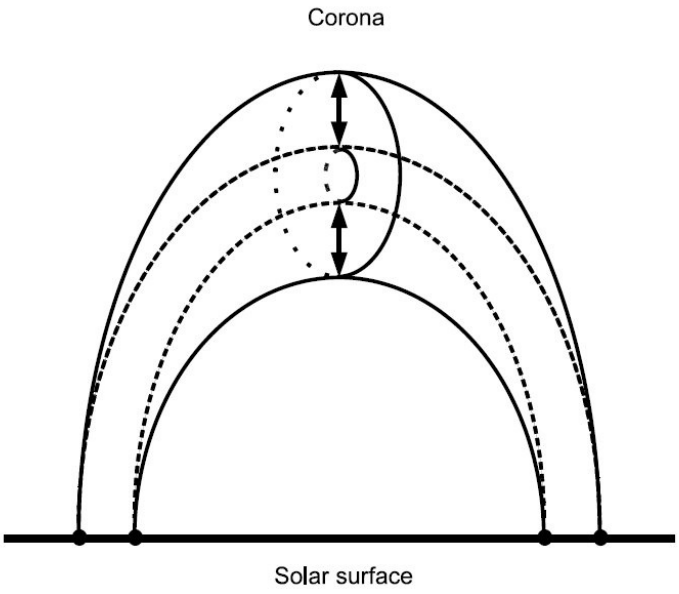

Figure 1.8: A typical coronal loop perturbed by the global, compressive sausage mode providing a non-uniform periodically varying cross-sectional area of the loop. Magnetic field and density perturbations are synchronous, and have maximum at the loop top, and nodes at the footpoints [adapted from Pascoe et al., 2007].

Another possibility for MHD-wave-driven QPPs in solar flares, which is an alternative to the described above processes of oscillatory variations of macroscopic flaring plasma parameters and kinematics of accelerated particles directly by the MHD modes of a coronal loop, is a periodic triggering of the primary energy release, the reconnection of the magnetic field lines, by external MHD waves. These waves may be transverse MHD oscillations in nearby plasma structures, for example a neighbouring loop, or may be approaching propagating fast waves generated elsewhere. For example, the periodically varying inflow of the plasma with the frozen-in magnetic field should modulate the reconnection rate in a current sheet or an X-point. Moreover, such a mechanism does not require the driving external MHD oscillation to be of a large amplitude, due to a very small thickness of the reconnecting current sheet.

The first consideration of this effect can be found in Sakai and Washimi [1982], where the influence of incoming fast magnetoacoustic waves on the tearing instability of a current sheet was considered. It was established there that the growth rate of the instability depends upon the spatial scale of the current sheet fragmentation, the magnetic Reynolds number, the perturbing wave amplitude, and the wave travel time across the current sheet. These results were obtained by averaging over

the oscillation period of the driving MHD mode, hence cannot address the question of the QPP's appearance in the system. However, this mechanism would probably lead to QPP generation.

Long-period QPPs observed in the hard X-ray and microwave bands in two remotely situated solar flares, with periods of about 10 min, were also associated with external fast magnetoacoustic oscillations in Foullon et al. [2005]. The global periods of standing MHD modes of a magnetic cylinder are determined by the cylinder length and the wave phase speed (see Eqs. (1.6)–(1.9)). However, the observed geometry of the flaring sites in the event analysed in Foullon et al. [2005], was not suitable for generating such long-period modes: phase speeds of unrealistic values would be required. Hence, the mechanism of a direct modulation of the flaring plasma conditions by the intrinsic MHD modes cannot explain the observed long periods. In addition, the observed variability of these two flaring sites situated far from each other, in different hemispheres, showed a clear similarity. It was suggested that QPPs could have a common source, for example a transverse kink oscillation of an external, trans-equatorial loop, operating as a connector for these two flaring sites. Indeed, such a loop was found in the EUV observations, but it was impossible to resolve its oscillations because of the insufficient time resolution of the EUV imager.

A theoretical foundation of this mechanism was developed by Nakariakov et al. [2006], where a detailed model of the interaction of transverse MHD waves, for example kink or sausage modes, in an external loop, with the flaring active region was designed (see the sketch in Fig. 1.9). The external oscillation can be either in the trapped or leaky regimes. Hence, the linkage of this oscillation with the flaring site is provided by the evanescent or leaky part of the oscillation. From the flaring site point of view, this external transverse oscillation looks like an incoming and outgoing periodic perpendicular plasma flow. Although these fast magnetoacoustic waves have relatively small initial amplitudes and periods, prescribed by the parameters of the external loop, approaching the magnetic null point of the flaring site, they rapidly grow as the fast speed decreases near the magnetic null point, and also by the effect of focusing [see also numerical simulations in McLaughlin and Hood, 2004]. The fast wave evolution in the vicinity of the X-point is accompanied by a dramatic increase in the density of the periodically varying electric current induced by the wave. When the current density becomes greater than some threshold value $j_{\rm thres}$, various microinstabilities are excited in the plasma in the vicinity of the X-point. These small-scale instabilities lead to the onset of the microturbulence, which can dramatically increase the transport coefficients in the plasma, in particular, producing "anomalous" resistivity. The resistivity η can then be modelled by the

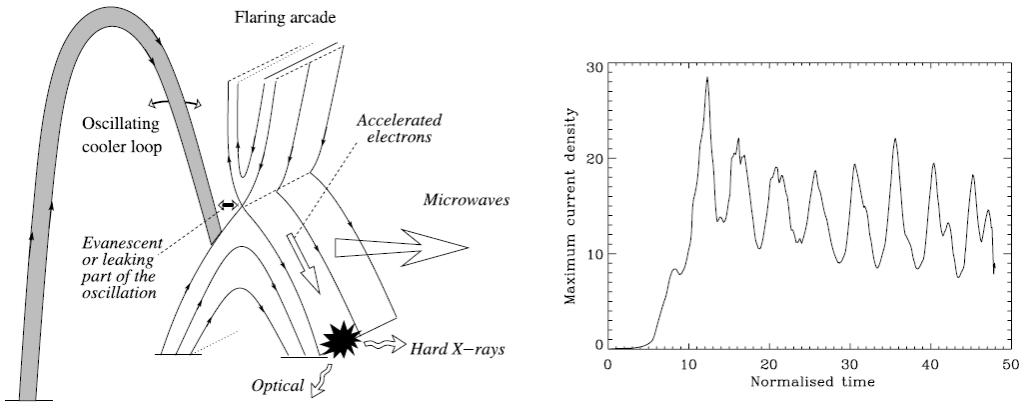

Figure 1.9: Left: schematic sketch of the mechanism of the generation of flaring QPP by an external magnetoacoustic oscillation. The cool (shaded) loop experiences transverse oscillations. A segment of the oscillating loop is situated nearby the flaring arcade. An external evanescent or leaking part of the oscillation can reach magnetic X-points or current sheets in the arcade, inducing quasi-periodic modulations of the electric current density. The resulting current-driven plasma microinstabilities are known to cause anomalous resistivity, which triggers magnetic reconnection in a periodic manner. Right: time evolution of the maximum electric current density in the vicinity of a 2D magnetic neutral point. The current is induced by a harmonic fast magnetoacoustic wave with a period of 5 time units, moving towards the neutral point. The initial relative amplitude of the wave is 1.5%. The plasma β is finite. The normalising values are the Alfvén speed at the computational domain boundary and the characteristic spatial scale of the magnetic field inhomogeneity [taken from Nakariakov et al., 2006].

piecewise relation,

$$\eta = \begin{cases} \eta_{\rm class}, & \text{for } |j| \leq j_{\rm thres}, \\ \eta_{\rm anom}, & \text{for } |j| > j_{\rm thres}, \end{cases} \tag{1.12}$$

where $\eta_{\rm class}$ and $\eta_{\rm anom} \gg \eta_{\rm class}$ are the classical and anomalous values of the resistivity, respectively. Oscillatory behaviour of the anomalous resistivity causes periodic triggering of the magnetic reconnection, which results, in turn, in the periodic acceleration of charged particles. The periodic variation of the density, energy, and pitch angle distribution of non-thermal electrons produces QPPs of hard X-ray, gamma-ray, microwave, and sometimes white light emissions. The period of these QPPs is prescribed by the external magnetoacoustic oscillation and magnetic properties of the flaring region, and is not determined by its geometrical size.

A similar mechanism, but associated with slow magnetoacoustic waves, was independently developed by Chen and Priest [2006]. The periodic modulation proposed was based on the variation of the plasma density in the vicinity of the reconnection site, generated by solar acoustic (p-mode) oscillations. Density variations can lead to the generation of the Buneman or ion-acoustic instabilities and, hence, cause anomalous resistivity.

The idea that flaring QPPs are triggered by external MHD waves is also consistent with the observed progression of a flaring QPP along the magnetic neutral line separating two ribbons in large solar flares [Nakariakov and Zimovets, 2011]. The impulsive energy releases are usually observed to propagate along the two-ribbon flaring structures at the speed of a few tens of km s^{-1}. This value of the speed is significantly lower than the Alfvén and sound speeds in the corona. However, it can be interpreted in terms of slow magnetoacoustic waves guided by a plasma arcade in the direction perpendicular to the magnetic field. In a uniform medium slow magnetoacoustic waves are able to propagate either strictly along the magnetic field lines or weakly obliquely, in a rather narrow cone along the field. However, in the presence of plasma non-uniformities these oblique slow waves can bounce between two reflecting or refracting boundaries situated across the field, for example the footpoints of the coronal magnetic flux tubes, and thus move gradually in the direction perpendicular to the field.

In this scenario, a slow magnetoacoustic perturbation excited by the energy release somewhere at the top of the arcade propagates obliquely towards the arcade footpoints. There it experiences reflection by the sharp gradient of the sound speed and returns back to the top of the arcade. This results into a slow motion along the arcade axis, across the field (see the model geometry in Fig. 1.10). According to Nakariakov and Zimovets [2011], the obliqueness angle of the most efficient

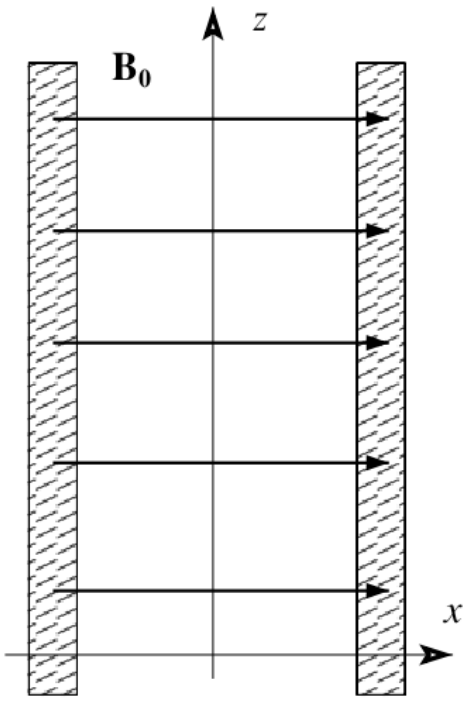

Figure 1.10: Simplified 2D model of the plasma arcade in a two-ribbon solar flare (top view). The thick horizontal lines show the magnetic field lines inside the loops, which form the arcade. The hatched regions show their footpoints, and correspond to the flare ribbons – the regions of the chromosphere where the hard X-ray, gamma-ray and white light emissions are observed during the flare. An oblique slow magnetoacoustic wave excited somewhere at the top of the arcade propagates towards the footpoints, where it gets reflected on the sharp gradient of the sound speed and propagates back to the top of the arcade. There the wave triggers another energy release, and the scenario repeats. This results in a slow motion (with the speed of a few tens of km s^{-1}) of the hard X-ray, gamma-ray and white-light sources along the arcade axis, across the magnetic field, in the form of quasi-periodic bursts [taken from Nakariakov and Zimovets, 2011].

perpendicular propagation is about 25°–28°, while the perpendicular wave vector is determined by the width of the waveguide and the distance between the footpoints along the magnetic field lines in the arcade. Hence, the wave arrives back at the top of the arcade at a location slightly shifted along the arcade main axis. Approaching the X-point above the arcade, the slow wave triggers another energy release – another burst of QPP. Moreover, the induced energy release reinforces the slow perturbation, compensating its dissipative and scattering losses. The period of the generated QPP is then determined by the speed of the triggering slow magnetoacoustic wave and the travel path. Usually, it is about 10–300 s, which is similar to the second harmonic of the longitudinal mode of a coronal loop.

In addition, the discussed scenario can successfully address another interesting feature of flaring QPP often seen in observations, the presence of double maxima in the elementary bursts [Tajima et al., 1987; Zimovets and Struminsky, 2009]. According to the developed model, it may occur due to some natural asymmetry in the location of the wave source or in the arcade geometry. In this case, the slow pulses reflected from the opposite footpoints, arrive at the arcade top and trigger the next energy releases asynchronously, i.e. at slightly different times and locations. Similar asymmetric conditions in the propagation of longitudinal plasma flows evaporated from both footpoints may trigger the Kelvin–Helmholtz instability in the loop top, resulting into the development of magnetohydrodynamic turbulence and formation of hard X-ray sources at the loop apex [Fang et al., 2016].

Nonlinear mechanisms for QPP: current sheet oscillations and spontaneous reconnection

Quasi-periodic pulsations in solar flares are often observed to exhibit typical signatures of nonlinear processes. These signatures are rather different and non-unique. For example, it can be a direct dependence of the oscillation period upon the oscillation amplitude in a signal, anharmonicity of the oscillation profile, and nonstationarity [for a more detailed consideration of highly nonlinear wave processes in multifluid plasmas see e.g. Dubinov et al., 2012a,b; Dubinov and Kolotkov, 2012, and references therein]. In the parlance of spectral analysis, these effects can lead to the generation of higher harmonics and re-distribution of spectral energy across the components. Indeed, many solar flares, including the most powerful of them, are found to have non-stationary QPP with an anharmonic, in particular symmetric triangular profile shape (see e.g. Figs. 1.3 and 1.11, where examples of such QPPs are presented).

All mechanisms for QPP generation, described in the above section, are

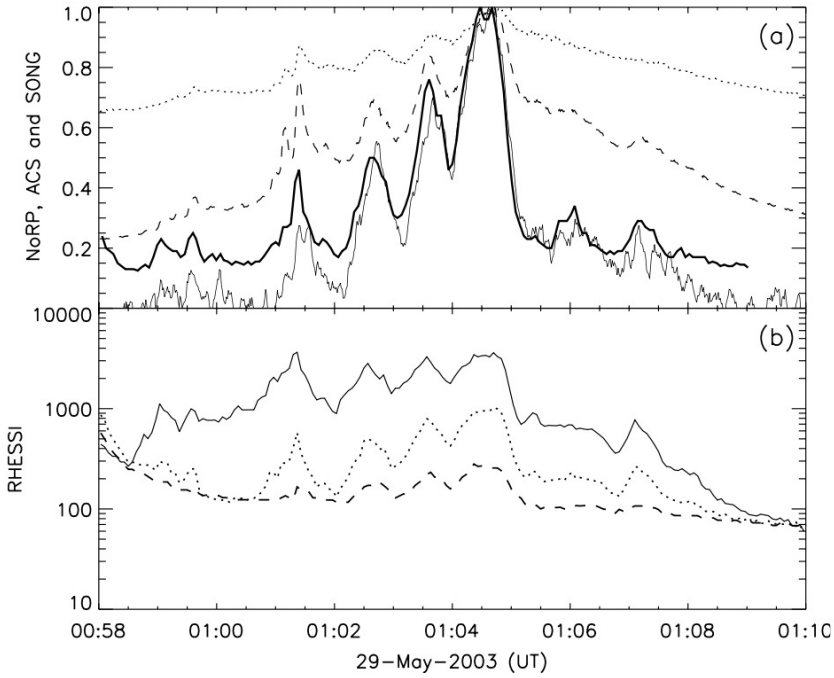

Figure 1.11: A typical QPP with an anharmonic triangular profile shape and relatively stable period, in a solar flare. The event occurred on 29 May 2003 and was observed with the Nobeyama Radiopolarimeters (NoRP) in microwaves, and in hard X-rays by the RHESSI spacecraft, the anticoincidence shield (ACS) of the SPI spectrometer on INTEGRAL, and the SOlar Neutrons and gamma-rays experiment (SONG) on CORONAS-F. Panel (a): NoRP flux at 17 GHz (the dashed curve) and 35 GHz (the dotted curve), the ACS count rate (>80 keV, the thin solid curve) and the SONG 80–200 keV count rate (the thick solid curve). Panel (b): the RHESSI corrected count rate in the channels 25–50 keV (solid), 50–100 keV (dotted) and 100–300 keV (dashed) [taken from Nakariakov et al., 2010b].

based upon the interaction of the flaring site with linear small amplitude MHD waves (internal or external), and hence cannot address these observational nonlinear properties. However, various nonlinear regimes of the magnetic reconnection driving the flare, may also efficiently contribute to producing of QPP of the electromagnetic radiation, if they occur in an oscillatory manner. Such oscillatory or rather repetitive regimes of non-stationary reconnection are known as "magnetic dripping" models [see e.g. Nakariakov et al., 2010b, where this term was introduced], which represent a gradual accumulating of free magnetic energy and consequent rapid release of it, when some threshold value is achieved.

The first illustration of such a process was seen in the numerical simulation of the dynamic phase of magnetic reconnection in a large-scale two dimensional current sheet, located above the flaring loop in the standard model of a flare [Kliem et al., 2000]. The simulated reconnection was caused by anomalous resistivity, which was a self-consistent parameter in the model and determined by the electron-ion drift velocity, proportional to the electric current density (cf. Eq. (1.12)). The repetitive regime was found to be provided by the coalescence of continuously generated magnetic islands (or plasmoids), which resulted in the formation of one or several hot and dense larger plasmoids. When finally such a plasmoid becomes sufficiently large, it is rapidly ejected upwards or downwards along the current sheet. Usually a plasmoid is ejected at about the Alfvén speed [see e.g. Shibata and Magara, 2011], that consequently enables a new magnetic flux to refill in the current sheet, thus reinforcing the reconnection. However, if the plasma is unable to carry a sufficient amount of the magnetic flux into the diffusion region to support the Alfvénic outflow in a steady Petchek state, the system continuously switches between the fast Petchek and slow Sweet–Parker regimes of reconnection. The repetitive ejections of each plasmoid were found to be accompanied by bursts of accelerated charged particles, which in turn created periodic enhancements of the observed emission in all bands associated with non-thermal electrons (namely, microwaves, hard X-rays, gamma-rays and white light, and indirectly, via the evaporation of the chromospheric plasma, in soft X-rays and EUV). The period of pulsations, predicted by the model, is determined by the plasma concentration n_0 and temperature T_0 inside the current sheet, and the external magnetic field B_0,

$$P \propto n_0^{-1/2} T_0^2 B_0^{-1}. \tag{1.13}$$

For the plasma concentrations in the range 10^9–10^{10} cm^{-3}, the time intervals between the pulsations can be 0.4–20 s. This model is rather suitable for QPPs with

partly irregular intervals between the peaks, as the plasmoid shedding is a rather irregular process.

Another possibility providing the oscillatory regime of magnetic reconnection is based on the coupling of the tearing and Kelvin–Helmholtz instabilities of the current sheet. It occurs in the presence of sufficiently fast shear flows and beams, propagating at Alfvénic or super-Alfvénic speeds aligned to the magnetic field in the vicinity of the current layers. This effect is most pronounced if the plasma β is greater than unity, i.e. when thermodynamical processes dominate in the plasma. In this case, overstable nonlinearly coupled tearing and Kelvin–Helmholtz modes (experiencing several quasi-periodic oscillations before the current sheet gets destabilised and eventually disappears) lead to the observed non-thermal X-ray emission oscillations, which are believed to be directly caused by variations of the electric current magnitude in the reconnection region. The current fluctuations can affect the electric field magnitude and, consequently, modulate the electron acceleration rate [Heyvaerts et al., 1977]. Full-scale 2.5D compressive, visco-resistive MHD simulations of this phenomenon were performed by Ofman and Sui [2006], who found the oscillation periods to be about 50 Alfvén transit times across the current sheet half-width, giving about several tens of seconds for typical coronal plasma parameters.

A long-period repetitive magnetic reconnection in the current sheet spontaneously formed along a side interface between an emerging coronal loop and the neighbouring vertical magnetic field lines of the opposite polarity (see the geometry of the model in Fig. 1.12), should be also included into this group of "dripping" mechanisms. This model was studied numerically with 2.5D MHD simulations by Murray et al. [2009]. The interchange reconnection provides a reconfiguration of the magnetic topology, resulting in the generation of a new set of closed loops and a new open field with a footpoint near the emerged loops. During each separate act of reconnection the gas pressure in the bounded outflow region increases above the level of that in the inflow region, causing a series of reconnection reversals. Consequently, the reconnection energy releases occur in distinct bursts. The inflow and outflow magnetic fluxes of an individual burst become the outflow and inflow fluxes in the following burst of reconnection, respectively. Such a repetitive manner of reconnection modulates the electric current and heating in the plasma of the current sheet. Simulations showed that the maximum value of the current decreases with the development of the processes. Hence, the oscillations were found to be highly anharmonic, with periods varying from 1.5 to 32.1 min, depending on the parameters in the numerical model. This mechanism requires a dedicated detailed

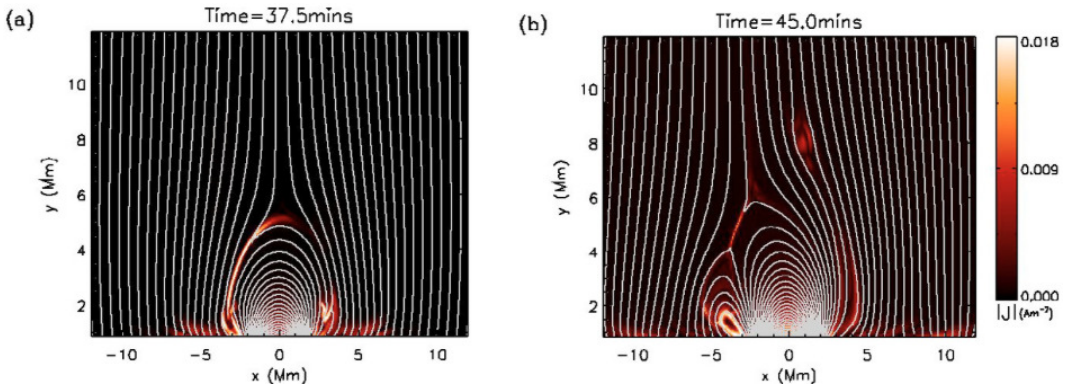

Figure 1.12: Results of 2.5D MHD numerical simulations of a spontaneous reconnection in the current sheet formed along the interface between an emerging loop and the oppositely directed vertical magnetic field lines (for example, of a neighbouring coronal hole). In the left-hand side of the loop system, the emerged field is directed positively (outwards from the solar surface), while the adjacent coronal hole field is of the opposite direction. Panel (a) shows the current sheet formation at the left-hand interface between these two flux systems at a certain instant of the computational time. The magnetic topology reconfigurated by the reconnection is shown in panel (b). The colour scheme shows the current density [adapted from Murray et al., 2009].

investigation, first of all addressing the effect of the plasma parameters, especially the value of the resistivity, on the period.

A theoretical model describing small amplitude magnetoacoustic oscillations of a two-dimensional X-type magnetic neutral point was developed by Craig and McClymont [1991]. The equilibrium magnetic field lines were taken to be coplanar (with $B_z = 0$), and frozen into a circular radial boundary. Neglecting gas pressure, viscosity, and assuming a constant value of resistivity in the background plasma of a uniform density, combination and subsequent linearisation of the induction equation for the magnetic field and the Euler equation resulted in a second-order governing evolutionary equation

$$\ddot{A} - \eta \nabla^2 \dot{A} = r^2 \nabla^2 A, \tag{1.14}$$

written in terms of the perturbations of a magnetic field vector potential $A(r, \phi, t)$, where r and ϕ are the polar coordinates with the origin at the centre of the X-point, η is the constant dimensionless resistivity of the medium, and double-dots denote the second time derivative. Equation (1.14) reveals both a diffusive behaviour determined by the second term on the left-hand side of the equation, and oscillations described by two other terms. Additionally, the "frozen" boundary conditions (the

perturbation $A = \text{const}$ at the boundary $r = 1$) were used, forcing the system to be closed, with no magnetic flux or plasma entering or leaving the volume. In the vicinity of the X-point, that is $r \ll r_c$ (where $r_c \propto \eta^{1/2}$ is the skin depth), Eq. (1.14) reduces to the diffusion equation, $\dot{A} = \eta \nabla^2 A$. Its radial solutions are determined by the Bessel function $J_m(x)$ of order m. In the advection region ($r_c < r \leq 1$), Eq. (1.14) is transformed into the wave equation, $\ddot{A} = r^2 \nabla^2 A$ ($\nabla^2 A$ vanishes at the boundary $r = 1$, where the perturbation $A = \text{const}$), revealing the characteristic time scale $\delta t \approx |\log \eta|$ of the wave propagation from the outer boundary into the diffusion region $r < r_c$.

The radial solutions of the diffusion equation derived from Eq. (1.14) in the case of $r \ll r_c$, showed that the perturbations with $m = 0$ (here m is the azimuthal wave number, hence the perturbations are of a sausage symmetry) are the only modes allowing for a topological reconnection. This is because only the Bessel function $J_0(x)$ has a non-zero value at the origin. The higher m radial modes rapidly decay in the outer non-resistive medium ($r_c < r \leq 1$), similarly to the damping of a fluid motion by finite viscosity, and are therefore not able to affect the global magnetic topology. In particular, the slowest decaying $m = 0$ mode for $\eta \approx 10^{-14}$ (a plausible coronal value) was found to have an oscillation period of about 60 Alfvén times (r/C_A, based on the Alfvén speed at the external boundary radius, r), and the perturbation decays in about three cycles of oscillations.

A substantial extension of the proposed model was performed by McLaughlin et al. [2012]. In this work, finite amplitude oscillations of a magnetic null point, excited by a fast magnetoacoustic wave, were studied numerically in a compressible, resistive 2D MHD simulation accounting for a non-zero thermal pressure effect. Two phases of the null point dynamics were identified: an impulsive phase (during the first 90 s of the whole 480 s simulated time-domain) and a stationary phase. In the impulsive regime, oscillations of the magnetic field, density, electric current and induced plasma flows were found to be rather irregular, consisting of a number of sharp intense spikes, each lasting for about 10–20 s. In the stationary phase, the signal was much cleaner and closer to a decaying sinusoidal function, with a stable period comparable to that of the $m = 0$ oscillating radial mode found in Craig and McClymont [1991].

All these mechanisms of a non-steady time-dependent magnetic reconnection clearly address basic observational properties of QPPs, such as simultaneous presence of pulsations in the light curves of different bands, as they are caused by the same factor – modulated rate of the accelerated particles generation; and a deep modulation depth of QPP, as it is determined by the variations of a non-thermal

electron density. However, these explanations still contain several unanswered questions: in particular, it is not clear how the time-dependent reconnection can give a high monochromaticity and quality of some QPP, presence of several distinct significant periodicities; the properties of the non-thermal electron energy spectra produced by those mechanisms are also still to be revealed.

The nonlinear regime of the coalescence of two twisted current-carrying flux tubes can also provide repetitive energy bursts in solar flares [Tajima et al., 1987], and is widely considered to be responsible for producing QPPs. In this model the current sheet is formed in the region of coalescence of two colliding magnetic loops with identically directed magnetic twists (see the schematic sketch in Fig. 3.4), which are driven towards each other by the relative motion of their footpoints in the photosphere. The nonlinear evolution of this explosive coalescence was studied analytically and numerically with MHD and particle-in-cell simulations. The results obtained with these essentially different and independent approaches were found to be consistent with each other both qualitatively and in many detailed aspects. More specifically, in the analytical model the governing second-order nonlinear ordinary differential equation, which describes the time evolution of the current sheet formed by the collision of two plasmoids, has the normalised form

$$\ddot{\zeta} = -\zeta^{-2} + \beta\zeta^{-3}, \tag{1.15}$$

where ζ is a dimensionless function connected with the plasma parameters in the current sheet, for example with the magnetic field strength, as $B \propto \zeta^{-2}x/\lambda$, with x and λ being a spatial coordinate across the sheet and its thickness, respectively. The equilibrium state of such a current sheet is determined by the total pressure balance at the boundary, with the domination of the magnetic pressure in the inflow regions and the thermal plasma pressure inside the current sheet (see Fig. 1.13). In the normalisation, unperturbed values of the function ζ and plasma parameter β are unity. As the initial perturbation occurs, Eq. (1.15) describes sausage oscillations of the current sheet, with the minimum oscillation period measured in units of the Alfvén transit time $\tau_{\rm A} = \lambda/C_{\rm A}$ across the sheet,

$$P = 2\pi\beta^{3/2}\tau_{\rm A}, \tag{1.16}$$

which is about a fraction of a second for typical flaring conditions. However, in the nonlinear regime of the current sheet evolution, the oscillation period increases with the amplitude and can reach 1 s or longer for sufficiently large amplitudes. This is a common property of nonlinear oscillations, which can be also recognised, for ex-

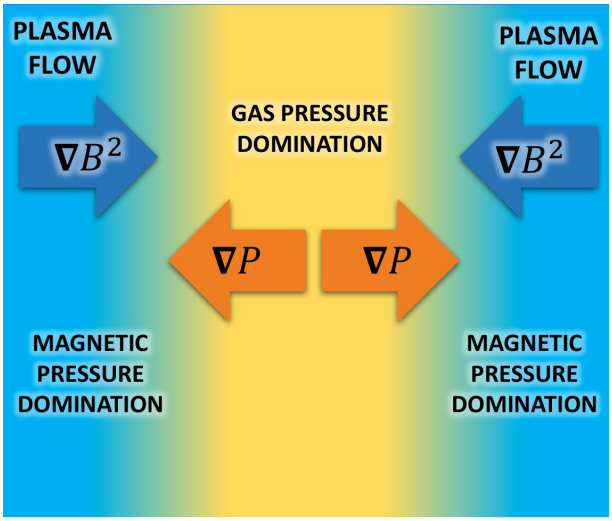

Figure 1.13: Interface between two coalescing plasmoids, with the domination of the magnetic pressure in the inflow regions and the thermal plasma pressure inside the current sheet formed by the coalescence. The equilibrium state of such a current sheet is determined by the total pressure balance at its boundaries.

ample, in Dubinov et al. [2012a,b] where highly nonlinear waves in multicomponent plasmas are considered. According to the definition of ζ, the periodic solutions of Eq. (1.15) represent oscillatory variations of the magnetic field in the current sheet. The magnitude of the associated bursts of the electric field was found to grow up in the nonlinear phase even more rapidly than the magnetic field, which results in the efficient periodic acceleration of charged particles.

The analytical model developed by Tajima et al. [1987] is based upon a two-fluid hydrodynamic description of the plasma, generally allowing the ion and electron plasma components to evolve separately. Such a formulation naturally implies the presence of a broad range of solutions in the model, with a variety of characteristic time scales, namely, from the electron plasma period to the ion plasma period or longer. However, Tajima et al. [1987] derived governing equation (1.15) and analysed its oscillatory solutions only in the assumption of a quasi-neutral plasma, i.e. when the electron and ion plasma densities are strictly equal to each other, but the electrostatic field is still treated to have non-zero values. This special case is valid only for long-period oscillations (with periods much longer than the ion plasma period), and cannot address higher-frequency effects, for example the local electric charge separation in the current sheet. This omission is rectified in Sec. 3.2, where the solution of the problem is generalised for both low- and high-frequency

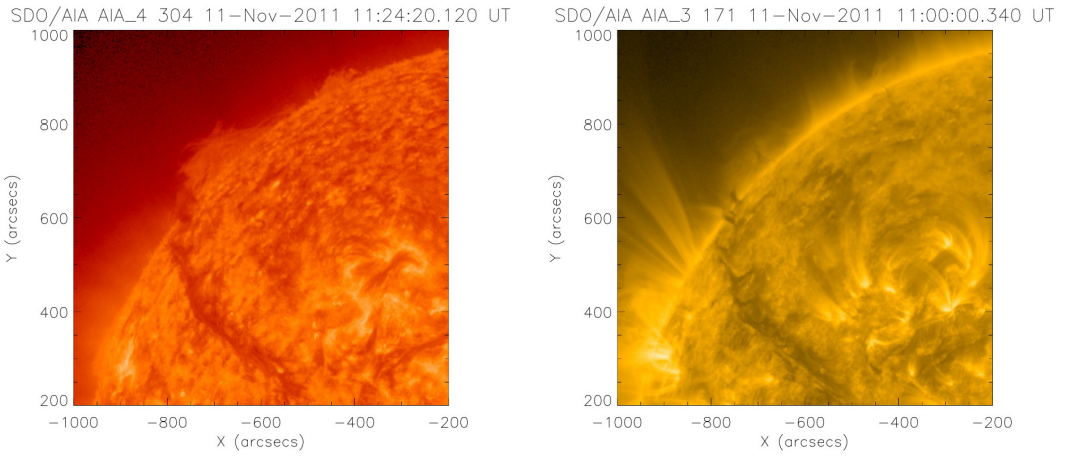

Figure 1.14: A typical off-limb solar prominence and on-disk filament, observed with SDO/AIA in 304 Å (left) and 171 Å (right) channels [see Parenti, 2014].

oscillations, including solutions of Eq. (1.15) as a limiting case.

1.3 Prominences

Solar *prominences* are among the most intriguing objects observed in the solar corona. They are condensations of plasma at temperatures of about 10^4 K (typical for the chromosphere), levitating in the much hotter solar corona with temperatures typically greater than 10^6 K [see e.g. Parenti, 2014, for a comprehensive review]. Unambiguous scientific evidences of prominences in the solar corona are dated to the second half of the 19th century [Tandberg-Hanssen, 1998]. Prominences are observed in the emission in the optical and EUV lines formed at low temperatures, such as the Hα and 304 Å channels, or in the absorption in some EUV lines at higher temperature formation (see Fig. 1.14). The term "prominence" is usually referred to the structures which are seen off the solar limb. However, when they are located on the solar disk, they appear in the form of long dark threads (the darkness is due to the absorption processes of the radiation coming from lower layers of the solar atmosphere) and they are historically defined as filaments. In addition, prominences present different morphologies and characteristics. A thorough statistical investigation of solar prominences has been recently accomplished by McCauley et al. [2015], using the observational data obtained with the Solar Dynamics Observatory (SDO).

The main questions related to prominences concern the physical mechanisms involved in their formation and evolution. Indeed, prominences can be generally

attributed to two categories: quiescent prominences, which are observed floating in the low solar corona with time scales ranging from hours to several days before they slowly fade out or dissolve; and erupting prominences, which become unstable in the presence of certain physical conditions. As a consequence of the prominence eruption, a coronal mass ejection (CME) can be formed and expelled from the solar corona. The eruption is believed to be accompanied by a sudden reconnection of the magnetic field lines, where prominences are regarded as the inner part of a magnetic flux rope system. The loss of equilibrium can be caused by various reasons: eruptions can be triggered by a nearby flare [Panesar et al., 2015], or in response to an emerging magnetic flux or variation of the local magnetic helicity [Yeates and Mackay, 2009], or maybe due to the action of MHD waves, as observed for some events before the eruption onset [see e.g. the discussion in Shen et al., 2014a].

1.3.1 Observations of oscillations in quiescent prominences

Quiescent prominences are also very dynamic, being subjected to MHD oscillations [Arregui et al., 2012]. These oscillatory variations in prominences can be separated into transverse oscillations [e.g. Hershaw et al., 2011; Asai et al., 2012; Shen et al., 2014b] and longitudinal oscillations [e.g. Vršnak et al., 2007; Zhang et al., 2012; Luna et al., 2014]. Based on the direction of the filament main axis displacements, transverse oscillations can have horizontal [e.g. Kleczek and Kuperus, 1969; Hershaw et al., 2011; Shen and Liu, 2012], or vertical polarisations [e.g. Hyder, 1966; Eto et al., 2002; Okamoto et al., 2004; Kim et al., 2014; Mashnich and Bashkirtsev, 2016].

The vast majority of observational detections of periodic motions in prominences are based on the analysis of the Doppler velocity. In addition, other spectral indicators (e.g. the line width and intensity) are also used for searching for prominence oscillations. However, simultaneous observations of the oscillation with the same period in several of these spectral indicators are rather rare and require further detailed investigations. The observed values of the Doppler velocities usually peak at 2–3 $\mathrm{km\,s^{-1}}$ in amplitude, corresponding to a broad range of oscillation periods varying from a few tens of minutes to several hours [e.g. Mashnich and Bashkirtsev, 1990; Bashkirtsev and Mashnich, 1993; Oliver and Ballester, 2002; Arregui et al., 2012]. The oscillation amplitudes are typically seen to exponentially decay, with the oscillation quality factor (the dimensionless parameter comparing the exponential decay time to the oscillation period) being of 1–4 [e.g. Molowny-Horas et al., 1999]. The spatial distribution of these small amplitude variations is often found to be of a local nature, i.e. the oscillation of a given period is mainly pronounced in a certain part of the prominence and does not affect its whole body. In this context, Mashnich

et al. [2009] confirmed that periodicities can systematically vary over the on-disk filament length (or the off-limb prominence height), with the coherence spatial scales growing with the oscillation period. Small amplitude oscillations of prominences are normally seen to be not related to flare activity, and the question of their trigger still remains intensively debated [see e.g. Arregui et al., 2012, and references therein]. For example, Alfvén waves propagating upwards from the photosphere (or chromosphere) to the corona are believed to be able to perturb the dense prominence material penetrated by the vertical magnetic field lines. In this mechanism, the oscillation period should be fully prescribed by the driving wave motion. On the other hand, there is a number of studies where much longer and shorter periods than those of a photospheric magnetic driver were detected, indicating that this scenario of energy transfer is not unique and other possible candidates should be also taken into account.

Oscillatory variations with velocity amplitudes greater than or about the local sound and Alfvén speeds in prominences (which are about 10 $\mathrm{km\,s^{-1}}$ or larger for typical prominence conditions) are usually referred to as large amplitude oscillations [Tripathi et al., 2009]. In contrast to the small amplitude regime, large amplitude oscillations are mainly collective motions, which are always associated with active regions located nearby, for example occurring before prominence eruptions [e.g. Isobe and Tripathi, 2006] or triggered by a global coronal wave [e.g. Shen et al., 2014a]. In particular, Hershaw et al. [2011] investigated the interaction of a quiescent prominence with two consequent incoming coronal wave trains generated in a distant active region. One of these wave trains was observed to be sufficiently stronger than the other, possessing enough energy to excite horizontally polarised large amplitude oscillations of the prominence. The oscillation amplitude and period were found to depend on the prominence height and reached 50 $\mathrm{km\,s^{-1}}$ and 104 min, respectively. Despite numerous detections of such large amplitude oscillations in prominences, for example in the EUV and Hα lines, from the theoretical point of view there is an obvious lack of relevant analytical models addressing observed nonlinear properties. Furthermore, plasma in prominences is observed to show very complex dynamics, which has been described in terms of turbulent processes [e.g. Berger et al., 2010; Leonardis et al., 2012]. Such evidences may be strongly affected by thermodynamical processes acting in prominences, which can also influence the evolution of slow MHD waves [e.g. Kumar et al., 2016; Ballester et al., 2016]. In addition, the Kelvin–Helmholtz instability may take place during oscillations of prominences, sustaining the damping and plasma heating [e.g. Antolin et al., 2014; Okamoto et al., 2015; Terradas et al., 2016].

1.3.2 Analytical modelling of oscillations in prominences

Transverse oscillations of non-eruptive prominences have been analytically modelled based on natural MHD oscillations of the current-carrying toroidal magnetic ropes, accounting for the damping effect by an aerodynamic-like drag force of a linear [e.g. Vrsnak, 1990; Vrsnak et al., 1990] or quadratic [e.g. Cargill et al., 1994] proportionality to the plasma flow velocity. The governing equations were analysed in a small amplitude, linear regime, allowing the authors to investigate the mechanical stability of the system in its dependence on the intrinsic plasma parameters and its geometry. Nonlinear effects of the magnetic flux rope evolution, associated with the energy dissipation due to the drag force, are addressed by Farrugia et al. [1997]. The governing second-order ordinary differential equation describing the dynamics of such a nonlinear damped oscillator, has the form

$$\ddot{u} = Su^{-3} - Qu^{-1} + Ku^{1-2\gamma} - \nu\dot{u}, \tag{1.17}$$

where the evolution function $u(t)$ is determined via the physical parameters of the magnetic rope, and for example is connected to the internal plasma density ρ by $\rho \propto u^{-2}$, and γ is the adiabatic index. The first two terms on the right-hand side of Eq. (1.17) represent the axial and pinch magnetic forces, with the corresponding positive constants S and Q, respectively. The thermal gas pressure gradient is given by the third term (with the constant $K > 0$), and the last term is the dissipative force taken to be proportional to the product of the plasma density and the radial velocity, with ν being the viscosity coefficient. Two phases of the magnetic rope evolution, namely a continuous expansion and an oscillation phase, were revealed. Numerical analysis of Eq. (1.17) showed that in the large amplitude regime of the expansion phase the effect of the magnetic terms is negligibly small, and the dynamics is mainly governed by the interplay between the thermal pressure gradient and the dissipation. The oscillation phase was found to be highly sensitive to the value of the dissipative coefficient ν. In particular, for $\gamma = 1$ the shortest oscillation period (corresponding to the small amplitude case) was analytically obtained to depend upon the coefficient ν, plasma parameter β, and the ratio of the maximum values of the axial and azimuthal magnetic field components, $B_z^{\max}/B_\phi^{\max}$, as

$$P \propto \left\{ 2\left[1 - \frac{\beta}{4}\left(\frac{B_z^{\max}}{B_\phi^{\max}} \right)^2 \right]^2 - \frac{\nu^2 S}{4Q^2} \right\}^{-1/2}, \tag{1.18}$$

where the magnetic constants S and Q are introduced in Eq. (1.17). For fixed values of other parameters, period (1.18) is independent of the oscillation amplitude and is seen to increase with ν up to some critical value. However, in the nonlinear large amplitude regime the oscillation period effectively decreases due to the dissipative effect, as it additionally positively correlates with the oscillation amplitude. In addition to quiescent prominences, one can apply the model of toroidal currents to eruptive filaments too [e.g. Filippov et al., 2001]. However a further detailed consideration of these objects is out of the scope of the current discussion.

Comparison of the modelling and observational results showed that the equilibrium state of prominences in the solar corona is most likely supported by the magnetic field structures with a magnetic dip [see e.g. Filippov, 2016, for recent results]. This Kippenhahn–Schlüter type equilibrium [Kippenhahn and Schlüter, 1957] was used in theoretical models treating the prominence as a plasma slab embedded in a magnetic dip created by some sources at the surface of the Sun. In particular, MHD eigen modes of such a prominence structure, i.e. the fast and slow magnetoacoustic and Alfvén modes, with and without accounting for the gravity force, were investigated by Oliver et al. [1993] and Joarder and Roberts [1993], respectively. Global oscillations of prominences also modelled as a plasma slab in a magnetic dip with straight magnetic field lines anchored in vertical rigid boundaries (not connected to the solar surface) are considered in Anzer [2009].

Various thermodynamical processes are also widely considered to be responsible for long-period oscillations in quiescent prominences. In particular, an essentially nonlinear effect of the thermal over-stability in prominences can be caused by the imbalance of the plasma heating and energy losses due to the optically thin radiation and thermal conduction, and can lead to periodic variations of macroscopic parameters of the plasma, responsible for the emission intensity. A simplified model of this phenomenon, restricted to the field-aligned processes only, and neglecting induced variations of the magnetic field, was developed by Kuin and Martens [1982]. The system of two nonlinear first-order ordinary differential equations, describing the time evolution of thermodynamical processes in a hot coronal loop, is

$$\dot{T} = \rho^{-1}\left[1-\rho^2\Psi(T)-\Upsilon(T-1)\right], \tag{1.19}$$

$$\dot{\rho} = \Gamma\Upsilon(1-T^{-1}). \tag{1.20}$$

In this model the plasma is considered to be hydrodynamic, and the heating function was taken to be constant per unit volume. This model provides the relationship between the plasma mass density ρ and temperature T, which are normalised to their

equilibrium values. The time t is measured in units determined by the plasma equilibrium parameters, $\Psi(T)$ is the radiative loss function for an optically thin plasma, Γ ($0 \leq \Gamma \leq 1$) is a dimensionless constant which determines the chromospheric evaporation efficiency, and the dimensionless constant Υ is determined by a combination of initial plasma conditions. Numerical investigation of the coupled equations (1.19)–(1.20) showed that for $\Upsilon < 1$ the solutions readily approach a limit cycle in phase space, indicating the possibility of the existence of stable large amplitude periodic oscillations of the temperature and density inside the loop. The model was numerically extended by Müller et al. [2004] for a time-independent non-uniform heating source. The obtained results confirmed the existence of the limit cycle regime and, hence, proved the possibility of the thermally over-stable dynamics in coronal loops. In both Kuin and Martens [1982] and Müller et al. [2004], the oscillation periods were found to be of several hours. The presence of the limit cycle behaviour in the discussed models allows one to refer the revealed oscillations to as self- (or auto-) oscillations. By definition, self-oscillations have amplitudes and periods which are largely independent of the initial conditions, and are functions of the plasma parameters only, and can be considered as an example of the plasma self-organisation [Jenkins, 2013]. The concept of self-oscillations can also be applied to continuous finite amplitude transverse oscillations of prominences [e.g. Hillier et al., 2013], caused by the interaction of the overlying plasma non-uniformities with quasi-steady photospheric flows [Nakariakov et al., 2016a].

A more advanced analytical MHD model addressing the effect of the thermal over-stability on the parallel and perpendicular propagation of magnetoacoustic waves in a non-adiabatic plasma was developed by Chin et al. [2010]. The model takes into account a heating and radiative cooling function $\Lambda(p, \rho)$ determined by the plasma pressure p and mass density ρ, and parallel thermal conduction. Only the weakly nonlinear perturbations of the thermal equilibrium were studied. The effect of the heating/cooling function $\Lambda(p, \rho)$ on the evolution of the perturbation was considered to be of the same order of magnitude as the nonlinearity and damping by thermal conduction. Hence, the consideration was restricted to accounting for the linear and quadratic terms of Λ in its Taylor expansion, leading to the nonlinear evolutionary equation of the form of the generalised Burgers–Fischer equation. Analysis of the possible dynamical regimes described by this model confirmed the existence of periodic magnetoacoustic self-oscillations, highly depending upon the sign and value of the quadratic term of Λ.

Another essentially different approach describing quiescent prominence oscillations, based on the interaction of line currents through the electromagnetic Lorentz

force, was suggested by Kuperus and Raadu [1974]. In this mechanism the prominence is modelled as a straight current-carrying wire located at some height above the electrically conductive photosphere. Interaction of the prominence current with the conductive surface is described by the introduction of a virtual "mirror" current (the "mirror" effect) located below the photosphere, strictly symmetric with respect to the prominence. The Kuperus–Raadu model allows for vertical oscillations of the prominence, but does not describe horizontally polarised oscillations. Indeed, even a small displacement of the prominence current in the horizontal direction automatically causes a corresponding identical displacement of the mirror current, and thus the horizontal restoring force is absent from that model. Moreover, the Kuperus–Raadu model neglects the interaction of the prominence with external sources of the magnetic field. In particular, the prominence may be embedded in a magnetic dip, for example a Kippenhahn–Schlüter type magnetic configuration. In this case there could be restoring forces responsible for horizontal oscillations. Effects of the delayed response between the photosphere and the filament were investigated also within the concept of line current models in van den Oord et al. [1998]. In particular, it was shown that the Kippenhahn–Schlüter type equilibrium of a prominence can never be stable in the horizontal and vertical directions simultaneously, in other words the prominence position is always unstable, if the effect of the mirror current is neglected in the model. A new analytical model of both small and finite amplitude transverse oscillations of quiescent prominences in a magnetic environment, accounting for the magnetic dip provided by two photospheric sources and the mirror current effects, is developed in Chapter 4. In contrast to the results obtained by van den Oord et al. [1998], small amplitude analysis (Sec. 4.1) of the proposed model reveals the stability of the prominence in both horizontal and vertical directions simultaneously, while the nonlinear regime (Sec. 4.2) brings additional, more sophisticated effects on the prominence dynamics, for example such as a nonlinear coupling of the horizontal and vertical modes and the presence of metastable equilibria.

Advanced numerical simulations are also extensively used for modelling of oscillations in quiescent prominences. For instance, Antolin et al. [2015] performed numerical study of transverse MHD waves in a prominence flux tube. In their mechanism the Kelvin–Helmholtz instability takes place at the resonant absorption layer of the oscillating flux tube, dissipating energy from the transverse motions into the Alfvén continuum through the development of MHD turbulence. Properties of MHD oscillations as perturbations of a two-dimensional magnetostatic model of a prominence, taking into account the effects of gravity, were determined numerically by Terradas et al. [2013]. Large amplitude longitudinal oscillations in prominences

were modelled in terms of a so-called pendulum model by Luna and Karpen [2012]; Luna et al. [2016]. This model has been successfully adapted for a dipped magnetic field line configuration, and treats the gravity projected along the magnetic field lines as the restoring force. Here only several most recent numerical models of global prominence oscillations are briefly overviewed, while more comprehensive discussion of this issue would require a dedicated section and is out of the scope of this thesis.

Chapter 2

Spectral analysis of solar periodicities with the Hilbert–Huang transform (HHT)

2.1 HHT analysis in solar physics

The solar atmosphere evidently shows a wide range of periodicities detected throughout the whole electromagnetic spectrum. They have a different physical nature and causes, and their periods vary from a fraction of a second up to several years, and even to centuries. Some examples of the oscillatory processes responsible for the observed periodicities are the 11 yr solar cycle, the so-called quasi-biennial oscillations, the helioseismic variations [see e.g Hathaway, 2010; Bazilevskaya et al., 2014, and references therein for recent comprehensive reviews], MHD waves and oscillations in different plasma structures of the solar atmosphere [see De Moortel and Nakariakov, 2012; Liu and Ofman, 2014; Jess et al., 2015], and various quasi-periodic pulsations appearing in solar flare light curves [Nakariakov and Melnikov, 2009; Kupriyanova et al., 2010; Simões et al., 2015; Van Doorsselaere et al., 2016]. The vast majority of these quasi-periodic solar signals exhibit non-stationary, anharmonic and sometimes nonlinear behaviour. Traditionally, spectral analyses of solar periodicities are performed with the use of the Fourier transform based techniques, for example such as the periodogram and wavelets and other more advanced techniques specific for each separate branch of solar physics. However, the applicability of the Fourier transform has a few crucial shortcomings: namely, the analysed system must evolve

in a linear regime, and the data must be rigorously periodic or stationary. Most importantly, all these methods are based on the decomposition of a signal of interest into a set of *a priori* prescribed harmonic basis functions or their wavelets. Therefore, they cannot address the nonlinear, anharmonic and non-stationary nature of many observational signals from the Sun. An intensively developing alternative spectral method for the analysis of such nonlinear and non-stationary time-series is the Hilbert–Huang transform (HHT) technique [Huang et al., 1998; Huang and Wu, 2008]. It is based upon the empirical mode decomposition (EMD) of the signal of interest into a basis derived directly from the data by iterative searching for the local time scales naturally appearing in the signal. Being not restricted by an *a priori* assignment of the basis function, EMD operates adaptively and, hence, is essentially suitable for processing of non-stationary and nonlinear time-series typical for solar signals. The subsequent Hilbert transformation of the identified intrinsic mode functions (IMF) allows one to obtain their instantaneous frequency–power distributions, designated as the Hilbert power spectrum. These unique advantages of the HHT scheme attract a growing interest in its application to the analysis of quasi-periodic dynamical phenomena on the Sun.

The first step of the method, EMD of a given signal $X(t)$, is performed iteratively by a so-called "sifting" process. After having identified all the local extrema in the signal of interest, its upper and lower envelopes are constructed (e.g. via the spline interpolation). The mean $m_1(t)$ of the upper and lower envelopes is then subtracted from the signal,

$$h_1(t) = X(t) - m_1(t). \tag{2.1}$$

This procedure should be repeated k times until the number of extrema in the residue $h_1(t)$ differs from the number of zero crossings by not more than 1, and the first IMF $h_{1k}(t)$ is thus reached,

$$h_{1k}(t) = h_{1(k-1)}(t) - m_{1k}(t). \tag{2.2}$$

An additional stopping criterion is introduced by limiting the standard deviation of two consecutive sifting results $h_{1(k-1)}(t)$ and $h_{1k}(t)$ by a value between 0.2 and 0.3. In some cases this value can be reduced to enhance the sensitivity of the method. The first IMF $c_1(t) \equiv h_{1k}(t)$ contains the shortest time scale component of the signal. Then this IMF is subtracted from the original data set,

$$r_1(t) = X(t) - c_1(t), \tag{2.3}$$

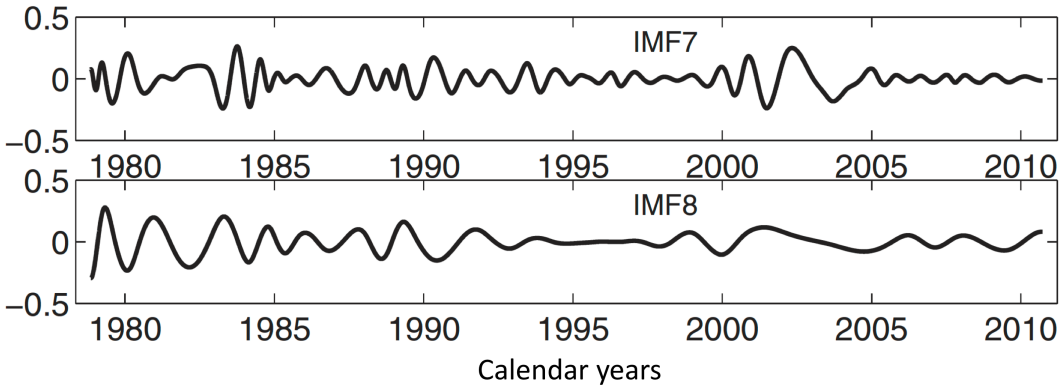

Figure 2.1: Intrinsic mode functions (IMF) 7 and 8 determined with EMD in the normalised total solar irradiance (TSI) records, with apparent mode-mixing pronounced at the time intervals between years 1980–1985 and 2000–2005 in both panels [adapted from Li et al., 2012].

and the procedure repeats, treating the residue $r_1(t)$ as a new input signal. This process is repeated revealing other empirical modes $c_n(t)$, until the last residue $r_n(t)$ becomes monotonic or aperiodic,

$$r_n(t) = r_{n-1}(t) - c_n(t). \tag{2.4}$$

Finally, the original signal can be reconstructed as a sum of all IMFs $c_j(t)$ and the last residue $r_n(t) \equiv r(t)$, which usually represents a slowly varying long-term trend of the original signal, so that

$$X(t) = \sum_{j=1}^{n} c_j(t) + r(t). \tag{2.5}$$

First applications of EMD showed that one of its major drawbacks is a systematic appearance of a mode-mixing (also often referred to as "leakage") problem, when a single IMF either consists of widely disparate scales, or a signal of a similar scale resides in different IMF components (see e.g. Fig. 2.1). To suppress such intrinsic mode leakages, the noise-assisted ensemble empirical mode decomposition (EEMD) was proposed [see Wu and Huang, 2009, for details]. EEMD determines the true IMF components by averaging of the statistical ensemble of independent trials, each consisting of the original data and an artificial white noise. In EEMD the white noise of a small but finite amplitude (e.g. 0.1–0.4 of the standard deviation of the original signal) is added uniformly over the whole frequency–time domain. Then

a new dummy signal is decomposed via EMD and the results are saved. In each individual realisation, the added noise may produce an even greater mode-mixing effect. However, a sufficient number of independent repetitions of this procedure and subsequent averaging of the whole ensemble lead to the IMF frequencies stabilisation, while the effect of white noise is statistically cancelled. The occasional trials in which the number of IMFs found in the signal with the added noise differs from that found in the original signal are disregarded.

Having obtained the set of true IMFs, the Hilbert transform is applied to each IMF, allowing one to calculate its instantaneous frequency and power. The Hilbert transform $H(t)$ of a signal $C(t)$ can be thought of as the Cauchy principal value of the integral

$$H(t) = \frac{1}{\pi} \int_{-\infty}^{+\infty} \frac{C(t')}{t' - t} dt'. \tag{2.6}$$

The signal $C(t)$ and its Hilbert transform $H(t)$ constitute a complex function, the analytical signal

$$Z(t) = C(t) + iH(t) = a(t)\mathrm{e}^{i\theta(t)}, \tag{2.7}$$

where $a(t) = \sqrt{C(t)^2 + H(t)^2}$ and $\theta(t) = \tan^{-1}[H(t)/C(t)]$ are the instant amplitude and phase, respectively. The instant frequency $\omega(t)$ is determined by the derivative of the instant phase $\theta(t)$, as

$$\omega(t) = \frac{d\theta(t)}{dt}. \tag{2.8}$$

The Hilbert power spectrum showing the power, determined as the amplitude $a(t)$ squared, as a function of the frequency and time, is obtained by combining the results of all IMFs or a partial set of them.

HHT and EMD have already been used in solar physics for analysing both long- and short-term periodicities. In particular, fundamental time scales, such as the 22 yr cycle and quasi-biennial oscillations of the solar magnetic field variability were identified with EMD in Vecchio et al. [2012a]. Terradas et al. [2004] applied EMD to propagating and standing waves in a coronal active region. Long-period oscillations of the gyroresonant emission from sunspot atmospheres with periods in the range of several tens of minutes were found in Chorley et al. [2010], and the presence of the oscillations was confirmed by EMD. Komm et al. [2001] used the HHT analysis to investigate whether the rotation rate in the convection zone shows any other systematic temporal variations besides the so-called torsional oscillation pattern in the upper convection zone. A new long-term period of 6 yr was detected.

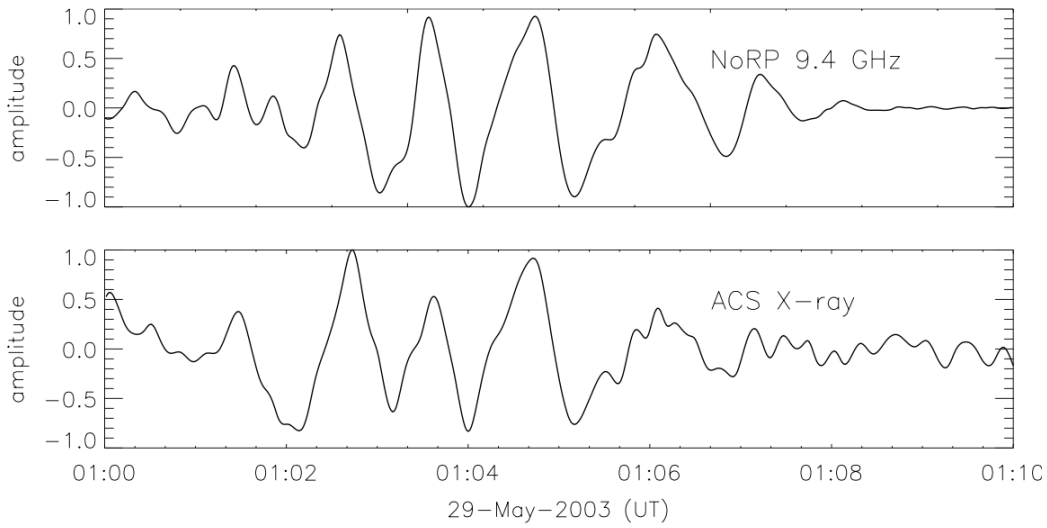

Figure 2.2: Oscillatory components of a solar flare occurred on 29 May 2003 (see Fig. 1.11), in the microwave flux at 9.4 GHz, measured with the NoRP (upper panel) and in the hard X-ray flux measured with ACS (lower panel). The oscillations were obtained by subtracting a high-frequency noise and aperiodic trend, determined with EMD, from the original signals shown in Fig. 1.11 [taken from Nakariakov et al., 2010b].

Long-term sunspot records were analysed with EMD by Li et al. [2007], revealing a set of periodic components of 1.3–1.4 yr, quasi-biennial oscillations, and the 11 yr and 22 yr solar activity cycle components. Intrinsic modes of the North–South sunspot time-series were found with EMD in Zolotova and Ponyavin [2007]. Acceleration and deceleration trends in the temporal variations of the rotational cycle length of the Sun were established with this method by Li et al. [2011], also revealing periodicities in the variation of the solar radius [Qu et al., 2015]. Also, periodicities in the monthly occurrence numbers and monthly mean energy of coronal mass ejections were studied with EMD by Gao et al. [2012]. Long-term variability of the coronal index was analysed with EMD by Deng et al. [2015]. The first successful use of EMD in the analysis of much shorter periodicities in the solar emission, such as QPPs in solar flares, can be found in Nakariakov et al. [2010b], where the technique was applied to the extraction of the high-frequency noise and aperiodic trend from the original data set shown in Fig. 1.11. Large amplitude oscillatory components of a symmetric triangular shape, obtained after subtracting these empirically identified noise and trend, are shown in Fig. 2.2. Another recent statistical study of more than hundred QPPs observed in the decay phase of solar and stellar flares, was performed

by Cho et al. [2016], where the non-harmonic trends of the analysed light curves were determined with EMD.

2.2 Empirical mode decomposition analysis of random processes in the solar atmosphere

2.2.1 Introduction

In addition to the variety of clear oscillations in the solar atmosphere, mentioned in the previous section and considered in detail in Chapter 1, broadband modes usually associated with noise often appear in solar signals of various types too. These noisy components may basically have different physical nature, for example they can be caused by instrumental artefacts or by random processes operating in the solar atmosphere. Interestingly, in the majority of previous studies these modes were usually ignored and simply disregarded in the analysis. However, recent works have shown that coloured noises can be recognised in solar and stellar flare light curves with the Fourier power spectrum, and accumulate significant part of a signal's spectral energy. They are manifested as a power-law-like Fourier power spectra, and seem to be intrinsic features of many observational data sets detected by different instruments. For example, Inglis et al. [2015] considered flare signals exhibiting QPP detected with the PROBA2 (Large Yield Radiometer), Fermi (Gamma-ray Burst Monitor), NoRH, and Yohkoh (HXT) instruments. They found that the majority of cases considered could be described by a power law in the Fourier power spectra. Signatures of strong noisy components with power-law-like Fourier power spectral densities were also detected in Gruber et al. [2011], where the RHESSI and Fermi (Gamma-ray Burst Monitor) observations of solar flares were considered. Application of the wavelet transform modulus maxima method showed the multifractal spectra of the temporal variation of the X-ray emission in solar flares [McAteer et al., 2007].

The interest in coloured noise in the solar atmosphere is connected with its possible link with various dynamical phenomena. For example, in the case of QPP in flares a frequency-dependent noise may be associated with stochastic regimes of magnetic reconnection (see e.g. Sec. 1.2.2 and references therein). In the case of the quiet Sun, the evolution of the noise with height may reveal the physical processes responsible for the generation, dissipation and evolution of MHD waves, turbulence, and episodic energy releases. Recently, Ireland et al. [2015] studied mean Fourier spectra of various regions of the solar corona observed at the 171 Å

and 193 Å wavelengths, and found that they can be described by a power law at lower frequencies, tailing to a flat spectrum at higher frequencies, plus a Gaussian-shaped contribution specific for different regions of the corona. Also, understanding of the noise is important for the development of automated detection techniques [e.g. Nakariakov and King, 2007; Sych et al., 2010; Ireland et al., 2010; Martens et al., 2012].

In contrast to the Fourier and wavelet spectral methods, behaviour of coloured noises with arbitrary power law indices in their spectral densities in the EMD analysis (see Sec. 2.1) has not been clearly revealed yet. The analysis has been restricted to the EMD of white noise [Wu and Huang, 2004]. Based on the empirical fact that EMD effectively operates as a dyadic filter [Flandrin et al., 2004], numerical experiments in Wu and Huang [2004] showed that IMFs obtained with EMD from a number of independent white noise samples are normally distributed, and the product of the IMF energy density and its mean period is constant. Furthermore, the energy density function was found to be chi-squared distributed. Analysis of a particular case of red noise in EMD has been made in Franzke [2009], revealing noise-like properties of the Earth's climate data.

This section is an adaptation of the work by Kolotkov et al. [2016a], it extends the studies of Wu and Huang [2004] and Franzke [2009], and reveals similar empirical properties of coloured noise in EMD, allowing for arbitrary power law indices in their power spectral densities, in application to the solar atmosphere. The energy densities of IMFs detected with EMD in coloured noise, are shown to be successfully described by a chi-squared distribution too. However the parameter of the distribution function, the number of degrees of freedom (DoF), needs to be adjusted accordingly for each sort of noise. For illustration of the reliability of the method, this EMD-based technique is adapted for analysing solar EUV data sets obtained with SDO/AIA, testing them in the manner described above for the presence of randomly distributed dynamical processes. In the pre-SDO era, only lower layers of the solar atmosphere were investigated for the presence of high-frequency tails in their dynamical spectra, which were found to vary significantly with height and magnetic properties of the region [see e.g. Evans et al., 1963; Orrall, 1966; Woods and Cram, 1981; Deubner and Fleck, 1990]. In this study the data obtained with the modern SDO/AIA instrument is used, which due to the advanced combination of its spatial and temporal resolutions and high values of the signal-to-noise ratio, allows one to examine the higher coronal altitudes of the solar atmosphere in the EUV band and directly compare their dynamical spectra with the chromospheric and photospheric layers. Application of the developed EMD-based noise–test to SDO/AIA data sets

revealed that they mainly consist of random signals represented by a combination of white noise at shorter-period spectral components and pinkish noises at longer periods, which in turn could be attributed to specific physical processes of an instrumental or natural origin, respectively.

2.2.2 Methodology and properties of coloured noises in EMD

Power spectral density S of coloured noise as a function of the frequency f can be written as $S = C/f^{\alpha}$, where C is a constant which can be reduced to unity by the appropriate normalisation without loss of generality, and α is a power law index characterising the steepness of the dependence, i.e. its "colour". In the further analysis, only non-negative values of α are considered. It should be mentioned that the introduced model of coloured noises breaks down when $f \to 0$. Noises with $\alpha = 0$ are usually referred to as white noise with a constant spectral energy for all considered frequencies, while non-zero values of α correspond to so-called coloured noise. In particular, $\alpha = 1$ describes a flicker (pink) noise, while $\alpha = 2$ gives a Brown(ian) (red) noise.

Wu and Huang [2004] analysed behaviour of white noise of length N with $\alpha = 0$ in EMD. Based on the numerical examples they established an empirical relation for the energy densities E_{m} of each separate IMF obtained with the EMD expansion of the white noise samples and their corresponding mean periods P_{m}, as $E_{\mathrm{m}}P_{\mathrm{m}} = \text{const}$. This empirical fact is directly related to the dyadic property of EMD. The dyadic nature of EMD in turn may be corrupted by the mode-mixing problem introduced in Sec. 2.1, causing remarkable deviations of the energy–period dependence of some particular IMF from the expected form. Additionally, the probability density function of each IMF was found to be normally distributed. The latter property leads to a chi-squared distribution of the IMF energy density E_{m} with k degrees of freedom (DoF):

$$f(E_{\mathrm{m}}) = \chi^2 \left(NE_{\mathrm{m}}, k\right). \tag{2.9}$$

By definition, white noise of length N contains N independent and random data points. Hence, each sample of such a white noise has its N DoF, which are evenly distributed across the Fourier power spectrum. As the white noise spectral energy is also evenly distributed across the spectrum, the number k in the chi-squared distribution (2.9) is proposed to be proportional to the mean modal energy, i.e. $k = N\bar{E}_{\mathrm{m}}$, where $\bar{E}_{\mathrm{m}} = \sum_{i=1}^{n} E_{\mathrm{m}_i}/n$ with n being a sufficiently large number of

white noise samples considered.

However, this simple rule should not work for coloured noises, in the case with $\alpha \neq 0$. Indeed, the spectral energy of coloured noises is distributed across the spectrum by the power law dependence mentioned above. Hence, data points of coloured noises are no longer independent, but instead they are correlated with each other. The latter makes the exact determination of the DoF number of the coloured noise, and consequently the DoF number of IMF obtained from such a noise with EMD, to be a non-trivial task. However, assuming again that the coloured noise IMFs are normally distributed, the modal energy E_{m} can be represented by a sum of k independent normal variables X_i with zero mean and variance σ, as

$$E_{\mathrm{m}} = \sum_{i=1}^{k} X_i^2. \tag{2.10}$$

In case of white noise, where the modal energies and the number of DoF are evenly distributed across the spectrum, the variance σ is of the same value for all IMFs. Hence, it can be normalised to unity, and the modal energy (2.10) is distributed by the chi-squared law (2.9) with k being the number of DoF [Wu and Huang, 2004]. In contrast, in the coloured noise case the number of DoF of some particular IMF may differ from its mean modal energy, and the corresponding normalisation is impossible. In this case, the quantity distributed by the chi-squared law is

$$Y = \sum_{i=1}^{k} \frac{X_i^2}{\sigma^2}, \tag{2.11}$$

with the values of σ, which in general may be different for different IMF. Using the fact that the mean value of Y is equal to the number of DoF, k, one can obtain from Eqs. (2.10) and (2.11) the value of σ of coloured noise IMFs as

$$\sigma^2 = \frac{N\bar{E}_{\mathrm{m}}}{k}. \tag{2.12}$$

Substituting (2.10) and (2.12) into (2.11), one can derive the probability density function of coloured noise IMFs energies E_{m} in a general form as

$$\tilde{f}(E_{\mathrm{m}}) = \frac{k}{N\bar{E}_{\mathrm{m}}} \chi^2 \left(\frac{kE_{\mathrm{m}}}{\bar{E}_{\mathrm{m}}}, k \right), \tag{2.13}$$

which is, in fact, the chi-squared distribution of the quantity $Y = kE_{\mathrm{m}}/\bar{E}_{\mathrm{m}}$, governed by a single parameter k being the number of DoF, and reducing to the corresponding white noise distribution (2.9) for $k = N\bar{E}_{\mathrm{m}}$.

From the practical point of view, distribution (2.13) can be represented by the functions $E_\pm$ giving its upper (e.g. 99%) and lower (e.g. 1%) confidence intervals, respectively. To obtain their dependences on the instant period P, $E_\pm(P)$, dependences $k(P)$ (DoF) and $\bar{E}_\mathrm{m}(P)$ (mean modal energy density) are empirically determined from numerical experiments and substituted in (2.13). More specifically, Fig. 2.3 shows several examples of the modal energy NE_m distribution of the synthetic noisy signals with $\alpha = 0$ (white noise) and $\alpha = 1.5$ (reddish noise), fitted by the probability density function (2.13) with DoF determined from the best fitting and the mean energy taken from the input data. The functional form of distribution (2.13) has been fitted to the binned histograms shown in Fig. 2.3 with the number of bins being 200. The fitting procedure is robust, giving identical results in a broad range of the number of bins tested, namely from 20 to 1000.

The mean modal energy $N\bar{E}_\mathrm{m}$ of white noise IMFs was found to change proportionally to the best fitted DoF (see Eq. (2.9)). However, in some cases the detected values of DoF may significantly differ from the mean modal energy. It additionally confirms the only approximate dyadic nature of EMD, with possible discrepancies caused by the mode-leakage problem. In contrast, the reddish noise with $\alpha = 1.5$ shows rather more complicated behaviour with inverse proportionality. For both noises DoF are found to decrease with the IMF number. Additionally, for both noises, IMFs with higher values of DoF show distributions of NE_m closer to the normal distribution, which is also a typical feature of the chi-squared distribution.

The dependence $\bar{E}_\mathrm{m}(P)$ is obtained by fitting the modal energy values averaged over each considered period with a linear function in a logarithmic scale (see Fig. 2.4). This also allows for the empirical determination of the α index in the dependence $S = 1/f^\alpha$. Indeed, assuming again the dyadic properties of EMD, we can calculate the energy density E_m of the m-th mode as:

$$E_\mathrm{m} = \int_{f_\mathrm{m}/\sqrt{2}}^{\sqrt{2}f_\mathrm{m}} \frac{df}{f^\alpha} = C_0 P_\mathrm{m}^{\alpha-1}, \tag{2.14}$$

where C_0 is some constant, and f_m and P_m are the modal frequency and period, respectively, with $f_\mathrm{m} = P_\mathrm{m}^{-1}$. Hence, according to (2.14), the empirical relation $E_\mathrm{m}P_\mathrm{m} = \mathrm{const}$ obtained for white noise ($\alpha = 0$) in Wu and Huang [2004] can be generalised to the form

$$E_\mathrm{m}P_\mathrm{m}^{1-\alpha} = \mathrm{const}, \tag{2.15}$$

for coloured noise with arbitrary values of α. A similar relation between modal energies and periods has been shown in Franzke [2009]. However, that study was

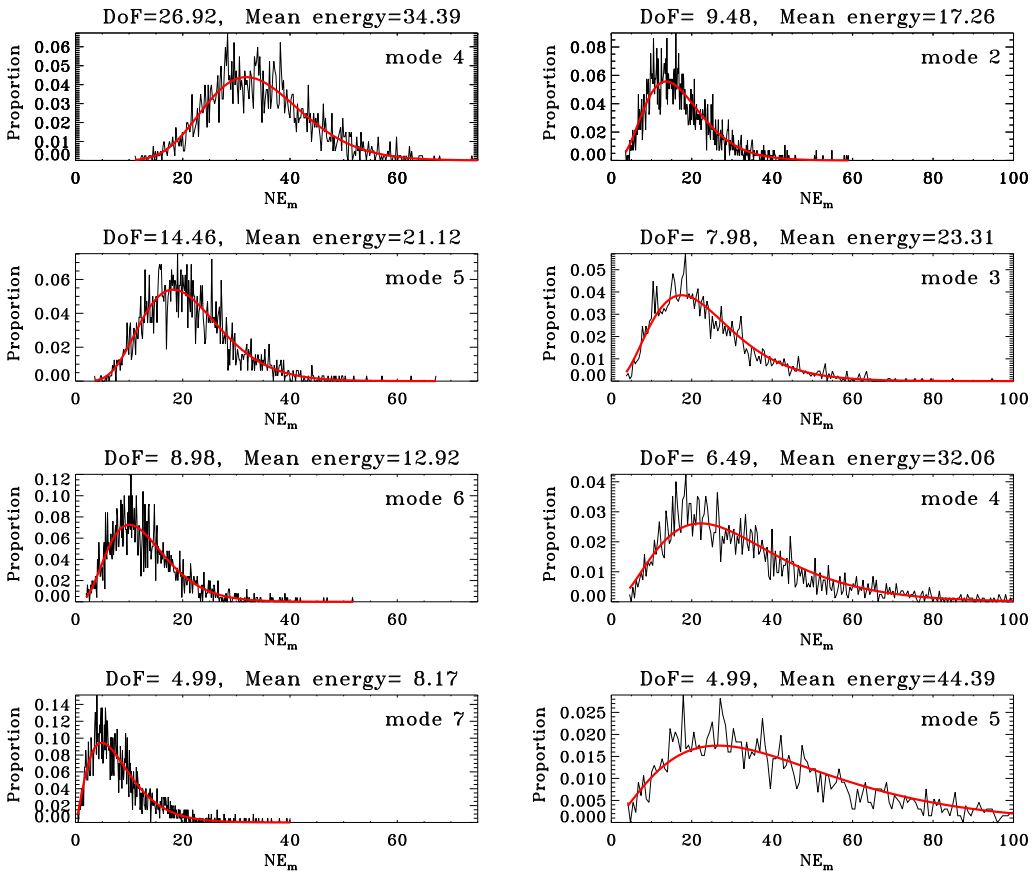

Figure 2.3: Histograms (black) showing the normalised modal energy NE_{m} fitted by distribution (2.13) (red) for several IMFs obtained with EMD from 2000 independent samples of synthetic white ($\alpha = 0$, left column) and coloured ($\alpha = 1.5$, right column) noise. Each noise sample contains $N = 500$ data points. All samples were normalised for their total energy to be unity.

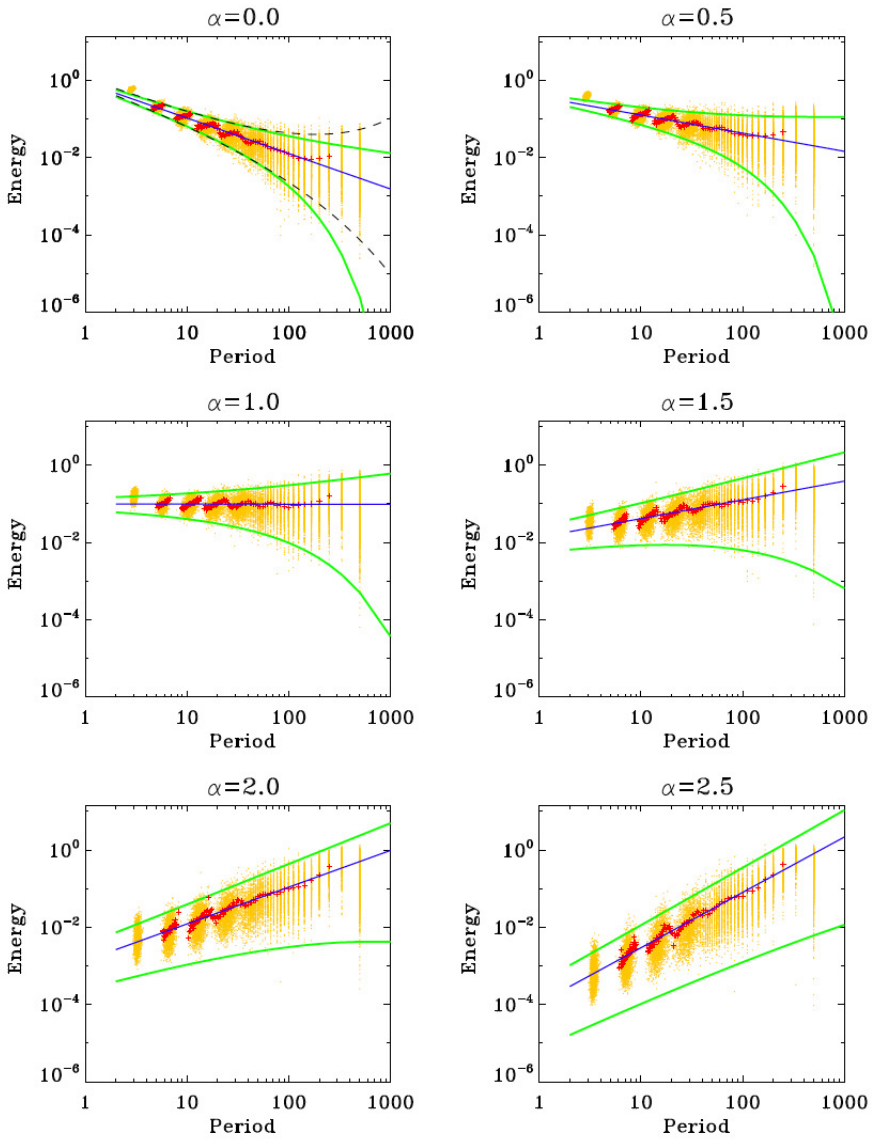

Figure 2.4: Energy–period distributions (yellow dots) of IMFs obtained with EMD from 2000 independent samples of synthetic noisy signals with $\alpha = 0$ (white noise), $\alpha = 0.5$, $\alpha = 1$ (flicker or pink noise), $\alpha = 1.5$, $\alpha = 2$ (Brown(ian) or red noise), and $\alpha = 2.5$. Each sample contains 500 data points. All samples were normalised for their total energy to be unity. Period is measured in dimensionless evenly sampled time-steps between the data points. The energy averaged over each period is indicated by the red crosses. Blue lines represent the empirical dependence of the mean modal energy $\bar{E}_{\mathrm{m}}$ upon the period P, obtained with linear fitting. Green lines show the $E_{\pm}(P)$ functions, the 99% and 1% confidence intervals, calculated for the chi-squared distribution given by (2.13). For white noise ($\alpha = 0$), the 99% confidence interval from Wu and Huang [2004], obtained as second-order Taylor expansion of the exact dependence, is shown with the dashed lines.

restricted to a particular case of red noise only. On a logarithmic scale, the slope of the line given by a $y = (\alpha - 1)x + b$ function with $y = \ln E_{\mathrm{m}}$, $x = \ln P_{\mathrm{m}}$, and $b = \ln C_0$, allows for the estimation of the empirical value of α, appearing in the analysed sample. Numerical experiments performed with the use of synthetic signals showed that such an empirical estimate gives values of α with relative errors of up to 3.3% (recall that the dyadic nature of EMD can still be significantly corrupted by the mode-leakage problem). It should be noted that coloured noise is known to exhibit self-similar behaviour, implying the spectral energy to continuously grow with the period up to infinite values in the most general case. However, in reality the longest available period is usually prescribed by the length of the observational time series, thus putting a restriction on the highest expected value of the spectral energy. Furthermore, the periods which are longer than the half-length of the analysed signal are not fitted, as the corresponding IMFs contain an insufficient number of extrema for the correct determination of their periods. Following Wu and Huang [2004], the first IMF (with the shortest period) is also excluded from fitting as it demonstrates rather abnormal behaviour in comparison with the other modes.

Substituting the empirical dependences $k(P)$ and $\bar{E}_{\mathrm{m}}(P)$ to the chi-squared distribution given by expression (2.13) one can calculate the corresponding confidence intervals $E_{\pm}(P)$. Figure 2.4 shows the energy–period dependences of different modes and corresponding confidence intervals obtained empirically with the method described above for noise with $\alpha = 0$ (white noise), $\alpha = 0.5$, $\alpha = 1$ (flicker or pink noise), $\alpha = 1.5$, $\alpha = 2$ (Brown(ian) or red noise), and $\alpha = 2.5$. The dependences are given by the dots showing the energy and mean period of each IMF. The corresponding modal energy and mean period were calculated as $NE_{\mathrm{m}} = \sum_{j=1}^{N} C_{\mathrm{m}_j}^2$ and $P_{\mathrm{m}} = 2N/b_{\mathrm{m}}$, respectively, with C_{m} being the m-th IMF, N is the total length of the signal, and b_{m} is the number of extrema in the m-th IMF. The dots are seen to scatter within the confidence intervals and are clustered together in separate groups indicating localisation of periods and energies of IMFs. In particular, numerical results obtained for the white noise samples are consistent with those shown in Wu and Huang [2004]. Their confidence intervals obtained with the second-order Taylor expansion of the exact dependences, and hence valid only in the regions with small deviations of E_{m} from the mean value, are also shown in Fig. 2.4.

In the case when one tests real signals for randomly distributed processes with an *a priori* unknown value of the power law index α, the analysis can be itemised in the following steps:

- Normalisation of the analysed samples so that their total energy is unity before

the EMD processing.

- Empirical estimation of the power law index α from the slope of the linear fitting of the modal energy averaged over each period in the form of Eq. (2.15).
- Construction of corresponding empirical dependences $\bar{E}_{\rm m}(P)$ in the form (2.15) and $k(P)$ for normalised synthetic coloured noise with a certain value of α determined above.
- Calculation of the confidence intervals $E_{\pm}(P)$ from the chi-squared distribution shown in Eq. (2.13) for the chosen sort of the coloured noise.

Having obtained $E_{\pm}(P)$, one can consider IMFs with an energy–period distribution within this interval to be related to a random process with a certain value of the power law index α.

2.2.3 Noise-testing of SDO/AIA data

The developed methodology is applied to the investigation of statistical properties of the EUV emission coming from the NOAA 11131 active region and its neighbourhood. The SDO/AIA observations are used, corresponding to different levels of the solar atmosphere: the upper photosphere (1600 Å), chromosphere (304 Å), and corona (171 Å). For each wavelength a continuous sequence of 500 images with the highest available cadence (12 s for 304 and 171 Å, and 24 s for 1600 Å) is analysed, starting on 8 December 2010, 00:00:00 UT, when the active region was close to the central meridian. There were no flares during the observational interval. The images were downloaded from the SDO data processing centre[1]. Before downloading, the images were cropped, de-rotated, and coaligned.

For investigating statistical properties of the intensity variations in different channels, two square regions of interest (ROI 1 and 2) shown in Fig. 2.5 were selected. Each ROI is of 50 pixels wide, giving 2500 different intensity signals coming from individual pixels. The first ROI is located in the quiet sun region eastwards from NOAA 11131 (heliographic coordinates: $\Theta = 29.23^{\circ}, \Phi = -17.46^{\circ}$). The second ROI is placed at the centre of the sunspot located in the NOAA 11131 active region (heliographic coordinates: $\Theta = 31.27^{\circ}, \Phi = -3.98^{\circ}$). This sunspot showed well pronounced 3-min oscillations, which were evidently detected with SDO/AIA in a number of previous studies [see e.g. Reznikova et al., 2012; Sych and Nakariakov, 2014; Yuan et al., 2014; Deres and Anfinogentov, 2015].

[1] http://jsoc.stanford.edu/

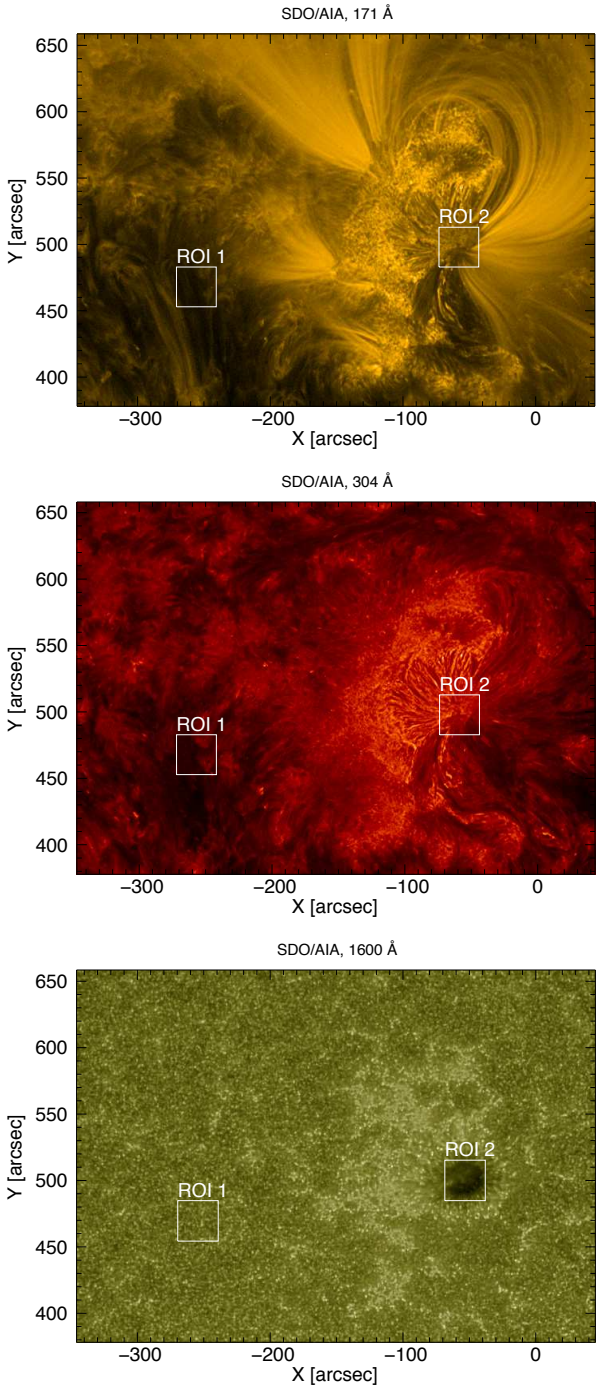

Figure 2.5: Active region NOAA 11131 observed with SDO/AIA at the 171 Å (top), 304 Å (middle), and 1600 Å (bottom) wavelengths. Images are taken at 00:00:00 UT, 8 December 2010. White squares show the regions of interest (ROI) for intensity variations considered in the analysis.

Following the method described above, it was empirically established that the intensity variations of the emission coming from each individual pixel of the quiet sun region, ROI 1, have coloured noise-like behaviour with the modal energy–period dependence in the form given by Eq. (2.15) (see Fig. 2.6). Therefore these intensity variation signals are considered as random processes with a power law spectral energy distribution. The specific value of the power law index α was empirically estimated for each wavelength in the same manner that had been used for synthetic noise (see Fig. 2.4), i.e. by the linear fitting of the average energies to dependence (2.15) in a logarithmic scale. The period ranges where the fittings were carried out, were chosen to correspond to the power-law-like parts of the spectra. The value of α was found to increase with height in ROI 1 from 0.86 ± 0.03 for the upper photosphere, the 1600 Å line, to 1.29 ± 0.02 for the chromosphere, 304 Å, and 1.32 ± 0.04 for the coronal 171 Å line, with corresponding 1-σ uncertainties. Such a behaviour of α indicates that higher-frequency oscillations are trapped deeper in the quiet sun atmosphere. In contrast, the intensity signals coming from the sunspot umbrae (ROI 2, see Fig. 2.7) in addition to a power-law-like spectral energy distribution, were found to contain several IMFs with periods of approximately 2–4 min and with energies significantly above the noise level. The latter groups of IMFs could be clearly associated with 3-min oscillations already found in this sunspot. The value of α estimated with the EMD-testing of the intensity signals coming from ROI 2 was found to decrease with height from 1.33 ± 0.04 for the upper photosphere (1600 Å), to 1.23 ± 0.1 for the chromosphere (304 Å), and 1.26 ± 0.13 for the corona (171 Å), with corresponding 1-σ uncertainties, i.e. lower-frequency processes dominate at lower levels of the sunspot atmosphere. Interestingly, the 171 Å and 304 Å intensity signals coming from ROIs 1 and 2 have nearly the same values of α, of about 1.2–1.3 corresponding to the pinkish noise behaviour. On the other hand, it changes dramatically for the 1600 Å line from about 0.86 in ROI 1 to 1.33 in ROI 2, indicating the change in the noise colour from pink (flicker) to reddish at lower altitudes of the solar atmosphere when transiting from quiet sun regions to sunspot umbrae. Figures 2.6 and 2.7 also show the Fourier spectra of the same observational data sets, allowing for comparison of the results obtained with these two essentially different spectral techniques. The Fourier spectra of separate signals from each individual pixel of ROIs 1 and 2 were averaged over each considered period. Similarly to the energy–period dependences of IMFs obtained with EMD, the mean Fourier spectra are also seen to have clear power-law-like regions at longer periods. The values of α detected with the mean Fourier spectra were found to be fully consistent with the corresponding values detected with the EMD-based testing.

More specifically, the top panels of Fig. 2.6 show the energy–period dependences of IMFs of the intensity variations from the quiet sun region (ROI 1), which look similar to each other at the 171 Å and 304 Å wavelengths. In the spirit of the examples of synthetic noises shown in Fig. 2.4, the dependences are shown by the dots clustered in groups corresponding to separate IMFs. The spectral energy distributions have non-trivial structures and can be described as a superposition of two random processes with different power law indices α for both 171 Å and 304 Å observational wavelengths. Indeed, at short periods (approximately shorter than 2 min) the process with $\alpha \approx 0$ (the white noise) dominates. The second component, with α being of about 1.32 and 1.29 for 171 Å and 304 Å, respectively (the pinkish noise), dominates at longer periods. These two noisy components could originate from different sources and hence belong to different physical processes of a natural or instrumental origin.

The confidence intervals of 99% and 1% significances (see Fig. 2.6) are calculated for both random components in the assumption of the chi-squared modal energy distribution given by Eq. (2.13). The maximum and minimum values of these intervals for each period give a general confidence interval for the superposition of both processes. The general confidence intervals are indicated by the green solid lines in Figs. 2.6 and 2.7. Energies of IMFs of 171 Å and 304 Å signals in the top plots of Fig. 2.6 are located mainly inside the confidence intervals. The only exception is the first (the shortest period) IMFs which have the energies above the upper confidence limit. Note, that the same feature of the first IMFs also appears in the energy–period distributions obtained for synthetic noises (see Fig. 2.4). Similar unusual behaviour of the first mode energy of the white noise samples was also reported in Wu and Huang [2004]. Hence, this effect is attributed to the intrinsic artefact of the EMD technique and is not discussed in the further analysis.

Another SDO/AIA data set taken from the lower level of ROI 1, namely the intensity signals at 1600 Å, shows similar spectral energy distribution well localised inside the general confidence interval with $\alpha \approx 0$ and $\alpha \approx 0.86$. The latter proves that the intensity variations observed in the quiet sun regions can be definitely considered as a random process with a power law spectral density distribution. However, the second group of 1600 Å IMFs with periods being between 3 and 4 min is located partly outside the interval and hence cannot be attributed to the noise. As the 1600 Å observational wavelength corresponds to the electromagnetic emission coming from the upper photosphere, these IMFs are likely to be associated with some specific periodic processes operating at lower levels of the solar atmosphere. For instance, the period corresponding to the acoustic cut-off frequency is known to

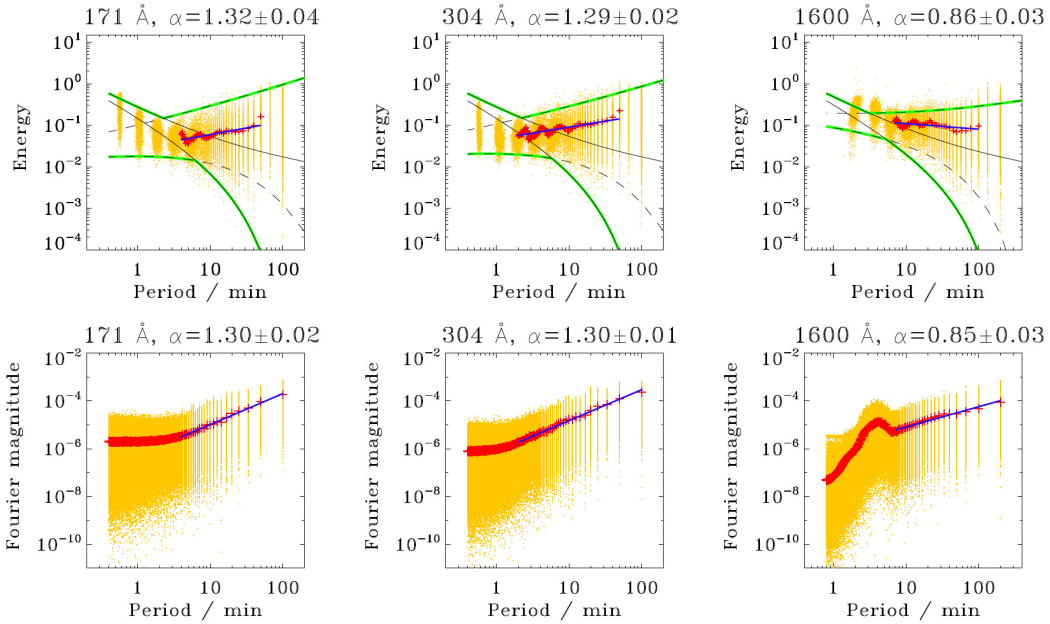

Figure 2.6: Top panels: energy–period dependences of IMFs obtained with EMD of SDO/AIA data taken from the NOAA 11131 active region, ROI 1 from 00:00 to 03:20 UT, 8 December 2010. The spectral power and periods of individual IMF are shown by yellow dots. Total number of considered observational samples is 2500, containing 500 data points each. The 99% and 1% confidence intervals are shown with the black solid (white noise) and dashed (coloured noises) lines. The energy averaged over each period is indicated by the red crosses. Blue lines represent the empirical dependence of the mean modal energy upon the period, obtained with the linear fitting. Green lines show the general confidence interval for the superposition of the white and coloured noises. Bottom panels: Fourier spectral power–period dependences of the same data sets as shown in the top panels. The spectral power and periods of individual Fourier harmonics are shown by yellow dots. The red crosses indicate the mean Fourier spectra. The blue lines are the best linear fit showing the power-law-like regions of the spectra. Values of the power law index α with corresponding 1-σ uncertainties are shown above each panel.

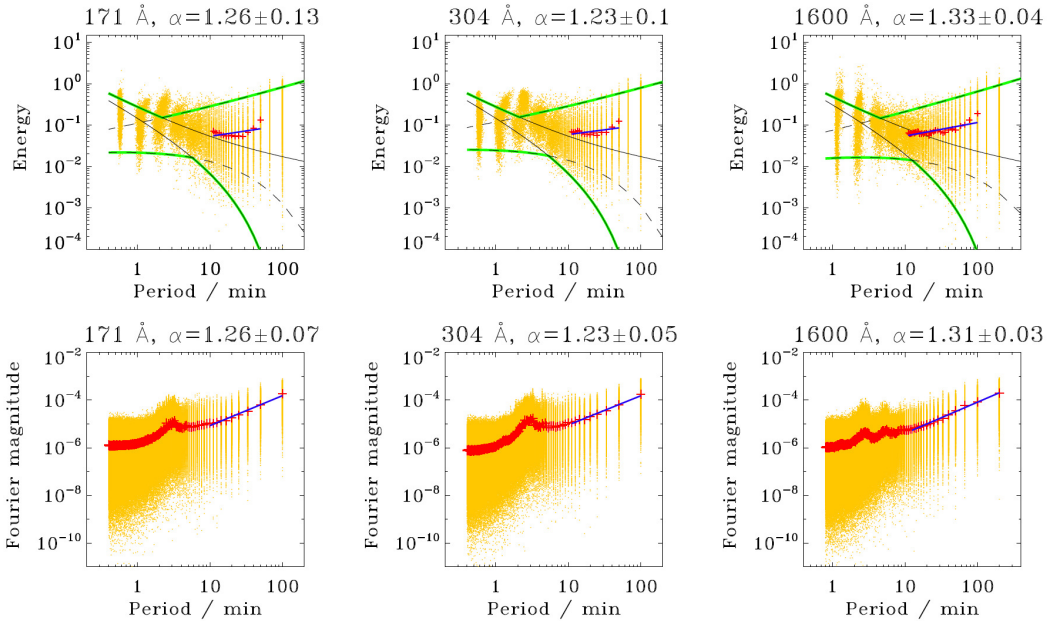

Figure 2.7: The same as shown in Fig. 2.6 for the SDO/AIA data sets taken from the NOAA 11131 active region, ROI 2.

be in the vicinity of 3–4 min.

Figure 2.7 shows the energy–period dependences of IMFs of 171 Å, 304 Å, and 1600 Å data sets taken from ROI 2. Similarly to the previous cases, the longer-period spectral components (with periods longer than 10 min approximately) can be described by a power law distribution with the index α being of about 1.26, 1.23, and 1.33, respectively. The spectral components with approximate periods shorter than 2 min are seen to be more related to the white noise distribution. As ROI 2 is located above the sunspot umbrae (see Fig. 2.5), EMD expansion of 171 Å and 304 Å data clearly gives a distinct group of IMFs with energies outside the general confidence interval. Their periods range approximately from 2 to 4 min, coinciding with typical periods of 3-min sunspot oscillations. Nearly the same periodicities can be also detected in the 1600 Å energy–period distribution. These results are in accordance with the behaviour of the mean Fourier spectra which are also shown in Fig. 2.7.

2.2.4 Discussion and conclusions

The study revealed empirical properties of synthetic coloured noises expanded via EMD, allowing for arbitrary values of the power law index α in the power spectral

density S as a function of the frequency f written in the form $S = 1/f^{\alpha}$. In analogy with Wu and Huang [2004] where the corresponding properties of the white noise ($\alpha = 0$) are given, new findings can be briefly itemised as follows:

- Based on the dyadic nature of EMD it was found that the energy density $E_{\rm m}$ of IMFs obtained from the coloured noise samples with EMD is connected with the mean modal period $P_{\rm m}$ through the relation $E_{\rm m}P_{\rm m}^{1-\alpha} = \text{const}$, derived in Eq. (2.15).

- Energies of IMFs of coloured noises were found to be chi-squared distributed, according to Eq. (2.13). The latter expression in turn reduces to the corresponding white noise distribution shown in Wu and Huang [2004], for the limiting case when $\alpha = 0$ and the IMF's numbers of DoF are proportional to the modal energies.

- Numerical experiments performed with the use of synthetic coloured noise samples showed that the chi-squared distribution for $E_{\rm m}$ is applicable to the noises with values of the power law index α being of up to 2 (see Fig. 2.4). While for higher values of α, for example for $\alpha = 2$ and $\alpha = 2.5$ shown in Fig. 2.4, the distribution of modal energies is seen to have a rather different form. The latter fact is related to the dyadic properties of EMD, indicating that they are mainly pronounced for coloured noises with approximate $\alpha < 2$, and are corrupted for noises with $\alpha \geq 2$ when correlation between data points is sufficiently strong in a signal.

Due to its adaptive nature and advantages in analysing non-stationary and nonlinear signals, EMD is an intensively used technique for the detection of quasi-periodicities in solar signals of various types (see Sec. 2.1 for details). Hence, the correct accounting for the background frequency-dependent random processes is certainly of a crucial importance when analysing oscillations in the solar atmosphere with EMD. In particular, the first signature which should be addressed when using EMD is the doubling of the modal periods (in EMD the periods of individual modes are not prescribed and are determined empirically). This dyadic behaviour is typical for EMD when it operates with noisy signals, and, hence, the IMFs with doubled periods should be rather referred to as some randomly distributed background process. There are a number of examples showing such a dyadic behaviour of IMF in solar signals. For example, similar behaviour can be recognised in Terradas et al. [2004] where a coronal loop oscillation was analysed with EMD. At least the three first modes of the EMD expansion shown there in Fig. 1 demonstrate the dyadic

behaviour with mean periods being of about 0.5, 1, and 2 min, respectively. Although only the first mode (with the shortest period) was treated by the authors as a noise, this dyadic property indicates that all these three modes together most likely should be referred to as some background noise-like process. Lee et al. [2015] recently reported the detection of periodic variations of the total solar irradiance during the last decade, found with the ensemble EMD technique. Analysed data sets were observed independently with SORCE/TIM, ACRIMSAT/ACRIM III, and SOHO/VIRGO instruments, and were found each to contain at least three IMFs with periods of about 16.7, 28.6, 58.8 d (TIM), 16.4, 32.5, 57.8 d (ACRIM III), and 16.1, 29.7, and 66 d (VIRGO), which may be also referred to as modes with dyadic properties. In all these examples for the exact determination of the power law index characterising the "colour" of the corresponding noisy components, further detailed analysis of the modal energies is required.

For illustration, the developed EMD-based method was applied for probing different layers of the solar atmosphere looking for the appearance of randomly distributed processes. The analysed intensity variation signals came from two regions of interest: one is located above a quiet sun area, and another is above a sunspot, both are related to the NOAA 11131 active region. In particular, the analysed sunspot was previously found to have clear 3-min oscillations with a non-regular deep-modulated wave-train profile shape [see e.g. Fig. 4 in Reznikova et al., 2012]. Due to its adaptive nature, EMD was chosen as the most suitable method for processing such sort of signals. It was found that the intensity variations of both quiet sun and sunspot regions at 171 Å (coronal level) and 304 Å (chromospheric level) indeed behave randomly and can be represented as a superposition of two noise-like processes with the corresponding power law index $\alpha \approx 0$ (the white noise component) at periods shorter than 2 min, and $\alpha \approx 1.2 - 1.3$ (the pinkish noise) at longer periods. These findings are consistent with, for example, the results obtained recently by Ireland et al. [2015] with the use of the mean Fourier spectra for the coronal emission at 171 Å and 193 Å wavelengths. There, the power law indices were found to range from 1.8 to 2.3 for both wavelengths, depending upon the analysed region. In addition to the coronal (171 Å) and chromospheric (304 Å) lines, in this study the emission intensity variations at 1600 Å corresponding to deeper layers of the solar atmosphere, were also analysed. Similarly to the upper levels, signals coming from the 1600 Å emission layer are also seen to be well represented by a combination of white and coloured noise. However, the corresponding coloured component experiences a dramatic change in the power law index from about 0.86 to 1.33 when transiting from the quiet sun to the sunspot atmosphere. The latter means the

domination of low-frequency processes deep inside the sunspot atmosphere, while characteristic frequencies for the quiet sun area decrease with height. In contrast to earlier works where the variations of slopes of the high-frequency spectral tails (at periods shorter than about 3 min) were considered (see e.g. Deubner and Fleck [1990], Fig. 5; Woods and Cram [1981], Fig. 1; Orrall [1966], Fig. 4; and Evans et al. [1963], Fig. 3), the present study considers the evolution of the spectral slopes from the photosphere to the corona in the extended range of periods up to 100 min. In addition to the randomly distributed background processes, groups of IMF with energies which are located significantly above the noise level, were also clearly detected by the method. In particular, their periods range from 2 to 4 min (for the sunspot regions) and may be clearly associated with 3-min sunspot oscillations. For the quiet sun region observed at 1600 Å, the energy distribution peaks at about 4 to 5 min, which can be considered as a manifestation of the p-modes or the oscillations with the acoustic cut-off frequency.

The mean Fourier spectra for the same data sets which were used in the EMD analysis, were also calculated. Results obtained with the Fourier technique are completely in accord with those obtained with EMD. In particular, the mean Fourier spectra were also found to contain the power-law-like regions at longer periods and tend to a flat shape at shorter periods, indicating that they also could be represented as a combination of the corresponding coloured and white noise-like components. By definition, the EMD and Fourier techniques are essentially different and independent spectral approaches based upon different principles and intrinsic properties. Hence, a full agreement between the results obtained separately with these two methods in the analysis evidently confirms the ability of EMD for the detection of random processes in solar signals, and justifies its applicability.

2.3 Long-period quasi-periodic oscillations of a small-scale magnetic structure on the Sun

2.3.1 Introduction

In contrast to oscillations in various large-scale structures of the solar atmosphere, for example such as coronal loops [e.g. De Moortel and Nakariakov, 2012], sunspots [e.g. Sych, 2016], and plages [e.g. Kobanov and Chelpanov, 2014], quasi-periodicities in smaller-scale solar magnetic structures with typical sizes of 4–10 arcsecs, such as faculae and pores, are less studied as their direct observations were unavailable due to the insufficient resolution of the previously used ground-based and spaceborne

observational instruments. However now, using the modern observational methods and newest satellite data with high spatial and temporal resolutions, researchers are able to investigate the oscillatory behaviour of such small-scale structures in different layers of the solar atmosphere. For example, recently Chelpanov et al. [2015] revealed quasi-periodic oscillations in the facular magnetic knots with periods of about 3 min. Additionally, the authors identified the longer-period oscillations (with periods of about 5–11 min) above the facula periphery regions in the 304 Å spectral line. The detected spatial and temporal distributions of the oscillations were proposed by the authors to be prescribed by the magnetic field lines topology in facular regions. Similar periodicities and the corresponding dependence of the oscillation period upon the magnetic properties of a facular region were found in Kobanov et al. [2015]. Freij et al. [2016] detected oscillations with periods from 3 to 20 min in the intensity of two isolated magnetic pores and interpreted them in terms of a slow magnetoacoustic sausage wave. Similarly, the facular brightness was found to be dependent on the convective and wave motions in a facular region by Kostik and Khomenko [2016]. Periodicities in the 5-min range were detected. In addition to the solar atmosphere, Sun-like stars are also observed to exhibit quasi-periodic intensity fluctuations on various time scales, which can be attributed to the evolution of small-scale structures on their surfaces [see e.g. Karoff et al., 2013].

So far the longest detected periodicities in small-scale structures on the Sun have been limited by a few tens of minutes and, in general, did not exceed a half an hour. This section demonstrates the presence of a long-period oscillation with a period ranging from about 80 to 230 min in a long-living small-scale photospheric structure related to a facula formation visible in the chromosphere, and is based on the work by Kolotkov et al. [2017]. It analyses the time-series of the average line-of-sight component of the magnetic field, obtained with SDO/HMI with the duration of 13 hours, using the HHT technique introduced in Sec. 2.1. Testing the significance of the identified empirical modes with the approach developed in Sec. 2.2, the white and pink noisy components superimposed on the original signal and a single significant oscillatory mode were distinguished.

2.3.2 Observations

The analysis is based on the line-of-sight magnetograms of the examined small-scale structure, observed by the Solar Dynamics Observatory Helioseismic and Magnetic Imager instrument (SDO/HMI) [Schou and Larson, 2011; Scherrer et al., 2012; Couvidat et al., 2016]. The spatial resolution of HMI (1 arcsec) allows one to successfully resolve the target structure of about 4–10 arcsecs in size.

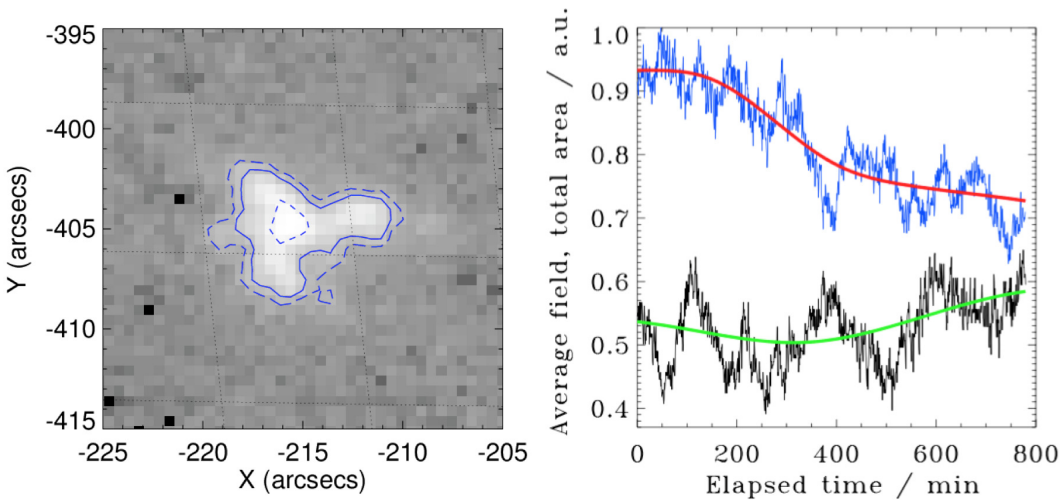

Figure 2.8: Left: SDO/HMI line-of-sight magnetogram of the analysed magnetic structure, measured at 23:00:45 UT on 6 July 2013. Blue contours show the magnetic field intensity levels of 70 G (dash), 100 G (solid), and 600 G (dash). Right: temporal variations of the average line-of-sight component of the magnetic field (blue) in the structure, integrated over the whole 100 G contour. The red solid line shows the long-term trend of the blue signal, determined as the last empirical mode with EMD (see Sec. 2.3.3). Variations of the total area inside the 100 G contour are shown by the black solid line, with the long-term trend (green line) determined also with EMD. Both original time-series were normalised to their maximum values (shown in arbitrary units), and the total area signal was slightly shifted downwards for a better visualisation. The elapsed time starts at 23:00:45 UT on 6 July 2013 and spans 13 hours of observations with a cadence of 45 s.

A snapshot of the analysed structure with the helioprojective Cartesian coordinates of its geometrical centre, X and Y being of about $[-216, -405]$ is shown in Fig. 2.8, left-hand panel at 23:00:45 UT. It is a positive polarity magnetic field structure, with initial linear sizes of about 7×5 arcsecs, estimated at the 100 G level of intensity. During the observational interval, the position of the structure's geometrical centre experienced stochastic (quasi-periodic) motions with amplitudes being up to a typical size of inter-granular lanes in the region of interest. In turn, the total area of the structure, estimated in the 100 G intensity contour, varied quasi-periodically in time with a gradually increasing long-term trend (see the right-hand panel in Fig. 2.8). The contour of 100 G was chosen as the most suitable for the analysis of the oscillations of the target structure as a whole. Indeed, it matches well the whole interior of the structure. On the other hand, its level is four times higher than that of the quiet sun in the magnetogram, which is about 20–25 G. Hence, the possible oscillations of the analysed structure should not be affected by the background processes operating in the neighbouring quiet sun atmosphere. The right-hand panel of Fig. 2.8 also shows the temporal variations of the average magnetic field strength, obtained by the integration over the whole 100 G contour, for each separate magnetogram during the whole observational interval of 13 hours. This time-series demonstrates a clear quasi-periodic behaviour of the average magnetic field in the structure and is a subject to a further spectral analysis.

2.3.3 HHT spectral analysis and significance test

Application of the EMD technique to the average magnetic field time-series shown in the right-hand panel of Fig. 2.8 gives 11 intrinsic empirical modes, with the longest-period 11th mode being a long-term trend shown in Fig. 2.8. The detected modes 1–7 and 9–10 have nearly stable periods, while the apparent non-stationarity of the original signal is mainly attributed to mode 8. Mean periods of the detected modes are estimated as $P = 2N/n$ where N is the total length of the analysed signal and n is the number of extrema in a mode, and are shown in Table 2.1. Except the highest amplitude mode 8 (see the ratio of the modal standard deviation, $\sigma_{\rm m}$ to the original signal standard deviation, σ_0 in Table 2.1), it shows the approximate dyadic behaviour of intrinsic modes 1–7 and 9–10, i.e. their mean periods constitute a nearly doubling sequence, with each next period to be about two times longer than the previous. According to Sec. 2.2 and Flandrin et al. [2004], the latter fact is typical for EMD when it operates with the signals containing white and coloured noisy components with a power law in their spectral energy distributions, and may indicate a random nature of these empirical modes. Similarly, the instant

Table 2.1: Mean periods and ratios of the modal standard deviation, $\sigma_{\rm m}$ to the original signal standard deviation, σ_0 of the empirical modes detected with EMD in the average magnetic field signal shown in Fig. 2.8, right-hand panel.

	Period (min)	$\sigma_{\rm m}/\sigma_0$		Period (min)	$\sigma_{\rm m}/\sigma_0$
M1	2.3	0.13	M6	36.3	0.14
M2	4.0	0.09	M7	74.3	0.14
M3	6.4	0.07	M8	120.0	0.31
M4	10.6	0.07	M9	156.0	0.08
M5	17.9	0.07	M10	312.0	0.10

amplitudes of modes 1–7 and 9–10 were found to be normally distributed, which is also consistent with their random origin [Wu and Huang, 2004], in contrast to the oscillation revealed by mode 8.

Writing the power spectral density S as a function of the frequency f as $S = 1/f^{\alpha}$, and following the recipe designed in Sec. 2.2, one can check the significance of the intrinsic modes, comparing them with the white and coloured noises, and empirically estimate the corresponding values of the power law index α. Introducing the energy E of an intrinsic mode as a sum of squares of its instant amplitudes in the time-series, Sec. 2.2 showed that, for the intrinsic modes obtained from synthetic coloured noise samples, it is connected with the mean modal period P as $EP^{1-\alpha} = \text{const}$ (see Eq. (2.15)). Figure 2.9, the left-hand panel shows the corresponding mean modal energy–period dependence plotted in a logarithmic scale for all intrinsic modes detected in the current analysis. Modal energies are shown with the corresponding uncertainties, allowing the instant energies of each mode to vary within 2σ, where σ is the half-level width of the instant energy distribution of each mode. Modes 1–3 (black circles) and modes 4–7 and 9–10 (green circles) are seen to lie around straight lines with the spectral slopes α of about 0 and 1, respectively. Here, these values of α are taken as illustrative examples only.

Figure 2.9 also illustrates the upper (99%) and lower (1%) confidence intervals of the white ($\alpha \approx 0$) and pink ($\alpha \approx 1$) noises, calculated in the assumption of a chi-squared modal energy distribution given by Eq. (2.13). The performed test shows that the detected shorter-period modes (1–3) have the energies lying strictly within the white noise confidence interval, that most likely indicates their white noise-like nature. In turn, the longer-period modes (4–7 and 9–10) have energies lying within the pink noise confidence interval, and, hence, should be attributed to flickering random processes in the solar atmosphere. In contrast, energy of mode 8 is well above the corresponding confidence intervals of both white and pink noises,

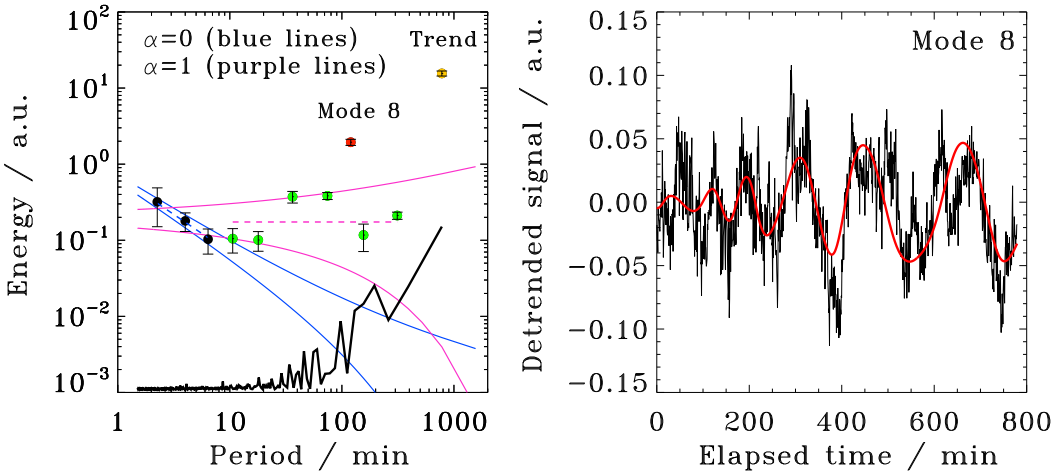

Figure 2.9: Left: mean modal energy–period dependence plotted in a logarithmic scale, for all intrinsic modes detected with EMD in the signal of interest shown in the right-hand panel of Fig. 2.8 in blue. Values of the mean energies and periods of modes 1–3 are shown by black circles, modes 4–7 and 9–10 are shown in green. The red circle indicates the mean energy and period of mode 8 shown in the right-hand panel. The yellow circle corresponds to the long-term trend of the signal, shown in the right-hand panel of Fig. 2.8 in red. Dashed blue and purple lines show the power law dependences $EP^{1-\alpha} = \text{const}$, with the spectral slopes $\alpha = 0$ and $\alpha = 1$, respectively. Blue solid lines show the 99% and 1% confidence intervals of the white noise ($\alpha \approx 0$), and the corresponding pink noise ($\alpha \approx 1$) confidence intervals are shown by the purple solid lines. The black solid line shows the Fourier energy spectrum of the original signal shown in the right-hand panel of Fig. 2.8 in blue, shifted downwards by an appropriate normalisation for a better visualisation. Right: the detrended average magnetic field strength (black solid line) shown in the right-hand panel of Fig. 2.8 in blue, and its intrinsic mode 8 (red solid line) detected with EMD.

indicating the statistical significance of only that mode as a true oscillatory signal among the whole set of the intrinsic modes detected in the average magnetic field time-series (Fig. 2.8). The Fourier spectrum shown in Fig. 2.9 also demonstrates the change in the spectrum slope gradient, i.e. in the noise colour, with a breaking point near a 20-min period, consistent with the results obtained with EMD. On the other hand, it does not show a pronounced periodic component. This discrepancy illustrates the advantage of EMD in the processing of non-stationary signals.

The right-hand panel of Fig. 2.9 demonstrates the normalised original signal with the long-term trend subtracted, and mode 8. The mode has a clear quasi-periodic behaviour with a growing period, accompanied by a simultaneous increase in the amplitude. The empirical dependence of the instantaneous oscillation pe-

riod upon the instantaneous oscillation amplitude of mode 8 is calculated with the use of the Hilbert transform, and is shown in Fig. 2.10, top left panel. It is a growing dependence that can be fitted by a power law of the form $Period\,[\mathrm{min}] = a \times [Amplitude/\max(Amplitude)]^b + c$, with $a \approx (141.56 \pm 56.91) \times 10^3$ min, $b \approx 2.31 \pm 0.14$, and $c \approx 78.36 \pm 2.45$ min. According to this fit, the period of mode 8 increases from about 80 min (for the lowest amplitude) up to about 230 min (for the highest amplitude). The dependence of the instantaneous period of mode 8 upon the variation of the instant average magnetic field (the red curve in Fig. 2.8), shown in the top right panel of Fig. 2.10, can be approximated by a power-law with an index of $-3/2$ (taken here as an illustrative example). Figure 2.10 also shows the dependences between the instantaneous period of mode 8 and the total area of the magnetic structure (bottom right panel) and its magnetic flux (bottom left panel), projected onto the plane of sky and determined as the product of the average magnetic field strength and the total area of the structure. No obvious correlation between the modal period and these two parameters was detected.

2.3.4 Discussion and conclusions

The quasi-periodic behaviour of the average magnetic field strength (shown in Fig. 2.8) measured with SDO/HMI in a photospheric small-scale magnetic element forming a facula at higher levels of the solar atmosphere, was analysed. The spectral analysis performed with the HHT technique decomposed the signal in 11 intrinsic empirical modes, with the last (11th) mode being a long-term aperiodic trend of the signal. The significance test showed that other nine empirical modes exhibit a nearly dyadic behaviour and are most likely related to the noisy components present in the original signal. They can be characterised by a power law index being of about 0 (thus representing the white noise component dominating in the short-period, 2–6 min, part of the spectrum) and of about 1 (i.e. the pink or the so-called "flicker" noise dominating at longer periods of 10–310 min). Only a single mode was found to have statistically significant oscillatory properties. It has a gradually increasing oscillation amplitude, and its oscillation period grows with the amplitude from about 80 to 230 min.

The detected white and coloured noises could manifest different physical processes of a natural or instrumental origin. The presence of the power-law-like regions in power spectra of the signals detected at various heights of the solar atmosphere seems to be a common feature. For example, similar values of the power law index (about 0.9–1.3) were found in Sec. 2.2, Figs. 2.6 and 2.7 in the EUV emission intensity variations observed with SDO/AIA in the upper photospheric (1600 Å)

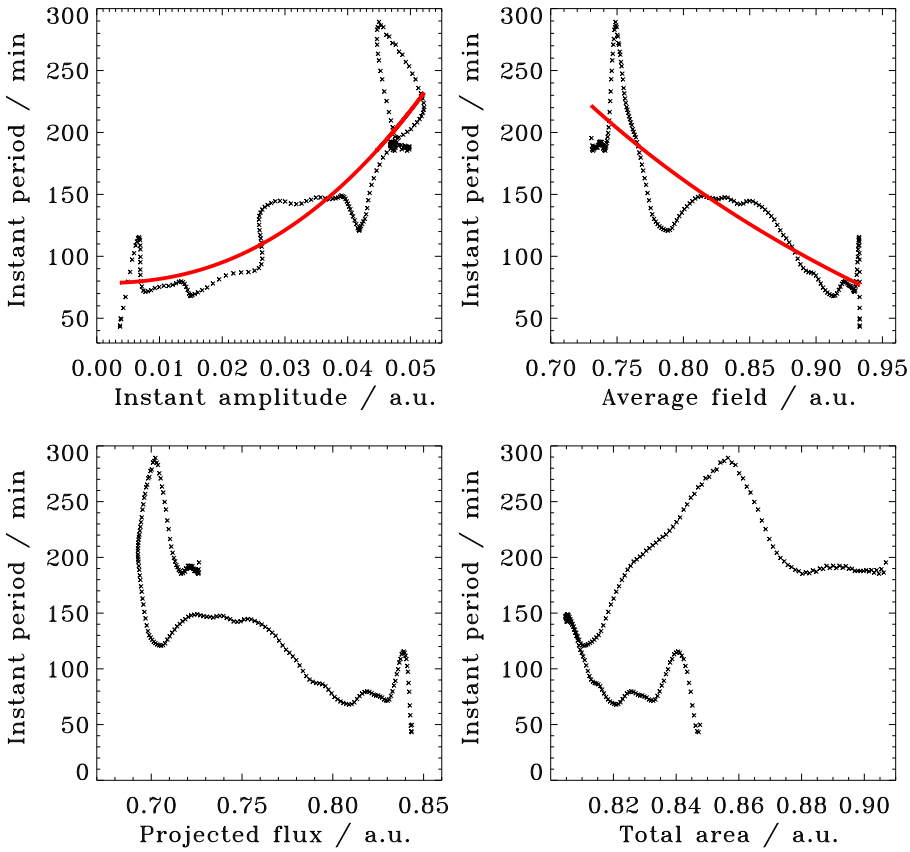

Figure 2.10: Top left: dependence of the instantaneous oscillation period upon the instantaneous oscillation amplitude in mode 8 shown in the right-hand panel of Fig. 2.9. The red solid line indicates the best fit of the empirical period–amplitude dependence by a power-law function (see Sec. 2.3.3 for the fitting details). Top right: dependence of the instantaneous period of mode 8 upon the long-term trend of the average magnetic field signal, shown in the right-hand panel of Fig. 2.8. The red curve shows the best fit of the empirical dependence by the power law function with the index of $-3/2$. Bottom left: dependence of the instantaneous period of mode 8 upon the long-term variation of the normalised line-of-sight magnetic flux of the structure, projected onto the plane of sky. Bottom right: dependence of the instantaneous period of mode 8 upon the long-term trend of the total area signal, shown in the right-hand panel of Fig. 2.8.

layer of the non-flaring solar atmosphere. The higher, chromospheric and coronal layers of the non-flaring solar atmosphere also often show the presence of randomly distributed processes characterised by the power law indices ranging from 1.2 to 2.3 depending upon the magnetic properties of the analysed region [see e.g. Sec. 2.2 and Ireland et al., 2015].

The period of the statistically significant oscillation revealed by mode 8, which is in the range from 80 to 230 min, is far too long to be linked with an MHD oscillation of the observed chromospheric or photospheric structure. Indeed, taking the Alfvén speed equal to the photospheric sound speed, 10 $\mathrm{km\,s^{-1}}$, a natural MHD oscillation with a 180-min ($\approx 10,000$ s) period should have a wavelength of about 100 Mm. On the other hand, similar periodicities could be induced by the dynamical interaction of photospheric magnetic structures with the boundaries of supergranula cells [Strekalova et al., 2016], while this mechanism requires further investigation. In particular, it is not clear whether the detected variation of the oscillation period with the amplitude and the mean magnetic field could be consistent with the driven motions caused by the supergranulation flows.

Another possibility is connected with the periodic motions appearing during the magnetic flux emergence [see e.g. Emonet et al., 2001; Cheung et al., 2006]. In this effect, the period P is prescribed by the vortex shedding, $P \propto d/V$, where d is the emerging magnetic flux tube diameter and V is the emergence speed [see e.g. Nakariakov et al., 2009]. Taking that the flux tube diameter depends on the magnetic field strength as $B^{-1/2}$ (the magnetic flux conservation) and the emergence speed is proportional to the magnetic field, one can obtain that the oscillation period scales with the magnetic field as $P \propto B^{-3/2}$. This behaviour is consistent with the scaling seen in Fig. 2.10. However, more detailed modelling of this phenomenon is required. The scaling of the instant oscillation period with the projected magnetic flux and the total photospheric area of the magnetic structure did not give conclusive results.

2.4 HHT analysis of periodicities in the solar activity cycles 22, 23, and 24

2.4.1 Introduction

The Sun's magnetic activity varies primarily on a time scale of 11 yr. However, both longer- and shorter-term periodicities are also frequently associated with solar-magnetic activity [see Usoskin, 2013; Bazilevskaya et al., 2014, for recent reviews].

This section investigates activity-related periodicities that can be extracted from data recorded over the last two-and-a-half solar cycles (from 1985 to 2014), concentrating on periodicities less than (but including) 11 yr. Periodicities in the range of 1–4 yr are often referred to as quasi-biennial oscillations [QBO, Bazilevskaya et al., 2014], while periodicities shorter than 1 yr, are often referred to as Reiger-type periodicities [e.g. Chowdhury and Ray, 2006; Ballester et al., 2004; Krivova and Solanki, 2002; Boberg et al., 2002]. The periodicities appear to be ubiquitous, being detected in activity proxies that are sensitive to the solar interior, and extending right out to the interplanetary medium [see e.g. Bazilevskaya et al., 2014].

Solar activity periodicities are hard to characterise: even the 11 yr cycle is known to vary in both the amplitude and length [e.g. Hathaway, 2010]. Usually, for the spectral analysis of long-term solar activity, Fourier transforms and other Fourier-based techniques are used. However, all of them have disadvantages associated with the *a priori* prescription of the basis function and summarised in Sec. 2.1. As an alternative, the Krylov–Bogolyubov "averaging" method was successfully applied to the analysis of weakly nonlinear non-stationary Wolf number data by Nagovitsyn [1997]. It is based on the expansion of the original signal into a set of harmonic functions with time-dependent amplitudes, frequencies and phases. Determination of these functions, consequently, allows one to construct an amplitude–frequency diagram, which is a nonlinear analog of the power spectrum of a linear process. Another method suitable for nonlinear and non-stationary data processing is the proper orthogonal decomposition (POD). This tool, combined with the wavelet analysis, was used to investigate the spatial-temporal behaviour of the large time scale green coronal emission line at 530.3 nm [Vecchio and Carbone, 2008, 2009]. However, they were unable to adequately describe the 11 yr solar cycle using POD modes.

In this study five measures of the solar activity are considered, which are sensitive to different regions of the solar atmosphere: 10.7 cm radio flux[2], helioseismic frequency shift, and the sunspot area[3] signals recorded from the whole Sun disk and from the Northern and Southern hemispheres separately. The 10.7 cm radio flux is a proxy for solar activity in the upper chromosphere and lower corona, and is sensitive to both strong and weak magnetic field regions [Tapping, 1987]. Helioseismology uses the Sun's natural oscillations to characterise conditions beneath the surface of the Sun. It is well know that the frequencies of the helioseismic acoustic oscillations (known as p-modes) vary throughout the 11 yr solar cycle and, there-

[2]http://www.ngdc.noaa.gov/stp/space-weather/solar-data/solar-features/solar-radio/noontime-flux/penticton/

[3]http://solarscience.msfc.nasa.gov/greenwch.shtml

fore, can be considered as proxies of solar activity [e.g. Woodard and Noyes, 1985; Elsworth et al., 1990; Pallé et al., 1990]. One of the most obvious manifestations of solar activity on the solar surface is sunspots. Sunspot area provides a measure of the photospheric magnetic flux [Hathaway, 2010]. Sunspot area has the advantage that one can consider the total sunspot area or one can consider the Northern and Southern hemispheres independently, gaining insights into the well known North–South asymmetry [Norton et al., 2014]. In other words, in contrast with the other proxies considered here, sunspot area signal contains information about the spatial structure of the Sun's activity.

While numerous studies have looked at variations on time scales shorter than 11 yr that are present in the 10.7 cm flux and sunspot area, characterisations of the shorter-term signals in helioseismic data are less abundant. For example, Simoniello et al. [2013] used a wavelet analysis to study variations in helioseismic p-mode frequencies and found a broad peak in the global wavelet spectrum that extended between the periods of approximately one and four years. This broad peak covers numerous individual periodicities identified in other activity proxies. However, such a broad spectrum could also be an indication of temporal instability in the periodicity. Howe et al. [2000] used helioseismic p-modes to identify a 1.3-yr signal in variations in the solar rotation profile at a radius of $0.72R_{\odot}$. However, other authors were not able to verify the results [e.g. Antia and Basu, 2000], and the follow-up study demonstrated that the signal appeared to disappear around year 2000 [Howe et al., 2011]. Inherent in the problem are necessary limitations on the temporal resolution with which changes in helioseismic parameters can be determined: it is necessary to consider time-series accumulated over of the order of months to allow the frequencies of the individual modes to be determined accurately and precisely.

Characterisation of the helioseismic signal could help to discriminate between the different models proposed to explain the QBO-like variations. Different helioseismic p-modes are sensitive to different but overlapping regions of the solar interior, and so determining how solar cycle variations differ from mode to mode can help characterise the magnetic field in the solar interior. Such characterisation has frequently been performed for the 11 yr solar cycle. For example, the observed frequency dependence in the amplitude of the solar cycle variations implies that the dominant perturbation is confined to near-surface regions [e.g. Libbrecht and Woodard, 1990]. Basu et al. [2012] demonstrated that the region responsible for the 11 yr perturbation may be thinner in cycle 23 than in cycle 22. Its smaller amplitude and shorter time scale makes characterisation of the QBO more difficult.

In this section the application of the HHT technique improved by the noise-assisted ensemble EMD (EEMD, see Sec. 2.1) for analysing periodicities observed in the solar activity cycles 22, 23, and 24 is described, that could allow for better characterisation of the helioseismic signal. It is demonstrated to be able to not only successfully reproduce known results for the 10.7 cm flux and sunspot area signals, but also to reveal periodicities and characteristics in the helioseismic data that are consistent with the other activity proxies. This is important as to resolve QBO variations, helioseismic data are often determined from overlapping time-series and so data points are correlated, which has consequences for the significance of any determined signals.

The primary EMD expansion of the original signal has already been used in a long-term solar activity data analysis. More specifically, it was employed for studying the time evolution of the radial, meridional and east–west components of the global solar magnetic field in Vecchio et al. [2012a] by using magnetic synoptic maps covering the time interval from 1976 to 2003. Fundamental timescales of the solar magnetic field variability, such as the 22 yr cycle and quasi-biennial oscillations, were identified. The time modulations both of the interplanetary cosmic rays and of the solar neutrino flux were analysed with EMD in Vecchio et al. [2010]. All analysed signals span the time interval from 1974 to 2001. In Vecchio et al. [2012b] a more detailed joint EMD and wavelet transform analysis of the longer cosmic ray intensity records (from 1953 to 2004) was performed. Comparison of the periodicities obtained from the above mentioned data sets with the modes derived from the sunspot area and the coronal green line signals allowed the authors to establish a direct connection between solar neutrinos and cosmic rays with the evolution of the solar magnetic field. Also, the Gnevyshev gap phenomenon was explained as the superposition of QBO with the 11 yr cycle. Intrinsic modes of the monthly averaged North–South sunspot area records for the time interval of 129 yr, from 1874 to 2003 were identified with EMD in Zolotova and Ponyavin [2007]. Application of EMD allowed for the separation of the North–South sunspot activity into high- and low-frequency parts. This in turn led to the establishment of the amplitude and phase synchronisations of the detected high- and low-frequency components.

In this section based on the work by Kolotkov et al. [2015a], the HHT and EEMD techniques are applied to the solar cycle proxies measured more recently, in 1985–2014. This study can be considered as a development of the works by Zolotova and Ponyavin [2007] and Vecchio et al. [2010, 2012a,b], by applying the more statistically robust EEMD technique instead of EMD, and using the helioseismic data sets which have been analysed neither with EEMD nor with EMD before. In

addition, the Hilbert transformation allows one to reveal the temporal variability of instantaneous periods, naturally appearing in the detected empirical modes.

2.4.2 Data

The Birmingham Solar Oscillations Network [BiSON, Davies et al., 2014] is a ground-based network of six stations that make helioseismic Doppler velocity observations of the Sun. BiSON has now been accumulating observations for over 30 yr making it the longest running helioseismic observatory, and ideal for studies of the solar cycle. Here data obtained between 1 January 1985 and 11 April 2014 is considered, covering two-and-a-half solar cycles, including the recent extended minimum. The BiSON data used here benefit from improved calibration procedures, which produce higher signal-to-noise ratios [Davies et al., 2014]. BiSON makes unresolved (*Sun-as-a-star*) observations of the Sun, meaning that only those modes with the largest horizontal spatial scales (low-degree) have detectible amplitudes in frequency spectra. However, these are the truly global modes of the Sun and so their parameters (such as frequency), which are sensitive to the magnetic field in the solar interior, can be considered as global proxies of solar activity.

In order to determine how the mode frequencies vary with time it is necessary to divide the long time-series into shorter subsets. The time subsets are then converted to Fourier power spectra in which the oscillations appear as distinct peaks. These subsets must be short enough to resolve the time variations (such as the 11 yr solar cycle) but long enough that when converted to power spectra there is sufficient resolution to accurately and precisely determine the mode frequencies. Here, the subsets of length 108 days (d) with start times that are separated by 36 d are chosen for the analysis. Only modes with degrees $0 \leq l \leq 2$ in the frequency range $2400 \leq \nu \leq 3500$ μHz are considered, as these modes have the highest amplitudes in *Sun-as-a-star* data and their frequencies can be obtained most accurately. The frequencies were obtained by fitting the asymmetric profile of Nigam and Kosovichev [1998], using the Maximum Likelihood Estimation technique [Fletcher et al., 2009]. The frequency shifts were determined in the manner described by Broomhall et al. [2009]. Namely, a "reference" set of frequencies was obtained by determining the average frequency of each individual mode across all subsets. For each individual subset and mode the change in frequency compared to this reference set was determined. Finally the average across all modes was determined for each subset. The uncertainties on the average frequencies were based on the uncertainties associated with the original fitted frequencies. The result is a time-series of average frequency shifts (with data points separated by 36 d) that covers approximately 29 yr and is

ideal for studying solar cycle associated variations (see Fig. 2.11).

In addition to the helioseismic data, which can be considered as a proxy of the Sun's magnetic field in the solar interior, the sunspot area observed by the Royal Greenwich Observatory [Hathaway, 2010], and the 10.7 cm solar radio flux [F10.7, Tapping, 1987] are also considered (see Fig. 2.11). The sunspot area is a measure of the photospheric magnetic flux. Both the total sunspot area and separately the sunspot area in the Northern and Southern hemispheres are analysed. F10.7 is a proxy of the magnetic field in the upper chromosphere/lower corona.

Although daily values of the activity proxies were initially obtained, F10.7 and sunspot area signals were averaged over each 10 d, that sufficiently reduces the computational time used by EEMD. The 10 d smoothed values were independent, i.e. each data point in the smoothed time-series is separated by 10 d. In addition, to ensure compatibility with the helioseismic results, the F10.7 signal was also smoothed over the same 108 d subsets from which the helioseismic frequency shifts were obtained. This smoothing was performed with some overlap: each 108 d smoothed value was separated from its predecessor by 36 d. This test, therefore, ensures compatibility with the helioseismic results both in terms of the different smoothing time scales, but also allows for an assessment of the impact on the results of using overlapping, and therefore correlated data.

2.4.3 Analysis

The signals of five observational proxies, shown in Fig. 2.11, were analysed with the HHT method, starting with the noise-assisted EEMD expansion. The value of the white noise amplitude [0.2 of the standard deviation of the original signal, according to Wu and Huang, 2009] used in the EEMD, was chosen to be comparable with the values of the helioseismic data uncertainties. The Hilbert transform was applied separately to each of the found empirical modes to reveal the instant period–time variations, designated as the Hilbert spectrum. The instantaneous period regularly varies around some average value (see Fig. 2.12), which is referred to as the most probable mean period of each mode.

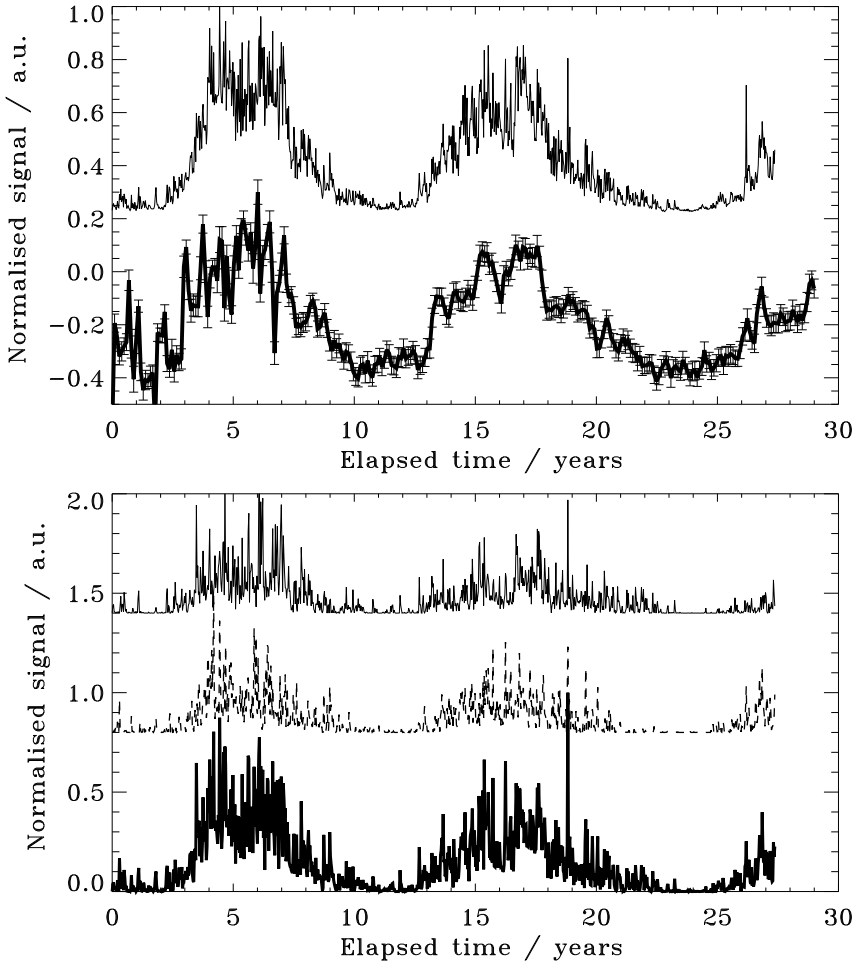

Figure 2.11: Upper panel: raw data signal of the 10.7 cm radio flux intensity (upper thin solid line), provided by the National Geophysical Data Center (NGDC), and the raw data of the helioseismic frequency shift with uncertainties (bottom thick solid line), detected with the Birmingham Solar Oscillations Network (BiSON). The signals are normalised to their maximum values, and the frequency shift signal is slightly shifted downwards for better visualisation. Bottom panel: Sunspot area signals, recorded from the whole Sun disk (bottom thick solid line), from the Northern solar hemisphere (middle dashed line), and from the Southern hemisphere (upper thin solid line), by the Royal Observatory, Greenwich. The signals are normalised to the maximum value of the bottom signal, and signals from separate hemispheres are shifted upwards for better visualisation. The elapsed time is measured from 1 January 1985.

Table 2.2: Average intrinsic periodicities of the signals of five solar cycle proxies, estimated with the HHT technique. The periods are measured in days, and their significances σ_{peak} are estimated in the units of the standard deviations, calculated separately for each probability histogram of each Hilbert spectrum.

10.7 cm radio flux		Frequency	Sunspot area recorded from			Mean
108 d smooth	10 d smooth	shift	whole Sun	Northern hemisphere	Southern hemisphere	period
Period (days)/ σ_{peak}	Period (days)/ σ_{peak}	Period (days)/ σ_{peak}	Period (days)/ σ_{peak}	Period (days)/ σ_{peak}	Period (days)/ σ_{peak}	Period (days)
	22^{+21}_{-2}/ 5.5		23^{+11}_{-2}/ 5.9	25^{+15}_{-5}/ 4.8	28^{+6}_{-7}/ 6.6	25^{+7}_{-2}
	46^{+22}_{-8}/ 6		43^{+24}_{-10}/ 5.6	40^{+19}_{-7}/ 6.1	48^{+9}_{-13}/ 6.6	44^{+10}_{-5}
			80^{+52}_{-24}/ 6.5	75^{+48}_{-24}/ 5.1	71^{+45}_{-16}/ 5.4	75^{+28}_{-13}
	96^{+18}_{-29}/ 5.8	101^{+36}_{-11}/ 5.5		98^{+106}_{-28}/ 5.6		98^{+38}_{-14}
			128^{+70}_{-28}/ 5.2		125^{+32}_{-41}/ 5.5	127^{+38}_{-25}
	140^{+120}_{-40}/ 5.6				160^{+30}_{-25}/ 6.9	150^{+62}_{-24}
		216^{+162}_{-50}/ 4.4	198^{+105}_{-31}/ 6.4	214^{+39}_{-70}/ 7	222^{+72}_{-24}/ 8.3	213^{+52}_{-24}
256^{+6}_{-37}/ 6.4	290^{+81}_{-95}/ 7.4			294^{+141}_{-47}/ 8.7		292^{+81}_{-53}
360^{+122}_{-77}/ 5.4	328^{+149}_{-15}/ 10	378^{+74}_{-35}/6	408^{+47}_{-148}/ 8.3	435^{+154}_{-145}/ 8.8	426^{+9}_{-98}/ 10.5	395^{+46}_{-46}
708^{+215}_{-163}/ 4.4	690^{+80}_{-200}/ 13		625^{+65}_{-240}/ 9.5	563^{+178}_{-128}/ 10.6		626^{+69}_{-113}
885^{+177}_{-200}/ 7.6	833^{+417}_{-63}/ 14	965^{+46}_{-233}/ 7.4	930^{+180}_{-190}/ 11.1	952^{+477}_{-82}/ 14.5	833^{+76}_{-33}/ 17.7	903^{+133}_{-64}
1180^{+337}_{-214}/ 7.1	1110^{+710}_{-340}/ 11.3	1250^{+520}_{-239}/ 6.8	1538^{+280}_{-538}/ 12.9	1818^{+182}_{-151}/ 18.4	1400^{+268}_{-223}/ 15.8	1423^{+196}_{-146}
4248^{+2832}_{-1213}/ 7	4000^{+2670}_{-665}/ 23.2	4250^{+2830}_{-710}/ 12.2	4500^{+2170}_{-1160}/ 17.3	4000^{+1000}_{-667}/ 23.9	4000^{+2667}_{-667}/ 19.1	4150^{+1058}_{-357}

Average periodicities

The results, obtained with the HHT analysis of the raw data signals, are summarised in Table 2.2. Intrinsic periodicities were found simultaneously in different proxies and were separated into three distinct groups: short-term variations (with periods shorter than 0.5 yr), quasi-biennial oscillations (with typical periods from 0.5 yr up to 3.9 yr), and longer periodicities, e.g. such as the 11 yr cycle. These mean periods were estimated from the probability histograms of the corresponding Hilbert spectra. A particular example of this technique is shown in the right-hand panel of Fig. 2.12. Such a histogram is calculated as the number of times each period appears in the Hilbert spectrum. Assuming that the periodicity is stationary, for each empirical mode this distribution has a Gaussian-like shape with a distinct peak, designated as the most probable period of the mode. The significances, σ_{peak}, of these peaks were estimated by comparing the peak height (which is unity after normalisation to its maximum) with the value of the standard deviation of the whole probability histogram (see the right panel of Fig. 2.12). All significances were found to be greater than or equal to 4.4 standard deviations. Furthermore, according to Table 2.2, σ_{peak} grows with increasing modal period, indicating that the Hilbert spectrum of a mode with a longer period varies less in time, allowing the mean periodicity to be determined more accurately. The negative and positive error bars of all the obtained average periods were estimated at the half-level width of the corresponding probability histogram. These uncertainties indicate some instability in the periodicities, primarily arising from epochs around solar minimum, when the amplitudes of the signals are relatively low.

Time variability of the empirical modes

Figure 2.13 shows several examples of empirical intrinsic modes of the investigated raw signals, obtained with the EEMD expansion. The intrinsic modes plotted in the top panel of Fig. 2.13 have a mean period of 626^{+69}_{-113} d (≈ 1.7 yr) and are obtained from the sunspot area signals, recorded from the Northern solar hemisphere and from the whole disk, and the F10.7 intensity, respectively. The middle panel shows the modes with the mean period of 903^{+133}_{-64} d (≈ 2.5 yr), obtained from the helioseismic frequency shift and the F10.7 intensity. Finally, in the bottom panel of Fig. 2.13, the longest 11 yr empirical modes are shown, which were obtained using all proxies. All modes are normalised to their maximum values and are slightly shifted upwards or downwards for better visualisation, hence, the information about the absolute amplitude is artificially eliminated. Nevertheless, for all the proxies examined the

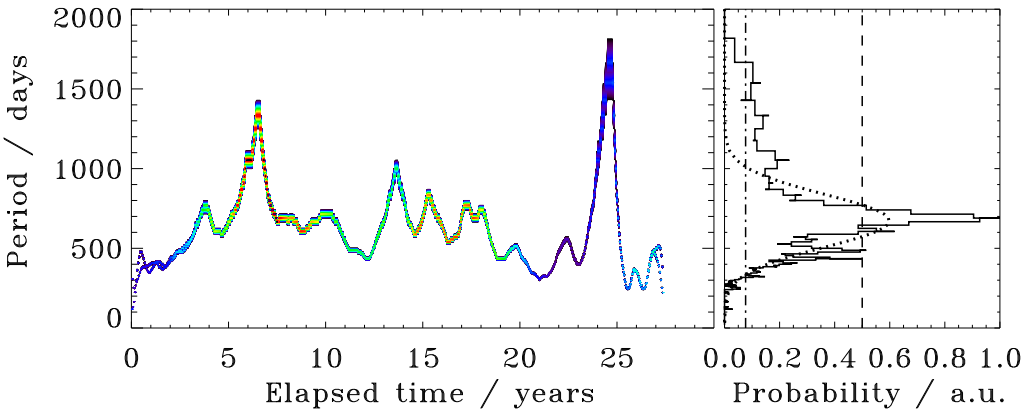

Figure 2.12: Left-hand panel: Hilbert spectrum, dependence of the instantaneous period upon time, of intrinsic mode 7 of the radio flux signal (see Fig. 2.11), shown in Fig. 2.13 (line (3) in the upper panel), determined with EEMD and characterised by the average period of about 690 d (≈ 2 yr), i.e. a quasi-biennial oscillation. The elapsed time is measured from 1 January 1985. The colour scheme is used for the instant spectral power, with the red/blue colour corresponding to the highest/lowest power, respectively. Right-hand panel: histogram (solid line), representing the most probable mean period of the Hilbert spectrum. It is calculated as the number of times each period appears in the Hilbert spectrum. The distribution has a Gaussian-like shape with the distinct peak at about 690 d (≈ 2 yr), designated as the mean most probable period of the empirical mode. The best fitted Gaussian function of the form $y(x) = a \exp([x-b]^2/2c^2)$, where $a \approx 0.6$, $b \approx 672.8$, and $c \approx 166.3$, is shown by the dotted line, the half-level of the histogram is shown by the dashed line. The vertical dot-dashed line shows the value of the standard deviation of the histogram. The probability is normalised to its maximum value.

absolute amplitudes of the 11 yr modes were found to be much greater, generally by a factor of 5, than that of the shorter-period modes.

According to Table 2.2, the quasi-biennial oscillations of the sunspot area proxies with the average period of 626 d were found only in the signals from the whole Sun disk and from the Northern hemisphere, and are absent in the Southern hemisphere. Hence, one can expect that lines 1 and 2 in the upper panel of Fig. 2.13 demonstrate in-phase behaviour. Indeed, correlation analysis of these lines showed that the cross correlation coefficient varies from 0.8 to 0.9 at time lags of 0.1–0.2 yr (6–12% of the modal average period), except between 3 yr and 13 yr and between 17.1 yr to 18.6 yr, where the modes were artificially corrupted by the decomposition process. The time lags found are within the error bars of the estimation, generated by HHT (see Table 2.2). Similar in-phase behaviour can be recognised in the intrinsic modes of the sunspot area signals with a shorter mean period of 127 d (see Fig. 2.14). In this case the obtained periodicities were found to appear simultaneously in the whole Sun signal and in the Southern hemisphere only, and are absent from the signal from the Northern hemisphere.

The modes with a mean period of 903 d, obtained from the helioseismic frequency shifts and the F10.7 signal and presented in the middle panel of Fig. 2.13, show rather out-of-phase behaviour during the maximum of the cycle 22, but are in phase during the maximum of the cycle 23. Moreover, in-phase behaviour of those modes is also seen at the very beginning of the cycle 24. The quasi-biennial and longer periodicities obtained from the 108 d smoothed overlapping F10.7 data were found to be consistent with those obtained for the 10 d smoothed data. As one might expect short-term periodicities were not detected in the 108 d smoothed data because the time resolution is not fine enough. The middle panel of Fig. 2.13 allows for comparison of one of the intrinsic modes found in both the 10 d and 108 d smoothed F10.7 data. Except the edge effects of EEMD, the agreement is predominantly very good. The obtained mean periods are also in good agreement (all within 1σ, see Table 2.2), and, although the modes are less significant in the 108 d smoothed data, they are all still significant. This indicates that the EEMD technique is not adversely affected by the fact that correlated data were used and, therefore, the intrinsic modes obtained from the helioseismic data can be trusted.

The 11 yr cycle is clearly detected in all proxies and is shown in the bottom panel of Fig. 2.13. The signatures of the so-called "extended" last minimum are well pronounced in these curves too. It is also clearly seen that 11 yr maxima of the sunspot area signals recorded separately from the Northern and Southern hemispheres are slightly shifted with respect to each other.

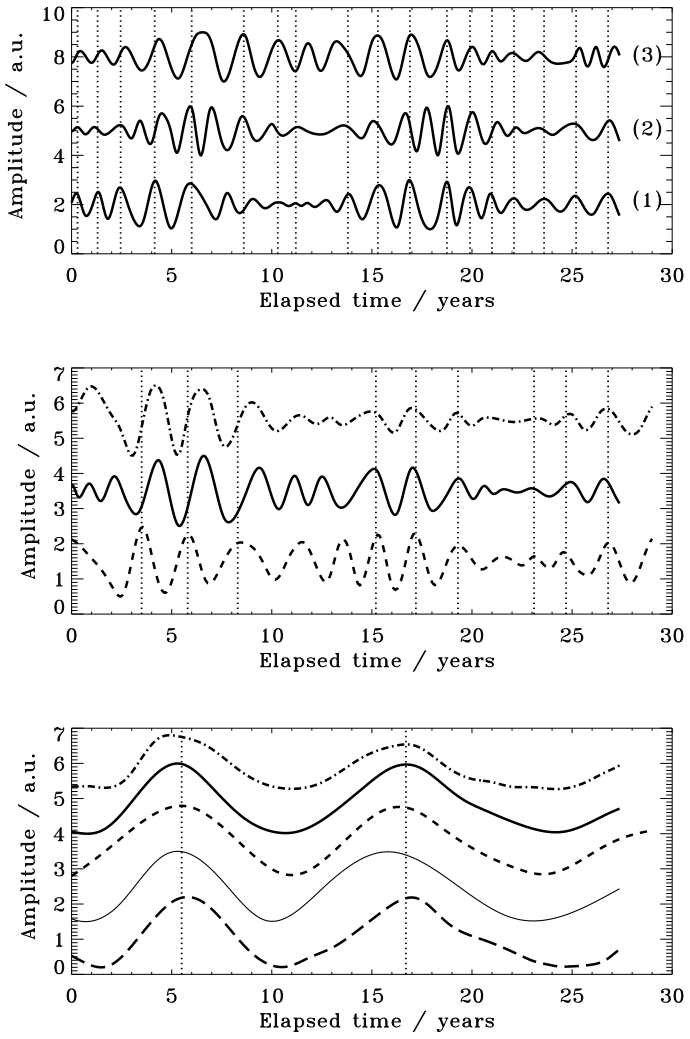

Figure 2.13: Upper panel: intrinsic empirical modes with the mean period of 626^{+69}_{-113} d (≈ 1.7 yr) of the sunspot area signal recorded from the Northern hemisphere (line 1), from the whole Sun disk (line 2), and the 10.7 cm radio flux intensity (line 3). Middle panel: intrinsic empirical modes with the mean period of 903^{+133}_{-64} d (≈ 2.5 yr) of the helioseismic frequency shift (bottom dashed line), and of the 10.7 cm radio flux intensity obtained from the signals smoothed over 10 d (middle solid line) and over 108 d (upper dot-dashed line). Bottom panel: the longest 11 yr empirical modes of the sunspot area signal recorded from the Southern solar hemisphere (bottom long-dashed line), from the Northern hemisphere (thin solid line), the helioseismic frequency shift signal (dashed line), the sunspot area signal recorded from the whole Sun disk (thick solid line), and the 10.7 cm radio flux intensity (upper dot-dashed line). Dotted vertical lines in all the panels show *in-phase/out-of-phase* behaviour of the modes. All signals are normalised to their maximum values and shifted accordingly to provide better visualisation. The elapsed time is measured from 1 January 1985.

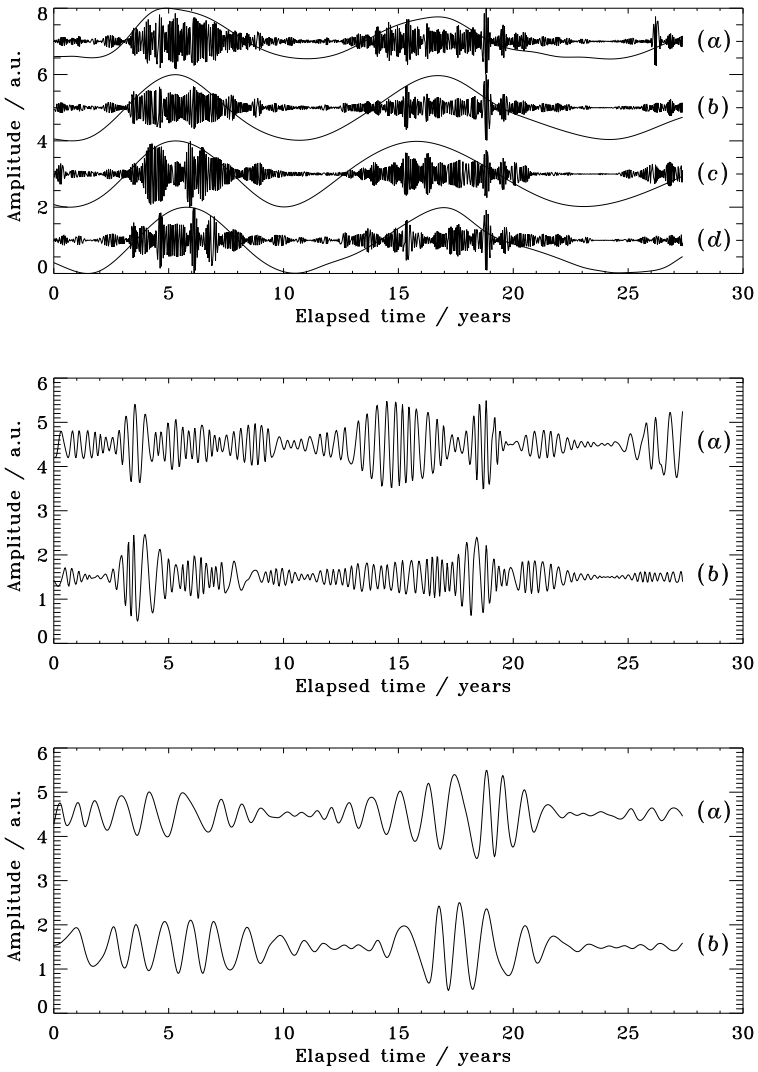

Figure 2.14: Upper panel: intrinsic empirical modes with the mean period of 25^{+7}_{-2} d of the 10.7 cm radio flux intensity (a), of the total sunspot area (b), and from the Northern (c) and Southern (d) hemispheres. The over-plotted thin solid lines show the corresponding 11 yr intrinsic modes. Middle panel: intrinsic empirical modes with the mean period of 127^{+38}_{-25} d of the sunspot area signal recorded from the whole Sun disk (a), and from the Southern hemisphere (b). Bottom panel: empirical modes of the Northern (a) and Southern (b) sunspot area signals, with the average periods of 435^{+154}_{-145} d and 426^{+9}_{-98} d, respectively. All signals are normalised to their maximum values and shifted accordingly to provide better visualisation. The elapsed time is measured from 1 January 1985.

Figure 2.14 shows the most representative examples of the identified short-term empirical modes, with mean periods of 25, 127, and 395 d. These modes are seen to have clear amplitude modulation that is highly correlated with the corresponding 11 yr cycle, appearing as a sudden increase of the modal amplitude during the 11-yr-cycle maximum. Moreover, the modal patterns observed around the solar maxima exhibit additional amplitude modulations, with periodicities much shorter than 11 yr, and demonstrate a wave train behaviour. Rapid intensive fluctuations (also called "surges") were also found to occur during the solar maxima and are pronounced, for example, in the 25 d period modes. One such surge appearing at the vicinity of 19 yr of the elapsed time (the end of the solar cycle 23, see Fig. 2.14) was detected in all short-term modes and corresponds to the beginning of the extended minimum between the cycles 23 and 24. The fine properties described above are common to all short-term variations, as well as partly appearing in several of the shortest QBO modes, and require further, more detailed investigations.

2.4.4 Discussion and conclusions

The spectral analysis of periodicities in the solar activity cycles 22, 23, and 24 (1985–2014) performed by the HHT method is presented, considering the following solar observational proxies: helioseismic frequency shift, 10.7 cm radio flux, and sunspot area signals from the whole Sun disk, and from the Northern and Southern hemispheres separately. Similar periodicities were detected in different proxies independently and simultaneously, and were distinguished into three groups: short-term variations (with periods shorter than 0.5 yr), likely related to the so-called Reiger-type periodicities [Rieger et al., 1984]; quasi-biennial oscillations [QBO, Bazilevskaya et al., 2014], with periods in the range of 0.5–3.9 yr; and longer periodicities, such as the 11 yr cycle. Hence, all detected periodicities are consistent with previous, well-known results. In particular, using the above listed proxies, which are different to the ones analysed with EMD in Vecchio et al. [2010, 2012a,b], the same types of periodicities, such as the QBO and 11 yr modes, were extracted. In addition, similar periodicities were detected with EMD in the records of the daily coronal index of Fe XIV emission from 1939 to 2008 [Deng et al., 2015]. Furthermore, the presented findings were obtained with the noise-assisted ensemble EMD (EEMD), which provides more statistically robust results. The fact that similar periodicities are independently detected in different observational proxies evidently confirms their physical nature.

The shortest detected mean period of about 25 d is clearly associated with the monthly solar rotation. It was detected in all observational proxies, except

the helioseismic frequency shift (see Table 2.2), determined from the time-series of 108 d in length, not resolving such short periodicities. Furthermore, the next identified Reiger-type mean periods, such as 44, 75, 98, 127, and 150 d, are seen to be the approximate multiples of 25 d. This ordering was also detected in Bai [2003], where periodicities of the solar flare occurrence rate during the cycles 19–23 were analysed. This finding was claimed to support the idea that the 25 d period is one of the fundamental periods of the Sun, and various observational proxies (e.g. the sunspot area and the 10.7 cm radio flux) of the solar magnetic activity often exhibit periodicities at its multiples [Bai and Sturrock, 1991]. The mechanisms possibly responsible for such an ordering remain uncertain. The 25 d periodicity can be also related to the monthly evolution of the photospheric magnetic field, associated with the solar rotation. In particular, Knaack et al. [2005] found similar ordering of the Reiger-type periodicities in the analysis of the monthly variations of the photospheric magnetic field. In addition, shorter-period modes of several observational proxies, namely 22, 46, and 96 d variations of the 10.7 cm radio flux intensity and 23, 43, and 80 d variations of the sunspot area records, demonstrate approximate doubling of the modal period. According to the EMD-based noise–test technique developed in Sec. 2.2, such a dyadic behaviour could indicate the relation of these modes to randomly distributed dynamical processes in the solar atmosphere.

Some of the identified modes are seen to have clear 11 yr modulation of their amplitudes, appearing as a rapid increase in the modal amplitude in phase with the 11 yr solar cycle maxima and subsequent decrease during solar minima. This modulation is indeed highly correlated with the extracted 11 yr modes, and is mainly pronounced in the shorter-period modes (all Reiger-type periodicities and a few short-period QBO modes), while the longer-period modes were found to have rather stable amplitudes. Similar 11 yr amplitude modulation of the short-period modes has been found in earlier solar epochs: Zolotova and Ponyavin [2007] analysed sunspot area signals from the Northern and Southern hemispheres for the time interval of 129 yr from 1874 to 2003 with EMD. The authors separated obtained results into the high- and low-frequency parts. The common signal, constructed as a sum of the high-frequency components with periods up to 3 yr, showed evident 11 yr amplitude modulation for both hemispheres. Usage of the EEMD expansion in the present study, which prevents the mode leakage artefact, allowed one to determine such 11 yr amplitude modulation in each individual high-frequency mode. This in turn led to the revealing of fine structures, such as the rapid intensive surges and additional amplitude modulation of the modes in form of oscillating trains. These findings support the idea that the large-scale magnetic field related to the 11 yr solar

cycle consists of much smaller unipolar magnetic elements of several arcseconds in size, which were observed, for example, by Benevolenskaya [2010] for the cycle 23. In Sec. 2.3, such small-scale magnetic elements were found to demonstrate a quasi-periodic behaviour of their magnetic flux with periods of a few hours or longer [see e.g. Benevolenskaya, 2010], which could affect the short-period variations detected in this work. The strong coupling of the fine structures shown in Fig. 2.14 with the 11 yr cycle also indicates their production by the global dynamo, for example via the turbulent cascade, rather than by the local dynamo. Such a discrimination between the dynamo models can be established as the local dynamo is known to be essentially decoupled from the solar activity, and contributes to a background quiet sun magnetic field only [Stenflo, 2013].

The use of the sunspot area signals simultaneously from the whole visible disk and from the Northern and Southern hemispheres separately, allowed one to analyse the spatial structure of the Sun's activity. For example, the empirical mode with the mean period of about 626 d, which is detected in the total Sun sunspot area, can be associated with a signal coming from the Northern hemisphere. While the empirical mode with the mean period of about 127 d, which is also found in the total Sun sunspot area, can be associated with a signal produced in the Southern hemisphere (see Table 2.2). These findings can be considered as additional signatures of the North–South (NS) asymmetry in the solar hemispheres evolution [e.g. Badalyan and Obridko, 2011; Mandal and Banerjee, 2016]. Similarly, Zolotova and Ponyavin [2007] found a randomly mixed phase behaviour in the described above high-frequency components of the sunspot area signals decomposed via EMD, supporting the general idea that the Northern and Southern solar hemispheres evolve rather differently. Application of the EEMD method allows one to specify two particular modes (with the mean periods of about 626 d and 127 d) from the mentioned above high-frequency range, demonstrating clear indications of the NS asymmetry. In contrast, all identified empirical modes from the low-frequency part in Zolotova and Ponyavin [2007] (with periods longer than 3 yr) were found to be well synchronised in phase, i.e. signatures of the NS asymmetry were absent, which is also in general consistence with the results of this work. Another evidence of the NS asymmetry obtained in the present study, is that the maxima of the detected 11 yr modes, corresponding to the epochs of the highest solar activity, in sunspot area signals from the Northern and Southern hemispheres are shifted in time with respect to each other. This indicates slightly different periods of time when the hemispheres exhibit maximum magnetic activity. This effect is well known and widely observed [see Norton et al., 2014, for a recent review].

The average periodicities reported in Sec. 2.4.3 were estimated as the most probable periods of the empirical modes with usage of the averaging histogram technique described above. However, application of the HHT method allows one to determine actual time variability of each modal period and amplitude too. All modes were found to have rather unstable instantaneous periods, differently varying around a mean value from one oscillation cycle to another (see examples of modes in Figs. 2.13, 2.14). In particular, the empirical mode with the mean period of about 426 d of the Southern sunspot area signal (Fig. 2.14) exhibits nearly stable period behaviour throughout the entirety of cycle 22, while the periodicity changes dramatically (up to values of about 600 d for at least three cycles of oscillation) during cycle 23. Such strong deviations of the instant period from the mean value are occasionally observed. Additionally, as the EMD technique is originally based on the searching for the local time scales in the signal, and, hence, is suitable for analysing essentially anharmonic signals, signatures of the so-called "extended" solar minimum were successfully established in the work. They are clearly pronounced as a sudden change in the slope of almost all detected 11 yr modes during the decaying phase of the 23rd solar maximum. The obtained results (e.g. the number of empirical modes identified in each observational proxy, average periods, oscillation profiles) were found to be robust in the used range of the intrinsic parameters of EEMD, such as the stopping criterion of the "sifting" process in each EMD trial and the amplitude of the added white noise (see Sec. 2.1 for details).

The analysis also demonstrated that the EEMD technique is an effective tool for characterising variations in the properties of helioseismic parameters on time scales shorter than 11 yr, and, therefore, for characterising variations in the Sun's internal magnetic field. Good agreement was found with the other activity proxies for both those smoothed over independent 10 d intervals, and those smoothed over overlapping 108 d intervals. This is important since helioseismic investigations of the Sun's activity cycles frequently consider overlapping, and therefore, correlated data, which can affect the significance of any determined signals. It has been demonstrated that the quasi-biennial signal in the helioseismic data can be split into two main modes, with periods of about 965 and 1250 d. Both lie within the broad peak found using wavelet techniques by Simoniello et al. [2013].

2.5 Multi-mode quasi-periodic pulsations in a solar flare

Quasi-periodic pulsations (QPP) in solar flares are often observed to posses multiple or non-stable periods and anharmonic profiles, which are considered in detail in

Sec. 1.2.2 and illustrated in Figs. 1.3, 1.11, and 2.2. In addition to the standard Fourier approach, the wavelet technique is extensively used for their spectral analysis [see e.g. Mathioudakis et al., 2003; Kupriyanova et al., 2010]. Another method allowing for processing non-stationary QPPs is the Wigner–Ville analysis. It has been applied to the examination of solar QPPs, for example, in Kislyakov et al. [2006] and Khodachenko et al. [2011]. Essentially, all these methods are based on the Fourier transform and are therefore not able to address the observed nonlinear properties of solar QPPs (see Sec. 2.1). In particular, there is a question of whether the observed symmetric triangular shape of the oscillations shown in Figs. 1.3 and 1.11 indicates the nonlinear nature of these QPPs, or it appears because of a superposition of several short-living harmonic signals of different frequencies. In this section, which is an adaptation of the work by Kolotkov et al. [2015b], the analysis of a QPP in a solar flare is performed with the HHT technique, revealing the presence of three oscillatory modes in the analysed QPP, one of which has an oscillation period positively correlating with the amplitude.

2.5.1 Observations

The examined QPP is observed in an X3.2-class solar flare occurred on 14 May, 2013 that was situated on the North–East limb of the Sun at the position N08E77 in the active region NOAA 11748. The flare had a duration of two hours (23:59–02:00 UT) with a peak time at 01:11 UT. The impulsive phase lasted approximately from 01:00 UT to 01:30 UT. The event was observed with the Nobeyama Radioheliograph [NoRH, see Nakajima et al., 1994] and Radio Polarimeters [NoRP, see Nakajima et al., 1985]. The maximum radio emission reached $1,985$ sfu at 17 GHz, with a maximum radio brightness of 1.3×10^8 K. In the impulsive phase (approximately since 01:05 UT), observations in the radio band show quasi-periodic pulsations that are most pronounced in the 17 GHz band. The impulsive phase of this flare was missing by RHESSI.

Figure 2.15 shows the spatial distribution of the radio emission intensity R+L at the 17 GHz band detected with NoRH in the flaring site at 01:06 UT. This instant of time corresponds to the start of well developed QPPs. The source of the enhanced microwave emission has a distinct loop-like shape. The approximate size of the area in Fig. 2.15 containing the loop-like structure in the plane of sky is about 42×39 Mm. The estimated visible width of the loop-like radio source in Fig. 2.15 is about 8 Mm, its approximate length is about 40 Mm, assuming it is semi-circular with the radius equal to the half-distance between the Northern and Southern footpoints, considering the plane of the loop to be parallel to the image

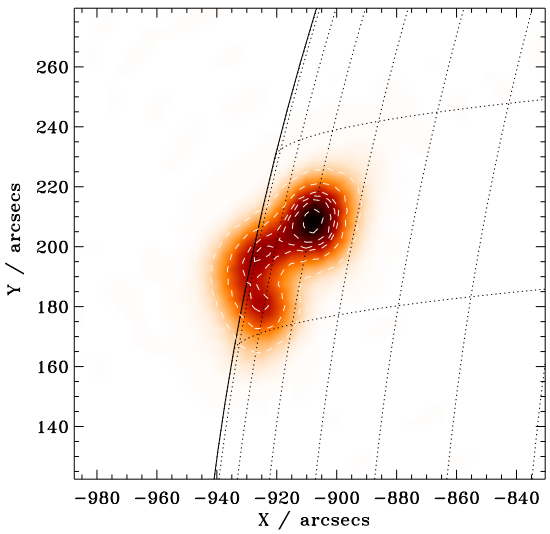

Figure 2.15: Spatial distribution of the radio emission intensity (R+L) in the 17 GHz band, obtained with the Nobeyama Radioheliograph for an X3.2-class solar flare occurred on 14 May, 2013 at 01:06 UT. The darker colours indicate the regions of the enhanced emission intensity. White dashed contours show the levels 0.9, 0.7, 0.59, 0.5, 0.3, 0.1, and 0.02 of the maximum brightness.

plane.

In the EUV band, rapidly decaying kink oscillations of coronal loops with periods of several minutes in this active region were detected with SDO/AIA after the impulsive phase of the flare, at 01:11 UT, while the oscillations discussed in this section are not seen. Kink oscillations of neighbouring loops were excited simultaneously, but got rapidly out of phase. In the following they are not considered in detail.

In Fig. 2.16 the correlation curve obtained with NoRH at 17 GHz, and the integrated R+L intensity (the total flux at 17 GHz) obtained with NoRP, are shown. The correlation curve gives the time variation of the averaged values of correlation coefficients of antenna pairs, after removing the short base-line pairs, of NoRH. It is especially sensitive to strong microwave signals coming from small-scale sources on the Sun, with sizes up to 24 arcsec. For the study of QPP in the discussed flare, the NoRH correlation curve is more suitable than the imaging data cube, as the flare site is located near the limb. Signals of such flares may be adversely affected both by the instrumental phase artefacts (e.g. the jitter effect) and by the background emission from the Sun, the Earth's atmosphere, and of other objects, corrupting the imaging

information. Hence, it is non-trivial to synthesise a reliable full-time imaging data cube for this flare, and it was not done in this study. The NoRP total flux signal is obtained by integrating the radio flux over the whole disk of the Sun. Therefore the total flux signal contains the contribution of various large-scale sources together with the fine sources of interest. Thus, for the purposes of this work, the integral signal is less suitable in comparison with the correlation amplitude curve.

The impulsive phase of the flare, presented in Fig. 2.16, corresponds to the appearance and subsequent development of a compact radio source near the Northern footpoint of the extended loop-like structure, shown in Fig. 2.15. It can be associated with a magnetic loop with a strong magnetic field, radiating primarily by the gyrosynchrotron mechanism. According to NoRP data, the power spectrum of the radiation looks like a non-monotonic function with the peak frequency between 9.4 GHz and 17 GHz. Additionally, the degree of polarisation of the studied signal at 17 GHz is about 6%. Therefore the combination of the described above properties, such as the presence of the peak frequency in the radiation power spectrum, relatively low degree of polarisation, and sufficiently high radio brightness of the signal, indicates the gyrosynchrotron nature of the signal[4].

The NoRH correlation curve and the NoRP total flux signals are found to correlate well with each other. The cross-correlation coefficient is equal to 0.8 at zero time lag. In both these signals, QPPs are clearly pronounced and have a symmetric triangular shape. The instant period of pulsations, determined by eye, is about 40 s. It varies approximately from 20 to 100 s during the flare development. The clear non-stationarity and anharmonicity of these QPPs suggest the application of the HHT method to their analysis.

2.5.2 HHT analysis

The results of applying EEMD to the NoRH correlation signal shown in Fig. 2.16 are presented in Fig. 2.17. The white noise amplitude was taken as 0.2 of the standard deviation of the original signal (see Sec. 2.1). Results obtained with the slightly lower or higher amplitudes of the white noise, for example 0.15 and 0.3 were found to be similar. The decomposition gives six intrinsic modes. The application of the noise–test scheme developed in Sec. 2.2 to the intrinsic empirical modes shown in Fig. 2.17, allows for the estimation of the power law index α in the dependence of the total modal energy upon the mean modal period, given by Eq. (2.15). It is found to be of 2.8 ± 0.3 with the corresponding 1σ uncertainty (see Fig. 2.18). Such a high value of the power law index indicates the presence of a strong correlation

[4]See paragraph 4.6.7. of the NoRH manual, http://solar.nro.nao.ac.jp/norh/doc/manuale.pdf

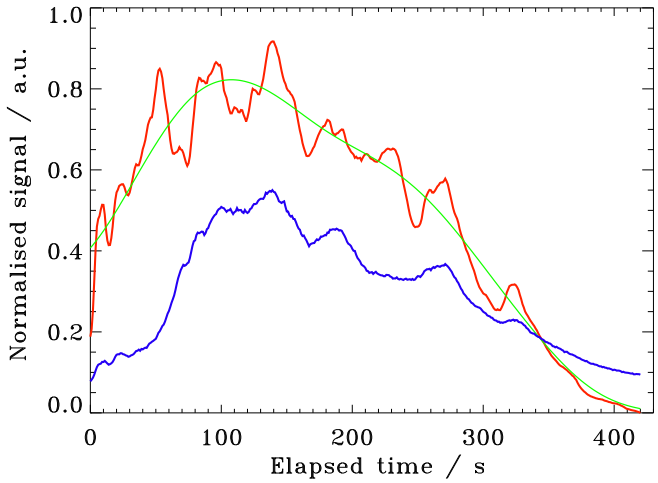

Figure 2.16: Red line: Correlation curve obtained with the Nobeyama Radioheliograph at 17 GHz. Green line: the aperiodic trend of the signal shown in red, determined as the last EMD mode. Blue line: Integrated intensity R+L at 17 GHz, obtained with the Nobeyama Radiopolarimeters. The horizontal axis shows the time elapsed since 01:05:22 UT. Both signals are normalised to a constant value and shifted upwards or downwards for better visualisation.

between data points in the original signal, and corrupts the dyadic properties of EMD, which were found to be mainly pronounced for random signals with power law indices up to 2 (see the discussion in Sec. 2.2.4). This in turn prevents the following usage of the chi-squared distribution (2.13) and the construction of corresponding confidence intervals for the assessment of a statistical significance of the detected modes. Nevertheless, the first two modes, 1 and 2, are seen to be too weak (by about two orders of magnitude weaker than the modes 3–5, see Fig. 2.18), and, hence, are neglected in the following analysis. The last mode, 6, displays an aperiodic and non-harmonic trend of the original signal shown in Fig. 2.16. Thus, modes 3, 4, 5 are found to be of interest for further investigation.

Mode 5 has a well-pronounced decaying oscillatory pattern with an apparent frequency modulation. The instant period of the oscillation decreases with time from 95 to 61 s. The decrease in the period is accompanied by the decrease in the amplitude. The dependence of the amplitude on the period was fitted by an empirical linear law of a $Amplitude/\max(Amplitude) = a \times Period[\mathrm{s}] - b$ form, where $a = 2.9 \times 10^{-4}$ s^{-1}, and $b = 1.45 \times 10^{-2}$. The damping time, 250 s, equals to 3 instant periods of the oscillation. The amplitude of mode 3 also shows a decaying

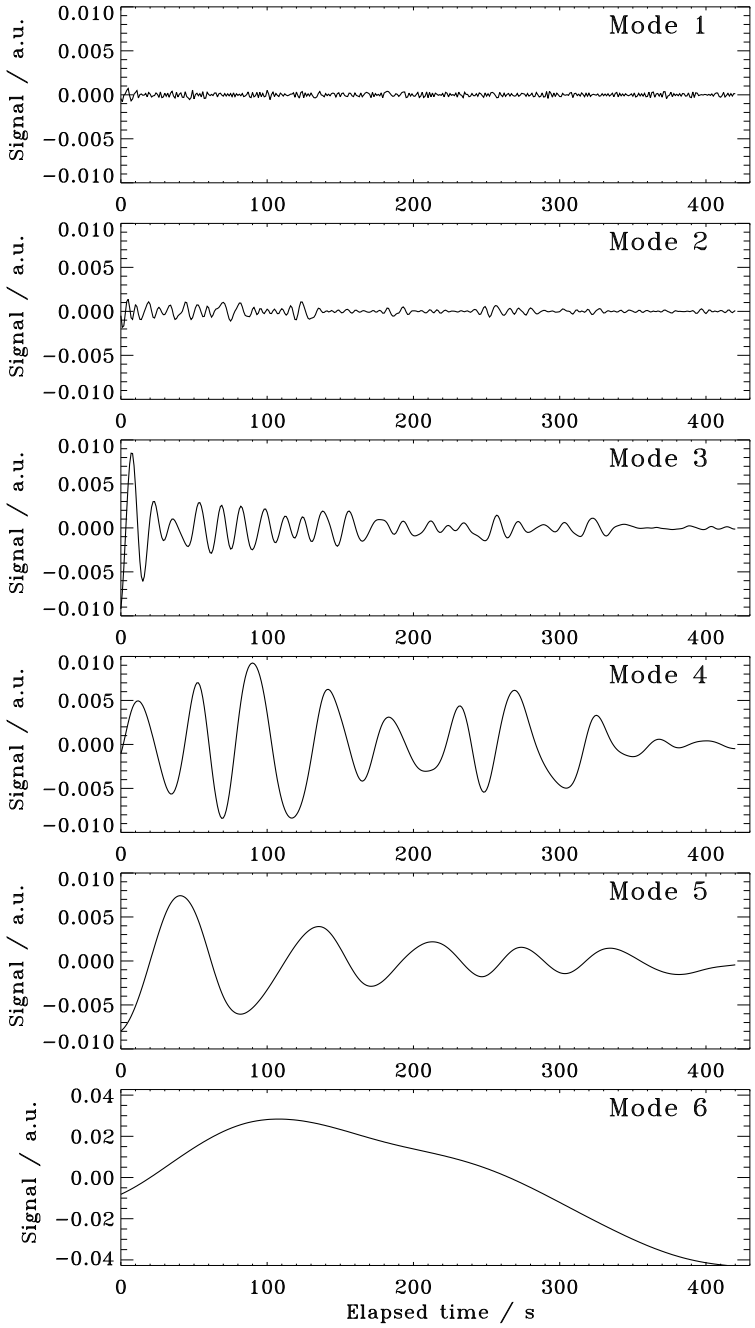

Figure 2.17: Intrinsic mode functions detected with the ensemble empirical mode decomposition (EEMD) technique in the NoRH correlation signal, presented in Fig. 2.16. All modes are normalised to the maximum value of the correlation signal. The elapsed time starts at 01:05:22 UT.

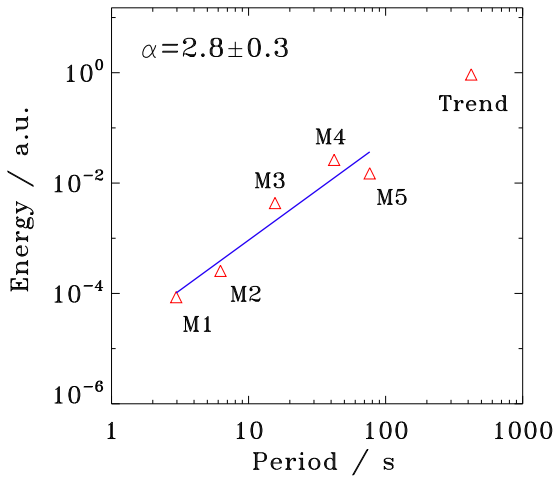

Figure 2.18: Normalised total energy–mean period diagram of the intrinsic modes (quasi-periodic modes 1–5 and aperiodic trend) shown in Fig. 2.17, plotted on a logarithmic scale. The blue line indicates the best linear fit of Eq. (2.15) to the observed dependence.

behaviour, with an average period of about 15 s. The damping time is 90 s, that is about six periods of the oscillation. Also, the amplitude of mode 3 has a noisy modulation. The behaviour of mode 4 is different from modes 3 and 5, it can be rather described as a sequence of oscillation trains with an average period of about 45 s.

The upper panel of Fig. 2.19 shows the Hilbert spectrum of the set of intrinsic modes 3, 4 and 5. It is evident that the modes occupy three distinct spectral bands. The values of instant frequencies of different modes are seen to vary around a certain mean value. More specifically, the frequency of mode 3 varies around 0.065 Hz (15 s). The instant frequency of mode 4 is localised in the vicinity of 0.022 Hz (45 s). Mode 5 has the average instant frequency about 0.01 Hz (100 s). The scattering of the instant frequency of mode 3 is an intrinsic feature of HHT of noisy signals [see e.g. Huang et al., 1998] and is similar to the appearance of side lobes in, for example, Fourier periodograms of noisy signals. The apparent small split of the lowest-frequency curve into two curves is an artefact caused by the edge effect of HHT. Despite this visual separation, each instant of time there is a single value of the frequency in this mode, that jumps between two extreme, sufficiently close values in certain time intervals.

Composing the signal as the sum of modes 3, 4, 5, one can obtain the Fourier

power spectrum of the composed signal, shown in the bottom panel of Fig. 2.19. It also gives well-pronounced peaks approximately at 0.067 Hz, 0.022 Hz and 0.01 Hz, that is in a good agreement with the results obtained by HHT. Thus, the EMD technique also works as an adaptive filter for subtracting the noise and trend from the initial data set. The secondary peaks at 0.013 and 0.017 Hz, and 0.029 and 0.033 Hz are attributed to the amplitude modulation of the 45 s mode, evident in Fig. 2.17. Three Gaussian filters (see Fig. 2.19) with the widths 0.005–0.015 Hz, 0.015–0.03 Hz, and 0.04–0.08 Hz measured at their half-levels were then used to reconstruct the empirical modes 3, 4, 5 from the Fourier power spectrum. The filters are sufficiently narrowband for the clear discrimination of the EMD modes, and sufficiently broadband to include their amplitude and period modulations. The obtained results are shown in Fig. 2.20. The cross-correlation coefficients of empirical modes 3, 4, 5 and the corresponding narrowband signals obtained from the Fourier power spectrum are 0.90, 0.89 and 0.87 respectively. In particular, the bandpass of the 45 s mode with its four side lobes, determined by EMD, confirms its amplitude modulation.

2.5.3 Discussion of results and conclusions

The HHT technique is applied to the analysis of anharmonic non-stationary quasi-periodic pulsations in a microwave correlation signal of a solar flare, obtained with the Nobeyama Radioheliograph at 17 GHz. The analysed signal has a pronounced symmetric-triangular quasi-periodic pattern. The method of ensemble empirical mode decomposition revealed that the signal consists of three intrinsic quasi-periodic modes. The Hilbert transformation showed that instant frequencies of these intrinsic modes are localised in certain spectral intervals, with the mean periods of about 15, 45 and 100 s.

The longest-period, 100 s intrinsic mode is a decaying oscillation, with a decay time of 250 s. The shortest-period, 15 s intrinsic mode shows a similar behaviour, with a decay time of 90 s. The quality of the 15 s mode is higher than that of the 100 s mode, as the ratio of the decay time to the mean period in this mode is six. Such decaying oscillations are often seen in light curves of solar and stellar flares [see e.g. Wang, 2011; Anfinogentov et al., 2013; Cho et al., 2016], including the microwave band [Kim et al., 2012]. Those oscillations have been interpreted as standing linear slow magnetoacoustic waves. Damping of these waves is usually associated with thermal conduction [e.g. De Moortel and Hood, 2003]. However, the decrease in the efficiency of the damping with increase of the frequency is inconsistent with the interpretation of the damping in terms of thermal conduction [e.g.

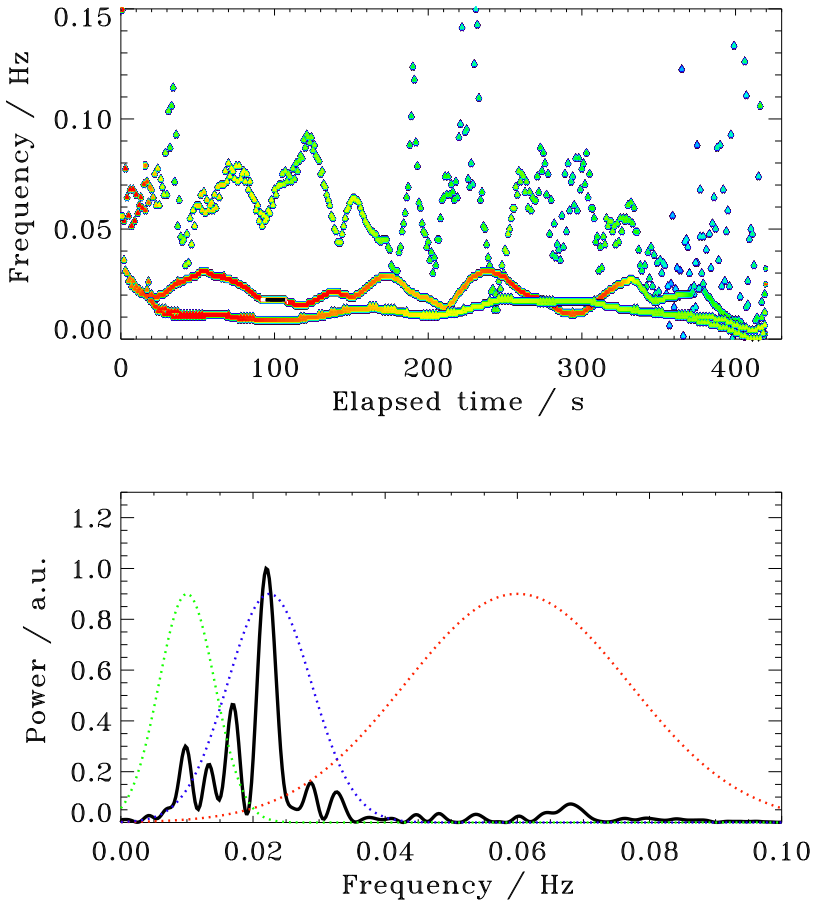

Figure 2.19: Upper panel: Hilbert spectrum (the instant frequency–time distribution) of empirically determined intrinsic modes 3, 4, 5. The instant spectral power is shown by the colour scheme, with the red/blue colour corresponding to the higher/lower power, respectively. The elapsed time starts at 01:05:22 UT. Bottom panel: Fourier power spectrum of the signal obtained as the sum of intrinsic modes 3, 4, 5. The Fourier power is normalised to the highest value. The narrowband Gaussian filters at 0.005–0.015 Hz (green), 0.015–0.03 Hz (blue), and 0.04–0.08 Hz (red) are shown by the dotted curves.

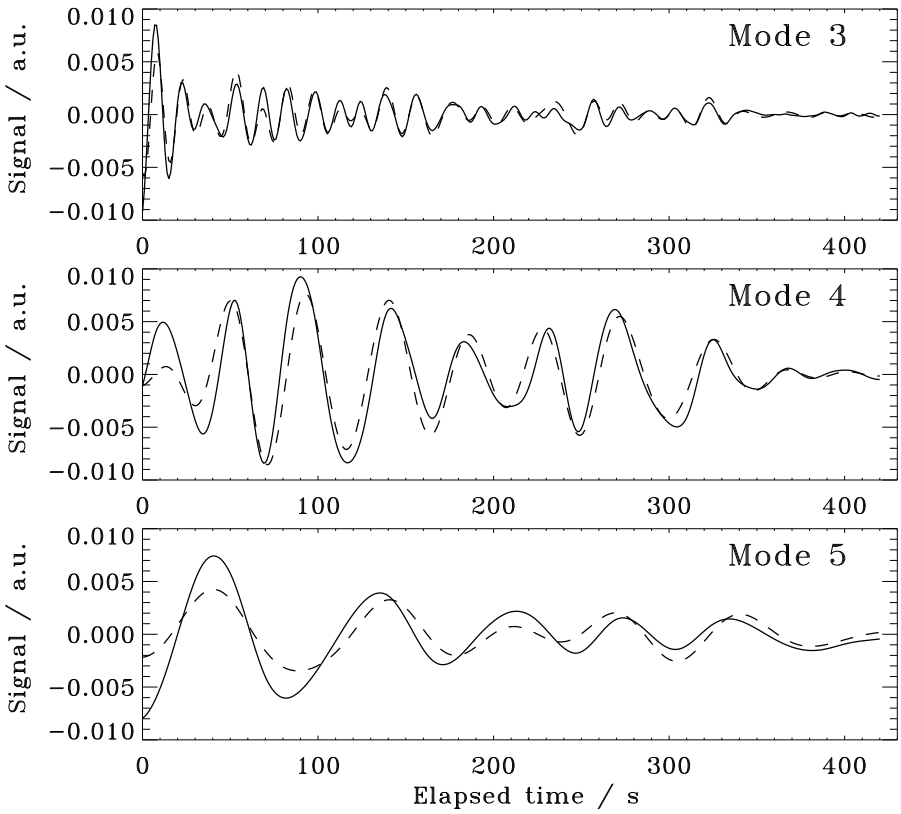

Figure 2.20: Empirical intrinsic modes 3, 4, 5 (solid lines) and the narrowband signals obtained from the Fourier power spectrum (dashed lines), shown in Fig. 2.19. All lines are normalised to the highest value of the NoRH correlation signal (see Fig. 2.16). The elapsed time starts at 01:05:22 UT.

Ofman and Wang, 2002]. The damped oscillations detected in this study also have other properties that make them different from the standing slow waves revealed before. Namely, the detected periods (15 and 100 s) of the decaying oscillations are much shorter than the known examples of standing slow magnetoacoustic oscillations [at least several minutes or longer, see Wang, 2011], while close to those found by Cho et al. [2016] for soft X-ray emission in solar flares. Perhaps the short periods of the observed oscillations can be attributed to the short length of the oscillating loop. However, even for the 100 s mode the phase speed of a fundamental standing slow mode, estimated as the ratio of the double length of the oscillating loop, 2×40 Mm, and the oscillation period, 100 s (see Eq. (1.8)), is 800 $\mathrm{km\,s^{-1}}$. For this phase speed to be the sound speed the plasma temperature should be about 30 MK. A plasma with such a temperature should be filling the flaring loop for the duration of the oscillation, about 5 min. For the 15 s mode, with the phase speed of 5.3 $\mathrm{Mm\,s^{-1}}$, to be a standing acoustic oscillation, the plasma temperature should be unrealistically much higher, about 1,230 MK. Therefore, if the detected 100 s and 15 s periodicities are caused by standing acoustic oscillations, their wavelength should be much shorter than the length of the observed microwave loop, giving lower phase speeds. Otherwise it would require an unrealistically high temperature. Thus, one should not disregard this interpretation entirely for the 100 s mode, but should not consider it as the most favourable one.

Another MHD mode of coronal plasma structures is the standing kink oscillation (see Sec. 1.2.2). According to Eq. (1.5), the phase speed of the kink mode is determined by the kink speed, $C_{\mathrm{k}} \approx 2^{1/2} C_{\mathrm{A0}}$, where C_{A0} is the Alfvén speed inside the dense oscillating loop, and is independent of the plasma temperature. Observed kink modes usually have phase speeds around 1 $\mathrm{Mm\,s^{-1}}$ and are also seen to decay over a few periods, consistent with the behaviour of the 100 s mode. In contrast, the phase speed of the 15 s mode, 5.3 $\mathrm{Mm\,s^{-1}}$, is possibly too high for this mode too. An option is that the 15 s mode is a higher longitudinal harmonics of the kink mode [see e.g. Andries et al., 2009, for the discussion of the higher harmonics of the kink mode]. However, in this case it should be the 6th or 7th harmonics, provided the 100 s mode is the fundamental one, and the naturally arising question is why only the fundamental and the 6th or 7th harmonics are excited in the loop.

A more realistic assumption is that the 15 s mode is of a different azimuthal symmetry, for example the sausage mode. In favour of this interpretation is that the previous identification of the fundamental sausage modes of flaring loops had a similar period of 16 s [Nakariakov et al., 2003]. In the leaky regime that is characterised by the decay of the wave amplitude, the period is prescribed by the transverse travel

time at the internal fast magnetoacoustic speed, $P_{\rm saus} \approx 2.62a/C_{\rm A0}$, where a is the effective radius of the loop [e.g. Nakariakov et al., 2012]. Assuming that the 100 s oscillation is caused by the fundamental kink mode and the 15 s oscillation is the fundamental leaky sausage mode of the same loop, one can use the expressions given above to find that $L/a \approx 12$ that is consistent by the order of magnitude with the observed aspect ratio (see Fig. 2.15). The ratio of the average periods of long-period and short-period modes estimated in this study is consistent with the result found by Van Doorsselaere et al. [2011].

The 45 s mode is found to have a wave-train behaviour. However, as only two trains of oscillations are seen, the latter conclusion does not seem to be sufficiently justified. The nature of this oscillation is not clear, while by its period can be the second harmonics of the kink mode

The decrease in the amplitude of the 100 s oscillation is accompanied by the decrease in the period, from about 100 to 60 s. Such a behaviour has been found in other physical systems and may be associated with nonlinear effects: a finite amplitude regime with the oscillation period determined by the amplitude [Dubinov et al., 2012a,b]. This phenomenon has not been studied in the context of solar flare QPP yet, and needs to be addressed in future studies.

Thus, the HHT analysis reveals that the apparent anharmonic shape of QPP in the analysed flare results from a superposition of three intrinsic modes. The simultaneous presence of multiple different periodicities has been found in QPPs before [e.g. Inglis and Nakariakov, 2009; Kupriyanova et al., 2013]. However in those studies the main emphasis was put on the superposition of harmonic modes, while this work demonstrated that QPPs may be a superposition of decaying or modulated modes.

This study also demonstrated that in addition to the distinguishing of randomly distributed variations of the quiet sun (Sec. 2.2), detection of the modulated oscillation in a small-scale photospheric structure (Sec. 2.3), and comprehensive search for the periodicities associated with the long-term solar activity cycle (Sec. 2.4), the HHT method is a useful technique that can provide the unique spectral information about quasi-oscillatory processes in solar flares too. This information may be important for revealing physical processes operating in flares.

Chapter 3

Equilibria and oscillations of current sheets

3.1 Kinetic model of force-free current sheets with inhomogeneous transverse profiles

3.1.1 Introduction

Current sheets (CS) play a central role in the initiation of active phenomena in space, astrophysical and laboratory plasmas [Schindler, 2006; Yamada et al., 2010]. In particular, CSs are believed to appear in the solar atmosphere [Parker, 1994; Priest and Forbes, 2000], solar wind [Gosling, 2012], planetary magnetospheres [Jackman et al., 2014; Petrukovich et al., 2015], and in pulsar winds [Beskin et al., 2015]. Magnetic reconnection occurring within CSs results in the transformation of magnetic field energy into kinetic energy of the plasma and accelerated non-thermal charged particles, and hence the kinetic bulk energy [Treumann and Baumjohann, 2013; Zelenyi and Artemyev, 2013]. In addition, CSs act as effective waveguides for MHD waves [Smith et al., 1997; Fruit et al., 2002a,b; Lee and Hau, 2008] that could be responsible for solar coronal heating [De Moortel and Browning, 2015]. In turn, remote observations of the MHD waves guided by solar coronal CSs allow for diagnostics of properties of these CSs [Nakariakov and Ofman, 2001; De Moortel and Nakariakov, 2012; Jelínek and Karlický, 2012; Mészárosová et al., 2014].

The study of CS instabilities and properties of guided MHD waves and oscillations requires the development of equilibrium CS models. Since space and astrophysical plasmas are often considered to be collisionless, the development of the CS models should be based on the set of Vlasov–Maxwell equations. More specifically,

the widely used Harris model [Harris, 1962] presents a 1D kinetic CS with the magnetic field $\mathbf{B} = B_0 \tanh(z/\lambda)\mathbf{e}_x$ (where B_0 is the magnetic field strength, and λ is the CS thickness). In the Harris model the variation of the magnetic pressure across the CS is compensated by the plasma pressure gradient. However, observations in the near Earth space have evidently required development of generalised Harris models that would take into account several plasma populations [Zelenyi and Krasnoselskikh, 1979; Yoon and Lui, 2004], power-law energy distribution functions of charged particles [Fu and Hau, 2005], a non-zero guiding magnetic field $B_y(z)$ [Roth et al., 1996; Panov et al., 2011], and a possible bifurcation (or splitting) of the current density profile [Génot et al., 2005; Camporeale and Lapenta, 2005; Yoon et al., 2014]. These models have also been generalised for relativistic plasmas typical for pulsar winds [Balikhin and Gedalin, 2008; Kocharovsky et al., 2010]. CSs formed in planetary magnetotails often include a finite B_z component (directed across the CS plane, i.e. the magnetic reversal geometry) due to the planetary dipolar magnetic field. In 1D models including a finite B_z [see Sitnov et al., 2000, 2006; Zelenyi et al., 2011] the tangential magnetic field stresses (along the x and y axes) are balanced by the non-diagonal elements of the pressure tensor. In contrast, in 2D generalisations of the Harris model these stresses are balanced by the gradients of the isotropic gas pressure tensor [Kan, 1973; Birn et al., 2004; Yoon and Lui, 2005; Ceccherini et al., 2005; Vasko et al., 2013].

Force-free CSs constitute an important class of plasma structures formed particularly in low-β plasmas. Moreover, force-free CSs are the states of minimum energy for a closed plasma system with a fixed helicity [Biskamp, 1997]. In force-free CSs the current density is predominantly field-aligned. Force-free CSs are thought to be typical for pulsar wind plasmas [Guo et al., 2014; Mochol and Pétri, 2015], and may also be formed in the solar corona [Priest and Forbes, 2000]. In addition, force-free CSs are quite typical for the Jupiter's magentotail [Artemyev et al., 2014] and sometimes are observed in the Earth's magnetotail [Artemyev et al., 2013; Vasko et al., 2014]. Similar force-free CSs are formed in laboratory plasmas [Frank et al., 2009].

The first kinetic model of a 1D force-free CS with the magnetic field $\mathbf{B} = B_0 \tanh(z/\lambda)\mathbf{e}_x + B_0 \cosh^{-1}(z/\lambda)\mathbf{e}_y$ was developed by Harrison and Neukirch [2009b]; Neukirch et al. [2009]. In that model, the plasma pressure and the magnetic pressure $\left(B_x^2 + B_y^2\right)/8\pi$ are uniform across the CS. In contrast to the models described above, in this case the force balance is provided by the non-zero value of the shear magnetic field B_y instead of the plasma pressure gradient. Subsequently, this model has been generalised for non-Maxwellian distribution functions of charged particles

[Wilson and Neukirch, 2011], and relativistic plasmas [Stark and Neukirch, 2012]. Kinetic models of a force-free CS with a periodic transverse structure have been developed by Abraham-Shrauner [2013]. Similarly to the Harris model, in Harrison and Neukirch [2009b] the CS thickness depends on the parameters of charged particles distribution functions, and may be larger than the characteristic kinetic scales.

The class of force-free models suggested by Harrison and Neukirch [2009b]; Neukirch et al. [2009] has one significant drawback. In these models the plasma temperature and density distributions are uniform across the CS. However, in the case when the CS spatial scale is much larger than the characteristic ion gyroradius (this regime can be referred to as an MHD limit, although the plasma can be collisionless), it should be possible to set arbitrary temperature and density profiles across the CS, keeping the uniform pressure to ensure the total pressure balance in the transverse direction. In a realistic physical system (e.g. in the solar atmosphere) the density and temperature distributions across the CS are prescribed by the boundary conditions at some surface (crossed by all field lines) and local heating mechanisms (e.g. the Ohmic heating that is localised in the region of the strongest electric current density). Thus, physical reasoning suggests that models developed by Harrison and Neukirch [2009b]; Neukirch et al. [2009] set highly restrictive conditions on the density and temperature distributions. In the present study based on the work by Kolotkov et al. [2015c], that model is generalised, incorporating inhomogeneous distributions of the plasma temperature and density in the direction across the CS.

3.1.2 Analysis

It was shown [see e.g. Schindler and Birn, 2002; Schindler, 2006; Harrison and Neukirch, 2009a] that for 1D CSs with the magnetic field $\mathbf{B} = B_x(z)\mathbf{e}_x + B_y(z)\mathbf{e}_y$ where the z-axis is directed across the CS, the set of Vlasov–Maxwell equations can be reduced to Ampere's law in the following form:

$$\frac{d^2 A_x}{dz^2} = -4\pi \frac{\partial P_{zz}}{\partial A_x}, \tag{3.1}$$

$$\frac{d^2 A_y}{dz^2} = -4\pi \frac{\partial P_{zz}}{\partial A_y}, \tag{3.2}$$

where A_x and A_y are the components of the magnetic field vector potential ($B_x = -dA_y/dz$ and $B_y = dA_x/dz$), and P_{zz} is the zz-component of the plasma pressure

tensor. The latter is given by

$$P_{zz}(A_x, A_y, \varphi) = \sum_{\mathrm{s=i,e}} \int m_\mathrm{s} v_z^2 f_\mathrm{s}(\mathbf{v}, \mathbf{r}) d^3\mathbf{v}, \tag{3.3}$$

where the indices $s = i, e$ are used for the plasma species designation (an electron-ion plasma is considered), φ is the scalar potential corresponding to the electric field $E_z = -d\varphi/dz$ arising due to the electron–ion decoupling, m_s denotes the particle masses, and $f_\mathrm{s}(\mathbf{v}, \mathbf{r})$ are the particles' distribution functions that satisfy the Vlasov equation.

The Vlasov equation can be solved by choosing the distribution function as an arbitrary function of the particles' integrals of motion. In the chosen 1D configuration there are three integrals of motion: the total energy $H_\mathrm{s} = m_\mathrm{s}\mathbf{v}^2/2 + q_\mathrm{s}\varphi$ and two generalised momenta $p_{x\mathrm{s}} = m_\mathrm{s} v_x + q_\mathrm{s} A_x$ and $p_{y\mathrm{s}} = m_\mathrm{s} v_y + q_\mathrm{s} A_y$ (q_s is a particle charge, $q_\mathrm{i} = -q_\mathrm{e} \equiv e$), so that the Vlasov equation is solved by assuming $f_\mathrm{s}(\mathbf{v}, \mathbf{r}) = f_\mathrm{s}(H_\mathrm{s}, p_{x\mathrm{s}}, p_{y\mathrm{s}})$. In this analysis, CSs with the transverse scale exceeding the Debye length are considered, so that the plasma is assumed to be quasi-neutral. The quasi-neutrality condition can be written as $\partial P_{zz}/\partial\varphi = 0$ [see Schindler and Birn, 2002; Schindler, 2006]. This condition allows one to determine the distribution of the electrostatic potential $\varphi = \varphi(A_x, A_y)$.

The standard procedure for developing a kinetic CS model consists of the choice of the particles' distribution functions and the analysis of Eqs. (3.1) and (3.2). An alternative, inverse approach is to set *a priori* a magnetic field configuration, and determine the corresponding distribution functions. The latter approach was chosen by Harrison and Neukirch [2009b] to develop the model of a 1D force-free CS with homogenous transverse profiles for density and temperature. Importantly, in the inverse approach the distribution functions are not determined uniquely and can be arbitrarily changed without changing the magnetic field configuration [see Channell, 1976, for details]. This ambiguity is used in the present work to generalise the force-free CS model, including transverse inhomogeneities of the plasma parameters, by an appropriate choice of the particle distribution functions.

The magnetic field of a force-free Harris sheet has the following non-zero components:

$$B_x = B_0 \tanh(z/\lambda), \tag{3.4}$$

$$B_y = B_0 \cosh^{-1}(z/\lambda), \tag{3.5}$$

where the constants B_0 and λ are the magnetic field amplitude and the CS transverse scale length, respectively. The current densities corresponding to this magnetic field

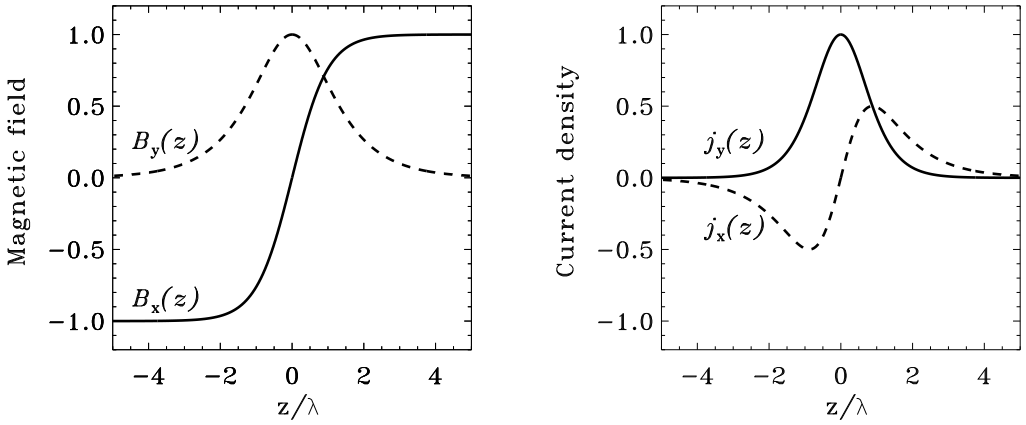

Figure 3.1: Components of the magnetic field in a force-free Harris current sheet, given by Eqs. (3.4), (3.5) (left-hand panel), and the corresponding current densities (right-hand panel). Both components of the magnetic field are normalised to the field amplitude B_0. Current components are normalised to their amplitude $cB_0/(4\pi\lambda)$.

are $j_x = cB_0/(4\pi\lambda)\tanh(z/\lambda)/\cosh(z/\lambda)$ and $j_y = cB_0/(4\pi\lambda)\cosh^{-2}(z/\lambda)$. The magnetic field components $B_x(z)$, $B_y(z)$ and the corresponding current densities are shown in Fig. 3.1. The vector potential corresponding to the force-free CS given by (3.4) and (3.5), has two components:

$$A_x = 2B_0\lambda \tan^{-1}\left[\exp\left(z/\lambda\right)\right], \tag{3.6}$$

$$A_y = -B_0\lambda \ln\left[\cosh\left(z/\lambda\right)\right]. \tag{3.7}$$

According to Harrison and Neukirch [2009b], Eqs. (3.1) and (3.2) have the following solution $P_{zz}(A_x, A_y)$ in the class of additive functions, i.e. $P_{zz}(A_x, A_y) = P_1(A_x) + P_2(A_y)$:

$$P_{zz} = \frac{B_0^2}{8\pi}\left[\frac{1}{2}\cos\left(\frac{2A_x}{B_0\lambda}\right) + \exp\left(\frac{2A_y}{B_0\lambda}\right)\right] + P_0, \tag{3.8}$$

where P_0 is a uniform pressure of the background plasma. Harrison and Neukirch [2009b] found a distribution function $f_{\rm s}^{\rm hn}(H_{\rm s}, p_{x{\rm s}}, p_{y{\rm s}})$ that allows one to obtain P_{zz}

in form (3.8) directly from expression (3.3):

$$f_{\rm s}^{\rm hn} = n_{0\rm s}\left(\frac{m_{\rm s}\beta_{\rm s}}{2\pi}\right)^{3/2} e^{-\beta_{\rm s}H_{\rm s}}[\exp(\beta_{\rm s}u_{y\rm s}p_{y\rm s}) + a_{\rm s}\cos(\beta_{\rm s}u_{x\rm s}p_{x\rm s}) + b_{\rm s}], \tag{3.9}$$

where $u_{x\rm s}$, $u_{y\rm s}$, $a_{\rm s}$, $b_{\rm s}$, and $\beta_{\rm s}$ are some positive constants. The first term in the distribution function $f_{\rm s}^{\rm hn}$ has the same form as in the Harris model and corresponds to the population responsible for the current density j_y. The second term describes the particle population carrying the current j_x and generating the magnetic field component B_y given by Eq. (3.5). The last term corresponds to the background plasma which does not contribute to the current. However, the choice of the distribution function of form (3.9) results in uniform density and temperature profiles across the CS [Harrison and Neukirch, 2009b; Abraham-Shrauner, 2013]. These conditions put strong restrictions on the solution from a physical point of view. In fact, it would be natural to expect that the plasma temperature and density are non-uniform across the CS, as the plasma may be hotter in the vicinity of regions of higher electric current due to heating, for example Ohmic heating, or current-driven microturbulence. The need for a non-uniform distribution of the plasma temperature and density can also be connected with boundary conditions.

In order to obtain the equilibrium state of the force-free CS with inhomogeneous density and temperature profiles, the distribution function $f_{\rm s}^{\rm hn}$ must be adjusted accordingly. Such a modification of $f_{\rm s}^{\rm hn}$ can be achieved by introducing different temperatures for the two current-carrying populations. Namely, the parameter $\beta_{\rm s}$ in expression (3.9) characterises the temperature of both particle populations. One can introduce a more general distribution function assuming that the second current-carrying population is characterised by a temperature different by a positive factor of η. The new distribution function $f_{\rm s}$ can be written in the following form:

$$f_{\rm s} = n_{0\rm s}\left(\frac{m_{\rm s}\beta_{\rm s}}{2\pi}\right)^{3/2} [e^{-\beta_{\rm s}H_{\rm s}}\exp(\beta_{\rm s}u_{y\rm s}p_{y\rm s}) +$$

$$+ a_{\rm s}\eta^{3/2}e^{-\eta\beta_{\rm s}H_{\rm s}}\cos(\eta\beta_{\rm s}u_{x\rm s}p_{x\rm s}) + b_{\rm s}\eta^{3/2}e^{-\eta\beta_{\rm s}H_{\rm s}}]. \tag{3.10}$$

The function $f_{\rm s}$ reduces to the function $f_{\rm s}^{\rm hn}$ (3.9) for $\eta = 1$. Similarly to the distribution function given by expression (3.9), the first term in f_s is identical to the Harris model, whereas the second term corresponds to the second current-carrying population with a different temperature. Basically, the distribution function of

the background plasma can be chosen arbitrarily, with only the positiveness of f_s required to be satisfied. In this work, the temperatures of the second current-carrying and background populations are assumed to be the same. In this case the condition $b_\mathrm{s} > a_\mathrm{s}$ ensures the positiveness of the function f_s over the entire phase space $(\mathbf{v}, \mathbf{r})$.

Substitution of distribution function (3.10) into Eq. (3.3) allows one to calculate a new pressure function P_{zz}:

$$P_{zz}(A_x, A_y, \varphi) = \sum_{\mathrm{s=i,e}} \beta_\mathrm{s}^{-1} n_{0\mathrm{s}} G_\mathrm{s}(A_x, A_y, \varphi), \tag{3.11}$$

where

$$G_\mathrm{s} = e^{-\beta_\mathrm{s} q_\mathrm{s} \varphi} \exp(\beta_\mathrm{s} q_\mathrm{s} u_{y\mathrm{s}} A_y) \exp(\beta_\mathrm{s} m_\mathrm{s} u_{y\mathrm{s}}^2/2) +$$

$$+ a_\mathrm{s} \eta^{-1} e^{-\eta \beta_\mathrm{s} q_\mathrm{s} \varphi} \exp\left(-\beta_\mathrm{s} m_\mathrm{s} \eta u_{x\mathrm{s}}^2/2\right) \cos(\eta \beta_\mathrm{s} u_{x\mathrm{s}} q_\mathrm{s} A_x) + b_\mathrm{s} \eta^{-1} e^{-\eta \beta_\mathrm{s} q_\mathrm{s} \varphi}.$$

The total electric charge density σ can be determined as a function of A_x and A_y by taking the derivative of the pressure P_{zz} given by Eq. (3.11), with respect to the electric potential φ [see Schindler, 2006]:

$$\sigma = -\frac{\partial P_{zz}}{\partial \varphi} = \sum_{\mathrm{s=i,e}} q_\mathrm{s} n_{0\mathrm{s}} N_\mathrm{s}(A_x, A_y, \varphi), \tag{3.12}$$

where $n_{0\mathrm{s}} N_\mathrm{s}$ is the density of the species s, and N_s is determined as

$$N_\mathrm{s} = e^{-\beta_\mathrm{s} q_\mathrm{s} \varphi} \exp(\beta_\mathrm{s} q_\mathrm{s} u_{y\mathrm{s}} A_y) \exp(\beta_\mathrm{s} m_\mathrm{s} u_{y\mathrm{s}}^2/2) +$$

$$+ a_\mathrm{s} e^{-\eta \beta_\mathrm{s} q_\mathrm{s} \varphi} \exp\left(-\beta_\mathrm{s} m_\mathrm{s} \eta u_{x\mathrm{s}}^2/2\right) \cos(\eta \beta_\mathrm{s} u_{x\mathrm{s}} q_\mathrm{s} A_x) + b_\mathrm{s} e^{-\eta \beta_\mathrm{s} q_\mathrm{s} \varphi}.$$

Applying the quasi-neutrality condition $\sigma = 0$, satisfied by $N_\mathrm{i}(A_x, A_y, \varphi) = N_\mathrm{e}(A_x, A_y, \varphi)$, one can determine the transverse profile of the scalar potential φ. In the case when φ does not vanish, the initial assumption that $P_{zz}(A_x, A_y)$ is an additive function, i.e. $P_{zz} = P_1(A_x) + P_2(A_y)$, cannot be fulfilled. This study is therefore focused on a particular class of models satisfying the exact neutrality condition with $\varphi = 0$, imposing the following relations between the microscopic

parameters of the ion and electron distribution functions:

$$\begin{aligned} n_{0\mathrm{e}}\exp(\beta_\mathrm{e} m_\mathrm{e} u_{y\mathrm{e}}^2/2) &= n_{0\mathrm{i}}\exp(\beta_\mathrm{i} m_\mathrm{i} u_{y\mathrm{i}}^2/2) \equiv n_0, \\ a_\mathrm{e} n_{0\mathrm{e}}\exp\left(-\beta_\mathrm{e} m_\mathrm{e}\eta u_{x\mathrm{e}}^2\right) &= a_\mathrm{i} n_{0\mathrm{i}}\exp\left(-\beta_\mathrm{i} m_\mathrm{i}\eta u_{x\mathrm{i}}^2\right) \equiv a_0, \\ b_\mathrm{e}\exp(-\beta_\mathrm{e} m_\mathrm{e} u_{y\mathrm{e}}^2/2) &= b_\mathrm{i}\exp(-\beta_\mathrm{i} m_\mathrm{i} u_{y\mathrm{i}}^2/2) \equiv b_0, \\ -\beta_\mathrm{e} u_{x\mathrm{e}} = \beta_\mathrm{i} u_{x\mathrm{i}}, &\qquad -\beta_\mathrm{e} u_{y\mathrm{e}} = \beta_\mathrm{i} u_{y\mathrm{i}}. \end{aligned}$$

If one of these conditions is violated, the electrostatic field appears, and the developed approach becomes inapplicable. Taking these relations into account, one finds that the pressure P_{zz} of the neutral plasma can be re-written in the following form:

$$P_{zz} = \left(\beta_\mathrm{e}^{-1} + \beta_\mathrm{i}^{-1}\right) n_0[\exp(-e\beta_\mathrm{e} u_{y\mathrm{e}} A_y) + a_0\eta^{-1}\cos(\eta e\beta_\mathrm{e} u_{x\mathrm{e}} A_x) + b_0\eta^{-1}]. \quad (3.13)$$

Direct comparison of (3.13) with (3.8) allows one to establish the following relations between the microscopic and macroscopic parameters of the model:

$$B_0^2 = 8\pi n_0\left(\beta_\mathrm{e}^{-1} + \beta_\mathrm{i}^{-1}\right), \quad (3.14)$$

$$a_0 = \eta/2,\ b_0 = 8\eta\pi P_0/B_0^2,\ u_{y\mathrm{s}} = \eta u_{x\mathrm{s}}, \quad (3.15)$$

$$\lambda = \left[2\pi n_0 e^2 u_{y\mathrm{e}}^2\beta_\mathrm{e}^2(\beta_\mathrm{i}^{-1} + \beta_\mathrm{e}^{-1})\right]^{-1/2}. \quad (3.16)$$

Equation (3.16) is of a special importance, as it links the CS thickness λ to the parameters of the equilibrium distribution function (3.10). This, in turn, provides a relation between the force-free coefficient $\alpha(z) = (c/4\pi)[\lambda\cosh(\mathrm{z}/\lambda)]^{-1}$ (defined as $\mathbf{j} = \alpha\mathbf{B}$, see Eqs. (3.4)–(3.5)) and the microscopic parameters of the distribution function.

In Eq. (3.12), the plasma density $n = n_{0\mathrm{i}}N_\mathrm{i} = n_{0\mathrm{e}}N_\mathrm{e}$ is determined as

$$n = n_0\left[\exp(e\beta_\mathrm{i} u_{y\mathrm{i}} A_y) + a_0\cos(\eta e\beta_\mathrm{i} u_{x\mathrm{i}} A_x) + b_0\right].$$

Using the explicit dependencies $A_{x,y}(z)$ given by Eqs. (3.6) and (3.7), one obtains the explicit expression for the plasma density $n(z)$:

$$n(z) = n_0\left(\frac{\eta}{2} + b_0\right) + n_0(1-\eta)\cosh^{-2}(z/\lambda). \quad (3.17)$$

The plasma density can also be written as $n = n_1 + n_2$, where $n_1 = n_0\cosh^{-2}(z/\lambda)$ is the density of the first current carrying population, while $n_2 = n_0 b_0 + n_0\eta[1/2 - \cosh^{-2}(z/\lambda)]$ is the combined density of the second current-carrying population and background population. The density of the first population peaks in the central

region of the CS, while the total density of other populations has a minimum there. These separate populations still correspond to the same plasma species. Substitution of Eqs. (3.6) and (3.7) into Eq. (3.13) allows one to calculate the explicit value of the pressure P_{zz}, which is uniform according to the force-free condition:

$$P_{zz} = n_0 \eta^{-1} \left(\beta_{\rm e}^{-1} + \beta_{\rm i}^{-1}\right) \left(\frac{\eta}{2} + b_0\right). \tag{3.18}$$

Equation (3.18) together with (3.17) gives the variation of the plasma temperature $T = P_{zz}/n(z)$ across the CS:

$$T(z) = \frac{\eta^{-1} \left(\beta_{\rm i}^{-1} + \beta_{\rm e}^{-1}\right) \cosh^2(z/\lambda)}{2(1-\eta)/(\eta + 2b_0) + \cosh^2(z/\lambda)}. \tag{3.19}$$

One can clearly see that the plasma temperature (3.19) and density (3.17) transverse profiles are uniform ($n = n_0\,(1/2 + b_0)$ and $T = \beta_{\rm i}^{-1} + \beta_{\rm e}^{-1}$) only in the case $\eta = 1$, consistent with the original model of Harrison and Neukirch [2009b]. In the case when the temperatures of the current-carrying populations are different, i.e. $\eta \neq 1$, the plasma temperature and density profiles become non-uniform. The case when $\eta > 1$ ($\eta < 1$) describes a CS with the first current-carrying population hotter (colder) than the second population. The density and temperature profiles normalised to their values at the CS boundary $n_0(\eta/2 + b_0)$ and $\eta^{-1}(\beta_{\rm e}^{-1} + \beta_{\rm i}^{-1})$, respectively, are illustrated in Figs. 3.2 and 3.3. To keep the distribution function given by Eq. (3.10) positive, the density of the background population should be set appropriately. The condition $b_0 > a_0 = \eta/2$ ensures that the distribution function is positive over the entire phase space $(\mathbf{v}, \mathbf{r})$.

In Fig. 3.2 the parameter $b_0 = 10$ is fixed and the density and temperature profiles are illustrated for various values of the parameter η ($\eta < 2b_0$). For $\eta > 1$ the temperature peaks at the CS central region, while the density is depleted so that the plasma pressure P_{zz} is uniform (as it should be for a force-free CS). Larger values of the parameter η result in a stronger plasma density depletion in the CS central region. We note that in the limiting case $\eta \gg 1$ and $b_0 \approx \eta/2$ (not illustrated in Fig. 3.2 where the parameter b_0 is fixed), the plasma density in the central region of the CS asymptotically tends to a small value. The temperature peak in the CS central region forms due to the first current-carrying population which is hotter than the second population (in the case $\eta > 1$) and localised near the CS central region (as $n_1 = n_0 \cosh^{-2}(z/\lambda)$). The density of the second, colder, current-carrying population increases towards the CS boundary leading to the plasma temperature decrease.

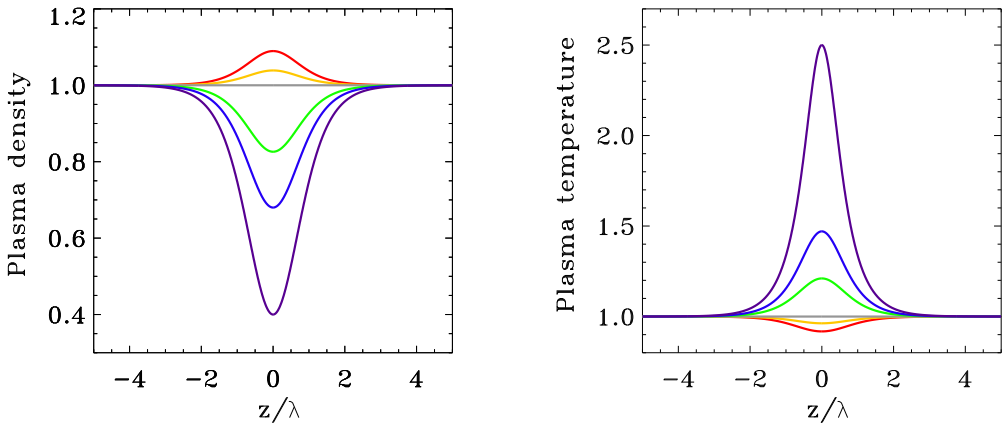

Figure 3.2: Density and temperature profiles across a current sheet, determined by Eqs. (3.17) and (3.19), plotted for $b_0 = 10$ and $\eta = 0.1$ (red lines), $\eta = 0.6$ (orange lines), $\eta = 1$ (grey lines), $\eta = 3$ (green lines), $\eta = 5$ (blue lines), $\eta = 10$ (purple lines). The plasma density profile is normalised to $n_0(\eta/2 + b_0)$. The temperature profile is normalised to $(\beta_\mathrm{i} + \beta_\mathrm{e})/\eta\beta_\mathrm{i}\beta_\mathrm{e}$.

For $\eta < 1$ the first current-carrying population is colder than the second population. In contrast to the previous case, Fig. 3.2 shows that the plasma temperature has a minimum in the CS central region, while the plasma density peaks therein. The density peak is larger for smaller values of η. In the limiting case $\eta \approx 0$, the density variation across the CS is less than ten percent of the plasma density at the CS boundary. Equation (3.17) shows that for $\eta \approx 0$ the plasma density in dimensionless units is $n(z) = 1 + b_0^{-1}\cosh^{-2}(z/\lambda)$, so that ten percent density variation corresponds to $b_0 = 10$, i.e. to the assumed density of the background population.

In Fig. 3.3 the temperature ratio η is fixed to a small value $\eta = 0.1$, implying the second current-carrying population to be ten times hotter than the first one. In turn, the density of the background population b_0 is varied, satisfying the condition $b_0 > \eta/2$ to ensure the positiveness of the distribution functions (3.10). Smaller values of the background population density are found to result in a larger variation of the plasma density across the CS. In particular, for $b_0 = 0.1$ the plasma density (temperature) in the CS central region is ten times larger (smaller) than at the CS boundary. In the limit $b_0 \gg 1$ the plasma density and temperature become approximately uniform across CS.

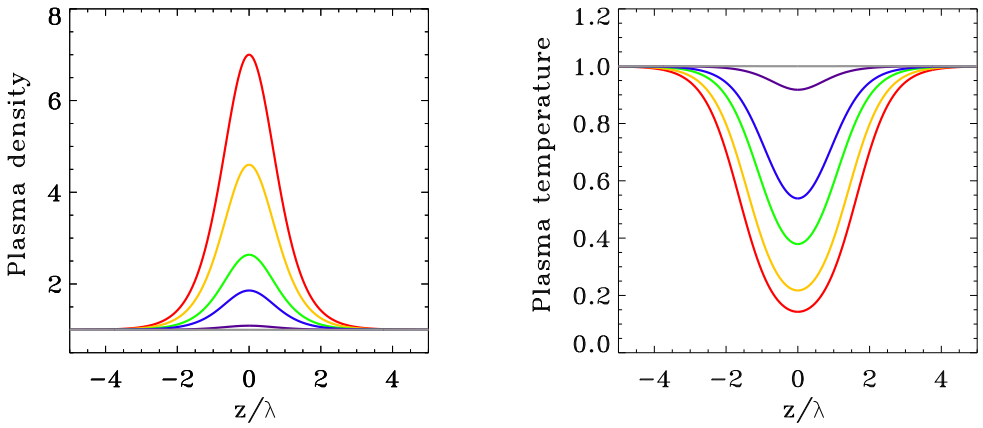

Figure 3.3: Density and temperature profiles across a current sheet, determined by Eqs. (3.17) and (3.19), plotted for $\eta = 0.1$ and for various values of the background plasma density: $b_0 = 0.1$ (red lines), $b_0 = 0.2$ (orange lines), $b_0 = 0.5$ (green lines), $b_0 = 1$ (blue lines), $b_0 = 10$ (purple lines). The limit $b_0 \gg 1$ is shown by the horizontal grey lines. The plasma density profile is normalised to $n_0(\eta/2 + b_0)$. The temperature profile is normalised to $(\beta_\mathrm{i} + \beta_\mathrm{e})/\eta\beta_\mathrm{i}\beta_\mathrm{e}$.

3.1.3 Discussion and conclusions

The 1D model of equilibrium force-free CSs is developed, taking into account density and temperature variations across the CS that can arise in realistic natural and laboratory plasma systems either due to the boundary conditions or Ohmic heating in the region of the enhanced current density localisation. The latter process should be slow enough to consider the developed model as quasi-stationary. One of the motivations for this work was a shortcoming of the model by Harrison and Neukirch [2009b], which only provides uniform density and temperature profiles, and does not inform whether inhomogeneous profiles of the plasma parameters consistent with MHD solutions are possible. In fact, it is clear that as the CS thickness becomes larger than characteristic kinetic scales, it should be possible to set arbitrary density and temperature profiles across the CS, while maintaining a constant plasma pressure. In contrast to force-free CSs with a finite B_z component, where the field lines are curved and cross the entire CS [e.g. Vasko et al., 2014], preventing arbitrary transverse distributions of plasma parameters even in the MHD limit, in the models designed here without a regular B_z the field lines are straight and "tied" each to a certain z coordinate. The plasma parameters can therefore be set arbitrarily along each field line satisfying the condition of total pressure balance,

not only in the MHD limit, i.e. when the CS thickness is much larger than kinetic scales, but in the kinetic regime too.

In the proposed model the plasma density and temperature may either increase or decrease in the CS central region. Such configurations can be found in a number of astrophysical and space plasma systems, in particular in solar coronal streamers and in macroscopic CSs over the reconnection sites in solar flares [see e.g. Sec. 1.2.1 and Li et al., 2016]. The force-free CS models with the plasma density peaked in the CS central region, developed here, represent effective waveguides for MHD waves. Specifically, regions of decreased Alfvén speed are fast magnetoacoustic waveguides. Currently, coronal MHD seismology studies assume that CSs are described by the Harris model [e.g. Smith et al., 1997; Jelínek and Karlický, 2012; Mészárosová et al., 2014], where the plasma β is infinite in the CS central region (where the magnetic field vanishes), and drops to some small values at the CS boundary. In the force-free models developed in this section, the plasma β is always constant across the CS, and is given by $\beta = 8\pi P_{zz}/B_0^2 = 1/2 + b_0/\eta$, according to Eq. (3.18) and using the relation $B_0^2 = 8\pi n_0(\beta_\mathrm{i}^{-1} + \beta_\mathrm{e}^{-1})$. Taking into account that $b_0 > \eta/2$ to ensure the positiveness of the particle distribution functions, one finds that in the developed force-free CSs the parameter $\beta > 1$. Thus, the properties of MHD waves guided by such a CS should be different from those in the Harris model [Jelínek and Karlický, 2012; Mészárosová et al., 2014]. The properties of MHD waves in such a force-free configuration are worth considering and may be used for MHD seismology purposes [Nakariakov and Ofman, 2001; De Moortel and Nakariakov, 2012].

3.2 Nonlinear oscillations of coalescing magnetic flux ropes

3.2.1 Introduction

An important phenomenon is a coalescence of two magnetic islands, which occurs in the interaction of two twisted magnetic flux tubes (ropes) of the same sign of helicity. This process is believed to occur in very different plasma environments, for instance the solar corona [e.g. Kliem et al., 2000; Nakariakov et al., 2016b], the Earth's magnetosphere [e.g. Ma and Bhattacharjee, 1999; Nakariakov et al., 2016b], magnetar atmospheres [e.g. Uzdensky, 2011], and laboratory plasmas [e.g. Ono et al., 1987]. Dynamical processes in current sheets (CS) which may be formed by the coalescence, have interesting observational manifestations, in particular various oscillations de-

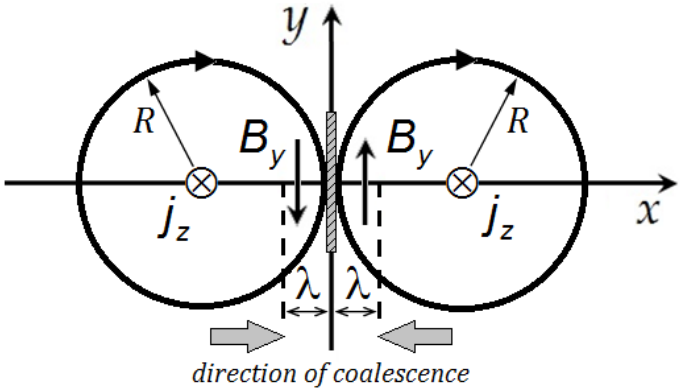

Figure 3.4: Formation of a thin 1.5D current sheet (the hatched vertical slab) by coalescence instability. j_z – z-component of the plasma current generating the poloidal magnetic field; λ – scale length of the poloidal magnetic field B_y where the field lines can be considered as straight, λ is small in comparison with the radii of the colliding magnetic ropes R.

tected remotely and *in situ* [e.g. Sergeev et al., 2003; Bárta et al., 2008; Nakariakov and Melnikov, 2009; Karlický, 2014; Li et al., 2016]. An analytical two-fluid model of the nonlinear stage of the coalescence process, designed by Tajima et al. [1987] predicts a highly-nonlinear oscillatory regime (see Sec. 1.2.2).

In the model of Tajima et al. [1987] (see Fig. 3.4) two co-aligned plasma currents j_z generate poloidal magnetic fields which are oppositely directed along the y-axis in the region of the coalescence, which thus becomes a CS. It was numerically found that in the explosive regime of the coalescence there appears a specific spatial scale λ of the poloidal magnetic field (small in comparison with the radii of the colliding magnetic ropes, R), where the field lines can be considered as straight, and the CS can be considered as one-dimensional. Hence for transverse oscillations of the CS, one can take that $\partial/\partial x \gg \partial/\partial y, \partial/\partial z$ and $\nabla = \{\partial/\partial x, 0, 0\}$. The oscillation could be described by perturbations of the electric field $\mathbf{E} = \{E_x, 0, E_z\}$ and magnetic field $\mathbf{B} = \{0, B_y, 0\}$, the bulk plasma velocities of ion and electron plasma species $\mathbf{V}_{\mathrm{i,e}} = \{V_{x\,\mathrm{i,e}}, 0, V_{z\,\mathrm{i,e}}\}$, and the variations of the ion n_i and electron n_e concentrations. In this definition of the electric field $\mathbf{E}$, the x-component E_x is related to the electrostatic field generated by the electric charge separation according to Poisson's law, while the z-component E_z is the induced electric field by Faraday's law. Dynamics of these quantities is governed by two–fluid hydrodynamic equations and Maxwell equations.

In Tajima et al. [1987] self-similar solutions of the governing equations were

obtained by introducing dimensionless time-dependent scale factors $a = a(t)$ and $b = b(t)$ separately for electron and ion dynamics, respectively, connected with the plasma species concentrations as $n_\mathrm{e} = n_0/a$, and $n_\mathrm{i} = n_0/b$, where $n_0 = n_{0\mathrm{e}} = n_{0\mathrm{i}}$ is the equilibrium concentration. Tajima et al. [1987] obtained an analytical solution of the problem only for the limiting case when $a = b$, and, hence, the electron and ion plasma concentrations were taken to be always strictly equal to each other, $n_\mathrm{e} = n_\mathrm{i}$. The electrostatic field E_x was considered to be non-zero, which is a crucial condition for the oscillatory behaviour of the CS, generated by this mechanism. Strictly speaking, this so-called quasi-neutrality assumption is valid only for low-frequency processes. However, the model contains the non-zero value of the electron mass m_e, as well as the finite values of the electron and ion plasma frequencies, ω_e and ω_i. Hence, it would be natural to expect that the model also describes high-frequency oscillations, where the electric charge separation effects are important.

In this section based on the work by Kolotkov et al. [2016b], the possibility of a nonlinear oscillatory regime of the evolution of a CS formed by a coalescence of two magnetic ropes without the quasi-neutrality condition, is demonstrated. The scale factors $a(t)$ and $b(t)$ are considered to be not equal to each other, i.e. local electric charge separation is allowed. The new solution covers both low-frequency oscillations, including the limiting case $n_\mathrm{e} = n_\mathrm{i}$ considered by Tajima et al. [1987], and the high-frequency case where the electric charge separation cannot be neglected.

3.2.2 Analysis

Under the simplifying assumptions described above, it was shown in Tajima et al. [1987] that the evolution of a CS is governed by the following equations (namely, Eqs. (23) and (24) in Tajima et al. [1987]):

$$\frac{\mathrm{d}^2 a}{\mathrm{d}\, t^2} = -\omega_\mathrm{e}^2 \left(\frac{a}{b} - 1\right) - \frac{m_\mathrm{i}}{m_\mathrm{e}} \frac{C_\mathrm{A}^2}{\lambda^2 a^2} + \frac{m_\mathrm{i}}{m_\mathrm{e}} \frac{C_\mathrm{s}^2}{\lambda^2 a^\gamma}, \tag{3.20}$$

$$\frac{\mathrm{d}^2 b}{\mathrm{d}\, t^2} = \omega_\mathrm{i}^2 \left(1 - \frac{b}{a}\right), \tag{3.21}$$

where $\omega_{\mathrm{e,i}}^2 = 4\pi n_0 e^2/m_{\mathrm{e,i}}$ are electron and ion plasma frequencies; $C_\mathrm{A}^2 = B_0^2/4\pi m_\mathrm{i} n_0$ is the Alfvén speed squared, with B_0 and n_0 being the equilibrium values of the poloidal magnetic field and plasma concentration; $C_\mathrm{s}^2 = P_0/m_\mathrm{i} n_0$ is the sound speed squared, with P_0 being the equilibrium thermodynamical gas pressure; γ is the adiabatic constant; and λ, in the spirit of the previous Sec. 3.1, is the thickness of the CS. The magnetic field is assumed to be strong enough, so the ionic β is sufficiently small allowing for the neglecting of the ion temperature, hence the pressure P_0 is

associated with the electron temperature.

Introducing a small parameter $\epsilon = \omega_{\rm i}^2/\omega_{\rm e}^2 = m_{\rm e}/m_{\rm i}$ and the normalised time $s = t\omega_{\rm i}$, one can re-write Eqs. (3.20) and (3.21) as

$$\frac{\mathrm{d}^2 a}{\mathrm{d}\, s^2} = -\frac{1}{\epsilon}\left\{\frac{a}{b} - 1 + \frac{\phi}{a^2} - \frac{\psi}{a^\gamma}\right\}, \tag{3.22}$$

$$\frac{\mathrm{d}^2 b}{\mathrm{d}\, s^2} = 1 - \frac{b}{a}, \tag{3.23}$$

where $\phi = \left(C_{\rm A}/\lambda\omega_{\rm i}\right)^2$ and $\psi = \left(C_{\rm s}/\lambda\omega_{\rm i}\right)^2$ are dimensionless constants.

Using the static solution of (3.22)–(3.23) obtained for $\mathrm{d}/\mathrm{d}\, s = 0$,

$$\bar{a} = \bar{b} = \left(\frac{\phi}{\psi}\right)^{\frac{1}{2-\gamma}} = \left(\frac{C_{\rm A}^2}{C_{\rm s}^2}\right)^{\frac{1}{2-\gamma}} = \left(\frac{B_0^2}{4\pi P_0}\right)^{\frac{1}{2-\gamma}}, \tag{3.24}$$

and normalising (3.22)–(3.23) to the dimensionless value $\bar{a}$, one can re-write Eqs. (3.20)–(3.21) as:

$$\frac{\mathrm{d}^2 A}{\mathrm{d}\,\tau^2} = -\frac{1}{\epsilon}\left\{\frac{A}{B} - 1 + \frac{\bar{\phi}}{A^2} - \frac{\bar{\phi}}{A^\gamma}\right\}, \tag{3.25}$$

$$\frac{\mathrm{d}^2 B}{\mathrm{d}\,\tau^2} = 1 - \frac{B}{A}, \tag{3.26}$$

with $a(s) = \bar{a}\, A(\tau)$, $b(s) = \bar{a}\, B(\tau)$, $s = \bar{a}^{1/2}\tau$, and $\phi = \bar{a}^2\, \bar{\phi}$. In this normalisation the quantities A and B are equal to unity at the initial instant of time, $A(0) = B(0) = 1$.

Nonlinear analysis with the Bernoulli pseudopotential

As ϵ tends to 0, for the left-hand side of Eq. (3.25) to be finite, the term {..} on the right-hand side must tend to zero too. This condition in turn allows one to determine the explicit dependence $B\,(A)$:

$$B\,(A) = \frac{A^{\gamma+3}}{A^{\gamma+2} - \bar{\phi}(A^\gamma - A^2)}, \tag{3.27}$$

which reduces to $A = B$ in the limit considered by [Tajima et al., 1987] for small values of the parameter $\bar{\phi}$.

Substitution of (3.27) into (3.26) leads to the second-order ordinary differential equation (ODE) for the function $A(\tau)$:

$$f(A)\frac{\mathrm{d}^2 A}{\mathrm{d}\,\tau^2} + \frac{\mathrm{d}\, f(A)}{\mathrm{d}\, A}\left(\frac{\mathrm{d}\, A}{\mathrm{d}\,\tau}\right)^2 = g(A), \tag{3.28}$$

where the functions $f(A)$ and $g(A)$ are defined as:

$$f(A) = \frac{A^{2(\gamma+2)} - 3\bar{\phi}A^{2(\gamma+1)} + \bar{\phi}(\gamma+1)A^{\gamma+4}}{\left(A^{\gamma+2} - \bar{\phi}A^{\gamma} + \bar{\phi}A^{2}\right)^{2}}, \tag{3.29}$$

$$g(A) = 1 - \frac{A^{\gamma+2}}{A^{\gamma+2} - \bar{\phi}A^{\gamma} + \bar{\phi}A^{2}}. \tag{3.30}$$

Equation (3.28) describes an oscillatory evolution of the CS. Writing $p(A) = \mathrm{d}A/\mathrm{d}\tau$ allows one to reduce the second-order ODE (3.28) to the first-order Bernoulli equation:

$$f(A)\frac{\mathrm{d}\,p(A)}{\mathrm{d}\,A} + \frac{\mathrm{d}\,f(A)}{\mathrm{d}\,A}p\,(A) = \frac{g(A)}{p(A)}, \tag{3.31}$$

with the first integral

$$\frac{1}{2}\left[f(A)\frac{\mathrm{d}\,A}{\mathrm{d}\,\tau}\right]^{2} + U_{\mathrm{B}}(A) = \mathrm{const}, \tag{3.32}$$

allowing for the application of the mechanical analogy method. Indeed, considering A and τ as a generalised spatial coordinate and time, respectively, Eq. (3.32) has the form of a conservation energy law with a generalised potential energy $U_{\mathrm{B}}(A)$, also called the Bernoulli pseudopotential:

$$U_{\mathrm{B}}(A) = -\int_{1}^{A} f(A)g(A)\,\mathrm{d}A. \tag{3.33}$$

Analysis of second-order ODEs with the Bernoulli pseudopotential technique [Dubinov and Sazonkin, 2010] is a recent extension of the Sagdeev potential method used, in particular, in Tajima et al. [1987]. In contrast to the Sagdeev method, this approach allows one to analyse a broader class of second-order ODEs with a squared first derivative, as it appears in Eq. (3.28). The importance of the Bernoulli technique in this work and its ability to analyse the corresponding type of ODEs should be additionally emphasised, as it is crucial for the solution of the general problem with $A \neq B$ [cf. Tajima et al., 1987]. In the mechanical analogy given by (3.32) the function $f^2(A)$ acts as an effective mass, and the oscillating "particle" position is governed by the potential $U_{\mathrm{B}}(A)$. In Tajima et al. [1987] where the particular case $A = B$ was considered, the mass function is a constant, and the Bernoulli potential reduces to the Sagdeev potential. More details about the Bernoulli pseudopotential technique and examples of its application to analysis of nonlinear ion–acoustic waves and super-nonlinear shear Alfvén waves in multi-component plasmas can be found in Dubinov and Sazonkin [2010]; Dubinov et al. [2011, 2012a,b], and in references

therein. Applications of the Bernoulli pseudopotential method to the analysis of nonlinear fluctuations in self-gravitating quantum plasmas and in two- and three-dimensional graphene-like fluids are shown in Akbari-Moghanjoughi [2014, 2013], respectively.

Small amplitude limit

A solution of Eq. (3.28) is obtained by considering the function $A(\tau)$ to be of a small amplitude and with the initial value of unity: $A(\tau) = 1 + \varepsilon x(\tau)$. In this first-order expansion ε is a small parameter, and $x(\tau)$ characterises the small amplitude variations of the function $A(\tau)$. Substitution of this expansion to Eqs. (3.29) and (3.30) gives, up to the first order of ε:

$$g = \varepsilon x \bar{\phi}(2-\gamma). \tag{3.34}$$

$$f = 1 - \bar{\phi}(2-\gamma) + \varepsilon x \bar{\phi}\{6 - \gamma(\gamma+1) - 2(2-\gamma)[1-\bar{\phi}(2-\gamma)]\}, \tag{3.35}$$

Using (3.34)–(3.35) to re-write Eq. (3.28), and neglecting the terms higher than the first order of ε, one obtains

$$\frac{\mathrm{d}^2 x}{\mathrm{d}\tau^2} + \frac{\bar{\phi}(2-\gamma)}{\bar{\phi}(2-\gamma)-1} x = 0. \tag{3.36}$$

Equation (3.36) is a harmonic oscillator equation, with the period

$$P = 2\pi \left[1 + \bar{\phi}^{-1}(\gamma-2)^{-1}\right]^{1/2} \tag{3.37}$$

in normalised units. For $\gamma = 3$, the expression reduces to $P = 2\pi\left(1+\bar{\phi}^{-1}\right)^{1/2}$, and tends to 2π for large values of $\bar{\phi}$.

3.2.3 Nonlinear oscillations

Consider specific examples of the Bernoulli pseudopotential energy $U_{\mathrm{B}}(A)$ given by Eq. (3.33) and the corresponding numerical solutions of Eq. (3.28) for various combinations of the initial parameters. Figure 3.5 shows that U_{B} has a minimum at the point $A = 1$, corresponding to the stable equilibrium state of the CS, determined by static solution (3.24). Such a profile allows for the existence of both linear and nonlinear periodic solutions of Eq. (3.28) above the equilibrium. Two different cases of U_{B} were found: when its left-hand, with respect to the minimum, slope reaches the maximum value faster than the right-hand slope, and the other case when the right-hand slope reaches the maximum faster. The behaviour is prescribed by the

value of the parameter $\bar{\phi}$. The threshold value of $\bar{\phi}$ which determines when $U_{\rm B}$ changes the behaviour, is about 0.685. At that value of $\bar{\phi}$ the maximum values of the left-hand and right-hand slopes of $U_{\rm B}$ are nearly same.

Figure 3.6 shows the time variations of the plasma species concentrations $n_{\rm e}$ and $n_{\rm i}$, obtained numerically from Eq. (3.28), and corresponding to the different cases of $U_{\rm B}$ shown in Fig. 3.5. As follows from Eq. (3.27), the charge separation reaches a large value for large values of $\bar{\phi}$, and is almost negligible for small $\bar{\phi}$. Top panels of Fig. 3.6 demonstrate two essentially opposite limits: small amplitude quasi-linear oscillations obtained near the bottom of the potential well where it can be approximated by a parabolic function; and large amplitude nonlinear oscillations obtained near the limit height of $U_{\rm B}(A)$ (see Fig. 3.5). The total energy of oscillations of a pseudo-particle in a pseudopotential well is determined by the initial value of the first derivative of a generalised coordinate with respect to a generalised time, meaning the kinetic energy of an initial excitation in Eq. (3.32). In this study non-zero values of the first derivatives used as the initial conditions for Eq. (3.28) correspond to the initial speed of the coalescing ropes.

According to Eq. (3.37), for small amplitudes, the oscillation period grows to arbitrarily long values for small $\bar{\phi}$, while for large $\bar{\phi}$ the period tends to the constant value $2\pi(C_{\rm s}/C_{\rm A})^{1/2}\omega_{\rm i}^{-1}$ in physical units. Figure 3.5, bottom panels show the dependence of the period on the amplitude of the electron concentration variations, $\delta n_{\rm e}$, in the nonlinear regime. For $\bar{\phi} < 0.685$ the period is highly dependent upon the amplitude. For $\bar{\phi} > 0.685$ the oscillations are almost isochronous (their period depends weakly upon the amplitude even in the nonlinear regime), that can be explained by the shape of the function $U_{\rm B}\,(A)$ with the corresponding value of $\bar{\phi} = 5$ (see Fig. 3.5, top right panel). Indeed, when $\bar{\phi} = 5$, the maximum value of the right-hand slope of $U_{\rm B}$ is located much above the left-hand one, which results in the almost symmetric shape of $U_{\rm B}$ in the regions supporting oscillations. Although dependence (3.37) was initially derived for the small amplitude linear solutions of Eq. (3.28), the isochronous nature of the illustrative examples in Figs. 3.5 and 3.6 allows one to utilise it for the nonlinear oscillations too, when large values of $\bar{\phi}$ are considered. For small $\bar{\phi}$ (when $\bar{\phi} < 0.685$, see Fig. 3.5) the shape of $U_{\rm B}$ allows for longer-period oscillations.

The electrostatic field $E_x\,(\tau)$ generated by the local charge separation with the use of Poisson's equation is given by:

$$E_x\,(\tau) = \frac{4\pi e n_0 \lambda}{\bar{a}} \left(\frac{1}{B\,(\tau)} - \frac{1}{A\,(\tau)} \right), \tag{3.38}$$

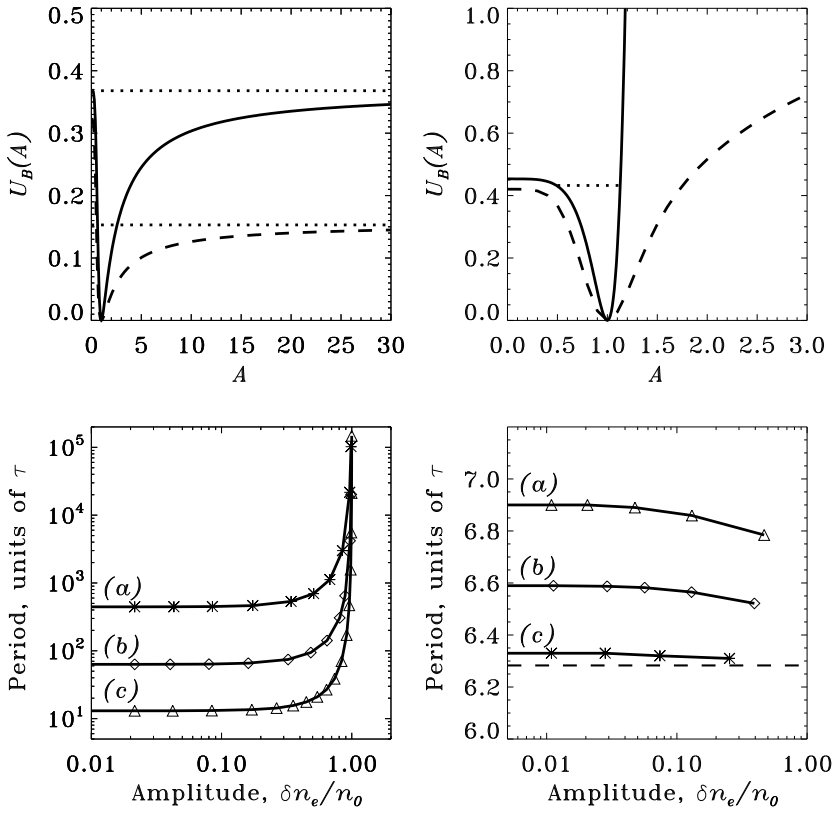

Figure 3.5: Top: Bernoulli pseudopotential $U_{\rm B}(A)$ (3.33) plotted for $\gamma = 3$ and for: $\bar{\phi} = 0.685$ (left solid), $\bar{\phi} = 0.3$ (left dashed); and $\bar{\phi} = 5$ (right solid), $\bar{\phi} = 2$ (right dashed). The upper horizontal dotted line in the left-hand panel shows the energy level above which $U_{\rm B}(A)$ experiences the change of behaviour, the bottom dashed line shows the energy level of the oscillation shown in Fig. 3.6, left bottom panel. The horizontal dotted line in the right-hand panel indicates the energy level of the nonlinear signal shown in Fig. 3.6, right top and bottom panels. Bottom: the oscillation period–amplitude dependence shown for $\bar{\phi} = 2 \times 10^{-4}\,(a),\ 10^{-2}\,(b),$ and $0.3\,(c)$ (the small $\bar{\phi}$ regime, left-hand panel); and for $\bar{\phi} = 5\,(a),\ 10\,(b),\ 100\,(c)$ (the large $\bar{\phi}$ regime, right-hand panel), and $\bar{\phi} \to \infty$ (the period equals to 2π, dashed line). The period is measured in the units of $(C_{\rm s}/C_{\rm A})^{1/2}\omega_{\rm i}^{-1}$.

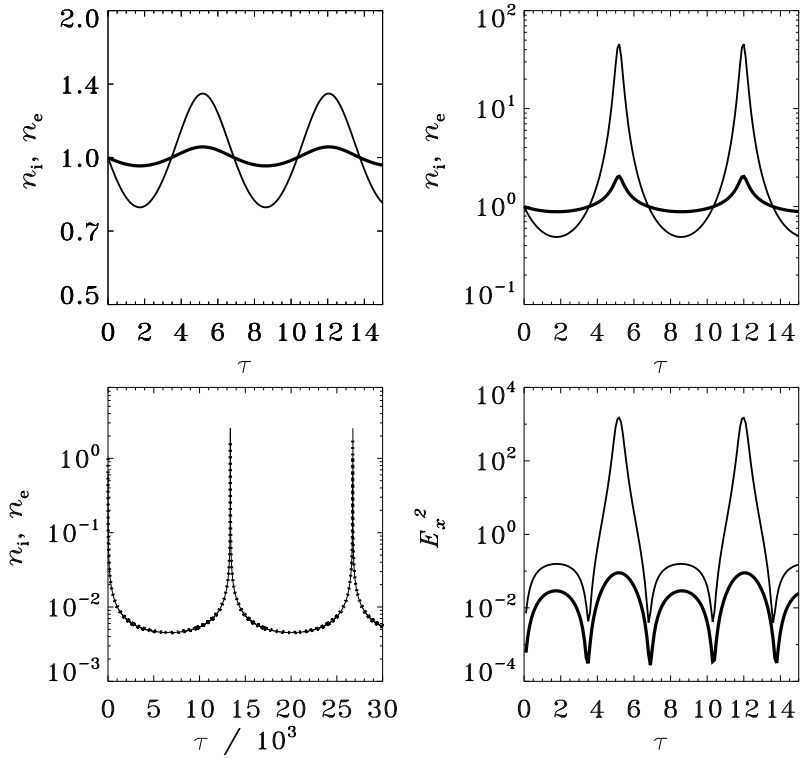

Figure 3.6: Top: variations of the electron $n_e = n_0/a$ (thick lines) and ion $n_i = n_0/b$ (thin lines) concentrations, where the scale factors a and b are obtained from the numerically obtained solutions $A(\tau)$ of Eq. (3.28) with $\gamma = 3$, $\bar{\phi} = 5$, $A(0) = 1$, and $\dot{A}(0) = 0.04$ (left-hand panel, quasi-linear oscillation); and $\dot{A}(0) = 0.155$ (right-hand panel, nonlinear oscillation). Bottom left: variations of n_e (dotted line) and n_i (solid line, almost indistinguishable from the dotted line) for $\gamma = 3$, $\bar{\phi} = 0.3$, $A\,(0) = 1$, and $\dot{A}(0) = 0.426$ (highly nonlinear case). Both functions n_e and n_i are normalised to $n_0\bar{a}^{-1}$. Bottom right: variation of the electrostatic field energy E_x^2 normalised to $(4\pi e n_0 \lambda \bar{a}^{-1})^2$, generated by the local charge separation, in the quasi-linear (thick line) and nonlinear (thin line) regimes of the current sheet oscillation, shown in the top panels. The vertical axes in all panels are plotted on a logarithmic scale. The time τ is measured in the units of $(C_s/C_A)^{1/2}\omega_i^{-1}$.

where $A(\tau)$ is obtained numerically from Eq. (3.28) (see Fig. 3.6), and $B(\tau)$ from Eq. (3.27). In Eq. (3.38) the expressions $n_0/\bar{a}_0 B$ and $n_0/\bar{a}_0 A$ correspond to the ion and electron concentrations, n_i and n_e, respectively.

While the cases with $\bar{\phi} < 0.685$ result in long-period oscillations with small local electric charge separation (see Fig. 3.6), and hence, give low values of the electric field E_x, larger values of $\bar{\phi}$ allow for short-period oscillations with large electric field (see Fig. 3.6). A small amplitude solution of Eq. (3.28) results in periodic small amplitude variations of E_x^2, which are still quasi-harmonic with a doubled period. In the nonlinear case, the oscillations have large amplitude spikes of the electric field with a clear asymmetry of the positive and negative half-periods. The highest electric field is generated during the positive half-periods of the density oscillations when the strongest charge separation occurs.

3.2.4 Discussion and conclusions

This work revealed a nonlinear oscillatory regime of the evolution of a CS formed by the coalescence of two magnetic flux ropes, which is accompanied by a significant electric charge separation and generation of strong electric field. The characteristic time scales are shorter than the time of magnetic reconnection that is neglected. Specific regimes of the oscillations are determined by the dimensionless parameter $\bar{\phi} = (C_\mathrm{A}/C_\mathrm{s})^6(\lambda_\mathrm{D}/\lambda)^2 \approx \beta^{-3}(\lambda_\mathrm{D}/\lambda)^2$ (3.25), where λ is the characteristic CS thickness, $\lambda_\mathrm{D} = C_\mathrm{s}/\omega_\mathrm{i}$ is the plasma Debye length, and β is the ratio of gas and magnetic pressures in the plasma. These nonlinear oscillations are rather intrinsic, and may occur in coalescence of magnetic islands in natural (e.g. solar, space, magnetospheric) and laboratory plasmas.

The solutions obtained for small values of the parameter $\bar{\phi} < 0.685$ describe perpendicular oscillations of the CS, when electrons and ions oscillate almost together and the effects of the local electric charge separation are negligibly small. The $\bar{\phi} = 0$ limit gives the solutions found by Tajima et al. [1987] for $n_\mathrm{e} = n_\mathrm{i}$. For sufficiently thin CSs (i.e. for $\lambda \approx \lambda_\mathrm{D}$) this regime is reached when the plasma is of sufficiently high β. For thicker sheets ($\lambda \gg \lambda_\mathrm{D}$) this regime can be achieved for smaller β. For $\bar{\phi} > 0.685$, the oscillations produce high spikes of the electric field caused by the electric charge separation. In both regimes, low amplitude oscillations have a harmonic shape, while high amplitude oscillations have a highly anharmonic shape: a series of distinct symmetric spikes.

In the small $\bar{\phi}$ regime, the nonlinear oscillation periods reach values that are several orders of magnitude larger than the ion plasma period (see Fig. 3.5). For example, for a 1 GHz electron plasma frequency and $C_\mathrm{A} \approx 4.8 \times 10^2\,\mathrm{km\,s^{-1}}$ and

$C_\mathrm{s} \approx 2.4 \times 10^2\,\mathrm{km\,s^{-1}}$ giving $C_\mathrm{s}/C_\mathrm{A} \approx 0.5$, typical for the coronal sites of solar flares [Nakariakov et al., 2003], the CS oscillation periods can reach one second or longer. Periods of this order of magnitude are often detected in the solar flare emission [e.g. Aschwanden, 1987; Nakariakov and Melnikov, 2009], and can appear, for example, in the gyrosynchrotron emission because of the modulation of the local electron plasma frequency (see Sec. 1.2.2). For lower values of β these periods can be reached for thicker CSs. In the previous example, if the CS thickness is about 1 Mm with the plasma Debye length of about 1 cm, the 1 s periods occur for the highly nonlinear large amplitude oscillations with $\delta n_\mathrm{e} \approx n_0$.

In the large $\bar{\phi}$ regime, oscillation periods are shorter than for small $\bar{\phi}$, and approach the value $2\pi(C_\mathrm{s}/C_\mathrm{A})^{1/2}\omega_\mathrm{i}^{-1}$. Thus, for low values of β, which are also observed in solar coronal plasma structures [e.g. $\beta \approx 0.01$, Zhang et al., 2015], for the electron plasma frequencies of about 0.4 GHz, typical periods of CS oscillations are of a few microseconds.

Chapter 4

Transverse oscillations of quiescent prominences in a magnetic field dip

4.1 Small amplitude oscillations and stability

4.1.1 Introduction

Coronal mass ejections are known to be the most powerful and geoeffective phenomena occurring in the solar atmosphere. An important role in their initiation is assigned to the evolution of prominences, cold and dense plasma clouds floating in the magnetised environment of the solar corona. The equilibrium of prominences is thought to be of a magnetic origin (e.g. Lorentz force), being able to counteract the gravity. In turn, gradient pressure forces can provide an additional support. Considering this basic idea, the following two-dimensional (2D) models of the prominence equilibrium were developed: the Kippenhahn–Schlüter [KS, Kippenhahn and Schlüter, 1957] and the Kuperus–Raadu models [KR, Kuperus and Raadu, 1974]. The KS model considers the prominence as a plasma slab embedded in a magnetic field with a dip created by some external sources (e.g. photospheric currents). The magnetic dip outlines the region of a magnetic polarity inversion, which justifies the general empirical evidence that prominences lie above the polarity inversion line (also called a neutral line) of large extended bipolar regions [e.g. Bosman et al., 2012]. In the KR model the prominence is assumed to be a straight current-carrying horizontal wire located at some height above the conductive photosphere. The support against the gravity is provided by an upward magnetic force acting on the prominence and caused by a virtual "mirror" current, which is located below the

photosphere and strictly symmetrical to the prominence. Interestingly, the magnetic topology associated with the KR model resembles that of a coronal cavity, that is a large quasi-circular structure observed off limb in the EUV band, and containing a prominence in its interior [Habbal et al., 2010; Gibson et al., 2010]. However, these models separately are not able to provide an exhaustive picture on transverse oscillations observed in prominences (see Sec. 1.3, where the observational evidence of oscillations in prominences and corresponding analytical models are described in detail). For example, the KR model alone allows only for vertically polarised oscillations, while in the pure KS model horizontally polarised oscillations cannot coexist with the vertically polarised ones since the system becomes unstable [van den Oord et al., 1998].

A synthesis of these two models, that is a prominence embedded in a magnetic field dip generated by two photospheric currents, accounting also for the effects of the prominence current interaction with the conducting photosphere is developed by Kolotkov et al. [2016c] and is presented in this chapter. The prominence is modelled as a line current located above the photosphere at a given height, thus being a subject to the gravity and Lorentz forces, which are attributed to the interaction between the photospheric and prominence currents. In this section, horizontally and vertically polarised transverse oscillations are analysed in the linear regime, the equations of motion are analytically derived, and dependence of the oscillation properties (e.g. the period) upon the parameters of the system (e.g. the currents in the prominence and at the photosphere) are determined. In addition, investigation of the mechanical stability of the system shows that the prominence can be stable simultaneously in both horizontal and vertical directions for a certain range of parameters.

4.1.2 Model, forces, and equilibrium

The magnetic field topology with a magnetic dip, shown in Fig. 4.1, is configured by two co-aligned spatially separated photospheric currents (with d being the half-distance between the currents) of the same magnitude, I. The prominence itself is modelled as a massive straight wire representing a magnetic rope with a current i which is located at some height h above the photosphere. It in turn causes a so-called "mirror" current (see the KR model) due to conductive properties of the photosphere. By its definition, the mirror current is oppositely directed with respect to the prominence current i, has the same magnitude, and is located at the distance $2\,h$ strictly below the prominence current (see Fig. 4.1). In this model the prominence can interact with the coronal surroundings through the corresponding mutual interaction of the magnetic fields produced by the prominence i and photospheric I

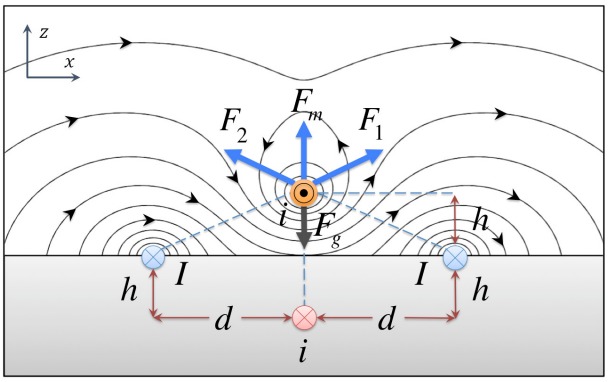

Figure 4.1: Sketch showing a massive prominence (the brown blob) with a line current i located at the height h above the photosphere, in the magnetic dip configured by two photospheric currents I, with d being the half-distance between the currents. The mirror current i (the pink blob) generated due to conductive properties of the photosphere is located strictly below the prominence. The field lines of the total magnetic field produced by the photospheric, mirror, and prominence sources are shown for $h = 0.5\,d$ and $i = 0.5\,I$.

currents.

The equilibrium of a prominence in such a magnetic environment is provided by the Lorentz and gravity force balance:

$$\mathbf{F}_1 + \mathbf{F}_2 + \mathbf{F}_\mathrm{m} + \mathbf{F}_\mathrm{g} = 0, \tag{4.1}$$

where $F_1 = F_2 = k_1/(d^2 + h^2)^{1/2}$ are the Lorentz forces per unit length acting between the photospheric currents I and the prominence current i, with $k_1 = \mu_0 I i/2\pi$; $F_\mathrm{m} = k_2/2\,h$ is the mirror force between the prominence and the mirror current, with $k_2 = \mu_0 i^2/2\pi$; and $F_\mathrm{g} = \rho g$ is the gravity force which is assumed to be constant in the model, with ρ being a linear mass density of the prominence (its volume mass density multiplied by the cross-sectional area), measured in $\mathrm{kg\,m^{-1}}$. Note, that according to the definition of the mirror current, the mirror force F_m acting on the prominence is always directed upwards and strictly along the vertical axis, and cannot contribute to horizontal dynamics of the prominence.

In fact, the system is completely defined by the geometrical parameters h and d, and magnetic constants k_1 and k_2 (written in terms of I and i), while the appropriate mass density ρ of the prominence necessary for its vertical equilibrium, is determined by the following condition (4.2). However, for seismological purposes it is also useful to re-write this condition through the parameters h and ρ, assuming

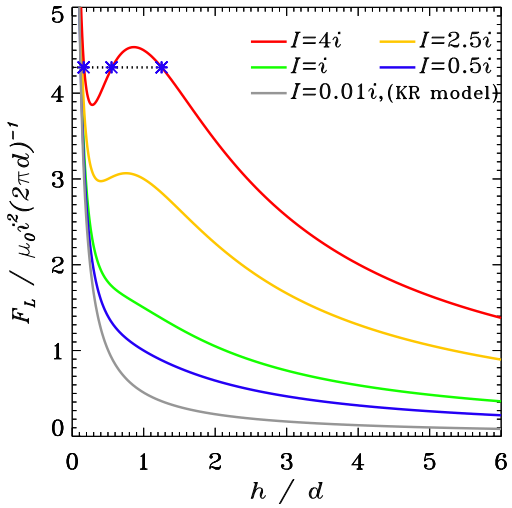

Figure 4.2: The magnetic force $F_{\rm L}$ (4.2) acting upwards on the equilibrium prominence for different values of the prominence i and photospheric I currents. The horizontal dotted line shows an example of the constant gravity force ρg needed to satisfy equilibrium condition (4.2). This example shows that the system may have up to three different equilibria (blue asterisks) depending upon values of the parameters of the model.

them to be available *a priori* from observations:

$$F_{\rm L} \equiv \frac{2k_1 h}{d^2+h^2} + \frac{k_2}{2h} = \rho g, \text{ and } d^2 = \frac{4k_1 h^2}{2\rho g h - k_2} - h^2. \tag{4.2}$$

The horizontal equilibrium of the prominence in turn is not affected by the essentially vertical forces $\mathbf{F}_{\rm m}$ and $\mathbf{F}_{\rm g}$, and is provided automatically by the balance between horizontal components of $\mathbf{F}_1$ and $\mathbf{F}_2$ due to horizontal symmetry of the model. Equations (4.2) put the first constrain on the parameters of the model. Indeed, for a given distance d to have a real value in the equilibrium condition, the parameters need to be related as:

$$k_2 < 2\rho g h < 4k_1 + k_2. \tag{4.3}$$

Inequality (4.3) describes a condition necessary for the equilibrium of the prominence to exist, between its gravitational energy and the total magnetic energy (written in terms of k_1 and k_2), generated by the prominence and photospheric currents, i and I, respectively. Thus, when $2\rho g h > 4k_1 + k_2$, the magnetic background cannot sustain the prominence, and it falls to the surface. In the other case, when $2\rho g h < k_2$, the prominence's magnetic energy exceeds the gravitational energy, and the prominence

lifts off.

According to Eq. (4.2), the vertical component of the total Lorentz force acting on an unperturbed prominence, $F_{\rm L}$ gradually decreases with height for all values of the photospheric currents I being less or equal to the prominence current i, and may have both negative and positive gradients for $I > i$. Consequently, for $I < i$ the system is able to have only a single equilibrium determined by the $F_{\rm L} = \rho g$ balance, while for $I > i$ there are at most three possibilities to satisfy the force balance condition, and hence, up to three equilibria of the system at different heights may exist. Corresponding examples are shown in Fig. 4.2 for different values of the I/i ratio.

For the case when the prominence is perturbed by an oblique displacement with corresponding x and z components, the equations of motion of the prominence in the horizontal (x-) and vertical (z-) directions can be written as

$$\rho \frac{d^2\, x}{d\, t^2} = F_x, \tag{4.4}$$

$$\rho \frac{d^2\, z}{d\, t^2} = F_z, \tag{4.5}$$

where

$$F_x = \frac{2k_1 x[(h+z)^2 + x^2 - d^2]}{(d^2 - x^2)^2 + 2(d^2 + x^2)(h+z)^2 + (h+z)^4} \approx \frac{2k_1(h^2 - d^2)}{(d^2 + h^2)^2}\, x,$$

$$F_z = \frac{2k_1(h+z)[d^2 + x^2 + (h+z)^2]}{(d^2 - x^2)^2 + 2(d^2 + x^2)(h+z)^2 + (h+z)^4} + \frac{k_2}{2h+z} - \rho g$$
$$\approx \left[\frac{2k_1(d^2 - h^2)}{(d^2 + h^2)^2} - \frac{k_2}{4h^2}\right] z$$

are the projections of the total force given in Eq. (4.1) on the horizontal and vertical axes. It should be emphasised, that for $I = 0$ (i.e. $k_1 = 0$, pure KR model) the horizontal force F_x (4.4) is zero for any horizontal displacement, indicating the contribution of the mirror force $F_{\rm m}$ to vertical dynamics only. Treating the displacements x and z to be small, total forces can be expanded up to the first order of x and z. Note that the first-order Taylor expansion in Eq. (4.5) has been derived accounting for condition (4.2) for the vertical equilibrium of the prominence. As this study is restricted to linear perturbations only, both forces F_x (4.4) and F_z (4.5) lose their dependence on z and x, respectively, and horizontally and vertically polarised oscillations become independent of each other and hence can be considered

separately. While the other case of finite values of x and z, leading to the nonlinear coupling between horizontal and vertical motions of the prominence, is addressed in the following Sec. 4.2.

4.1.3 Small amplitude vertically polarised oscillations

Consider the case when the initial displacement of the prominence is directed strictly along the vertical z-axis, assuming $x = 0$ and $z \neq 0$ in Eq. (4.5). In this case the vertical component F_z of the total force acting on the prominence has the form

$$F_z = \frac{2k_1(h+z)}{d^2+(h+z)^2} + \frac{k_2}{2h+z} - \rho g, \tag{4.6}$$

where the first term on the right-hand side corresponds to the Lorentz force acting on the perturbed prominence from two photospheric currents, the second term is the corresponding mirror force, and the last term is the gravity force assumed to be constant on the scale of the vertical displacement in the oscillation.

With the use of the first-order Taylor expansion of the perturbed vertical force F_z written in (4.5), the equation of motion of the prominence along the vertical axis is

$$\ddot{z} + (2\pi/P_z)^2 \; z = 0. \tag{4.7}$$

Equation (4.7) is a harmonic oscillator equation and describes small amplitude vertically polarised oscillations of the prominence with the period (expressed either in terms of h and d, or via ρ and h):

$$P_z = P_{\rm KR}\left[1 + 8\frac{k_1}{k_2}\frac{h^2(h^2-d^2)}{(d^2+h^2)^2}\right]^{-1/2} = \frac{P_{\rm KR}\sqrt{k_1 k_2}}{\left[(2\rho g h - k_2)^2 - 2k_2(2\rho g h - k_2) + k_1 k_2\right]^{1/2}}, \tag{4.8}$$

where d^2 in form (4.2) has been substituted, and $P_{\rm KR} = 2\pi\sqrt{4\rho h^2/k_2}$ is the period of prominence oscillations in the absence of the photospheric currents effect (i.e. the limiting case corresponding to the KR model). Demanding the constants k_1 and k_2 (i.e. the currents I and i) to have non-zero values in the model, period (4.8) can be reduced to the KR limit when the half-distance d between the external currents tends to infinity. This limiting case can be achieved when $2\rho g h = k_2$ (see Eq. (4.2)). In other cases, period (4.8) has a non-trivial dependence upon the currents I and i, height h, and mass density ρ. Its dependence upon the current ratio I/i (i.e. k_1/k_2) for different values of $2\rho g h/k_2$ (also including the KR limit $2\rho g h = k_2$) is shown in Fig. 4.3.

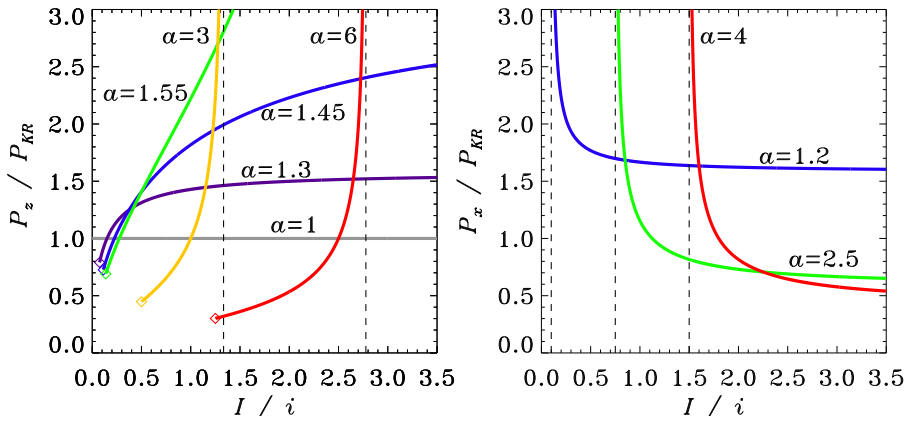

Figure 4.3: Left: Period P_z (4.8) of vertical oscillations of a prominence vs. the current ratio I/i for different values of the dimensionless parameter $a = 2\rho gh/k_2$. Note, the case $a = 1$ corresponds to the KR limit [Kuperus and Raadu, 1974] when the effect of the photospheric currents is negligibly small. Right: Period P_x (4.12) of horizontal oscillations depending upon the same parameters I/i and a as shown in the left-hand panel. Dashed lines in both panels show a threshold values of I/i where periods (4.8) and (4.12) become imaginary, and corresponding instabilities develop.

General dependence of the vertical dynamics of the prominence described by Eq. (4.7) upon the parameters of the model, can be also derived analytically. More specifically, when the prominence current dominates in the system, i.e. $0 < k_1/k_2 < 1$, Eq. (4.7) shows always stable solutions for the vertical displacement. The particular case when the prominence i and photospheric I currents are of the same magnitude, i.e. $k_1 = k_2$, also corresponds to an always stable state of the prominence oscillating harmonically around the equilibrium position with a period $P = P_{\rm KR}|(d^2 + h^2)/(3h^2 - d^2)|$. In both these cases, only conditions (4.2) and (4.3) providing existence of the initial equilibrium of the system should be satisfied for h and d. In contrast, for the photospheric currents domination ($k_1/k_2 > 1$) there is a parametric region of a vertical instability (see Fig. 4.4) determined by condition (4.3) and the following relations (written either in terms of h and d or via ρ and h):

$$\frac{d\sqrt{k_2}}{\left[4k_1 - k_2 + 4\sqrt{k_1^2 - k_1k_2}\right]^{1/2}} < h < \frac{d\sqrt{k_2}}{\left[4k_1 - k_2 - 4\sqrt{k_1^2 - k_1k_2}\right]^{1/2}},$$

$$\text{or} \quad k_1 + k_2 - \sqrt{k_1^2 - k_1k_2} < 2\rho gh < k_1 + k_2 + \sqrt{k_1^2 - k_1k_2}. \tag{4.9}$$

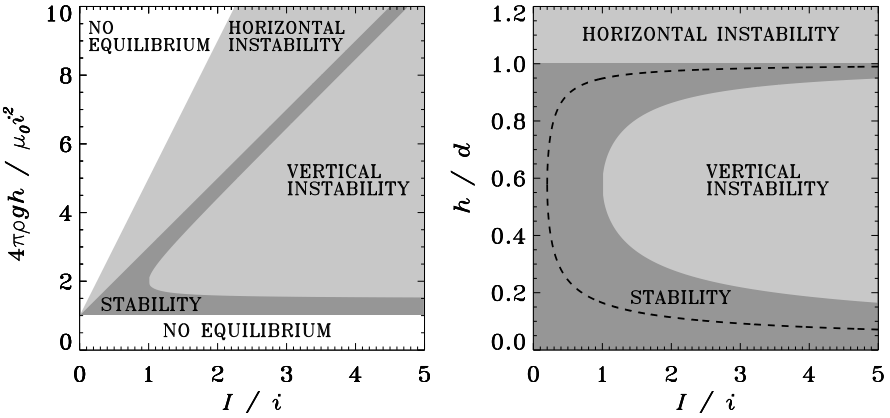

Figure 4.4: Parametric regions of the prominence instability, determined by equilibrium condition (4.3), (4.9) (vertical instability), and (4.13) (horizontal instability). Left-hand and right-hand panels show the corresponding regions determined via ρ and h, and h and d, respectively. The dashed line shows the nonlinear resonance condition between finite amplitude vertical and horizontal oscillatory modes, determined by Eq. (4.28) in Sec. 4.2, where the frequency of the vertical mode is twice the horizontal mode frequency .

4.1.4 Small amplitude horizontally polarised oscillations

Now the case with $z = 0$ is considered, i.e. the initial displacement of the prominence is directed strictly along the horizontal x-axis. In this case the force F_x (4.4) acting on the prominence along the horizontal axis reduces to

$$F_x = \frac{2k_1 x[h^2 - d^2 + x^2]}{(d^2 - x^2)^2 + 2(d^2 + x^2)h^2 + h^4}. \tag{4.10}$$

Using the Taylor expansion of the force F_x up to the first order of the small perturbations x and z, given by Eq. (4.4), the equation of motion describing small amplitude dynamics of the prominence along the horizontal axis is

$$\ddot{x} + (2\pi/P_x)^2\, x = 0. \tag{4.11}$$

Similarly to the vertically polarised oscillatory modes described above, Eq. (4.11) shows harmonic oscillations of the prominence around the equilibrium position ($x = 0$ and $z = 0$), with the period P_x,

$$P_x = P_{\rm KR}\sqrt{\frac{k_2}{8k_1}\frac{(d^2+h^2)^2}{h^2(d^2-h^2)}} = \frac{P_{\rm KR}\sqrt{k_1 k_2}}{[2k_1(2\rho gh - k_2) - (2\rho gh - k_2)^2]^{1/2}}. \tag{4.12}$$

Note, that in the KR limit that can be achieved when $2\rho gh = k_2$ (see Eq. (4.2)), the value of P_x tends to infinity. Behaviour of the period (4.12) for various other values of ratios $2\rho gh/k_2$ and I/i is shown in Fig. 4.3.

The regions on the parametric plane where the period P_x has imaginary values (i.e. the condition of the horizontal instability of the prominence) with accounting for conditions (4.2) and (4.3), are shown in Fig. 4.4, and are expressed as

$$h > d, \quad \text{or} \quad 2k_1 + k_2 < 2\rho gh < 4k_1 + k_2. \tag{4.13}$$

4.1.5 Discussion and conclusions

The developed model provides a simple, analytical treatment of global transverse oscillations and mechanical stability of quiescent prominences. In this context, the term "global" denotes the collective nature of the considered oscillations, when the prominence oscillates as a whole, in contrast to the oscillations of individual threads. The term is connected with the observational manifestation of the considered oscillations, rather than a specific interpretation, for example a fundamental longitudinal harmonic of a kink or sausage oscillation. Properties of the oscillations are determined by the value of the electric current in the prominence, its density and height above the photosphere, and the parameters of the magnetic dip caused by external magnetic sources. As mentioned above, in the linear regime considered in this section, the vertically and horizontally polarised oscillations are essentially decoupled, and the obliquely or elliptically polarised oscillations can be represented as a linear superposition of separate vertical and horizontal modes. Furthermore, the stability conditions in both z- and x-directions, given in Eqs. (4.9) and (4.13), do not interfere with each other, and the oscillation periods given by expressions (4.8) and (4.12) in both directions are independent.

For the prominence current domination in the considered magnetic system ($I/i < 1$), the prominence displacements in both vertical and horizontal directions are found to be stable [cf. van den Oord et al., 1998] when the prominence's height h above the photosphere is less than the half-distance d between the photospheric current sources configuring the dip (see Fig. 4.4). In the case when the external currents dominate ($I/i > 1$), the prominence is stable only in narrow regions of the parameters, determined by conditions (4.9) and (4.13). These analytical findings are in accordance with numerous observational results describing the prominence instability occurring when its height h reaches some critical value [see e.g. Vršnak, 2008].

Exact analytical dependences of the periods of the prominence oscillations

upon the parameters of the system, derived in Eqs. (4.8) and (4.12), allow for seismological diagnostics of the current in the prominence. For example, taking a typical value of $P_{\rm KR} \approx 20$ min [Kuperus and Raadu, 1974] and fixing $h = 0.6\,d$, for the observed periods of the vertical transverse oscillations, $P_z \approx 80$ min [Bocchialini et al., 2011], the prominence current i with respect to the photospheric current I, according to Eq. (4.8), can be estimated as $I \approx 0.94\,i$. With the use of the ratio I/i and the geometrical parameters of the model, h and d, one can estimate the coronal magnetic field at the prominence's equilibrium position, caused by the external photospheric sources, I as $B/B_0 = (I/i)\,2h/\sqrt{d^2+h^2}$, where B_0 is the magnetic field caused by the interaction of the prominence current i with the conductive photosphere, used in the KR model in the absence of external magnetic sources. In addition, the developed model can also be used for numerical modelling of the excitation of prominence oscillations [e.g. Takahashi et al., 2015].

The proposed model developed within the line currents concept should be considered as a simplified one, and clearly misses a number of important physical phenomena. In fact, it neglects partial ionisation and dissipative effects. They can affect, in particular, time evolution of the oscillations, leading to their damping or amplification. Another potentially important effect is connected with the magnetic field curvature and the finite wave number of the perturbations in the direction along the current, that are important, for example, for kink oscillations of coronal loops [e.g. Edwin and Roberts, 1983] and prominence threads [e.g. Cargill et al., 1994; Joarder et al., 1997; Vršnak, 2008]. They add the additional restoring force that may decrease the oscillation period. It also does not consider thermodynamical effects affecting the prominence development itself [e.g. Kuin and Martens, 1982]. In addition, in the developed model the electric currents are considered to be linear, i.e. a wire-like. However, there may be important effects connected with the spatial distribution of the current in the plane of the oscillation. For example, in a more general model, a prominence could possibly be considered as a vertical current sheet. In that case parameters of the modes of oscillations may get some dependence on height, which may be relevant to the interpretation of some observational finding [e.g. Hershaw et al., 2011]. However, a further discussion of this issue would be out of the scope of this study.

4.2 Finite amplitude regime of oscillations

Another important limitation of the solution obtained in Sec. 4.1 is that it considers only small amplitude oscillations and does not account for the effects of finite am-

plitudes, which are often detected in observations (see Sec. 1.3.1 for details). This section demonstrates further development of the proposed model, accounting now for the effects of finite amplitudes. It shows that the finite amplitude equations of motion in the vertical and horizontal directions are nonlinearly coupled with each other (Sec. 4.2.1), in contrast to the linear small amplitude regime considered in Sec. 4.1, where the motions are essentially independent. Analysis of a fully nonlinear case (Sec. 4.2.2) also reveals the presence of metastable equilibria characterised by a threshold value of the prominence energy, above which it becomes unstable. Therefore, accounting for nonlinear terms in the governing equations makes the dynamics of the system more various and rich of interesting features.

4.2.1 Nonlinear coupling and resonance of vertically and horizontally polarised oscillations

Dynamics of the prominence in a magnetic field dip (see Fig. 4.1), perturbed by an oblique displacement with the corresponding x (horizontal) and z (vertical) components, is governed by the set of equations (4.4)–(4.5). In the linear regime treating the displacements x and z to be small and, hence, using the first-order Taylor expansions of Eqs. (4.4) and (4.5), the vertical and horizontal modes were found to be essentially decoupled, therefore, were considered separately in Sec. 4.1. However, with the use of the Taylor expansion up to the second order of the displacements x and z, Eqs. (4.4) and (4.5) can be re-written as

$$\frac{d^2\,x}{d\,t^2} = \alpha x + \mu x z, \tag{4.14}$$

$$\frac{d^2\,z}{d\,t^2} = \eta z + \delta x^2 + \sigma z^2, \tag{4.15}$$

where

$$\alpha = \frac{2k_1(h^2-d^2)}{\rho(d^2+h^2)^2}, \quad \mu = \frac{4k_1 h(3d^2-h^2)}{\rho(d^2+h^2)^3}, \quad \eta = \frac{2k_1(d^2-h^2)}{\rho(d^2+h^2)^2} - \frac{k_2}{4\rho h^2},$$

$$\delta = \frac{2k_1 h(3d^2-h^2)}{\rho(d^2+h^2)^3}, \quad \sigma = \frac{2k_1 h(h^2-3d^2)}{\rho(d^2+h^2)^3} + \frac{k_2}{8\rho h^3}.$$

In contrast to the first-order expansion of Eqs. (4.4) and (4.5), Eqs. (4.14) and (4.15) are coupled through the second-order terms on their right-hand sides.

The set of coupled nonlinear equations (4.14)–(4.15) represents a conservative system, and for certain values of the parameters α, μ, η, δ, and σ was previously found to be integrable with the Hamiltonian of a Hénon–Heiles form [see e.g.

Eqs. (3.1) in Bountis et al., 1982, the special case of $\mu = 2$ and $\delta = 1$]. In the present analysis general solutions of Eqs. (4.14)–(4.15) are obtained, allowing for arbitrary values of those parameters, using the perturbation theory approach. Expressing the displacements x and z through a small parameter ϵ as $x \equiv \epsilon x$ and $z \equiv \epsilon z$ and expanding the new x and z with respect to ϵ, $x = x_1 + \epsilon x_2$ and $z = z_1 + \epsilon z_2$, one can re-write Eqs. (4.14) and (4.15) as

$$\frac{d^2 x_1}{d t^2} + \epsilon \frac{d^2 x_2}{d t^2} = \alpha x_1 + \epsilon(\alpha x_2 + \mu x_1 z_1), \tag{4.16}$$

$$\frac{d^2 z_1}{d t^2} + \epsilon \frac{d^2 z_2}{d t^2} = \eta z_1 + \epsilon(\eta z_2 + \delta x_1^2 + \sigma z_1^2). \tag{4.17}$$

The parameter ϵ demonstrates the smallness of the prominence displacements in comparison with the equilibrium geometrical parameters d and h. In such a representation of x and z, the lowest-order terms, x_1 and z_1, correspond to the decoupled harmonic oscillations of the prominence, while the higher-order components, x_2 and z_2, describe, in particular, the coupling between the horizontal and vertical modes. Indeed, collecting together the terms with the lowest order of the parameter ϵ in Eqs. (4.16) and (4.17), one obtains

$$\frac{d^2 x_1}{d t^2} + \omega_1^2 x_1 = 0, \tag{4.18}$$

$$\frac{d^2 z_1}{d t^2} + \omega_2^2 z_1 = 0, \tag{4.19}$$

where $\omega_1^2 = -\alpha$ and $\omega_2^2 = -\eta$. The behaviour of ω_1 and ω_2 and their dependence on the geometrical parameters of the model, h and d, magnetic constants, k_1 and k_2, and the prominence mass density, ρ, and the associated linear oscillations, have been investigated in detail in Sec. 4.1, where the notations $\omega_1 = 2\pi/P_x$ and $\omega_2 = 2\pi/P_z$ were used, with P_x (4.12) and P_z (4.8) being the horizontal and vertical oscillation periods, respectively. Equations (4.18) and (4.19) have harmonic solutions written as

$$x_1(t) = A_1 \sin(\omega_1 t + \phi_1), \tag{4.20}$$

$$z_1(t) = A_2 \sin(\omega_2 t + \phi_2), \tag{4.21}$$

where A_1, A_2, ϕ_1, and ϕ_2 are the constants determined from the initial conditions.

Then combine the terms of the first order of ϵ in Eqs. (4.16) and (4.17), so

that

$$\frac{d^2\,x_2}{d\,t^2}+\omega_1^2 x_2=\frac{A_1A_2}{2\mu^{-1}}\left\{\cos\left[(\omega_1-\omega_2)t+(\phi_1-\phi_2)\right]-\right. \tag{4.22}$$
$$\left.\cos\left[(\omega_1+\omega_2)t+(\phi_1+\phi_2)\right]\right\},$$

$$\frac{d^2\,z_2}{d\,t^2}+\omega_2^2 z_2=A_1^2\delta\sin^2(\omega_1 t+\phi_1)+A_2^2\sigma\sin^2(\omega_2 t+\phi_2), \tag{4.23}$$

where the solutions for $x_1(t)$ and $z_1(t)$, given by Eqs. (4.20) and (4.21), have been used. Solutions of Eqs. (4.22)–(4.23) can be written in a general form as

$$x_2(t)=B_1\sin(\omega_1 t+\psi_1)+\frac{A_1A_2}{2\mu^{-1}}\left\{\frac{\cos[(\omega_1-\omega_2)t+(\phi_1-\phi_2)]}{\omega_2(2\omega_1-\omega_2)}+\right.$$
$$\left.\frac{\cos[(\omega_1+\omega_2)t+(\phi_1+\phi_2)]}{\omega_2(2\omega_1+\omega_2)}\right\}, \tag{4.24}$$

$$z_2(t)=B_2\sin(\omega_2 t+\psi_2)+\frac{A_1^2\delta}{2}\frac{\cos[2(\omega_1 t+\phi_1)]}{4\omega_1^2-\omega_2^2}+\sigma A_2^2\frac{\cos[2(\omega_2 t+\phi_2)]}{6\omega_2^2}+$$
$$\frac{\delta A_1^2+\sigma A_2^2}{\omega_2^2}, \tag{4.25}$$

where B_1, B_2, ψ_1, and ψ_2 are the constants determined from the initial conditions.

Thus, combining solutions (4.20)–(4.21) for x_1 and z_1 and (4.24)–(4.25) for x_2 and z_2, and recalling that $x=x_1+\epsilon x_2$ and $z=z_1+\epsilon z_2$, the oscillatory solution of Eqs. (4.14)–(4.15) can be written as

$$x(t)=C_1\sin(\omega_1 t+\Theta_1)+\frac{C_1C_2}{2\mu^{-1}}\left\{\frac{\cos[(\omega_1-\omega_2)t+(\Theta_1-\Theta_2)]}{\omega_2(2\omega_1-\omega_2)}+\right.$$
$$\left.\frac{\cos[(\omega_1+\omega_2)t+(\Theta_1+\Theta_2)]}{\omega_2(2\omega_1+\omega_2)}\right\}, \tag{4.26}$$

$$z(t)=C_2\sin(\omega_2 t+\Theta_2)+\frac{\delta C_1^2}{2}\frac{\cos[2(\omega_1 t+\Theta_1)]}{4\omega_1^2-\omega_2^2}+\sigma C_2^2\frac{\cos[2(\omega_2 t+\Theta_2)]}{6\omega_2^2}, \tag{4.27}$$

where $C_{1,2}\equiv[A_{1,2}^2+B_{1,2}^2+2A_{1,2}B_{1,2}\cos(\phi_{1,2}-\psi_{1,2})]^{1/2}$ and $\tan(\Theta_{1,2})=[A_{1,2}\sin(\phi_{1,2})+B_{1,2}\sin(\psi_{1,2})]/[A_{1,2}\cos(\phi_{1,2})+B_{1,2}\cos(\psi_{1,2})]$, with $\epsilon=1$. The use of $\epsilon=1$ in expressions (4.26)–(4.27) does not contradict to the sense of generality as it was employed only for the quantification of the smallness of amplitudes of the higher-order components (B_1, B_2, A_1^2, A_2^2, and A_1A_2) in comparison with the lowest harmonic amplitudes, A_1 and A_2. The set of solutions (4.26)–(4.27) describes the coupled

horizontal and vertical oscillatory dynamics of the prominence and, importantly, implies a nonlinear resonance condition $2\omega_1 = \omega_2$, appearing in both polarisations simultaneously. One can re-write this resonance condition in terms of the intrinsic physical parameters of the model, h, d, k_1 and k_2, as

$$h = d\left[\frac{20k_1 - k_2 \pm 4\sqrt{25k_1^2 - 5k_1k_2}}{40k_1 + k_2}\right]^{1/2}. \tag{4.28}$$

This dependence is illustrated in Fig. 4.4, where the current ratio I/i, shown on the horizontal axis, is equivalent to k_1/k_2. Note, that the resonant condition (4.28) implicitly accounts for the dependence on the prominence mass via the equilibrium condition (4.2).

As long as $2\omega_1 \neq \omega_2$, the prominence space dynamics governed by set (4.14)–(4.15), is described by solutions (4.26)–(4.27). However, in the special resonant case, when $2\omega_1 = \omega_2$, solutions (4.26)–(4.27) break down and are no longer applicable. To describe analytically the prominence behaviour in the resonant case with $2\omega_1 = \omega_2$, one can introduce an additional slow time variable $\tau = \varepsilon t$ with ε being a small parameter, and allow the amplitudes A_1 and A_2 in harmonic solutions (4.20)–(4.21) to be slowly varying functions of τ, $A_1 = A_1(\tau)$ and $A_2 = A_2(\tau)$. In such a formulation the time derivative transforms to $d/dt \equiv \partial/\partial t + \varepsilon(\partial/\partial\tau)$, and taking the initial phases to be zero one can re-write Eqs. (4.22)–(4.23) as

$$\frac{\partial^2 x_2}{\partial t^2} + \omega_1^2 x_2 = \frac{A_1 A_2}{2\mu^{-1}}\left\{\cos\left[(\omega_1 - \omega_2)t\right] - \cos\left[(\omega_1 + \omega_2)t\right]\right\} - 2\frac{d\,A_1}{d\,\tau}\omega_1\cos(\omega_1 t), \tag{4.29}$$

$$\frac{\partial^2 z_2}{\partial t^2} + \omega_2^2 z_2 = \frac{A_1^2\delta}{2} + \frac{A_2^2\sigma}{2} - \frac{A_1^2\delta}{2}\cos(2\omega_1 t) - \frac{A_2^2\sigma}{2}\cos(2\omega_2 t) - 2\frac{d\,A_2}{d\,\tau}\omega_2\cos(\omega_2 t), \tag{4.30}$$

with an additional term appearing on the right-hand side of both equations. According to solutions (4.26)–(4.27), the resonance originates from the first and third terms on the right-hand side of Eqs. (4.29) and (4.30), respectively. Hence, they can be removed by demanding

$$\omega_2\frac{d\,A_1}{d\,\tau} - \frac{A_1 A_2}{2}\mu = 0, \tag{4.31}$$

$$2\omega_2\frac{d\,A_2}{d\,\tau} + \frac{A_1^2\delta}{2} = 0, \tag{4.32}$$

where the resonance condition $\omega_2 = 2\omega_1$ has been used. From Eq. (4.31) the function $A_2(\tau)$ can be expressed as

$$A_2 = \frac{2\omega_2}{\mu A_1}\frac{d\,A_1}{d\,\tau}. \tag{4.33}$$

Using (4.33), Eq. (4.32) reduces to the following second-order ODE

$$\frac{1}{A_1}\frac{d^2 A_1}{d\,\tau^2} - \frac{1}{A_1^2}\left(\frac{d\,A_1}{d\,\tau}\right)^2 + \lambda A_1^2 = 0, \tag{4.34}$$

with $\lambda = \mu\delta/8\omega_2^2$. Then writing $d\,A_1/d\,\tau = P(A_1)$, and hence $d^2A_1/d\,\tau^2 = P(d\,P/d\,A_1)$, Eq. (4.34) takes the form

$$\frac{1}{A_1}\frac{d}{d\,A_1}\left(\frac{P^2}{2}\right) - \frac{P^2}{A_1^2} = -\lambda A_1^2. \tag{4.35}$$

With the use of a new variable $s = A_1^2$, so that $d/d\,A_1 = 2A_1(d/d\,s)$, Eq. (4.35) can be re-written as

$$\frac{d\,P^2}{d\,s} - \frac{P^2}{s} = -\lambda s. \tag{4.36}$$

Now expressing the function P through a new unknown function $q(s)$ as $P^2 = sq(s)$, Eq. (4.36) goes to

$$\frac{d\,q}{d\,s} = -\lambda, \tag{4.37}$$

which can be integrated once and has the solution

$$q = q_0 - \lambda s, \tag{4.38}$$

with q_0 being a constant determined from the initial conditions $A_1(0) = A_0$ and $\dot{A}_1(0) = 0$, as $q_0 = \lambda A_0^2$.

Now recalling that $P = d\,A_1/d\,\tau$, $P^2 = sq(s)$, and $s = A_1^2$, one obtains the following equation

$$\left(\frac{d\,A_1}{d\,\tau}\right)^2 = A_1^2(q_0 - \lambda A_1^2), \tag{4.39}$$

whose integral has the form

$$\tau = \int_{A_0}^{A_1} \frac{d\,A_1}{A_1\sqrt{q_0 - \lambda A_1^2}} = \frac{1}{A_0(\lambda)^{1/2}}\,\mathrm{sech}^{-1}\left(\frac{A_1}{A_0}\right). \tag{4.40}$$

Using (4.40), one is able to write the explicit solution $A_1(\tau)$ as

$$A_1 = A_0\,\mathrm{sech}[A_0(\lambda)^{1/2}\tau]. \tag{4.41}$$

Substitution of (4.41) into (4.33) gives the explicit form of the dependence $A_2(\tau)$,

$$A_2 = -A_0 \left(\frac{\delta}{2\mu}\right)^{1/2} \tanh[A_0(\lambda)^{1/2}\tau]. \tag{4.42}$$

Having obtained the explicit solutions for $A_1(\tau)$ and $A_2(\tau)$, one can use them in the lowest-order harmonic solutions given in (4.20)–(4.21) to obtain

$$x_1 = A_0 \,\mathrm{sech}[A_0(\lambda)^{1/2}\tau] \sin(\omega_1 t), \tag{4.43}$$

$$z_1 = -A_0 \left(\frac{\delta}{2\mu}\right)^{1/2} \tanh[A_0(\lambda)^{1/2}\tau] \sin(\omega_2 t). \tag{4.44}$$

Finally, using the resonant condition $\omega_2 = 2\omega_1$ one can obtain an explicit relation between the vertical and horizontal coordinates, z_1 and x_1, describing the prominence space dynamics in the special resonant case:

$$z_1^2 = \frac{2\delta}{\mu} x_1^2 \sinh^2[A_0(\lambda)^{1/2}\tau] \left\{1 - \frac{x_1^2}{A_0^2} \cosh^2[A_0(\lambda)^{1/2}\tau]\right\}, \tag{4.45}$$

with λ and A_0 introduced above in Eqs. (4.34) and (4.38), respectively. Note that the coefficients μ, η, δ, appearing in Eq. (4.45) are all functions of the intrinsic parameters of the model, h, d, k_1, and k_2 (see Eqs. (4.14)–(4.15)), hence, their values should be chosen according to the resonant condition (4.28) when operating with solution (4.45). Prominence resonant space trajectories described by (4.45) are illustrated in Fig. 4.5, being Lissajous-like curves of a symmetric hourglass shape. In particular, Fig. 4.5 clearly shows the nonlinear mode coupling effect, i.e. the increase in the vertical amplitude of the prominence oscillation with time leads to the decrease in its horizontal amplitude, thus manifesting the conservation of energy in the system.

The spatial polarisation of nonlinear transverse oscillations of a prominence in both resonant and non-resonant cases is shown in Fig. 4.6. It demonstrates the evolutionary solutions of set (4.14)–(4.15), obtained with the initial conditions $x(0) = 0$, $z(0) = 0$, $\dot{x} = 0.01$ (written in the units of $\sqrt{k_2/\rho}$), and $\dot{z} = 0$, at three different time intervals of the prominence evolution. Such a set of the initial conditions implies that at the initial instant of time the prominence is located at the equilibrium position and is perturbed by a non-zero value of the horizontal speed. For a non-eruptive prominence with mass density $\sim 10^{-10}\,\mathrm{kg\,m^{-3}}$, diameter ~ 10 Mm, and prominence current $\sim 10^{10}$–10^{11} A [see e.g. Wu et al., 1994; Canou and Amari, 2010], the value of this speed in physical units would correspond to about 0.5–5 $\mathrm{km\,s^{-1}}$.

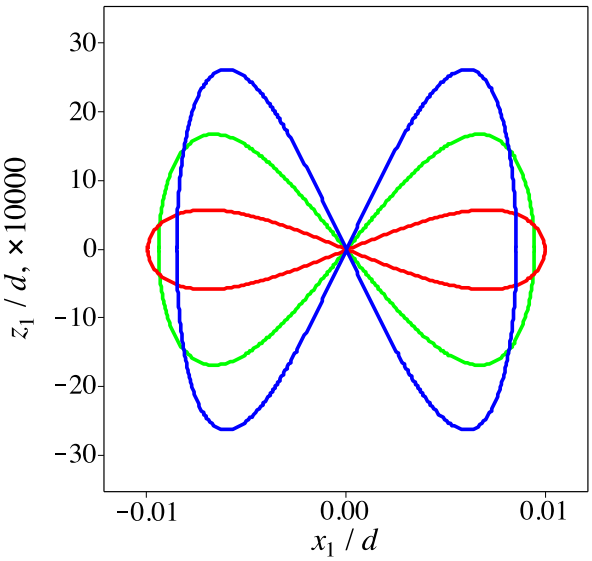

Figure 4.5: Displacements of the prominence in the saturated resonant nonlinear regime described by Eq. (4.45), shown for $h/d \approx 0.244$ (see Eq. (4.28)), $I/i = 0.5$, $A_0/d = 0.01$, and the time $\tau = 50$ (red), 150 (green), 250 (blue), measured in the units of $\sqrt{\rho d^2/k_2}$.

A possible driver is, for example, a global coronal wave [e.g. Hershaw et al., 2011; Shen et al., 2014a]. As the initial perturbation occurs, the prominence moves almost strictly along the x-axis (see panels (a) and (d) in Fig. 4.6) until its amplitude becomes sufficiently large (about a half of the maximum horizontal amplitude), and the vertical displacement of the prominence is generated by the nonlinear coupling mechanism described above. The latter clearly illustrates the uncoupled nature of the small amplitude prominence oscillations considered in Sec. 4.1, and, in contrast, the highly pronounced nonlinear coupling between larger amplitude vertical and horizontal displacements. Numerical tests performed with the use of Eqs. (4.4)–(4.5) and (4.14)–(4.15) solved by the 4th order Runge–Kutta scheme with the *dsolve* routine in Maple 2016, showed that the coupling works more efficiently for larger amplitude oscillations and for smaller angles between the direction of the initial perturbation and the horizontal axis (an attack angle). In the limiting case when the initial perturbation is directed strictly along the vertical axis, the set of equations (4.14)–(4.15) is uncoupled for arbitrarily large oscillation amplitudes. This is illustrated by Fig. 4.7, where the numerical dependence of the maximum vertical and horizontal displacement ratio upon the direction of the initial perturbation is shown for small and large amplitude cases. In the case of small amplitudes, the

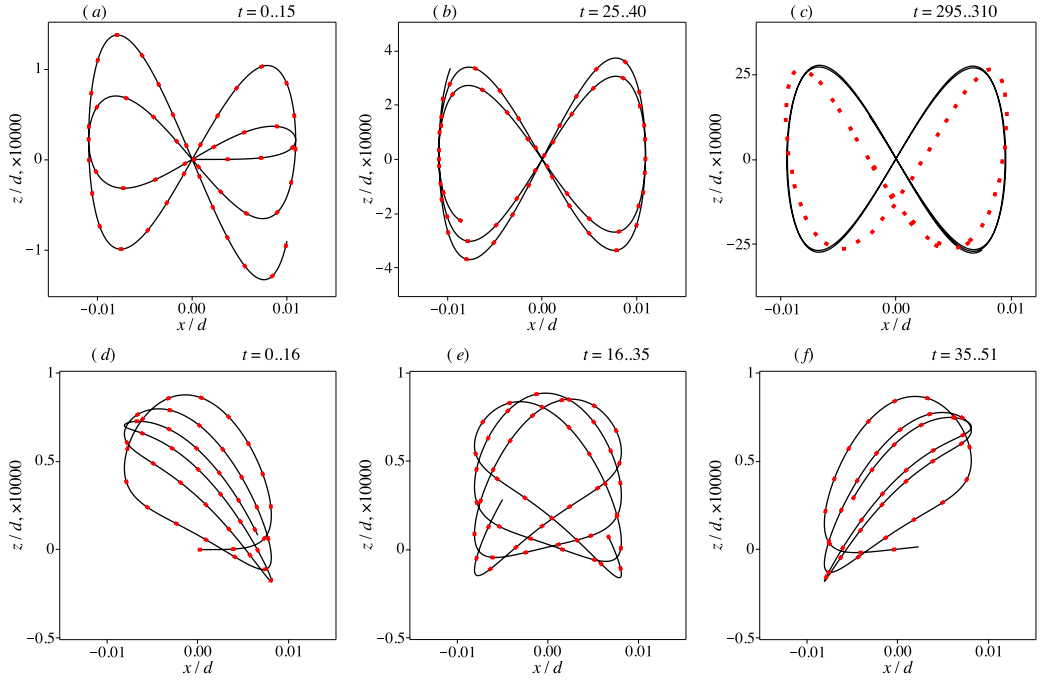

Figure 4.6: Displacements of a current-carrying prominence in a magnetic dip during three different time intervals (shown above each panel), determined numerically as solutions of Eqs. (4.14)–(4.15) (black solid lines) and Eqs. (4.4)–(4.5) (red dots), with the initial conditions $x(0) = 0$, $z(0) = 0$, $\dot{x} = 0.01$ (written in units of $\sqrt{k_2/\rho}$), and $\dot{z} = 0$. Panels (a)–(c) show a resonant case (see Eqs. (4.28) and (4.45) and Figs. 4.4 and 4.5) with $h/d \approx 0.244$ and $I/i = 0.5$. Panels (d)–(f) show a non-resonant case with $h/d = 0.3$ and $I/i = 1$. Time t is measured in the units of $\sqrt{\rho d^2/k_2}$.

nonlinear coupling between the vertical and horizontal modes is suppressed, and the dependence of the amplitude ratio upon the attack angle is naturally governed by a tangent function. In contrast, for larger amplitude displacements this dependence clearly deviates from the tangent dependence upon the attack angle at smaller angles of the initial perturbation, which is caused by strong nonlinear coupling.

In the resonant case, when the frequency of the vertical mode is twice the horizontal mode frequency, $2\omega_1 = \omega_2$ (top panels of Fig. 4.6), the horizontal displacement of the prominence achieves a nearly maximum amplitude during the first cycle of the prominence evolution (see panel (a), Fig. 4.6), while its vertical amplitude grows gradually, accompanied with the increasing ordering of the prominence trajectories in space. This evolution continues until the resonant limit cycle of a symmetric shape, described by Eq. (4.45) and shown in Fig. 4.5, is reached (panel (c), Fig. 4.6), when all trajectories are highly concentrated in space. In contrast, in

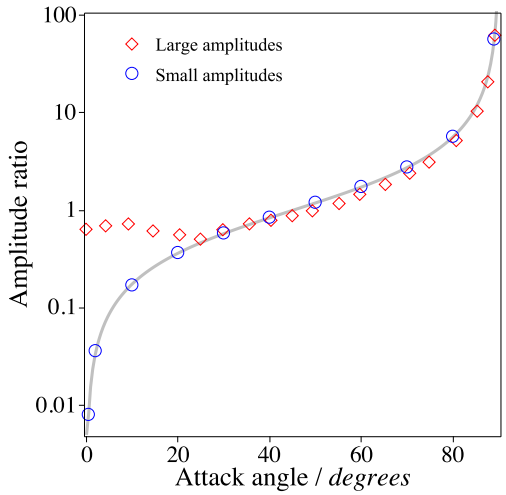

Figure 4.7: Dependence of the maximum vertical and horizontal displacement ratio upon the angle between the direction of the initial perturbation and the horizontal axis, shown for small (blue circles) and large (red diamonds) amplitude transverse oscillations of the prominence. The grey solid line shows the tangent of the attack angle. The vertical axis is shown in logarithmic scale. The example is shown for $h/d = 0.5$ and I/i=0.5, corresponding to a non-resonant case.

the non-resonant case (bottom panels in Fig. 4.6), the prominence trajectories do not experience such a localisation in space, and consequently the vertical displacement remains relatively small in amplitude in comparison with the resonant case during the whole prominence evolution. Non-resonant dynamics of the prominence can be represented by families of space trajectories, shown in panels (d) and (f), switching one to another through a transition state illustrated in panel (e). Figure 4.6 also shows the numerical solutions of the fully nonlinear set of equations (4.4)–(4.5), obtained for the same values of the physical parameters of the model and initial conditions as those of set (4.14)–(4.15). Both solutions are seen to be well consistent with each other justifying the analytical treatment of a non-resonant evolution of the prominence, developed in this section, except the saturated regime of the resonant case shown in panel (c). This apparent discrepancy indicates the presence of resonances also in other higher-order terms which are not accounted for by Eqs. (4.14)–(4.15). Despite these differences, the saturated resonant trajectories shown in panel (c) are seen to possess similar topologies and amplitudes, which justifies the resonant analytical solution (4.45) too.

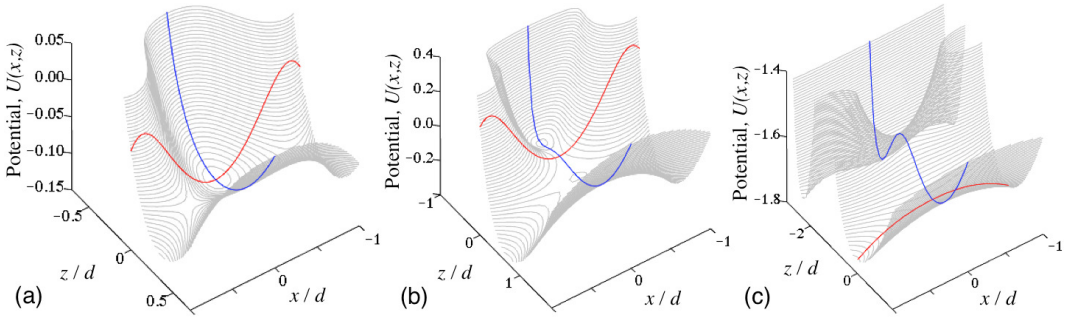

Figure 4.8: Potential energy $U(x, z)$ of the prominence, given by Eq. (4.48) and normalised to $k_2 = \mu_0 i^2/2\pi$. Panel (a): $h/d = 0.5$, $I/i = 0.5$ (region of full stability, Fig. 4.4). Panel (b): $h/d = 0.45$, $I/i = 1.5$ (vertical instability, Fig. 4.4). Panel (c): $h/d = 1.5$, $I/i = 0.5$ (horizontal instability, Fig. 4.4). Red and blue curves show $U(x, z = 0)$ and $U(x = 0, z)$ functions, respectively.

4.2.2 Large amplitude oscillations

Potential energy analysis

In this section larger amplitude prominence oscillations are considered by the analysis of Eqs. (4.4) and (4.5) with the exact expressions for the forces F_x and F_z, without usage of their Taylor expansions. First, note that the forces F_x and F_z acting on the prominence in the horizontal and vertical directions, respectively, can be re-written as

$$F_x = \frac{k_1}{2}\frac{\partial}{\partial x}\ln D, \tag{4.46}$$

$$F_z = \frac{\partial}{\partial z}\left[\frac{k_1}{2}\ln D + k_2 \ln(2h+z)\right] - \rho g, \tag{4.47}$$

where

$$D \equiv (d^2 - x^2)^2 + 2(h+z)^2(d^2 + x^2) + (h+z)^4.$$

Equations (4.4) and (4.5) are thus of a Hamiltonian form with $U(x, z)$ being the prominence potential energy, and dx/dt and dz/dt being the effective momenta. Using the relations $F_x = -\partial U/\partial x$ and $F_z = -\partial U/\partial z$, one can express the prominence effective potential energy $U(x, z)$ as

$$U(x, z) = -\frac{k_1}{2}\ln D - k_2 \ln(2h+z) + \rho g z + C, \tag{4.48}$$

where C is an arbitrary constant. Behaviour of the potential (4.48) is shown in Fig. 4.8 for three different combinations of the intrinsic parameters of the model (i.e.

h, d, k_1, and k_2), corresponding to three regions on the parametric diagram shown in Fig. 4.4. More specifically, all panels in Fig. 4.8 sustain small amplitude decoupled prominence oscillations: in vertical and horizontal directions simultaneously (panel (a)), in the horizontal direction only (panel (b)), and in the vertical direction only (panel (c)), which is consistent with the linear theory developed in Sec. 4.1. In the nonlinear limit, panel (a) shows the potential surface $U(x, z)$ with a local dip of the finite height, corresponding to a locally stable (or metastable) equilibrium of the prominence. Such a metastable prominence state allows for the essentially coupled nonlinear oscillations with a critical amplitude, above which the prominence becomes horizontally unstable. In turn, nonlinear large amplitude oscillations in the cases shown in panels (b) and (c) may quickly become unstable in the horizontal direction by the nonlinear coupling mechanism described above.

Maximum horizontal and vertical amplitudes

The dependence of the maximum oscillation amplitudes in a metastable prominence state upon the intrinsic physical parameters of the model (h, d, k_1, and k_2) is investigated here, addressing the potential energy configuration shown in Fig. 4.8, panel (a), with $h < d$ and $k_1 < k_2$. For that the positions x_m and z_c of the local extrema of the function $U(x, z)$ (4.48) are analysed by solving the following set of coupled equations

$$F_x(x_\mathrm{m}, z_\mathrm{c}) = 0, \tag{4.49}$$

$$F_z(x_\mathrm{m}, z_\mathrm{c}) = 0, \tag{4.50}$$

where F_x and F_z are the forces given in Eqs. (4.4) and (4.5), respectively. In addition to the trivial solution of set (4.49)–(4.50) with $x_\mathrm{m} = 0$ and $z_\mathrm{c} = 0$, corresponding to the initial equilibrium of the prominence, another real solution in the region of parameters $h < d$ and $k_1 < k_2$ is possible:

$$z_\mathrm{c} = \frac{(1/2)\, h}{k_2(h^2 + d^2) + 4h^2 k_1} \Big\{ 2k_1(d^2 - 5h^2) - k_2(h^2 + d^2) + \sqrt{[k_2(d^2 + h^2) + 2k_1(d^2 + 3h^2)]^2 + 8k_1 k_2(d^4 - h^4)} \Big\}, \tag{4.51}$$

$$|x_{\rm m}| = \left\{ d^2 - \frac{(1/4)\,h^2}{(k_2(h^2+d^2)+4h^2k_1)^2} \left[k_2(h^2+d^2) + 2k_1(d^2-h^2) \right.\right.$$
$$\left.\left. + \sqrt{[k_2(d^2+h^2)+2k_1(d^2+3h^2)]^2 + 8k_1k_2(d^4-h^4)} \right]^2 \right\}^{1/2}. \qquad (4.52)$$

The critical value $U_{\rm c}$ of the prominence potential energy, corresponding to these $x_{\rm m}$ and $z_{\rm c}$, can be found as $U_{\rm c} = U(x_{\rm m}, z_{\rm c})$ with the function $U(x, z)$ given in Eq. (4.48). This critical value $U_{\rm c}$ describes the highest prominence potential energy, above which the prominence has enough energy to escape the potential dip, becoming unstable in the horizontal direction. Figure 4.9, left-hand panel illustrates the equipotential levels corresponding to the closed contours in the (x, z)–plane, including the critical value $U_{\rm c}$ with the critical space contour shown in red. According to the left-hand panel of Fig. 4.9, the horizontal coordinate of the potential energy local extrema always shows the maximum possible horizontal amplitude $x_{\rm m}$ allowing for the stable large amplitude prominence oscillations with energies being below the critical value of $U_{\rm c}$. However, because of the vertical asymmetry of the prominence potential energy (directly connected to the vertical asymmetry of the whole model, see Fig. 4.1 in Sec. 4.1), the corresponding critical value of the vertical coordinate, $z_{\rm c}$, in general may represent not the highest possible vertical oscillation amplitude. The latter, in turn, can be represented as (see Fig. 4.9):

$$z_{\rm m} = z_{\rm c} + \delta z, \qquad (4.53)$$

and implicitly determined by the condition $U(x = 0, z_{\rm m}) = U_{\rm c}$, with $U_{\rm c} = U(x_{\rm m}, z_{\rm c})$ and $z_{\rm c}$ and $x_{\rm m}$ given in Eqs. (4.51)–(4.52).

In the limit $d \gg h$, when the external photospheric currents are located at sufficiently large but finite distances from the prominence position, and hence the magnetic dip is significantly shallowed, the maximum horizontal oscillation amplitude $x_{\rm m}$ can be estimated by the lowest-order expansion with respect to a small parameter h/d, as $x_{\rm m} \approx d$. This coincides with the case considered by Kuperus and Raadu [1974], where d tends to infinity and the magnetic dip is completely degenerated, therefore purely horizontal oscillations are essentially impossible and vertical oscillations may have large amplitudes limited by the height of the prominence above the surface of the Sun only. In contrast, the developed model supports oscillations in both directions simultaneously, and the appearance of a maximum vertical amplitude, $z_{\rm m}$ given in (4.53), is attributed to the impact of nonlinear coupling between the horizontal and vertical modes.

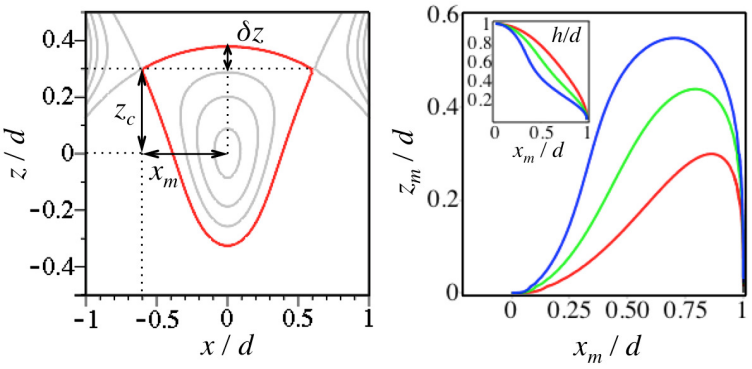

Figure 4.9: Left: space contours showing the equipotential levels of the prominence potential energy shown in Fig. 4.8, panel (a), up to the critical value shown in red and determined by $U_c = U(x_m, z_c)$, with $U(x, z)$, x_m, and z_c given in Eqs. (4.48), (4.52), and (4.51), respectively. Right: parametric plot showing the dependence of the maximum vertical amplitude, z_m of the prominence oscillation upon its maximum horizontal amplitude, x_m through the parameter h/d varying from 0 to 1 and shown in the left top corner (see Eqs. (4.52) and (4.53)). The dependences are shown for $k_1/k_2 = 0.9$ (blue), $k_1/k_2 = 0.5$ (green), and $k_1/k_2 = 0.2$ (red).

Dependence of the maximum horizontal and vertical amplitudes, x_m and z_m given by Eqs. (4.52)–(4.53) upon the intrinsic parameters of the model, including the limiting case $d \gg h$, is illustrated in Fig. 4.9, right panel. In contrast to the horizontal maximum amplitude x_m (4.52), which is a monotonically decreasing function of the prominence height above the photosphere, h, the vertical maximum amplitude z_m (4.53) has a maximum at a certain value of h. For example, for a nearly equal photospheric and prominence currents, $I = 0.9\,i$ (blue lines), the highest value of the maximum vertical amplitude appears for $h \approx 0.28\,d$ and is about $0.55\,d$, which forces the horizontal critical amplitude to be about $0.7\,d$.

Figure 4.10 shows the spatial structure of large amplitude transverse oscillations of the prominence, determined by the solution of the full set (4.4)–(4.5). Panel (a) illustrates the case when the prominence energy is slightly lower than the critical value of U_c, all amplitudes are always restricted by the maximum displacement (shown in red), corresponding to U_c, and hence the oscillations are always stable. Another case is shown in panel (b), when the prominence energy is slightly greater than U_c. In this regime oscillation amplitudes may exceed the critical values, which forces the prominence to become horizontally unstable in a few oscillation cycles. In physical units, for a non-eruptive prominence with mass density $\sim 10^{-10}\,\mathrm{kg\,m^{-3}}$, diameter ~ 10 Mm, and current $\sim 10^{10}$–10^{11} A, the values of the speeds mentioned

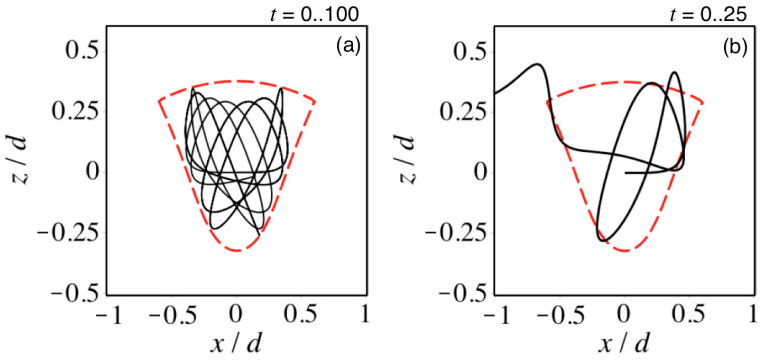

Figure 4.10: Displacements of the prominence in the large amplitude oscillatory regime, governed by Eqs. (4.4)–(4.5) with $h/d = 0.5$ and $k_1/k_2 = 0.5$, obtained with the initial conditions: $x(0) = 0$, $z(0) = 0$, $\dot{z} = 0$, and $\dot{x} = 0.26$ (in units of $\sqrt{k_2/\rho}$, panel (a)) and $\dot{x} = 0.3$ (same units, panel (b)). Time t is measured in units of $\sqrt{\rho d^2/k_2}$.

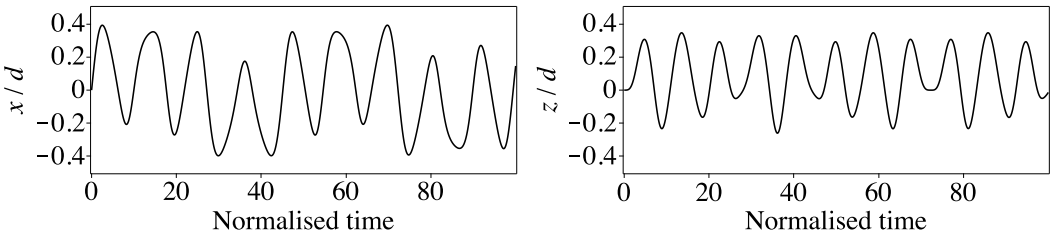

Figure 4.11: Temporal quasi-periodic variations of the horizontal (left-hand) and vertical (right-hand) displacements of the prominence in the large amplitude oscillatory regime shown in the left-hand panel of Fig. 4.10. Time is normalised to $\sqrt{\rho d^2/k_2}$.

in the captions, would correspond to about 13–151 km s^{-1}. It should be mentioned that in the stable regime shown in panel (a) of Fig. 4.10, the horizontally and vertically polarised modes are not strictly periodic, but could be considered as quasi-periodic with a relatively stable oscillation period and slowly modulated amplitude (see Fig. 4.11).

Periods of large amplitude oscillations

In this section typical periods of large amplitude nonlinear transverse oscillations in both horizontal and vertical directions are estimated analytically. For this, the conditions $z = 0$ and $x = 0$ are used in the equations of motion (4.4) and (4.5), respectively. In order to avoid the prominence instability caused by the nonlinear

mode coupling, the oscillation amplitudes in both directions are restricted to be lower than or equal to x_{m} (4.52) and z_{m} (4.53). The latter means that the prominence oscillates strictly inside the potential dip shown in Fig. 4.8, panel (a), and hence the oscillations are always stable.

Substituting $z = 0$ in the equation of motion along the horizontal axis (4.4), one can obtain its first integral representing the prominence's conservation energy law in the horizontal direction,

$$\frac{\rho}{2}\left(\frac{d\,x}{d\,t}\right)^2 + U_x(x) = \mathcal{E}_x, \tag{4.54}$$

where

$$U_x = -\frac{k_1}{2}\ln\left[\frac{(d^2-x^2)^2 + 2(d^2+x^2)h^2 + h^4}{(d^2+h^2)^2}\right]$$

is the prominence potential energy in the horizontal direction, which can be derived from Eq. (4.48) in the limit $z = 0$. The constant $\mathcal{E}_x$ in Eq. (4.54) shows the total energy of horizontal oscillations and can be obtained from the initial conditions $\dot{x}(0) = 0$ and $x(0) = A_x$, as

$$\mathcal{E}_x = -\frac{k_1}{2}\ln\left[\frac{(d^2-A_x^2)^2 + 2(d^2+A_x^2)h^2 + h^4}{(d^2+h^2)^2}\right],$$

with A_x being the horizontal oscillation amplitude.

The period P_x of the horizontal oscillations of an arbitrary amplitude as a function of the oscillation amplitude A_x and intrinsic parameters of the model, can be derived from Eq. (4.54) as

$$P_x = 4\sqrt{\rho}\int_0^{A_x}\frac{d\,x}{\sqrt{2(\mathcal{E}_x - U_x)}}, \tag{4.55}$$

where the functions U_x and $\mathcal{E}_x$ are determined in Eq. (4.54). Note, that for the case when the oscillation amplitude A_x is small, considered in Sec. 4.1, the period (4.55) becomes independent of the amplitude and reduces to Eq. (4.12).

The equation of motion along the vertical axis, (4.5), integrated once, leads to the conservation energy law in the vertical direction

$$\frac{\rho}{2}\left(\frac{d\,z}{d\,t}\right)^2 + U_z(z) = \mathcal{E}_z, \tag{4.56}$$

where the vertical potential energy, obtained from Eq. (4.48) with $x = 0$, is

$$U_z = -\frac{k_1}{2} \ln \left[\frac{d^4 + 2d^2(h+z)^2 + (h+z)^4}{(d^2+h^2)^2} \right] - k_2 \ln \left[\frac{2h+z}{2h} \right] + \rho g z,$$

and the total vertical oscillation energy can be determined from the initial conditions $\dot{z}(0) = 0$ and $z(0) = A_z$, with A_z being the vertical oscillation amplitude, as

$$\mathcal{E}_z = -\frac{k_1}{2} \ln \left[\frac{d^4 + 2d^2(h+A_z)^2 + (h+A_z)^4}{(d^2+h^2)^2} \right] - k_2 \ln \left[\frac{2h+A_z}{2h} \right] + \rho g A_z.$$

The vertical equilibrium condition (4.2) can be used in the above expressions for U_z and $\mathcal{E}_z$ to re-write the gravitational term ρg with the use of h, d, k_1, and k_2. The subsequent integration of Eq. (4.56) allows one to derive the approximate dependence of the period of arbitrarily large amplitude vertical oscillations upon the parameters of the model and the vertical oscillation amplitude A_z as

$$P_z = 4\sqrt{\rho} \int_0^{A_z} \frac{d\,z}{\sqrt{2(\mathcal{E}_z - U_z)}}, \tag{4.57}$$

with the functions U_z and $\mathcal{E}_z$ given above in Eq. (4.56). Similarly to the horizontal case, period (4.57) loses its dependence on the amplitude and reduces to Eq. (4.8) for small values of A_z.

Dependences of the horizontal and vertical oscillation periods, P_x (4.55) and P_z (4.57) upon the oscillation amplitudes A_x and A_z, respectively, are illustrated in Fig. 4.12 for different sets of the equilibrium parameters of the model, taken in the range $h < d$ and $k_1 < k_2$. In these examples the amplitudes A_z and A_x were additionally restricted by the maximum values of z_m (4.53) and x_m (4.52), respectively, corresponding to each particular set of parameters. The latter guarantees the prominence oscillations being always stable, even in the case of strong coupling between horizontal and vertical modes. More specifically, in the limiting case of small amplitudes, the periods in all panels are nearly constant, which coincides with the linear theory results obtained in Sec. 4.1, where the oscillations were found to be isochronous, i.e. the oscillation periods are independent of the oscillation amplitude (see Eqs. (4.8) and (4.12)). In contrast, in the nonlinear large amplitude regime the horizontal period P_x was found to be always increasing with the amplitude A_x (panels (a) and (b) in Fig. 4.12), with the highest increase appearing for larger values of h/d (panel (a)) and lower values of k_1/k_2 (or I/i, panel (b)). The dependence of the vertical period P_z upon the vertical amplitude A_z in the nonlinear case shows rather different behaviour (panels (c) and (d)). Namely, it increases with the amplitude

for lower values of h/d and k_1/k_2, and then changes its gradient to a negative one for higher values of these two parameters, through a transient state (green and blue lines in panels (c) and (d), respectively), where the periods are nearly constant for all allowed amplitudes. However, the period P_z was detected to be weakly dependent upon the amplitude A_z. Indeed, the nonlinear relative change of the vertical period P_z with the amplitude is of several percent only for all examples shown in panels (c) and (d).

4.2.3 Summary of results and conclusions

An analytical model of finite amplitude transverse oscillations of massive quiescent current-carrying prominences in a magnetic field dip was developed, representing a synthesis of the Kippenhahn–Schlüter [Kippenhahn and Schlüter, 1957] and Kuperus–Raadu [Kuperus and Raadu, 1974] models. The model accounts for the effect of a non-zero value of the electric current in the prominence, and is based upon the electromagnetic interaction between the prominence current and the external photospheric currents producing a magnetic dip. The prominence nonlinear oscillatory dynamics is determined by the oscillation amplitude and by the parameters of the initial equilibrium: value of the prominence current, its mass and position above the photosphere, and the properties of the magnetic dip. The equations of motion in the horizontal and vertical directions, (4.14)–(4.15) were derived and analysed for weakly nonlinear oscillations, which account for the effects of the quadratic nonlinearity. Also, the fully nonlinear exact set of the governing equations in both directions, (4.4)–(4.5) was studied.

Unlike the small amplitude case considered in Sec. 4.1, finite amplitude horizontal and vertical oscillations are found to be coupled with each other. In a weakly nonlinear case the mode coupling is governed by set (4.14)–(4.15). It represents an asymmetric nature of the mode coupling mechanism, i.e. the horizontal displacement is always able to generate the vertical displacement (see panels (a) and (d) in Fig. 4.6), while a pure vertical mode is fully uncoupled with the horizontal one. Such asymmetry in the coupling mechanism can be attributed to a vertical asymmetry of the initial equilibrium of the model (see Fig. 4.1 in Sec. 4.1). The efficiency of the coupling between the horizontal and vertical modes increases with the oscillation amplitude. In the case of oblique perturbations of the prominence, the mode coupling was detected to be more efficient for smaller angles between the direction of the initial perturbation and the horizontal axis, and is asymptotically degenerated when the prominence is perturbed almost perpendicular to the horizontal axis (see Fig. 4.7). For the case shown in Fig. 4.7 with $h = 0.5d$ and $I = 0.5i$, the ratio of

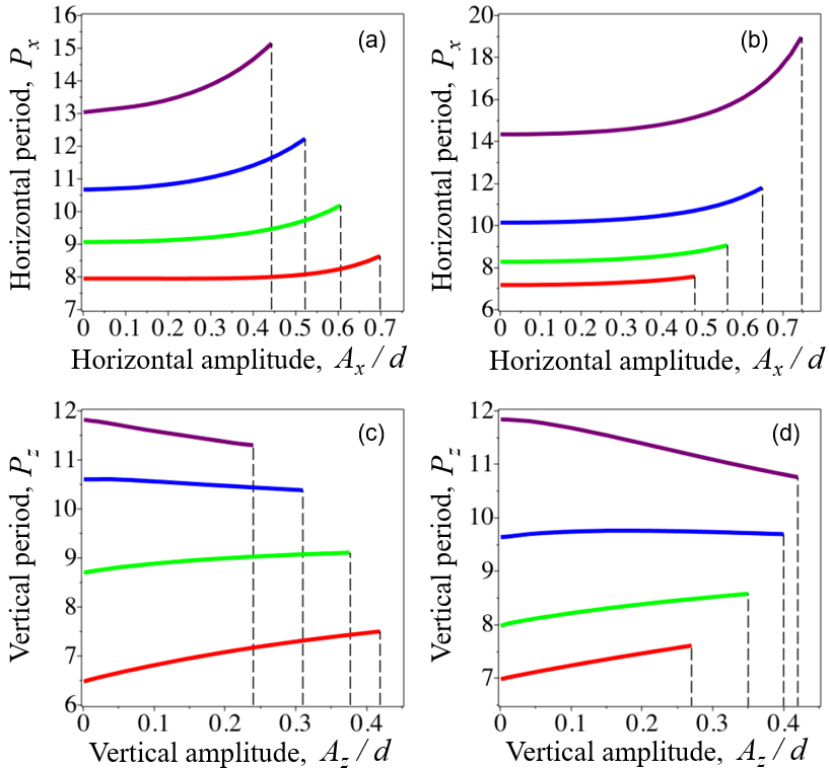

Figure 4.12: Dependences of periods of the horizontal and vertical oscillations, P_x (4.55) and P_z (4.57), respectively, upon the corresponding amplitudes, A_x and A_z, shown for different sets of the equilibrium parameters of the model. Panel (a): $h/d = 0.7$ (purple), 0.6 (blue), 0.5 (green), 0.4 (red); $k_1/k_2 = 0.5$. Panel (b): $h/d = 0.5$; $k_1/k_2 = 0.2$ (purple), 0.4 (blue), 0.6 (green), 0.8 (red). Panel (c): $h/d = 0.7$ (purple), 0.6 (blue), 0.5 (green), 0.4 (red); $k_1/k_2 = 0.5$. Panel (d): $h/d = 0.5$; $k_1/k_2 = 0.75$ (purple), 0.6 (blue), 0.4 (green), 0.2 (red). Vertical dashed lines indicate the maximum possible amplitudes, $x_{\rm m}$ and $z_{\rm m}$, determined by Eqs. (4.52) and (4.53), respectively, in each case. Periods P_z and P_x are measured in the units of $\sqrt{\rho d^2/k_2}$.

the maximum vertical and horizontal large amplitude displacements was found to be of about 0.5–0.7, even when the initial attack angles with respect to the horizon are small (approximately up to 25° with respect to the horizontal axis). The latter shows that the direction of the initial driver plays an important role in the initiation of the filament transverse oscillations, and due to strong mode coupling both vertically and horizontally polarised large amplitude displacements can be expected to be simultaneously detectable in observations, even if the initial perturbation, for example a global coronal shock wave, is directed almost horizontally [e.g. Berger et al., 2008; Shen et al., 2014b]. It should be pointed out, that in addition to the numerical studies based on the operation of the Kelvin–Helmholtz instability during the prominence evolution [e.g. Terradas et al., 2016], the designed model suggests an alternative mechanism for the excitation of the filament displacements in the direction perpendicular to the direction of the initial driver by the nonlinear mode coupling.

Spatial structure and temporal evolution of transverse oscillations of the prominence in a weakly nonlinear case are described by the general analytical solution of set (4.14)–(4.15), given by Eqs. (4.26)–(4.27). In the special case when the frequency of the vertical mode is twice the horizontal mode frequency, $\omega_2 = 2\omega_1$, solutions (4.26)–(4.27) imply a nonlinear resonance. The resonant condition written through the physical parameters of the initial equilibrium of the prominence is given by Eq. (4.28) and illustrated in Fig. 4.4. Prominence oscillatory dynamics in both resonant and non-resonant cases is shown in Fig. 4.6. Its space trajectories exhibit a Lissajous-like behaviour, with a limit cycle of a symmetric hourglass shape (Fig. 4.5 and panel (c) in Fig. 4.6), appearing in the resonant case and determined analytically by Eq. (4.45). Such a non-trivial polarisation of transverse oscillations is caused by the nonlinear coupling between vertical and horizontal displacements, described above, and potentially may be detected in observations [Hershaw et al., 2011; Pant et al., 2015].

Analysis of the fully nonlinear equations of motion (4.4)–(4.5) allowed for a comprehensive study of the prominence transverse oscillations of arbitrarily large amplitudes. More specifically, the set of equations (4.4)–(4.5) was found to be of a Hamiltonian form with the potential energy of the prominence, derived in the exact analytical form in Eq. (4.48). In the range of parameters $h < d$ and $I < i$ (full stability region in Fig. 4.4), the potential energy (4.48) was revealed to have a dip of a finite depth (panel (a) in Fig. 4.8), corresponding to a so-called metastable state of the prominence. It is characterised by a critical value of the prominence potential energy, below which the prominence is always stable and experiences oscillations

within the potential dip. In contrast, when its energy exceeds this threshold value, the prominence may escape the dip and become unstable in the horizontal direction, moving horizontally along the surface of the Sun and still remaining at a certain height. In other words, this equilibrium is always stable to small amplitude oscillations, while it becomes unstable when the amplitude exceeds a certain threshold. In particular, in this regime the prominence may experience several oscillation cycles of varying polarisation, and then become unstable (see the right-hand panel of Fig. 4.10). A similar behaviour was observed by Isobe and Tripathi [2006]. Similarly to a weakly nonlinear case (Fig. 4.6), large amplitude oscillatory trajectories also have a Lissajous-like shape, which is worth checking in observations. The maximum vertical and horizontal oscillation amplitudes, as well as the critical space contour, corresponding to that critical value of the prominence potential energy, are derived in Eqs. (4.52)–(4.53) and illustrated in Fig. 4.9. For a broad range of the intrinsic physical parameters of the model, h, d, i, and I, determining the initial equilibrium of the prominence, the values of the maximum vertical and horizontal amplitudes were found to be close to each other by an order of magnitude and comparable with typical geometrical sizes of the system, h and d. In the limiting case of large distances between the external photospheric currents, d, when the magnetic dip is sufficiently suppressed, the maximum horizontal amplitude, $x_{\rm m}$ is of about d, which is consistent with the Kuperus–Raadu model [Kuperus and Raadu, 1974].

Typical periods of horizontal and vertical large amplitude oscillations as functions of the oscillation amplitude and the prominence equilibrium parameters were estimated analytically in Eqs. (4.55) and (4.57). The horizontal oscillation period (panels (a) and (b) in Fig. 4.12) was found to increase with the amplitude and height of the filament above the photosphere, which is consistent with the recent observational results [Hershaw et al., 2011; Hillier et al., 2013]. In turn, the vertical oscillation period (panels (c) and (d) in Fig. 4.12) appears to increase with the amplitude for lower values of the ratios h/d and I/i, and decreases for higher values of these two parameters. In the limiting cases when $h \ll d$ and $i \approx I$, horizontal oscillations were found to be nearly isochronous, i.e. the oscillation periods weakly depend on the oscillation amplitude. Similarly, the approximate isochronous nature of the vertically polarised mode is detected for $h/d \approx 0.5$ and $I/i \approx 0.6$. Hence, in these special cases analytical dependences (4.8) and (4.12) of oscillation periods upon the intrinsic parameters of the magnetic system, derived for small amplitude oscillations in Sec. 4.1, can be used with a good certainty for observed transverse oscillations of an arbitrary amplitude. Another interesting feature clearly seen in Fig. 4.12 is that the dependences of the horizontal period upon the amplitude for

all shown examples have positive second derivatives (see panels (a) and (b)), while the corresponding dependences of the vertical period (panels (c) and (d)) are seen to have negative second derivatives. The latter fact could be straightforwardly used to distinguish between polarisations of observed large amplitude prominence oscillations as this quantity is rarely detectable without spectroscopic instruments. For example, Hillier et al. [2013] performed a statistical study of transverse finite amplitude oscillations in vertical prominence threads. They revealed a power law index in the dependence of the oscillation period upon the oscillation amplitude to be about 1.35, with a positive sign of its second derivative. According to the developed analysis, the considered transverse oscillations are of a horizontal polarisation, that agrees with the results of Hillier et al. [2013], where the oscillations were believed to be driven by horizontal photospheric motions.

Chapter 5

Conclusions

The thesis addresses observational and theoretical aspects of non-stationary, multi-modal and nonlinear oscillatory processes in the solar atmosphere. Such processes are ubiquitous, may be initiated by impulsive energy releases in active regions, or occur in a steadily varying plasma of the quiet Sun. Likewise, they are usually detected in almost all observational bands, with typical periods ranging from a fraction of a second up to tens of years and longer. These phenomena may have a crucial impact on both the evolution of the plasma of the solar atmosphere itself and the formation of the space climate in the near-Earth environment. Their unique properties (namely, non-stationarity and irregularity of oscillation profiles, finite amplitudes) lead to the need for advanced techniques allowing for their adequate analysis, and, on the other hand, for construction of corresponding analytical nonlinear models accounting for the observed effects and possessing the predictive capability. This thesis attacks both these challenges.

Chapter 1 introduces key elements of the solar atmosphere, i.e. its radial stratification, properties and morphology of the plasma of its different layers, describes their main building blocks: faculae, sunspots, granules and supergranules in the photosphere; chromospheric magnetic network and spicules; coronal magnetic flux tubes, loops and prominences. A particular attention is given to the physics of solar flares, spatially localised sudden brightenings of electromagnetic emission across almost the whole electromagnetic spectrum, on a time scale of several minutes. Observational manifestations of flaring events, as well as the standard model of a solar flare with magnetic reconnection operating as an effective engine, are considered in detail. An interesting intrinsic feature of the majority of flaring energy releases, quasi-periodic pulsations (QPP), is also comprehensively discussed. Observed QPPs are often seen to have clear nonlinear or multi-modal signatures:

non-stationary periods correlating with the oscillation amplitudes and non-harmonic profile shapes. From the theoretical point of view, possible mechanisms for QPPs, based on the modulation of the flaring emission by MHD eigen modes of coronal plasma structures (modelled as a plasma cylinder), and on the interaction of the flaring sites with external MHD oscillations, are also described. Another class of mechanisms which is also believed to be responsible for QPPs, is attributed to the "magnetic dripping" models. They are based on repetitive (or stochastic) regimes of magnetic reconnection and nonlinear oscillations of current sheets, and thus are able to address the observed sophisticated properties of QPPs. Observational evidence of oscillations in another group of intriguing objects visible in the solar corona, quiescent prominences, is also given in Chapter 1. These cool and dense plasma blobs magnetically supported against gravity in the much hotter and more rarefied environment, are seen to oscillate with both low (up to 5 $\mathrm{km\,s^{-1}}$) and large (typically greater than 10 $\mathrm{km\,s^{-1}}$) amplitudes. Analytical models based on the concepts of toroidal and linear currents are introduced.

Chapter 2 exposes original works on the spectral analysis of solar quasi-periodic signals with the Hilbert–Huang transform (HHT) technique. In contrast to standard Fourier transform based techniques, this method operates self-adaptively and, hence, is essentially suitable for analysing observational non-stationary and nonlinear time-series. More specifically, Sec. 2.2 presents an incorporation of the coloured noise (whose power spectral density S depends upon the frequency f as $S \propto f^{-\alpha}$) statistics into the HHT analysis, in the application to randomly distributed processes in the solar atmosphere. It designs a recipe allowing for clear distinguishing between statistically significant oscillatory phenomena and superimposed frequency-dependent background processes. As an illustration, EUV emission intensity variations observed with SDO/AIA in the upper photosphere, chromosphere, and corona, were processed with the developed technique. The signals were indeed found to be mainly represented by a combination of different coloured noises characterised by a specific value of the power law indices α, which in turn vary with both the height above the surface of the Sun and when transiting from the quiet sun region to the sunspot umbra. On the other hand, such clear periodicities as, for example, 3-min sunspot oscillations were detected to lie well above the noise level.

Section 2.3 uses the scheme developed in Sec. 2.2 for detection of a long-period quasi-periodic oscillation of a small-scale photospheric magnetic element involved in a facula formation higher in the chromosphere. The original observational time-series of the average line-of-sight component of the magnetic field in the structure, obtained with SDO/HMI, was found to consist of white ($\alpha \approx 0$) and pink

($\alpha \approx 1$) noisy components and a single oscillatory mode with statistically significant properties. Its oscillation period grows with the amplitude from about 80 to 230 min, while the mean magnetic field in the oscillating structure is seen to decrease. Such a behaviour could be interpreted either by the dynamical interaction of the structure with the boundaries of supergranula cells in the region of interest or in terms of the vortex shedding appearing during the magnetic flux emergence. However, a specific mechanism for the observed oscillation is still to be revealed.

A comprehensive search for long-term periodicities associated with solar magnetic activity cycles with the use of the HHT technique improved by the ensemble empirical mode decomposition (EEMD), is shown in Sec. 2.4. The observational interval spans about 29 yr (from 1985 to 2014), which corresponds to cycles 22, 23, and 24. Solar activity periodicities (including the 11 yr cycle) are known to vary in both the amplitude and length [e.g. Hathaway, 2010], which justifies the use of the HHT method for their analysis. The analysed raw data signals of five different observational proxies: the 10.7 cm radio flux intensity, the helioseismic frequency shift, and the sunspot area signals recorded from the whole solar disc, and separately from the Northern and Southern hemispheres, provided by the National Geophysical Data Center, BiSON observatories, and the Royal Observatory Greenwich, respectively, were expanded into a set of intrinsic modes. Instant and mean periods of each empirical mode were determined with the use of the Hilbert transform applied independently to each mode. The detected periodicities were attributed to three distinct groups: short-term or the Reiger-type variations (with periods shorter than 0.5 yr); quasi-biennial oscillations (QBO, with typical periods from 0.5 yr to 3.9 yr), and longer periodicities, such as the 11 yr cycle. A particular emphasis was put on the effectiveness of HHT for characterising periodicities in the helioseismic data, which are necessarily limited in their time resolution. The use of the sunspot area signals separately from the Northern and Southern hemispheres allowed for establishing signatures of the North–South (NS) asymmetry in the solar hemispheres evolution. Evidence of the "extended" solar minimum between cycles 23 and 24 was also detected. In addition, statistical properties of several shorter-period modes were found to indicate their relation to randomly distributed processes in the solar atmosphere, according to the noise-test scheme developed in Sec. 2.2.

The last section of Chapter 2, Sec. 2.5, shows the HHT spectral analysis of a multi-modal QPP observed in the microwave emission of an X3.2-class solar flare, with the NoRH and NoRP instruments. It was established that the QPP consists of at least three well-defined intrinsic modes, with mean periods of 15, 45, and 100 s. All the modes have quasi-harmonic behaviour with different modulation patterns.

Namely, the 15 and 100 s intrinsic modes reveal decaying oscillations, while the 45 s mode has a wave-train behaviour. Additionally, the instant period of the 100 s mode was found to decrease with the amplitude, which could be a manifestation of nonlinear effects, when the oscillation period is determined by the finite amplitude. Dynamical properties of detected intrinsic modes indicate that the 100 s and 15 s oscillations are likely to be associated with fundamental kink and sausage modes of the flaring loop, respectively.

Thus, Chapter 2 demonstrates that the HHT technique is a useful tool for spectral analysis of solar quasi-periodic signals of limited time resolution and with pronounced non-stationarity and anharmonicity. It was found to be effective in the analyses of time-series with different time scales, from tens of seconds (e.g. in QPPs, Sec. 2.5) to minutes (e.g. in sunspots, Sec. 2.2), hours (small-scale magnetic structures, Sec. 2.3), days, months, and years (solar activity periodicities, Sec. 2.4).

Chapter 3 develops analytical models for non-uniform equilibrium (Sec. 3.1) and nonlinear oscillations (Sec. 3.2) of a central element of active phenomena in the solar atmosphere, current sheets. More specifically, in realistic physical systems, inhomogeneities of the plasma temperature and density across the current sheet may arise naturally due to the boundary conditions or local plasma heating, for example via the Ohmic heating in the region of high electric current density or current-driven microturbulences. Hence, an advanced analytical model consistent with both the kinetic and MHD limits, of a one-dimensional current sheet, accounting for inhomogeneities of the macroscopic plasma parameters in the transverse direction is needed and is designed in Sec. 3.1. In the developed model, the current sheet is assumed to be force-free (i.e. with the field-aligned current density), and the plasma density and temperature may either be enhanced or depleted in the central region of the current sheet. Such current sheets with a non-uniform transverse profile of the Alfvén speed represent effective waveguides for MHD waves (in particular, for fast magnetoacoustic modes). Hence, the equilibrium model developed in Sec. 3.1 could be used as a good starting point in numerical simulations of MHD waves propagating along solar flare current sheets.

An important phenomenon in the evolution of current-carrying magnetic flux tubes (e.g. twisted loops) in the solar corona is their coalescence and subsequent formation of current sheets in the interface region. Section 3.2 develops an analytical model of highly nonlinear oscillations occurring during the coalescence of two magnetic flux ropes, based upon a two-fluid hydrodynamic description of the plasma. The model accounts for the effect of electric charge separation, and describes sausage oscillations of the current sheet formed by the coalescence. The oscillation period is

determined by the current sheet thickness, the plasma parameter β, and the oscillation amplitude. The oscillation periods are found typically to be greater or about the ion plasma oscillation period, while thinner/thicker current sheets oscillate with shorter/longer periods, respectively. In the nonlinear regime, the oscillations of the ion and electron concentrations have a shape of narrow symmetric spikes.

An analytical model for transverse oscillations of quiescent prominences embedded in the magnetised environment with a magnetic field dip, is developed in Chapter 4. Such magnetic configurations are often observed in the corona, and are believed to provide the equilibrium of quiescent prominences, counteracting the gravity. The prominence is modelled as a massive line current located above the photosphere and interacting with the magnetised environment via the Lorentz force. In this concept the magnetic dip is produced by two external current sources located at the photosphere. The mechanism accounts for the electrical conductivity of the photosphere, described by the inclusion of the virtual "mirror" current. Section 4.1 considers small perturbations of the initial equilibrium of the prominence, forcing it to oscillate in the linear regime, where the horizontal and vertical motions are independent of each other. In this case, properties of both vertical and horizontal oscillations are determined by the value of the prominence current, its density and height above the photosphere, and the parameters of the magnetic dip. The prominence can be stable in both horizontal and vertical directions simultaneously when the prominence current dominates in the system and its height is less than the half-distance between the photospheric sources. In contrast, finite amplitude horizontal and vertical oscillations (Sec. 4.2) were found to be strongly coupled between each other. The coupling is more efficient for larger amplitudes and smaller attack angles between the direction of the driver and the horizontal axis. The spatial structure of oscillations is represented by Lissajous-like curves with the limit cycle of an hourglass shape, appearing in the resonant case, when the frequency of the vertical mode is twice the horizontal mode frequency. A metastable equilibrium of the prominence was also revealed, which is stable to small amplitude displacements, and becomes horizontally unstable, when the amplitude exceeds a certain threshold value. In the nonlinear regime, the oscillation periods were found to be also dependent upon the oscillation amplitude. The developed model can be directly used for the interpretation of observational results and seismological purposes.

The carried out research develops and applies advanced techniques for the analysis of nonlinear and multi-modal non-stationary oscillatory processes in different plasma systems of the solar atmosphere and interior, and designs comprehensive theoretical models of these processes.

Bibliography

B. Abraham-Shrauner. Force-free Jacobian equilibria for Vlasov-Maxwell plasmas. *Physics of Plasmas*, 20(10):102117, October 2013. doi: 10.1063/1.4826502.

M. Akbari-Moghanjoughi. Universal aspects of localized excitations in graphene. *Journal of Applied Physics*, 114(7):073302–073302, August 2013. doi: 10.1063/1.4818707.

M. Akbari-Moghanjoughi. Large-amplitude solitons in gravitationally balanced quantum plasmas. *Physics of Plasmas*, 21(8):082707, August 2014. doi: 10.1063/1.4892556.

J. Andries, T. van Doorsselaere, B. Roberts, G. Verth, E. Verwichte, and R. Erdélyi. Coronal Seismology by Means of Kink Oscillation Overtones. *Space Science Reviews*, 149:3–29, December 2009. doi: 10.1007/s11214-009-9561-2.

S. Anfinogentov, V. M. Nakariakov, M. Mathioudakis, T. Van Doorsselaere, and A. F. Kowalski. The Decaying Long-period Oscillation of a Stellar Megaflare. *Astrophysics Journal*, 773:156, August 2013. doi: 10.1088/0004-637X/773/2/156.

H. M. Antia and S. Basu. Temporal Variations of the Rotation Rate in the Solar Interior. *Astrophysics Journal*, 541:442–448, September 2000. doi: 10.1086/309421.

P. Antolin, T. Yokoyama, and T. Van Doorsselaere. Fine Strand-like Structure in the Solar Corona from Magnetohydrodynamic Transverse Oscillations. *Astrophysics Journal Letters*, 787:L22, June 2014. doi: 10.1088/2041-8205/787/2/L22.

P. Antolin, T. J. Okamoto, B. De Pontieu, H. Uitenbroek, T. Van Doorsselaere, and T. Yokoyama. Resonant Absorption of Transverse Oscillations and Associated Heating in a Solar Prominence. II. Numerical Aspects. *Astrophysics Journal*, 809: 72, August 2015. doi: 10.1088/0004-637X/809/1/72.

U. Anzer. Global prominence oscillations. *Astronomy and Astrophysics*, 497:521–524, April 2009. doi: 10.1051/0004-6361/200811107.

I. Arregui, R. Oliver, and J. L. Ballester. Prominence Oscillations. *Living Reviews in Solar Physics*, 9, April 2012. doi: 10.12942/lrsp-2012-2.

A. V. Artemyev, A. A. Petrukovich, A. G. Frank, R. Nakamura, and L. M. Zelenyi. Intense current sheets in the magnetotail: Peculiarities of electron physics. *Journal of Geophysical Research (Space Physics)*, 118:2789–2799, June 2013. doi: 10.1002/jgra.50297.

A. V. Artemyev, I. Y. Vasko, and S. Kasahara. Thin current sheets in the Jovian magnetotail. *Plan. Sp. Sci.*, 96:133–145, June 2014. doi: 10.1016/j.pss.2014.03.012.

A. Asai, T. T. Ishii, H. Isobe, R. Kitai, K. Ichimoto, S. UeNo, S. Nagata, S. Morita, K. Nishida, D. Shiota, A. Oi, M. Akioka, and K. Shibata. First Simultaneous Observation of an Hα Moreton Wave, EUV Wave, and Filament/Prominence Oscillations. *Astrophysics Journal Letters*, 745:L18, February 2012. doi: 10.1088/2041-8205/745/2/L18.

M. J. Aschwanden. Theory of radio pulsations in coronal loops. *Solar Physics*, 111: 113–136, March 1987. doi: 10.1007/BF00145445.

O. G. Badalyan and V. N. Obridko. North-South asymmetry of the sunspot indices and its quasi-biennial oscillations. *New Astronomy*, 16:357–365, October 2011. doi: 10.1016/j.newast.2011.01.005.

T. Bai. Periodicities in Solar Flare Occurrence: Analysis of Cycles 19-23. *Astrophysics Journal*, 591:406–415, July 2003. doi: 10.1086/375295.

T. Bai and P. A. Sturrock. The 154-day and related periodicities of solar activity as subharmonics of a fundamental period. *Nature*, 350:141–143, March 1991. doi: 10.1038/350141a0.

M. Balikhin and M. Gedalin. Generalization of the Harris current sheet model for non-relativistic, relativistic and pair plasmas. *Journal of Plasma Physics*, 74: 749–+, April 2008. doi: 10.1017/S002237780800723X.

J. L. Ballester, R. Oliver, and M. Carbonell. Return of the Near 160 Day Periodicity in the Photospheric Magnetic Flux during Solar Cycle 23. *Astrophysics Journal Letters*, 615:L173–L176, November 2004. doi: 10.1086/426430.

J. L. Ballester, M. Carbonell, R. Soler, and J. Terradas. Prominence oscillations: Effect of a time-dependent background temperature. *Astronomy and Astrophysics*, 591:A109, June 2016. doi: 10.1051/0004-6361/201527953.

M. Bárta, B. Vršnak, and M. Karlický. Dynamics of plasmoids formed by the current sheet tearing. *Astronomy and Astrophysics*, 477:649–655, January 2008. doi: 10.1051/0004-6361:20078266.

V. S. Bashkirtsev and G. P. Mashnich. Some regularities of velocity oscillations in prominences. *Astronomy and Astrophysics*, 279:610–614, November 1993.

S. Basu, A.-M. Broomhall, W. J. Chaplin, and Y. Elsworth. Thinning of the Sun's Magnetic Layer: The Peculiar Solar Minimum Could Have Been Predicted. *Astrophysics Journal*, 758:43, October 2012. doi: 10.1088/0004-637X/758/1/43.

G. Bazilevskaya, A.-M. Broomhall, Y. Elsworth, and V. M. Nakariakov. A Combined Analysis of the Observational Aspects of the Quasi-biennial Oscillation in Solar Magnetic Activity. *Space Science Reviews*, 186:359–386, December 2014. doi: 10.1007/s11214-014-0068-0.

E. E. Benevolenskaya. Dynamics of the solar magnetic field from SOHO/MDI. *Astronomische Nachrichten*, 331:63, January 2010. doi: 10.1002/asna.200911251.

A. O. Benz. Flare Observations. *Living Reviews in Solar Physics*, 5:1, February 2008. doi: 10.12942/lrsp-2008-1.

T. E. Berger, R. A. Shine, G. L. Slater, T. D. Tarbell, A. M. Title, T. J. Okamoto, K. Ichimoto, Y. Katsukawa, Y. Suematsu, S. Tsuneta, B. W. Lites, and T. Shimizu. Hinode SOT Observations of Solar Quiescent Prominence Dynamics. *Astrophysics Journal Letters*, 676:L89, March 2008. doi: 10.1086/587171.

T. E. Berger, G. Slater, N. Hurlburt, R. Shine, T. Tarbell, A. Title, B. W. Lites, T. J. Okamoto, K. Ichimoto, Y. Katsukawa, T. Magara, Y. Suematsu, and T. Shimizu. Quiescent Prominence Dynamics Observed with the Hinode Solar Optical Telescope. I. Turbulent Upflow Plumes. *Astrophysics Journal*, 716:1288–1307, June 2010. doi: 10.1088/0004-637X/716/2/1288.

V. S. Beskin, S. V. Chernov, C. R. Gwinn, and A. A. Tchekhovskoy. Radio Pulsars. *Space Science Reviews*, June 2015. doi: 10.1007/s11214-015-0173-8.

J. Birn, M. F. Thomsen, and M. Hesse. Electron acceleration in the dynamic magnetotail: Test particle orbits in three-dimensional magnetohydrodynamic simulation fields. *Physics of Plasmas*, 11:1825–1833, May 2004. doi: 10.1063/1.1704641.

D. Biskamp. *Nonlinear Magnetohydrodynamics*. July 1997.

F. Boberg, H. Lundstedt, J. T. Hoeksema, P. H. Scherrer, and W. Liu. Solar mean magnetic field variability: A wavelet approach to Wilcox Solar Observatory and SOHO/Michelson Doppler Imager observations. *Journal of Geophysical Research (Space Physics)*, 107:1318, October 2002. doi: 10.1029/2001JA009195.

K. Bocchialini, F. Baudin, S. Koutchmy, G. Pouget, and J. Solomon. Oscillatory motions observed in eruptive filaments. *Astronomy and Astrophysics*, 533:A96, September 2011. doi: 10.1051/0004-6361/201016342.

E. Bosman, V. Bothmer, G. Nisticò, A. Vourlidas, R. A. Howard, and J. A. Davies. Three-Dimensional Properties of Coronal Mass Ejections from STEREO/SECCHI Observations. *Solar Physics*, 281:167–185, November 2012. doi: 10.1007/s11207-012-0123-5.

T. Bountis, H. Segur, and F. Vivaldi. Integrable Hamiltonian systems and the Painlevé property. *Phys. Rev. A*, 25:1257–1264, March 1982. doi: 10.1103/PhysRevA.25.1257.

C. S. Brady and T. D. Arber. Simulations of Alfvén and Kink Wave Driving of the Solar Chromosphere: Efficient Heating and Spicule Launching. *Astrophysics Journal*, 829:80, October 2016. doi: 10.3847/0004-637X/829/2/80.

A.-M. Broomhall, W. J. Chaplin, Y. Elsworth, S. T. Fletcher, and R. New. Is the Current Lack of Solar Activity Only Skin Deep? *Astrophysics Journal Letters*, 700:L162–L165, August 2009. doi: 10.1088/0004-637X/700/2/L162.

P. S. Cally. Leaky and non-leaky oscillations in magnetic flux tubes. *Solar Physics*, 103:277–298, February 1986. doi: 10.1007/BF00147830.

E. Camporeale and G. Lapenta. Model of bifurcated current sheets in the Earth's magnetotail: Equilibrium and stability. *Journal of Geophysical Research (Space Physics)*, 110:A07206, July 2005. doi: 10.1029/2004JA010779.

A. Canou and T. Amari. A Twisted Flux Rope as the Magnetic Structure of a Filament in Active Region 10953 Observed by Hinode. *Astrophysics Journal*, 715: 1566–1574, June 2010. doi: 10.1088/0004-637X/715/2/1566.

P. J. Cargill, J. Chen, and D. A. Garren. Oscillations and Evolution of Curved Current-carrying Loops in the Solar Corona. *Astrophysics Journal*, 423:854, March 1994. doi: 10.1086/173863.

F. Ceccherini, C. Montagna, F. Pegoraro, and G. Cicogna. Two-dimensional Harris-Liouville plasma kinetic equilibria. *Physics of Plasmas*, 12(5):052506, May 2005. doi: 10.1063/1.1899083.

P. J. Channell. Exact Vlasov-Maxwell equilibria with sheared magnetic fields. *Physics of Fluids*, 19:1541–1545, October 1976. doi: 10.1063/1.861357.

P. Charbonneau. Dynamo Models of the Solar Cycle. *Living Reviews in Solar Physics*, 7:3, December 2010. doi: 10.12942/lrsp-2010-3.

A. A. Chelpanov, N. I. Kobanov, and D. Y. Kolobov. Characteristics of oscillations in magnetic knots of solar faculae. *Astronomy Reports*, 59:968–973, October 2015. doi: 10.1134/S1063772915090036.

P. F. Chen and E. R. Priest. Transition-Region Explosive Events: Reconnection Modulated by p-Mode Waves. *Solar Physics*, 238:313–327, November 2006. doi: 10.1007/s11207-006-0215-1.

M. C. M. Cheung, F. Moreno-Insertis, and M. Schüssler. Moving magnetic tubes: fragmentation, vortex streets and the limit of the approximation of thin flux tubes. *Astronomy and Astrophysics*, 451:303–317, May 2006. doi: 10.1051/0004-6361:20054499.

R. Chin, E. Verwichte, G. Rowlands, and V. M. Nakariakov. Self-organization of magnetoacoustic waves in a thermally unstable environment. *Physics of Plasmas*, 17(3):032107, March 2010. doi: 10.1063/1.3314721.

I.-H. Cho, K.-S. Cho, V. M. Nakariakov, S. Kim, and P. Kumar. Comparison of Damped Oscillations in Solar and Stellar X-Ray flares. *Astrophysics Journal*, 830: 110, October 2016. doi: 10.3847/0004-637X/830/2/110.

N. Chorley, B. Hnat, V. M. Nakariakov, A. R. Inglis, and I. A. Bakunina. Long period oscillations in sunspots. *Astronomy and Astrophysics*, 513:A27, April 2010. doi: 10.1051/0004-6361/200913683.

P. Chowdhury and P. C. Ray. Periodicities of solar electron flare occurrence: analysis of cycles 21-23. *Monthly Notices of the Royal Astronomical Society*, 373:1577–1589, December 2006. doi: 10.1111/j.1365-2966.2006.11120.x.

S. Couvidat, J. Schou, J. T. Hoeksema, R. S. Bogart, R. I. Bush, T. L. Duvall, Y. Liu, A. A. Norton, and P. H. Scherrer. Observables Processing for the Helioseismic and Magnetic Imager Instrument on the Solar Dynamics Observatory. *Solar Physics*, 291:1887–1938, August 2016. doi: 10.1007/s11207-016-0957-3.

I. J. D. Craig and A. N. McClymont. Dynamic magnetic reconnection at an X-type neutral point. *Astrophysics Journal Letters*, 371:L41–L44, April 1991. doi: 10.1086/185997.

S. R. Cranmer. Self-Consistent Models of the Solar Wind. *Space Science Reviews*, 172:145–156, November 2012. doi: 10.1007/s11214-010-9674-7.

G. R. Davies, W. J. Chaplin, Y. Elsworth, and S. J. Hale. BiSON data preparation: a correction for differential extinction and the weighted averaging of contemporaneous data. *Monthly Notices of the Royal Astronomical Society*, 441:3009–3017, July 2014. doi: 10.1093/mnras/stu803.

I. De Moortel and P. Browning. Recent advances in coronal heating. *Royal Society of London Philosophical Transactions Series A*, 373:40269, April 2015. doi: 10.1098/rsta.2014.0269.

I. De Moortel and A. W. Hood. The damping of slow MHD waves in solar coronal magnetic fields. *Astronomy and Astrophysics*, 408:755–765, September 2003. doi: 10.1051/0004-6361:20030984.

I. De Moortel and V. M. Nakariakov. Magnetohydrodynamic waves and coronal seismology: an overview of recent results. *Royal Society of London Philosophical Transactions Series A*, 370:3193–3216, July 2012. doi: 10.1098/rsta.2011.0640.

L. H. Deng, B. Li, Y. Y. Xiang, and G. T. Dun. Multi-scale analysis of coronal Fe XIV emission: The role of mid-range periodicities in the Sun-heliosphere connection. *Journal of Atmospheric and Solar-Terrestrial Physics*, 122:18–25, January 2015. doi: 10.1016/j.jastp.2014.10.016.

B. R. Dennis and D. M. Zarro. The Neupert effect - What can it tell us about the impulsive and gradual phases of solar flares? *Solar Physics*, 146:177–190, July 1993. doi: 10.1007/BF00662178.

A. S. Deres and S. A. Anfinogentov. Measurement of the formation heights of UV and EUV emission above sunspot umbrae from observations of three-minute oscillations. *Astronomy Reports*, 59:959–967, October 2015. doi: 10.1134/S1063772915100017.

F.-L. Deubner and B. Fleck. Dynamics of the solar atmosphere. III - Cell-network distinctions of chromospheric oscillations. *Astronomy and Astrophysics*, 228:506–512, February 1990.

A. E. Dubinov and D. Y. Kolotkov. Ion-Acoustic Super Solitary Waves in Dusty Multispecies Plasmas. *IEEE Transactions on Plasma Science*, 40:1429–1433, May 2012. doi: 10.1109/TPS.2012.2189026.

A. E. Dubinov and M. A. Sazonkin. Nonlinear theory of ionic sound waves in a hot quantum-degenerate electron-positron-ion plasma. *Soviet Journal of Experimental and Theoretical Physics*, 111:865–876, November 2010. doi: 10.1134/S1063776110110178.

A. E. Dubinov, D. Y. Kolotkov, and M. A. Sazonkin. Nonlinear ion acoustic waves in a quantum degenerate warm plasma with dust grains. *Plasma Physics Reports*, 37:64–74, January 2011. doi: 10.1134/S1063780X10121037.

A. E. Dubinov, D. Y. Kolotkov, and M. A. Sazonkin. Nonlinear theory of ion-sound waves in a dusty electron-positron-ion plasma. *Journal of Technical Physics*, 57: 585–593, May 2012a. doi: 10.1134/S1063784212050088.

A. E. Dubinov, D. Y. Kolotkov, and M. A. Sazonkin. Supernonlinear Waves in Plasma. *Plasma Physics Reports*, 38:833–844, October 2012b. doi: 10.1134/S1063780X12090036.

G. A. Dulk. Radio emission from the sun and stars. *Annual review of astronomy and astrophysics*, 23:169–224, 1985. doi: 10.1146/annurev.aa.23.090185.001125.

P. M. Edwin and B. Roberts. Wave propagation in a magnetic cylinder. *Solar Physics*, 88:179–191, October 1983. doi: 10.1007/BF00196186.

Y. Elsworth, R. Howe, G. R. Isaak, C. P. McLeod, and R. New. Variation of low-order acoustic solar oscillations over the solar cycle. *Nature*, 345:322–324, May 1990. doi: 10.1038/345322a0.

T. Emonet, F. Moreno-Insertis, and M. P. Rast. The Zigzag Path of Buoyant Magnetic Tubes and the Generation of Vorticity along Their Periphery. *Astrophysics Journal*, 549:1212–1220, March 2001. doi: 10.1086/319469.

S. Eto, H. Isobe, N. Narukage, A. Asai, T. Morimoto, B. Thompson, S. Yashiro, T. Wang, R. Kitai, H. Kurokawa, and K. Shibata. Relation between a Moreton Wave and an EIT Wave Observed on 1997 November 4. *Astronomical Society of Japan, Publications*, 54:481–491, June 2002. doi: 10.1093/pasj/54.3.481.

J. W. Evans, R. Michard, and R. Servajean. Observational study of macroscopic inhomogeneities in the solar atmosphere. V. Statistical study of the time variations of the solar inhomogeneities. *Annales d'Astrophysique*, 26:368, February 1963.

X. Fang, D. Yuan, C. Xia, T. Van Doorsselaere, and R. Keppens. The Role of Kelvin-Helmholtz Instability for Producing Loop-top Hard X-Ray Sources in Solar Flares. *Astrophysics Journal*, 833:36, December 2016. doi: 10.3847/1538-4357/833/1/36.

C. J. Farrugia, V. A. Osherovich, and L. F. Burlaga. The non-linear evolution of magnetic flux ropes: 3. effects of dissipation. *Annales Geophysicae*, 15:152–164, February 1997. doi: 10.1007/s00585-997-0152-9.

B. Filippov. Filament shape versus coronal potential magnetic field structure. *Monthly Notices of the Royal Astronomical Society*, 455:1406–1413, January 2016. doi: 10.1093/mnras/stv2409.

B. P. Filippov, N. Gopalswamy, and A. V. Lozhechkin. Non-radial motion of eruptive filaments. *Solar Physics*, 203:119–130, October 2001. doi: 10.1023/A:1012754329767.

P. Flandrin, G. Rilling, and P. Goncalves. Empirical Mode Decomposition as a Filter Bank. *IEEE Signal Processing Letters*, 11:112–114, February 2004. doi: 10.1109/LSP.2003.821662.

G. D. Fleishman and V. F. Melnikov. Gyrosynchrotron Emission from Anisotropic Electron Distributions. *Astrophysics Journal*, 587:823–835, April 2003. doi: 10.1086/368252.

S. T. Fletcher, W. J. Chaplin, Y. Elsworth, and R. New. Efficient Pseudo-Global Fitting for Helioseismic Data. *Astrophysics Journal*, 694:144–150, March 2009. doi: 10.1088/0004-637X/694/1/144.

T. G. Forbes and E. R. Priest. A comparison of analytical and numerical models for steadily driven magnetic reconnection. *Reviews of Geophysics*, 25:1583–1607, November 1987. doi: 10.1029/RG025i008p01583.

C. Foullon, E. Verwichte, V. M. Nakariakov, and L. Fletcher. X-ray quasi-periodic pulsations in solar flares as magnetohydrodynamic oscillations. *Astronomy and Astrophysics*, 440:L59–L62, September 2005. doi: 10.1051/0004-6361:200500169.

A. Frank, S. Bugrov, and V. Markov. Enhancement of the guide field during the current sheet formation in the three-dimensional magnetic configuration with an X line. *Physics Letters A*, 373:1460–1464, April 2009. doi: 10.1016/j.physleta.2009.02.037.

C. Franzke. Multi-scale analysis of teleconnection indices: climate noise and nonlinear trend analysis. *Nonlinear Processes in Geophysics*, 16:65–76, February 2009.

N. Freij, I. Dorotovič, R. J. Morton, M. S. Ruderman, V. Karlovský, and R. Erdélyi. On the Properties of Slow MHD Sausage Waves within Small-scale Photospheric Magnetic Structures. *Astrophysics Journal*, 817:44, January 2016. doi: 10.3847/0004-637X/817/1/44.

G. Fruit, P. Louarn, A. Tur, and D. Le Quéau. On the propagation of magnetohydrodynamic perturbations in a Harris-type current sheet 1. Propagation on discrete modes and signal reconstruction. *Journal of Geophysical Research*, 107: 1411–+, November 2002a. doi: 10.1029/2001JA009212.

G. Fruit, P. Louarn, A. Tur, and D. Le QuéAu. On the propagation of magnetohydrodynamic perturbations in a Harris-type current sheet: 2. Propagation on continuous modes and resonant absorption. *Journal of Geophysical Research (Space Physics)*, 107:1412, November 2002b. doi: 10.1029/2001JA009215.

W.-Z. Fu and L.-N. Hau. Vlasov-Maxwell equilibrium solutions for Harris sheet magnetic field with Kappa velocity distribution. *Physics of Plasmas*, 12(7):070701, July 2005. doi: 10.1063/1.1941047.

P.-X. Gao, J.-L. Xie, and H.-F. Liang. Periodicity in the most violent solar eruptions: recent observations of coronal mass ejections and flares revisited. *Research in Astronomy and Astrophysics*, 12:322–330, March 2012. doi: 10.1088/1674-4527/12/3/008.

V. Génot, F. Mottez, G. Fruit, P. Louarn, J.-A. Sauvaud, and A. Balogh. Bifurcated current sheet: model and Cluster observations. *Plan. Sp. Sci.*, 53:229–235, January 2005. doi: 10.1016/j.pss.2004.09.048.

S. E. Gibson, T. A. Kucera, D. Rastawicki, J. Dove, G. de Toma, J. Hao, S. Hill, H. S. Hudson, C. Marqué, P. S. McIntosh, L. Rachmeler, K. K. Reeves, B. Schmieder, D. J. Schmit, D. B. Seaton, A. C. Sterling, D. Tripathi, D. R. Williams, and M. Zhang. Three-dimensional Morphology of a Coronal Prominence Cavity. *Astrophysics Journal*, 724:1133–1146, December 2010. doi: 10.1088/0004-637X/724/2/1133.

M. Goossens, J. Terradas, J. Andries, I. Arregui, and J. L. Ballester. On the nature of kink MHD waves in magnetic flux tubes. *Astronomy and Astrophysics*, 503: 213–223, August 2009. doi: 10.1051/0004-6361/200912399.

M. Goossens, J. Andries, R. Soler, T. Van Doorsselaere, I. Arregui, and J. Terradas. Surface Alfvén Waves in Solar Flux Tubes. *Astrophysics Journal*, 753:111, July 2012. doi: 10.1088/0004-637X/753/2/111.

J. T. Gosling. Magnetic Reconnection in the Solar Wind. *Space Science Reviews*, 172:187–200, November 2012. doi: 10.1007/s11214-011-9747-2.

D. Gruber, P. Lachowicz, E. Bissaldi, M. S. Briggs, V. Connaughton, J. Greiner, A. J. van der Horst, G. Kanbach, A. Rau, P. N. Bhat, R. Diehl, A. von Kienlin, R. M. Kippen, C. A. Meegan, W. S. Paciesas, R. D. Preece, and C. Wilson-Hodge. Quasi-periodic pulsations in solar flares: new clues from the Fermi Gamma-Ray Burst Monitor. *Astronomy and Astrophysics*, 533:A61, September 2011. doi: 10.1051/0004-6361/201117077.

B. V. Gudiksen, M. Carlsson, V. H. Hansteen, W. Hayek, J. Leenaarts, and J. Martínez-Sykora. The stellar atmosphere simulation code Bifrost. Code description and validation. *Astronomy and Astrophysics*, 531:A154, July 2011. doi: 10.1051/0004-6361/201116520.

F. Guo, H. Li, W. Daughton, and Y.-H. Liu. Formation of Hard Power Laws in the Energetic Particle Spectra Resulting from Relativistic Magnetic Reconnection. *Physical Review Letters*, 113(15):155005, October 2014. doi: 10.1103/PhysRevLett.113.155005.

S. R. Habbal, M. Druckmüller, H. Morgan, I. Scholl, V. Rušin, A. Daw, J. Johnson, and M. Arndt. Total Solar Eclipse Observations of Hot Prominence Shrouds. *Astrophysics Journal*, 719:1362–1369, August 2010. doi: 10.1088/0004-637X/719/2/1362.

E.G. Harris. On a plasma sheet separating regions of oppositely directed magnetic field. *Nuovo Cimento*, 23:115–123, 1962.

M. G. Harrison and T. Neukirch. Some remarks on one-dimensional force-free Vlasov-Maxwell equilibria. *Physics of Plasmas*, 16(2):022106–+, February 2009a. doi: 10.1063/1.3077307.

M. G. Harrison and T. Neukirch. One-Dimensional Vlasov-Maxwell Equilibrium for the Force-Free Harris Sheet. *Physical Review Letters*, 102(13):135003–+, April 2009b. doi: 10.1103/PhysRevLett.102.135003.

D. H. Hathaway. The Solar Cycle. *Living Reviews in Solar Physics*, 7:1, March 2010. doi: 10.12942/lrsp-2010-1.

J. Hershaw, C. Foullon, V. M. Nakariakov, and E. Verwichte. Damped large amplitude transverse oscillations in an EUV solar prominence, triggered by large-scale

transient coronal waves. *Astronomy and Astrophysics*, 531:A53, July 2011. doi: 10.1051/0004-6361/201116750.

J. Heyvaerts, E. R. Priest, and D. M. Rust. An emerging flux model for the solar flare phenomenon. *Astrophysics Journal*, 216:123–137, August 1977. doi: 10.1086/155453.

A. Hillier, R. J. Morton, and R. Erdélyi. A Statistical Study of Transverse Oscillations in a Quiescent Prominence. *Astrophysics Journal Letters*, 779:L16, December 2013. doi: 10.1088/2041-8205/779/2/L16.

C. Hornsey, V. M. Nakariakov, and A. Fludra. Sausage oscillations of coronal plasma slabs. *Astronomy and Astrophysics*, 567:A24, July 2014. doi: 10.1051/0004-6361/201423524.

R. Howe, J. Christensen-Dalsgaard, F. Hill, R. W. Komm, R. M. Larsen, J. Schou, M. J. Thompson, and J. Toomre. Dynamic Variations at the Base of the Solar Convection Zone. *Science*, 287:2456–2460, March 2000. doi: 10.1126/science.287.5462.2456.

R. Howe, R. Komm, F. Hill, J. Christensen-Dalsgaard, T. P. Larson, J. Schou, M. J. Thompson, and J. Toomre. Rotation-rate variations at the tachocline: An update. *Journal of Physics Conference Series*, 271(1):012075, January 2011. doi: 10.1088/1742-6596/271/1/012075.

N. E. Huang and Z. Wu. A review on Hilbert-Huang transform: Method and its applications to geophysical studies. *Reviews of Geophysics*, 46:RG2006, June 2008. doi: 10.1029/2007RG000228.

N. E. Huang, Z. Shen, S. R. Long, M. C. Wu, H. H. Shih, Q. Zheng, N.-C. Yen, C. C. Tung, and H. H. Liu. The empirical mode decomposition and the Hilbert spectrum for nonlinear and non-stationary time series analysis. *Royal Society of London Proceedings Series A*, 454:903, March 1998. doi: 10.1098/rspa.1998.0193.

C. L. Hyder. Winking Filaments and Prominence and Coronal Magnetic Fields. *ZAp*, 63:78, 1966.

A. R. Inglis and V. M. Nakariakov. A multi-periodic oscillatory event in a solar flare. *Astronomy and Astrophysics*, 493:259–266, January 2009. doi: 10.1051/0004-6361:200810473.

A. R. Inglis, J. Ireland, and M. Dominique. Quasi-periodic Pulsations in Solar and Stellar Flares: Re-evaluating their Nature in the Context of Power-law Flare Fourier Spectra. *Astrophysics Journal*, 798:108, January 2015. doi: 10.1088/0004-637X/798/2/108.

J. Ireland, M. S. Marsh, T. A. Kucera, and C. A. Young. Automated Detection of Oscillating Regions in the Solar Atmosphere. *Solar Physics*, 264:403–431, July 2010. doi: 10.1007/s11207-010-9592-6.

J. Ireland, R. T. J. McAteer, and A. R. Inglis. Coronal Fourier Power Spectra: Implications for Coronal Seismology and Coronal Heating. *Astrophysics Journal*, 798:1, January 2015. doi: 10.1088/0004-637X/798/1/1.

H. Isobe and D. Tripathi. Large amplitude oscillation of a polar crown filament in the pre-eruption phase. *Astronomy and Astrophysics*, 449:L17–L20, April 2006. doi: 10.1051/0004-6361:20064942.

C. M. Jackman, C. S. Arridge, N. André, F. Bagenal, J. Birn, M. P. Freeman, X. Jia, A. Kidder, S. E. Milan, A. Radioti, J. A. Slavin, M. F. Vogt, M. Volwerk, and A. P. Walsh. Large-Scale Structure and Dynamics of the Magnetotails of Mercury, Earth, Jupiter and Saturn. *Space Science Reviews*, 182:85–154, August 2014. doi: 10.1007/s11214-014-0060-8.

J. Jakimiec and M. Tomczak. Investigation of Quasi-periodic Variations in Hard X-rays of Solar Flares. *Solar Physics*, 261:233–251, February 2010. doi: 10.1007/s11207-009-9489-4.

P. Jelínek and M. Karlický. Magnetoacoustic waves in diagnostics of the flare current sheets. *Astronomy and Astrophysics*, 537:A46, January 2012. doi: 10.1051/0004-6361/201117883.

A. Jenkins. Self-oscillation. *Physics Reports*, 525:167–222, April 2013. doi: 10.1016/j.physrep.2012.10.007.

D. B. Jess, R. J. Morton, G. Verth, V. Fedun, S. D. T. Grant, and I. Giagkiozis. Multiwavelength Studies of MHD Waves in the Solar Chromosphere. An Overview of Recent Results. *Space Science Reviews*, 190:103–161, July 2015. doi: 10.1007/s11214-015-0141-3.

P. S. Joarder and B. Roberts. The modes of oscillation of a prominence. III. The slab in a skewed magnetic field. *Astronomy and Astrophysics*, 277:225, September 1993.

P. S. Joarder, V. M. Nakariakov, and B. Roberts. Oscillations in Prominence Fine-Structures. *Solar Physics*, 173:81–101, June 1997. doi: 10.1023/A:1004917710650.

J. R. Kan. On the structure of the magnetotail current sheet. *J. Geophys. Res.*, 78: 3773–3781, 1973. doi: 10.1029/JA078i019p03773.

M. Karlický. Solar flares: radio and X-ray signatures of magnetic reconnection processes. *Research in Astronomy and Astrophysics*, 14:753-772, July 2014. doi: 10.1088/1674-4527/14/7/002.

C. Karoff, T. L. Campante, J. Ballot, T. Kallinger, M. Gruberbauer, R. A. García, D. A. Caldwell, J. L. Christiansen, and K. Kinemuchi. Observations of Intensity Fluctuations Attributed to Granulation and Faculae on Sun-like Stars from the Kepler Mission. *Astrophysics Journal*, 767:34, April 2013. doi: 10.1088/0004-637X/767/1/34.

M. L. Khodachenko, K. G. Kislyakova, T. V. Zaqarashvili, A. G. Kislyakov, M. Panchenko, V. V. Zaitsev, O. V. Arkhypov, and H. O. Rucker. Possible manifestation of large-scale transverse oscillations of coronal loops in solar microwave emission. *Astronomy and Astrophysics*, 525:A105, January 2011. doi: 10.1051/0004-6361/201014860.

S. Kim, V. M. Nakariakov, and K. Shibasaki. Slow Magnetoacoustic Oscillations in the Microwave Emission of Solar Flares. *Astrophysics Journal Letters*, 756:L36, September 2012. doi: 10.1088/2041-8205/756/2/L36.

S. Kim, V. M. Nakariakov, and K.-S. Cho. Vertical Kink Oscillation of a Magnetic Flux Rope Structure in the Solar Corona. *Astrophysics Journal Letters*, 797:L22, December 2014. doi: 10.1088/2041-8205/797/2/L22.

R. Kippenhahn and A. Schlüter. Eine Theorie der solaren Filamente. Mit 7 Textabbildungen. *ZAp*, 43:36, 1957.

A. G. Kislyakov, V. V. Zaitsev, A. V. Stepanov, and S. Urpo. On the Possible Connection between Photospheric 5-Min Oscillation and Solar Flare Microwave Emission. *Solar Physics*, 233:89–106, January 2006. doi: 10.1007/s11207-006-2850-y.

J. Kleczek and M. Kuperus. Oscillatory Phenomena in Quiescent Prominences. *Solar Physics*, 6:72–79, January 1969. doi: 10.1007/BF00146797.

B. Kliem, M. Karlický, and A. O. Benz. Solar flare radio pulsations as a signature of dynamic magnetic reconnection. *Astronomy and Astrophysics*, 360:715–728, August 2000.

J. A. Klimchuk. Key aspects of coronal heating. *Philosophical Transactions of the Royal Society of London Series A*, 373:20140256–20140256, April 2015. doi: 10.1098/rsta.2014.0256.

R. Knaack, J. O. Stenflo, and S. V. Berdyugina. Evolution and rotation of large-scale photospheric magnetic fields of the Sun during cycles 21-23. Periodicities, north-south asymmetries and r-mode signatures. *Astronomy and Astrophysics*, 438:1067–1082, August 2005. doi: 10.1051/0004-6361:20042091.

N. Kobanov, D. Kolobov, and A. Chelpanov. Oscillations Above Sunspots and Faculae: Height Stratification and Relation to Coronal Fan Structure. *Solar Physics*, 290:363–380, February 2015. doi: 10.1007/s11207-014-0623-6.

N. I. Kobanov and A. A. Chelpanov. The relationship between coronal fan structures and oscillations above faculae regions. *Astronomy Reports*, 58:272–279, April 2014. doi: 10.1134/S1063772914030056.

V. V. Kocharovsky, V. V. Kocharovsky, and V. J. Martyanov. Self-Consistent Current Sheets and Filaments in Relativistic Collisionless Plasma with Arbitrary Energy Distribution of Particles. *Physical Review Letters*, 104(21):215002, May 2010. doi: 10.1103/PhysRevLett.104.215002.

D. Y. Kolotkov, A.-M. Broomhall, and V. M. Nakariakov. Hilbert-Huang transform analysis of periodicities in the last two solar activity cycles. *Monthly Notices of the Royal Astronomical Society*, 451:4360–4367, August 2015a. doi: 10.1093/mnras/stv1253.

D. Y. Kolotkov, V. M. Nakariakov, E. G. Kupriyanova, H. Ratcliffe, and K. Shibasaki. Multi-mode quasi-periodic pulsations in a solar flare. *Astronomy and Astrophysics*, 574:A53, February 2015b. doi: 10.1051/0004-6361/201424988.

D. Y. Kolotkov, I. Y. Vasko, and V. M. Nakariakov. Kinetic model of force-free current sheets with non-uniform temperature. *Physics of Plasmas*, 22(11):112902, November 2015c. doi: 10.1063/1.4935488.

D. Y. Kolotkov, S. A. Anfinogentov, and V. M. Nakariakov. Empirical mode decomposition analysis of random processes in the solar atmosphere. *Astronomy and Astrophysics*, 592:A153, August 2016a. doi: 10.1051/0004-6361/201628306.

D. Y. Kolotkov, V. M. Nakariakov, and G. Rowlands. Nonlinear oscillations of coalescing magnetic flux ropes. *Phys. Rev. E*, 93(5):053205, May 2016b. doi: 10.1103/PhysRevE.93.053205.

D. Y. Kolotkov, G. Nisticò, and V. M. Nakariakov. Transverse oscillations and stability of prominences in a magnetic field dip. *Astronomy and Astrophysics*, 590:A120, May 2016c. doi: 10.1051/0004-6361/201628501.

D. Y. Kolotkov, V. V. Smirnova, P. V. Strekalova, A. Riehokainen, and V. M. Nakariakov. Long-period quasi-periodic oscillations of a small-scale magnetic structure on the Sun. *Astronomy and Astrophysics*, 598:L2, February 2017. doi: 10.1051/0004-6361/201629951.

R. W. Komm, F. Hill, and R. Howe. Empirical Mode Decomposition and Hilbert Analysis Applied to Rotation Residuals of the Solar Convection Zone. *Astrophysics Journal*, 558:428–441, September 2001. doi: 10.1086/322464.

R. Kostik and E. Khomenko. The possible origin of facular brightness in the solar atmosphere. *Astronomy and Astrophysics*, 589:A6, May 2016. doi: 10.1051/0004-6361/201527419.

N. A. Krivova and S. K. Solanki. The 1.3-year and 156-day periodicities in sunspot data: Wavelet analysis suggests a common origin. *Astronomy and Astrophysics*, 394:701–706, November 2002. doi: 10.1051/0004-6361:20021063.

N. P. M. Kuin and P. C. H. Martens. On the thermal stability of hot coronal loops - The coupling between chromosphere and corona. *Astronomy and Astrophysics*, 108:L1–L4, April 1982.

S. Kumar, V. M. Nakariakov, and Y.-J. Moon. Effect of a Radiation Cooling and Heating Function on Standing Longitudinal Oscillations in Coronal Loops. *Astrophysics Journal*, 824:8, June 2016. doi: 10.3847/0004-637X/824/1/8.

M. Kuperus and M. A. Raadu. The Support of Prominences Formed in Neutral Sheets. *Astronomy and Astrophysics*, 31:189, March 1974.

E. G. Kupriyanova, V. F. Melnikov, V. M. Nakariakov, and K. Shibasaki. Types of Microwave Quasi-Periodic Pulsations in Single Flaring Loops. *Solar Physics*, 267: 329–342, December 2010. doi: 10.1007/s11207-010-9642-0.

E. G. Kupriyanova, V. F. Melnikov, and K. Shibasaki. Spatially Resolved Microwave Observations of Multiple Periodicities in a Flaring Loop. *Solar Physics*, 284:559–578, June 2013. doi: 10.1007/s11207-012-0141-3.

J. N. Lee, R. F. Cahalan, and D. L. Wu. The 27-day rotational variations in total solar irradiance observations: From SORCE/TIM, ACRIMSAT/ACRIM III, and SOHO/VIRGO. *Journal of Atmospheric and Solar-Terrestrial Physics*, 132:64–73, September 2015. doi: 10.1016/j.jastp.2015.07.001.

K.-W. Lee and L.-N. Hau. Characteristics of magnetohydrodynamic waves in Harris-type current sheet with guide magnetic field B_y. *Journal of Geophysical Research (Space Physics)*, 113:A12209, December 2008. doi: 10.1029/2008JA013459.

E. Leonardis, S. C. Chapman, and C. Foullon. Turbulent Characteristics in the Intensity Fluctuations of a Solar Quiescent Prominence Observed by the Hinode Solar Optical Telescope. *Astrophysics Journal*, 745:185, February 2012. doi: 10.1088/0004-637X/745/2/185.

K. J. Li, X. J. Shi, H. F. Liang, L. S. Zhan, J. L. Xie, and W. Feng. Variations of Solar Rotation and Sunspot Activity. *Astrophysics Journal*, 730:49, March 2011. doi: 10.1088/0004-637X/730/1/49.

K. J. Li, W. Feng, J. C. Xu, P. X. Gao, L. H. Yang, H. F. Liang, and L. S. Zhan. Why is the Solar Constant Not a Constant? *Astrophysics Journal*, 747:135, March 2012. doi: 10.1088/0004-637X/747/2/135.

L. P. Li, J. Zhang, J. T. Su, and Y. Liu. Oscillation of Current Sheets in the Wake of a Flux Rope Eruption Observed by the Solar Dynamics Observatory. *Astrophysics Journal Letters*, 829:L33, October 2016. doi: 10.3847/2041-8205/829/2/L33.

Q. Li, J. Wu, Z.-w. Xu, and J. Wu. Extraction of the Periodic Components of Solar Activity with the EMD Method. *Chinese Astronomy and Astrophysics*, 31: 261–269, July 2007. doi: 10.1016/j.chinastron.2007.06.002.

K. G. Libbrecht and M. F. Woodard. Solar-cycle effects on solar oscillation frequencies. *Nature*, 345:779–782, June 1990. doi: 10.1038/345779a0.

R. P. Lin, B. R. Dennis, G. J. Hurford, D. M. Smith, A. Zehnder, P. R. Harvey, D. W. Curtis, D. Pankow, P. Turin, M. Bester, A. Csillaghy, M. Lewis, N. Madden, H. F. van Beek, M. Appleby, T. Raudorf, J. McTiernan, R. Ramaty, E. Schmahl, R. Schwartz, S. Krucker, R. Abiad, T. Quinn, P. Berg, M. Hashii, R. Sterling, R. Jackson, R. Pratt, R. D. Campbell, D. Malone, D. Landis, C. P. Barrington-Leigh, S. Slassi-Sennou, C. Cork, D. Clark, D. Amato, L. Orwig, R. Boyle, I. S. Banks, K. Shirey, A. K. Tolbert, D. Zarro, F. Snow, K. Thomsen, R. Henneck, A. McHedlishvili, P. Ming, M. Fivian, J. Jordan, R. Wanner, J. Crubb, J. Preble,

M. Matranga, A. Benz, H. Hudson, R. C. Canfield, G. D. Holman, C. Crannell, T. Kosugi, A. G. Emslie, N. Vilmer, J. C. Brown, C. Johns-Krull, M. Aschwanden, T. Metcalf, and A. Conway. The Reuven Ramaty High-Energy Solar Spectroscopic Imager (RHESSI). *Solar Physics*, 210:3–32, November 2002. doi: 10.1023/A:1022428818870.

W. Liu and L. Ofman. Advances in Observing Various Coronal EUV Waves in the SDO Era and Their Seismological Applications (Invited Review). *Solar Physics*, 289:3233–3277, September 2014. doi: 10.1007/s11207-014-0528-4.

A. T. Y. Lui. Current disruption in the Earth's magnetosphere: Observations and models. *Journal of Geophysical Research*, 101:13067–13088, June 1996. doi: 10.1029/96JA00079.

M. Luna and J. Karpen. Large-amplitude Longitudinal Oscillations in a Solar Filament. *Astrophysics Journal Letters*, 750:L1, May 2012. doi: 10.1088/2041-8205/750/1/L1.

M. Luna, K. Knizhnik, K. Muglach, J. Karpen, H. Gilbert, T. A. Kucera, and V. Uritsky. Observations and Implications of Large-amplitude Longitudinal Oscillations in a Solar Filament. *Astrophysics Journal*, 785:79, April 2014. doi: 10.1088/0004-637X/785/1/79.

M. Luna, J. Terradas, E. Khomenko, M. Collados, and A. de Vicente. On the Robustness of the Pendulum Model for Large-amplitude Longitudinal Oscillations in Prominences. *Astrophysics Journal*, 817:157, February 2016. doi: 10.3847/0004-637X/817/2/157.

Z. W. Ma and A. Bhattacharjee. Sudden disruption of a thin current sheet in collisionless Hall magnetohydrodynamics due to secondary tearing and coalescence instabilities. *Geophysical Research Letters*, 26:3337–3340, 1999. doi: 10.1029/1999GL003627.

S. Mandal and D. Banerjee. Sunspot Sizes and the Solar Cycle: Analysis Using Kodaikanal White-light Digitized Data. *Astrophysics Journal Letters*, 830:L33, October 2016. doi: 10.3847/2041-8205/830/2/L33.

P. C. H. Martens, G. D. R. Attrill, A. R. Davey, A. Engell, S. Farid, P. C. Grigis, J. Kasper, K. Korreck, S. H. Saar, A. Savcheva, Y. Su, P. Testa, M. Wills-Davey, P. N. Bernasconi, N.-E. Raouafi, V. A. Delouille, J. F. Hochedez, J. W. Cirtain, C. E. Deforest, R. A. Angryk, I. de Moortel, T. Wiegelmann, M. K. Georgoulis, R. T. J. McAteer, and R. P. Timmons. Computer Vision for the Solar

Dynamics Observatory (SDO). *Solar Physics*, 275:79–113, January 2012. doi: 10.1007/s11207-010-9697-y.

G. P. Mashnich and V. S. Bashkirtsev. Observations of Doppler velocity oscillations of mass motion in a quiescent prominence during three consecutive days. *Astronomy and Astrophysics*, 235:428–430, August 1990.

G. P. Mashnich and V. S. Bashkirtsev. Motions and oscillations in a filament preceding its eruption. *Astronomy Reports*, 60:287–293, February 2016. doi: 10.1134/S1063772916020086.

G. P. Mashnich, V. S. Bashkirtsev, and A. I. Khlystova. Spatial distribution of oscillations in filaments. *Geomagnetism and Aeronomy*, 49:891–897, December 2009. doi: 10.1134/S0016793209070111.

M. Mathioudakis, J. H. Seiradakis, D. R. Williams, S. Avgoloupis, D. S. Bloomfield, and R. T. J. McAteer. White-light oscillations during a flare on II Peg. *Astronomy and Astrophysics*, 403:1101–1104, June 2003. doi: 10.1051/0004-6361:20030394.

R. T. J. McAteer, C. A. Young, J. Ireland, and P. T. Gallagher. The Bursty Nature of Solar Flare X-Ray Emission. *Astrophysics Journal*, 662:691–700, June 2007. doi: 10.1086/518086.

P. I. McCauley, Y. N. Su, N. Schanche, K. E. Evans, C. Su, S. McKillop, and K. K. Reeves. Prominence and Filament Eruptions Observed by the Solar Dynamics Observatory: Statistical Properties, Kinematics, and Online Catalog. *Solar Physics*, 290:1703–1740, June 2015. doi: 10.1007/s11207-015-0699-7.

J. A. McLaughlin and A. W. Hood. MHD wave propagation in the neighbourhood of a two-dimensional null point. *Astronomy and Astrophysics*, 420:1129–1140, June 2004. doi: 10.1051/0004-6361:20035900.

J. A. McLaughlin, J. O. Thurgood, and D. MacTaggart. On the periodicity of oscillatory reconnection. *Astronomy and Astrophysics*, 548:A98, December 2012. doi: 10.1051/0004-6361/201220234.

V. F. Melnikov, V. E. Reznikova, K. Shibasaki, and V. M. Nakariakov. Spatially resolved microwave pulsations of a flare loop. *Astronomy and Astrophysics*, 439: 727–736, August 2005. doi: 10.1051/0004-6361:20052774.

V. F. Melnikov, D. E. Gary, and G. M. Nita. Peak Frequency Dynamics in Solar Microwave Bursts. *Solar Physics*, 253:43–73, December 2008. doi: 10.1007/s11207-008-9275-8.

H. Mészárosová, M. Karlický, P. Jelínek, and J. Rybák. Magnetoacoustic Waves Propagating along a Dense Slab and Harris Current Sheet and their Wavelet Spectra. *Astrophysics Journal*, 788:44, June 2014. doi: 10.1088/0004-637X/788/1/44.

I. Mochol and J. Pétri. Very high energy emission as a probe of relativistic magnetic reconnection in pulsar winds. *Monthly Notices of the Royal Astronomical Society*, 449:L51–L55, April 2015. doi: 10.1093/mnrasl/slv018.

R. Molowny-Horas, E. Wiehr, H. Balthasar, R. Oliver, and J. L. Ballester. Prominence Doppler oscillations. In *JOSO Annu. Rep., 1998*, pages 126–127, 1999.

G. Mossessian and G. D. Fleishman. Modeling of Gyrosynchrotron Radio Emission Pulsations Produced by Magnetohydrodynamic Loop Oscillations in Solar Flares. *Astrophysics Journal*, 748:140, April 2012. doi: 10.1088/0004-637X/748/2/140.

D. A. N. Müller, H. Peter, and V. H. Hansteen. Dynamics of solar coronal loops. II. Catastrophic cooling and high-speed downflows. *Astronomy and Astrophysics*, 424:289–300, September 2004. doi: 10.1051/0004-6361:20040403.

M. J. Murray, L. van Driel-Gesztelyi, and D. Baker. Simulations of emerging flux in a coronal hole: oscillatory reconnection. *Astronomy and Astrophysics*, 494: 329–337, January 2009. doi: 10.1051/0004-6361:200810406.

I. N. Myagkova, S. N. Kuznetsov, V. G. Kurt, B. Y. Yuskov, V. I. Galkin, E. A. Muravieva, and K. Kudela. X-ray, γ-emission and energetic particles in near-Earth space as measured by CORONAS-F satellite: From maximum to minimum of the last solar cycle. *Advances in Space Research*, 40:1929–1934, 2007. doi: 10.1016/j.asr.2007.01.091.

Y. A. Nagovitsyn. A nonlinear mathematical model for the solar cyclicity and prospects for reconstructing the solar activity in the past. *Astronomy Letters*, 23: 742–748, November 1997.

H. Nakajima, H. Sekiguchi, M. Sawa, K. Kai, and S. Kawashima. The radiometer and polarimeters at 80, 35, and 17 GHz for solar observations at Nobeyama. *Astronomical Society of Japan, Publications*, 37:163–170, 1985.

H. Nakajima, M. Nishio, S. Enome, K. Shibasaki, T. Takano, Y. Hanaoka, C. Torii, H. Sekiguchi, T. Bushimata, S. Kawashima, N. Shinohara, Y. Irimajiri, H. Koshiishi, T. Kosugi, Y. Shiomi, M. Sawa, and K. Kai. The Nobeyama radioheliograph. *IEEE Proceedings*, 82:705–713, May 1994.

V. M. Nakariakov. MHD oscillations in solar and stellar coronae: Current results and perspectives. *Advances in Space Research*, 39:1804–1813, 2007. doi: 10.1016/j.asr.2007.01.044.

V. M. Nakariakov and D. B. King. Coronal Periodmaps. *Solar Physics*, 241:397–409, April 2007. doi: 10.1007/s11207-007-0348-x.

V. M. Nakariakov and V. F. Melnikov. Modulation of gyrosynchrotron emission in solar and stellar flares by slow magnetoacoustic oscillations. *Astronomy and Astrophysics*, 446:1151–1156, February 2006. doi: 10.1051/0004-6361:20053944.

V. M. Nakariakov and V. F. Melnikov. Quasi-Periodic Pulsations in Solar Flares. *Space Science Reviews*, 149:119–151, December 2009. doi: 10.1007/s11214-009-9536-3.

V. M. Nakariakov and L. Ofman. Determination of the coronal magnetic field by coronal loop oscillations. *Astronomy and Astrophysics*, 372:L53–L56, June 2001. doi: 10.1051/0004-6361:20010607.

V. M. Nakariakov and E. Verwichte. Coronal Waves and Oscillations. *Living Reviews in Solar Physics*, 2:3, July 2005. doi: 10.12942/lrsp-2005-3.

V. M. Nakariakov and I. V. Zimovets. Slow Magnetoacoustic Waves in Two-ribbon Flares. *Astrophysics Journal Letters*, 730:L27, April 2011. doi: 10.1088/2041-8205/730/2/L27.

V. M. Nakariakov, V. F. Melnikov, and V. E. Reznikova. Global sausage modes of coronal loops. *Astronomy and Astrophysics*, 412:L7–L10, December 2003. doi: 10.1051/0004-6361:20031660.

V. M. Nakariakov, C. Foullon, E. Verwichte, and N. P. Young. Quasi-periodic modulation of solar and stellar flaring emission by magnetohydrodynamic oscillations in a nearby loop. *Astronomy and Astrophysics*, 452:343–346, June 2006. doi: 10.1051/0004-6361:20054608.

V. M. Nakariakov, M. J. Aschwanden, and T. van Doorsselaere. The possible role of vortex shedding in the excitation of kink-mode oscillations in the solar corona. *Astronomy and Astrophysics*, 502:661–664, August 2009. doi: 10.1051/0004-6361/200810847.

V. M. Nakariakov, C. Foullon, I. N. Myagkova, and A. R. Inglis. Quasi-Periodic Pulsations in the Gamma-Ray Emission of a Solar Flare. *The Astrophysical Journal Letters*, 708:L47–L51, January 2010a. doi: 10.1088/2041-8205/708/1/L47.

V. M. Nakariakov, A. R. Inglis, I. V. Zimovets, C. Foullon, E. Verwichte, R. Sych, and I. N. Myagkova. Oscillatory processes in solar flares. *Plasma Physics and Controlled Fusion*, 52(12):124009, December 2010b. doi: 10.1088/0741-3335/52/12/124009.

V. M. Nakariakov, C. Hornsey, and V. F. Melnikov. Sausage Oscillations of Coronal Plasma Structures. *Astrophysics Journal*, 761:134, December 2012. doi: 10.1088/0004-637X/761/2/134.

V. M. Nakariakov, S. A. Anfinogentov, G. Nisticò, and D.-H. Lee. Undamped transverse oscillations of coronal loops as a self-oscillatory process. *Astronomy and Astrophysics*, 591:L5, June 2016a. doi: 10.1051/0004-6361/201628850.

V. M. Nakariakov, V. Pilipenko, B. Heilig, P. Jelínek, M. Karlický, D. Y. Klimushkin, D. Y. Kolotkov, D.-H. Lee, G. Nisticò, T. Van Doorsselaere, G. Verth, and I. V. Zimovets. Magnetohydrodynamic Oscillations in the Solar Corona and Earth's Magnetosphere: Towards Consolidated Understanding. *Space Science Reviews*, 200:75–203, April 2016b. doi: 10.1007/s11214-015-0233-0.

T. Neukirch, F. Wilson, and M. G. Harrison. A detailed investigation of the properties of a Vlasov-Maxwell equilibrium for the force-free Harris sheet. *Physics of Plasmas*, 16(12):122102, December 2009. doi: 10.1063/1.3268771.

W. M. Neupert. Comparison of Solar X-Ray Line Emission with Microwave Emission during Flares. *The Astrophysical Journal Letters*, 153:L59, July 1968. doi: 10.1086/180220.

R. Nigam and A. G. Kosovichev. Measuring the Sun's Eigenfrequencies from Velocity and Intensity Helioseismic Spectra: Asymmetrical Line Profile-fitting Formula. *Astrophysics Journal Letters*, 505:L51–L54, September 1998. doi: 10.1086/311594.

Z. Ning. Imaging Observations of X-Ray Quasi-periodic Oscillations at 3 - 6 keV in the 26 December 2002 Solar Flare. *Solar Physics*, 289:1239–1256, April 2014. doi: 10.1007/s11207-013-0405-6.

A. A. Norton, P. Charbonneau, and D. Passos. Hemispheric Coupling: Comparing Dynamo Simulations and Observations. *Space Science Reviews*, 186:251–283, December 2014. doi: 10.1007/s11214-014-0100-4.

L. Ofman and L. Sui. Oscillations of Hard X-Ray Flare Emission Observed by RHESSI: Effects of Super-Alfvénic Beams? *The Astrophysical Journal Letters*, 644:L149–L152, June 2006. doi: 10.1086/505622.

L. Ofman and T. Wang. Hot Coronal Loop Oscillations Observed by SUMER: Slow Magnetosonic Wave Damping by Thermal Conduction. *Astrophysics Journal Letters*, 580:L85–L88, November 2002. doi: 10.1086/345548.

T. J. Okamoto, H. Nakai, A. Keiyama, N. Narukage, S. UeNo, R. Kitai, H. Kurokawa, and K. Shibata. Filament Oscillations and Moreton Waves Associated with EIT Waves. *Astrophysics Journal*, 608:1124–1132, June 2004. doi: 10.1086/420838.

T. J. Okamoto, P. Antolin, B. De Pontieu, H. Uitenbroek, T. Van Doorsselaere, and T. Yokoyama. Resonant Absorption of Transverse Oscillations and Associated Heating in a Solar Prominence. I. Observational Aspects. *Astrophysics Journal*, 809:71, August 2015. doi: 10.1088/0004-637X/809/1/71.

R. Oliver and J. L. Ballester. Oscillations in Quiescent Solar Prominences Observations and Theory (Invited Review). *Solar Physics*, 206:45–67, March 2002. doi: 10.1023/A:1014915428440.

R. Oliver, J. L. Ballester, A. W. Hood, and E. R. Priest. Oscillations of a quiescent solar prominence embedded in a hot corona. *Astrophysics Journal*, 409:809–821, June 1993. doi: 10.1086/172711.

M. Ono, G. J. Greene, D. Darrow, C. Forest, H. Park, and T. H. Stix. Steady-state tokamak discharge via dc helicity injection. *Physical Review Letters*, 59: 2165–2168, November 1987. doi: 10.1103/PhysRevLett.59.2165.

F. Q. Orrall. Observational Study of Macroscopic Inhomogeneities in the Solar Atmosphere. VIII. Vertical Chromospheric Oscillations Measured in K_{3}. *Astrophysics Journal*, 143:917, March 1966. doi: 10.1086/148567.

P. L. Pallé, C. Régulo, and T. Roca Cortés. The Spectrum of Solar p-Modes and the Solar Activity Cycle. In Y. Osaki and H. Shibahashi, editors, *Progress of Seismology of the Sun and Stars*, volume 367 of *Lecture Notes in Physics, Berlin Springer Verlag*, page 129, 1990.

N. K. Panesar, A. C. Sterling, D. E. Innes, and R. L. Moore. Destabilization of a Solar Prominence/Filament Field System by a Series of Eight Homologous Eruptive Flares Leading to a CME. *Astrophysics Journal*, 811:5, September 2015. doi: 10.1088/0004-637X/811/1/5.

E. V. Panov, A. V. Artemyev, R. Nakamura, and W. Baumjohann. Two types of tangential magnetopause current sheets: Cluster observations and theory. *Journal of Geophysical Research (Space Physics)*, 116:A12204, December 2011. doi: 10.1029/2011JA016860.

V. Pant, A. K. Srivastava, D. Banerjee, M. Goossens, P.-F. Chen, N. C. Joshi, and Y.-H. Zhou. MHD Seismology of a loop-like filament tube by observed kink waves. *Research in Astronomy and Astrophysics*, 15:1713, October 2015. doi: 10.1088/1674-4527/15/10/008.

S. Parenti. Solar Prominences: Observations. *Living Reviews in Solar Physics*, 11, March 2014. doi: 10.12942/lrsp-2014-1.

E. N. Parker. Sweet's Mechanism for Merging Magnetic Fields in Conducting Fluids. *Journal of Geophysical Research*, 62:509–520, December 1957. doi: 10.1029/JZ062i004p00509.

E. N. Parker. Spontaneous current sheets in magnetic fields : with applications to stellar x-rays. *Spontaneous current sheets in magnetic fields : with applications to stellar x-rays. International Series in Astronomy and Astrophysics, Vol. 1. New York : Oxford University Press, 1994.*, 1, 1994.

D. J. Pascoe, V. M. Nakariakov, and T. D. Arber. Sausage oscillations of coronal loops. *Astronomy and Astrophysics*, 461:1149–1154, January 2007. doi: 10.1051/0004-6361:20065986.

D. J. Pascoe, V. M. Nakariakov, and E. G. Kupriyanova. Fast magnetoacoustic wave trains in magnetic funnels of the solar corona. *Astronomy and Astrophysics*, 560:A97, December 2013. doi: 10.1051/0004-6361/201322678.

W. D. Pesnell. Predictions of Solar Cycle 24. *Solar Physics*, 252:209–220, October 2008. doi: 10.1007/s11207-008-9252-2.

A. Petrukovich, A. Artemyev, I. Vasko, R. Nakamura, and L. Zelenyi. Current Sheets in the Earth Magnetotail: Plasma and Magnetic Field Structure with Cluster Project Observations. *Space Science Reviews*, 188:311–337, May 2015. doi: 10.1007/s11214-014-0126-7.

H. E. Petschek. Magnetic Field Annihilation. *NASA Special Publication*, 50:425, 1964.

E. Priest. *Magnetohydrodynamics of the Sun*. May 2014.

E. Priest and T. Forbes. *Magnetic Reconnection*. June 2000.

C. E. Pugh, D. J. Armstrong, V. M. Nakariakov, and A.-M. Broomhall. Statistical properties of quasi-periodic pulsations in white-light flares observed with Kepler. *Monthly Notices of the Royal Astronomical Society*, 459:3659–3676, July 2016. doi: 10.1093/mnras/stw850.

Z.-N. Qu, W. Feng, and H.-F. Liang. Periodicity of the solar radius revisited by using empirical mode decomposition and the Lomb—Scargle method. *Research in Astronomy and Astrophysics*, 15:879, June 2015. doi: 10.1088/1674-4527/15/6/010.

R. Ramaty. Gyrosynchrotron Emission and Absorption in a Magnetoactive Plasma. *Astrophysical Journal*, 158:753, November 1969. doi: 10.1086/150235.

F. Reale. Coronal Loops: Observations and Modeling of Confined Plasma. *Living Reviews in Solar Physics*, 11:4, December 2014. doi: 10.12942/lrsp-2014-4.

V. E. Reznikova, K. Shibasaki, R. A. Sych, and V. M. Nakariakov. Three-minute Oscillations above Sunspot Umbra Observed with the Solar Dynamics Observatory/Atmospheric Imaging Assembly and Nobeyama Radioheliograph. *Astrophysics Journal*, 746:119, February 2012. doi: 10.1088/0004-637X/746/2/119.

V. E. Reznikova, P. Antolin, and T. Van Doorsselaere. Forward Modeling of Gyrosynchrotron Intensity Perturbations by Sausage Modes. *Astrophysics Journal*, 785:86, April 2014. doi: 10.1088/0004-637X/785/2/86.

E. Rieger, G. Kanbach, C. Reppin, G. H. Share, D. J. Forrest, and E. L. Chupp. A 154-day periodicity in the occurrence of hard solar flares? *Nature*, 312:623–625, December 1984. doi: 10.1038/312623a0.

B. Roberts. Wave propagation in a magnetically structured atmosphere. I - Surface waves at a magnetic interface. *Solar Physics*, 69:27–38, January 1981a. doi: 10.1007/BF00151253.

B. Roberts. Wave Propagation in a Magnetically Structured Atmosphere - Part Two - Waves in a Magnetic Slab. *Solar Physics*, 69:39–56, January 1981b. doi: 10.1007/BF00151254.

M. Roth, J. de Keyser, and M. M. Kuznetsova. Vlasov Theory of the Equilibrium Structure of Tangential Discontinuities in Space Plasmas. *Space Science Reviews*, 76:251–317, May 1996. doi: 10.1007/BF00197842.

J.-I. Sakai and H. Washimi. A triggering of a solar flare by magnetosonic waves in a neutral sheet plasma. *Astrophysics Journal*, 258:823–834, July 1982. doi: 10.1086/160129.

T. Sato and T. Hayashi. Externally driven magnetic reconnection and a powerful magnetic energy converter. *Physics of Fluids*, 22:1189–1202, June 1979. doi: 10.1063/1.862721.

P. H. Scherrer, J. Schou, R. I. Bush, A. G. Kosovichev, R. S. Bogart, J. T. Hoeksema, Y. Liu, T. L. Duvall, J. Zhao, A. M. Title, C. J. Schrijver, T. D. Tarbell, and S. Tomczyk. The Helioseismic and Magnetic Imager (HMI) Investigation for the Solar Dynamics Observatory (SDO). *Solar Physics*, 275:207–227, January 2012. doi: 10.1007/s11207-011-9834-2.

K. Schindler. *Physics of Space Plasma Activity*. Cambridge University Press, November 2006. doi: 10.2277/0521858976.

K. Schindler and J. Birn. Models of two-dimensional embedded thin current sheets from Vlasov theory. *J. Geophys. Res.*, 107:1193–+, August 2002. doi: 10.1029/2001JA000304.

J. Schou and T. P. Larson. Extending Global Helioseismic Measurements From MDI to HMI. In *AAS/Solar Physics Division Abstracts #42*, page 1605, May 2011.

V. Sergeev, A. Runov, W. Baumjohann, R. Nakamura, T. L. Zhang, M. Volwerk, A. Balogh, H. Rème, J. A. Sauvaud, M. André, and B. Klecker. Current sheet flapping motion and structure observed by Cluster. *Geophysical Research Letters*, 30:1327, March 2003. doi: 10.1029/2002GL016500.

Y. Shen and Y. Liu. Observational Study of the Quasi-periodic Fast-propagating Magnetosonic Waves and the Associated Flare on 2011 May 30. *Astrophysics Journal*, 753:53, July 2012. doi: 10.1088/0004-637X/753/1/53.

Y. Shen, K. Ichimoto, T. T. Ishii, Z. Tian, R. Zhao, and K. Shibata. A Chain of Winking (Oscillating) Filaments Triggered by an Invisible Extreme-ultraviolet Wave. *Astrophysics Journal*, 786:151, May 2014a. doi: 10.1088/0004-637X/786/2/151.

Y. Shen, Y. D. Liu, P. F. Chen, and K. Ichimoto. Simultaneous Transverse Oscillations of a Prominence and a Filament and Longitudinal Oscillation of Another Filament Induced by a Single Shock Wave. *Astrophysics Journal*, 795:130, November 2014b. doi: 10.1088/0004-637X/795/2/130.

K. Shibasaki. High-Beta Disruption in the Solar Atmosphere. *Astrophysics Journal*, 557:326–331, August 2001. doi: 10.1086/321651.

K. Shibata and T. Magara. Solar Flares: Magnetohydrodynamic Processes. *Living Reviews in Solar Physics*, 8:6, December 2011. doi: 10.12942/lrsp-2011-6.

P. J. A. Simões, H. S. Hudson, and L. Fletcher. Soft X-Ray Pulsations in Solar Flares. *Solar Physics*, 290:3625–3639, December 2015. doi: 10.1007/s11207-015-0691-2.

R. Simoniello, K. Jain, S. C. Tripathy, S. Turck-Chièze, C. Baldner, W. Finsterle, F. Hill, and M. Roth. The Quasi-biennial Periodicity as a Window on the Solar Magnetic Dynamo Configuration. *Astrophysics Journal*, 765:100, March 2013. doi: 10.1088/0004-637X/765/2/100.

M. I. Sitnov, L. M. Zelenyi, H. V. Malova, and A. S. Sharma. Thin current sheet embedded within a thicker plasma sheet: Self-consistent kinetic theory. *J. Geophys. Res.*, 105:13029–13044, June 2000. doi: 10.1029/1999JA000431.

M. I. Sitnov, M. Swisdak, P. N. Guzdar, and A. Runov. Structure and dynamics of a new class of thin current sheets. *J. Geophys. Res.*, 111:8204–+, August 2006. doi: 10.1029/2005JA011517.

J. M. Smith, B. Roberts, and R. Oliver. Magnetoacoustic wave propagation in current sheets. *Astronomy and Astrophysics*, 327:377–387, November 1997.

C. R. Stark and T. Neukirch. Collisionless distribution function for the relativistic force-free Harris sheet. *Physics of Plasmas*, 19(1):012115, January 2012. doi: 10.1063/1.3677268.

J. O. Stenflo. Solar magnetic fields as revealed by Stokes polarimetry. *The Astronomy and Astrophysics Review*, 21:66, September 2013. doi: 10.1007/s00159-013-0066-3.

P. Strekalova, Yu. A. Nagovitsyn, A. Riehokainen, and V. Smirnova. Long quasi-periodic variations of the magnetic field of solar small-scale magnetic structures. *Geomagnetism and Aeronomy*, 56:1–8, 2016. doi: 10.1134/S0016793216080211.

P. A. Sweet. The Neutral Point Theory of Solar Flares. In B. Lehnert, editor, *Electromagnetic Phenomena in Cosmical Physics*, volume 6 of *IAU Symposium*, page 123, 1958.

R. Sych. MHD Wave in Sunspots. *Washington DC American Geophysical Union Geophysical Monograph Series*, 216:467–487, February 2016. doi: 10.1002/9781119055006.ch27.

R. Sych and V. M. Nakariakov. Wave dynamics in a sunspot umbra. *Astronomy and Astrophysics*, 569:A72, September 2014. doi: 10.1051/0004-6361/201424049.

R. Sych, V. M. Nakariakov, M. Karlicky, and S. Anfinogentov. Relationship between wave processes in sunspots and quasi-periodic pulsations in active region flares. *Astronomy and Astrophysics*, 505:791–799, October 2009. doi: 10.1051/0004-6361/200912132.

R. A. Sych, V. M. Nakariakov, S. A. Anfinogentov, and L. Ofman. Web-Based Data Processing System for Automated Detection of Oscillations with Applications to the Solar Atmosphere. *Solar Physics*, 266:349–367, October 2010. doi: 10.1007/s11207-010-9616-2.

T. Tajima, J. Sakai, H. Nakajima, T. Kosugi, F. Brunel, and M. R. Kundu. Current loop coalescence model of solar flares. *Astrophysics Journal*, 321:1031–1048, October 1987. doi: 10.1086/165694.

T. Takahashi, A. Asai, and K. Shibata. Prominence Activation By Coronal Fast Mode Shock. *Astrophysics Journal*, 801:37, March 2015. doi: 10.1088/0004-637X/801/1/37.

E. Tandberg-Hanssen. The History of Solar Prominence Research (Review). In D. F. Webb, B. Schmieder, and D. M. Rust, editors, *IAU Colloq. 167: New Perspectives on Solar Prominences*, volume 150 of *Astronomical Society of the Pacific Conference Series*, page 11, 1998.

K. F. Tapping. Recent solar radio astronomy at centimeter wavelengths - The temporal variability of the 10.7-cm flux. *Journal of Geophysical Research*, 92: 829–838, January 1987. doi: 10.1029/JD092iD01p00829.

J. Terradas, R. Oliver, and J. L. Ballester. Application of Statistical Techniques to the Analysis of Solar Coronal Oscillations. *Astrophysics Journal*, 614:435–447, October 2004. doi: 10.1086/423332.

J. Terradas, R. Soler, A. J. Díaz, R. Oliver, and J. L. Ballester. Magnetohydrodynamic Waves in Two-dimensional Prominences Embedded in Coronal Arcades. *Astrophysics Journal*, 778:49, November 2013. doi: 10.1088/0004-637X/778/1/49.

J. Terradas, R. Soler, M. Luna, R. Oliver, J. L. Ballester, and A. N. Wright. Solar Prominences Embedded in Flux Ropes: Morphological Features and Dynamics from 3D MHD Simulations. *Astrophysics Journal*, 820:125, April 2016. doi: 10.3847/0004-637X/820/2/125.

R. A. Treumann and W. Baumjohann. Collisionless Magnetic Reconnection in Space Plasmas. *Frontiers in Physics*, 1:31, December 2013. doi: 10.3389/fphy.2013.00031.

D. Tripathi, H. Isobe, and R. Jain. Large Amplitude Oscillations in Prominences. *Space Science Reviews*, 149:283–298, December 2009. doi: 10.1007/s11214-009-9583-9.

M. Ugai and T. Tsuda. Magnetic field-line reconnexion by localized enhancement of resistivity. I - Evolution in a compressible MHD fluid. *Journal of Plasma Physics*, 17:337–356, June 1977. doi: 10.1017/S0022377800020663.

I. G. Usoskin. A History of Solar Activity over Millennia. *Living Reviews in Solar Physics*, 10:1, March 2013. doi: 10.12942/lrsp-2013-1.

D. A. Uzdensky. Magnetic Reconnection in Extreme Astrophysical Environments. *Space Science Reviews*, 160:45–71, October 2011. doi: 10.1007/s11214-011-9744-5.

G. H. J. van den Oord, N. A. J. Schutgens, and M. Kuperus. The effect of delays on filament oscillations and stability. *Astronomy and Astrophysics*, 339:225–238, November 1998.

T. Van Doorsselaere, A. De Groof, J. Zender, D. Berghmans, and M. Goossens. LYRA Observations of Two Oscillation Modes in a Single Flare. *The Astrophysical Journal*, 740:90, October 2011. doi: 10.1088/0004-637X/740/2/90.

T. Van Doorsselaere, E. G. Kupriyanova, and D. Yuan. Quasi-periodic Pulsations in Solar and Stellar Flares: An Overview of Recent Results (Invited Review). *Solar Physics*, 291:3143–3164, November 2016. doi: 10.1007/s11207-016-0977-z.

S. Vasheghani Farahani, C. Hornsey, T. Van Doorsselaere, and M. Goossens. Frequency and Damping Rate of Fast Sausage Waves. *Astrophysics Journal*, 781:92, February 2014. doi: 10.1088/0004-637X/781/2/92.

I. Y. Vasko, A. V. Artemyev, V. Y. Popov, and H. V. Malova. Kinetic models of two-dimensional plane and axially symmetric current sheets: Group theory approach. *Physics of Plasmas*, 20(2):022110, February 2013. doi: 10.1063/1.4792263.

I. Y. Vasko, A. V. Artemyev, A. A. Petrukovich, and H. V. Malova. Thin current sheets with strong bell-shape guide field: Cluster observations and models with beams. *Annales Geophysicae*, 32:1349–1360, October 2014. doi: 10.5194/angeo-32-1349-2014.

A. Vecchio and V. Carbone. On the Origin of the Double Magnetic Cycle of the Sun. *Astrophysics Journal*, 683:536–541, August 2008. doi: 10.1086/589768.

A. Vecchio and V. Carbone. Spatio-temporal analysis of solar activity: main periodicities and period length variations. *Astronomy and Astrophysics*, 502:981–987, August 2009. doi: 10.1051/0004-6361/200811024.

A. Vecchio, M. Laurenza, V. Carbone, and M. Storini. Quasi-biennial Modulation of Solar Neutrino Flux and Solar and Galactic Cosmic Rays by Solar Cyclic Activity. *Astrophysics Journal Letters*, 709:L1–L5, January 2010. doi: 10.1088/2041-8205/709/1/L1.

A. Vecchio, M. Laurenza, D. Meduri, V. Carbone, and M. Storini. The Dynamics of the Solar Magnetic Field: Polarity Reversals, Butterfly Diagram, and Quasi-biennial Oscillations. *Astrophysics Journal*, 749:27, April 2012a. doi: 10.1088/0004-637X/749/1/27.

A. Vecchio, M. Laurenza, M. Storini, and V. Carbone. New Insights on Cosmic Ray Modulation through a Joint Use of Nonstationary Data-Processing Methods. *Advances in Astronomy*, 2012:834247, 2012b. doi: 10.1155/2012/834247.

B. Vrsnak. Eruptive instability of magnetic arcades. *Astrophysics and Space Science*, 170:141–147, August 1990. doi: 10.1007/BF00652660.

B. Vrsnak, V. Ruzdjak, R. Brajsa, and F. Zloch. Oscillatory motions in an active prominence. *Solar Physics*, 127:119–128, May 1990. doi: 10.1007/BF00158517.

B. Vršnak. Processes and mechanisms governing the initiation and propagation of CMEs. *Annales Geophysicae*, 26:3089–3101, October 2008. doi: 10.5194/angeo-26-3089-2008.

B. Vršnak, A. M. Veronig, J. K. Thalmann, and T. Žic. Large amplitude oscillatory motion along a solar filament. *Astronomy and Astrophysics*, 471:295–299, August 2007. doi: 10.1051/0004-6361:20077668.

T. Wang. Standing Slow-Mode Waves in Hot Coronal Loops: Observations, Modeling, and Coronal Seismology. *Space Science Reviews*, 158:397–419, July 2011. doi: 10.1007/s11214-010-9716-1.

D. G. Wentzel. Coronal heating. *NASA Special Publication*, 450, July 1981.

F. Wilson and T. Neukirch. A family of one-dimensional Vlasov-Maxwell equilibria for the force-free Harris sheet. *Physics of Plasmas*, 18(8):082108, August 2011. doi: 10.1063/1.3623740.

M. F. Woodard and R. W. Noyes. Change of Solar Oscillation Eigenfrequencies with the Solar Cycle. *Nat.*, 318:449–+, December 1985.

D. T. Woods and L. E. Cram. High resolution spectroscopy of the disk chromosphere. VII - Oscillations in plage and quiet sun regions. *Solar Physics*, 69:233–238, February 1981. doi: 10.1007/BF00149991.

G.-p. Wu, Z. Yin, and A.-a. Xu. Description of the current in eruptive prominences with helical structure. *Chinese Astronomy and Astrophysics*, 18:212–221, April 1994. doi: 10.1016/0275-1062(94)90104-X.

Z. Wu and N. E. Huang. A study of the characteristics of white noise using the empirical mode decomposition method. *Proceedings of the Royal Society of London Series A*, 460:1597–1611, June 2004. doi: 10.1098/rspa.2003.1221.

Z. Wu and N. E. Huang. Ensemble empirical mode decomposition: a noise-assisted data analysis method. *Advances in Adaptive Data Analysis*, 1(1):1–41, 2009.

M. Yamada, R. Kulsrud, and H. Ji. Magnetic reconnection. *Reviews of Modern Physics*, 82:603–664, January 2010. doi: 10.1103/RevModPhys.82.603.

A. R. Yeates and D. H. Mackay. Initiation of Coronal Mass Ejections in a Global Evolution Model. *Astrophysics Journal*, 699:1024–1037, July 2009. doi: 10.1088/0004-637X/699/2/1024.

P. H. Yoon and A. T. Y. Lui. Model of ion- or electron-dominated current sheet. *J. Geophys. Res.*, 109:11213–+, November 2004. doi: 10.1029/2004JA010555.

P. H. Yoon and A. T. Y. Lui. A class of exact two-dimensional kinetic current sheet equilibria. *J. Geophys. Res.*, 110:1202–+, January 2005. doi: 10.1029/2003JA010308.

P. H. Yoon, M. S. Janaki, and B. Dasgupta. Kinetic model of Janaki et al.'s bifurcated current sheet. *Journal of Geophysical Research (Space Physics)*, 119: 260–267, January 2014. doi: 10.1002/2013JA019617.

D. Yuan, R. Sych, V. E. Reznikova, and V. M. Nakariakov. Multi-height observations of magnetoacoustic cut-off frequency in a sunspot atmosphere. *Astronomy and Astrophysics*, 561:A19, January 2014. doi: 10.1051/0004-6361/201220208.

V. V. Zaitsev and A. V. Stepanov. On the origin of pulsations of type iv solar radio emission. plasma cylinder oscillations (i). *Issled. Geomagn. Aeron. Fiz. Solntsa*, 37:3–10, 1975.

V. V. Zaitsev and A. V. Stepanov. On the Origin of the Hard X-Ray Pulsations during Solar Flares. *Soviet Astronomy Letters*, 8:132–134, April 1982.

L. Zelenyi and A. Artemyev. Mechanisms of Spontaneous Reconnection: From Magnetospheric to Fusion Plasma. *Space Science Reviews*, 178:441–457, October 2013. doi: 10.1007/s11214-013-9959-8.

L. M. Zelenyi and V. V. Krasnoselskikh. Relativistic Modes of Tearing Instability in a Background Plasma. *Sov. Ast.* , 23:460, August 1979.

L. M. Zelenyi, H. V. Malova, A. V. Artemyev, V. Y. Popov, and A. A. Petrukovich. Thin current sheets in collisionless plasma: Equilibrium structure, plasma instabilities, and particle acceleration. *Plasma Physics Reports*, 37:118–160, February 2011. doi: 10.1134/S1063780X1102005X.

Q. M. Zhang, P. F. Chen, C. Xia, and R. Keppens. Observations and simulations of longitudinal oscillations of an active region prominence. *Astronomy and Astrophysics*, 542:A52, June 2012. doi: 10.1051/0004-6361/201218786.

Y. Zhang, J. Zhang, J. Wang, and V. M. Nakariakov. Coexisting fast and slow propagating waves of the extreme-UV intensity in solar coronal plasma structures. *Astronomy and Astrophysics*, 581:A78, September 2015. doi: 10.1051/0004-6361/201525621.

I. V. Zimovets and A. B. Struminsky. Imaging Observations of Quasi-Periodic Pulsatory Nonthermal Emission in Two-Ribbon Solar Flares. *Solar Physics*, 258: 69–88, August 2009. doi: 10.1007/s11207-009-9394-x.

N. V. Zolotova and D. I. Ponyavin. Synchronization in Sunspot Indices in the Two Hemispheres. *Solar Physics*, 243:193–203, July 2007. doi: 10.1007/s11207-007-0405-5.